UNIVERSITY OF SOUTHAMPTON

Faculty of Engineering and Physical Sciences
School of Engineering

Institute of Sound and Vibration Research

Development of Processing Methods for Measuring Combustion Noise in Turbofan Jet Engines

by

Anthony Hart

A thesis submitted for the degree of
Doctor of Philosophy

January 2020

UNIVERSITY OF SOUTHAMPTON

ABSTRACT

FACULTY OF ENGINEERING AND PHYSICAL SCIENCES
SCHOOL OF ENGINEERING
INSTITUTE OF SOUND AND VIBRATION RESEARCH

Doctor of Philosophy

DEVELOPMENT OF PROCESSING METHODS FOR MEASURING COMBUSTION NOISE IN TURBOFAN JET ENGINES

by Anthony Hart

Reducing the noise produced by civil aircraft is a key issue in the aviation industry. Due to successful reductions of other turbofan jet engine noise sources, combustion noise is becoming a more prominent noise source. The measurement of combustion noise in the far field of an engine is complicated by the presence of other noise sources.

An established method called 3S Array was developed to measure combustion noise but its use is limited by the assumptions required to implement this method. Conditions that the measured data needs to satisfy in order for the estimate to be valid have been identified in this thesis. An empirical method for calculating confidence intervals of this method has been developed and applied to measurements of a short cowl turbofan jet engine.

Three new methods have been developed during this project to extend and enhance the 3S Array method for a wider range of scenarios. The first method combines a modal isolation method with the 3S Array method to extend its upper frequency limit in the engine duct. This method was tested in no-flow laboratory experiments and was found to be effective. The second uses an inverse method to separate the two components of combustion noise (the direct noise and the indirect noise) in the combustor combined with the 3S Array method to identify the contributions of the two components to the far field noise. This method was also tested in no-flow laboratory experiments which were partially successful due to errors in the estimated transfer functions. The third method is a new coherence-based measurement technique called 3S PCCSM which is a variation of the 3S Array method. 3S PCCSM makes it possible to use advanced source location/beamforming methods to isolate the combution noise from the other noise sources. The 3S PCCSM method was applied to acoustic measurements of a short cowl turbofan jet engine using delay-and-sum beamforming and the inverse beamforming methods. Each of the methods developed in this thesis are modular and so can be combined as needed for different scenarios. The methods developed in this thesis have applications outside the measurement of combustion noise.

Contents

List of Figures

List of Tables

Declaration of Authorship

I, Anthony Hart, declare that this thesis entitled "Development of Processing Methods for Measuring Combustion Noise in Turbofan Jet Engines" and the work presented in it are my own and has been generated by me as the result of my own original research.

I confirm that:

1. This work was done wholly or mainly while in candidature for a research degree at this University;
2. Where any part of this thesis has previously been submitted for a degree or any other qualification at this University or any other institution, this has been clearly stated;
3. Where I have consulted the published work of others, this is always clearly attributed;
4. Where I have quoted from the work of others, the source is always given. With the exception of such quotations, this thesis is entirely my own work;
5. I have acknowledged all main sources of help;
6. Where the thesis is based on work done by myself jointly with others, I have made clear exactly what was done by others and what I have contributed myself;
7. Either none of this work has been published before submission, or parts of this work have been published as:
    - A. Hart, K. R. Holland, and P. Joseph, "A 3 microphone method to separate direct and indirect combustion noise inside a turbofan jet engine annular combustor," *24th International Conference of Sound and Vibration*, no. July, 2017.
    - A. Hart, K. Holland, and P. Joseph, "Enhancing Array Techniques for Measuring Jet Engine Combustion Noise Using a Modal Isolation Method," in *2018 AIAA/CEAS Aeroacoustics Conference*, AIAA AVIATION Forum, American Institute of Aeronautics and Astronautics, June 2018.

Signed:

Date: 28/01/2020

Acknowledgements

The work presented in this thesis would not have been possible without the help and support of many people. I would like to thank Rolls-Royce Plc. for the funding they provided (via the Rolls-Royce UTC in Gas Turbine Noise at the University of Southampton) as well as the support and access to data acquired from acoustic measurements of full-scale turbofan jet engines. I would also like to thank the EPSRC for the funding they provided via the University of Southampton.

My supervisors, Dr. Keith Holland and Prof. Phil Joseph have been invaluable in the assistance and support they provided me throughout the course of my PhD project and none of this work would have been possible without their guidance. I would like to thank Charlie House for the assistance he provided with the physical set-up and calibration of microphones during my experiments in the ISVR's Large Anechoic Chamber. I would like to thank the staff at the Rolls-Royce UTC in Gas Turbine Noise and the Institute of Sound and Vibration Research at the University of Southampton who have supported me throughout my time as a student at the university and have made my time at the university so enjoyable.

Lastly, I would like to thank my family, friends, supervisors and teachers over the years that have helped me to get to this point. This would not have been possible without you.

Nomenclature

Symbols

$A_{(m,n)}$	Amplitude of a mode (m, n)	Pa
B	Bin width for a spectral estimate	Hz
BT_{eqv}	Equivalent BT product when using overlapping segments to calculate spectral estimates	
c_0	Speed of sound in air at sea level with a temperature of 20°C	m s^{-1}
c_T	Speed of sound	m s^{-1}
$E[\,]$	Expectation operator	
F_s	Sampling frequency	Samples per second
f	Frequency	Hz
$f_{m,n}$	Cut-on frequency of a mode (m, n) in an annular duct	Hz
$G(\mathbf{x}\|\mathbf{y})$	Green's function that describes the acoustic pressure at $\mathbf{x}$ due to a source at location $\mathbf{y}$	
$G_{xx}(\omega)$	One sided autospectral density of the signal $x(t)$	
$G_{xy}(\omega)$	One sided cross-spectral density of the signals $x(t)$ and $y(t)$	
$\widehat{G}_{\nu_x\nu_x}$	Estimate of combustion noise that is present in signal $x(t)$ obtained using the 3S method	
$\mathbf{G}_{xx}$	Cross-spectral matrix of the signals in the vector $\mathbf{x}$	
I	Identity matrix	
J_m	Bessel function of the first kind	
k	Acoustic wavenumber	rad m^{-1}
$k_{z(m,n)}$	Axial wavenumber for a mode (m, n) in a cylindrical duct	rad m^{-1}
M	Mach number	
M_n	Number of microphones in an array.	
m_{iso}	Isolated azimuthal mode	
$p(\mathbf{x})$	Pressure at a location $\mathbf{x}$	Pa
R_s	Specific gas constant for dry air	J $kg^{-1}K^{-1}$
R_{xx}	Autocorrelation function of the signal $x(t)$	
R_{xy}	Cross-correlation function of the signals $x(t)$ and $y(t)$	
T	Signal length	s

T_s	Static temperature	K
T_{tot}	Total temperature	K
t	Time. The convention followed in this thesis is $e^{-j\omega t}$ for the phase variation of an acoustic wave with time.	s
U	Mean velocity of a fluid flow	m s^{-1}
w_c	Window correction factor	
$x_i(t)$	A time varying signal measured at location i	
Y_m	Bessel function of the second kind	
γ	Specific ratio of heats	
$\gamma^2_{xy}(\omega)$	The coherence function of the signals $x(t)$ and $y(t)$	
$\widehat{\gamma}^2_{xy}(\omega)\|_{\text{lower}}$	Minimum value of estimated coherence function where the distribution cross-spectral estimates can be described by a gamma distribution	
λ	Acoustic wavelength	m
λ^2_r	Regularisation parameter	
μ	The mean of a random variable	
$\nu_i(t)$	A time varying combustion noise signal measured at location i	Pa
ρ_0	Density of air at sea level with a temperature of 20°C	kg m^{-3}
σ	The standard deviation of a random variable	
$\psi_{(m,n)}$	Modeshape function for the mode (m, n)	
ω	Angular frequency	rad s^{-1}
*	Complex conjugate symbol	

Operators

$^{\mathbf{H}}$	Hermitian transpose operator
^{T}	Transpose operator
$*$	Convolution operator
∇	Gradient operator

Acronyms

ACARE	Advisory Council for Aviation Research and innovation in Europe
APU	Auxiliary Power Unit
CBMT	Coherence-Based Measurement Techniques
cdf	Cumulative density function
CSA	Component Spectral Analysis
CSD	Cross-Spectral Density
CSM	Cross-Spectral Matrix
HP	High Pressure
LP	Low Pressure
MIMO	Multiple Input Multiple Output
NGV	Nozzle Guide Vanes
PCCSM	Partially Coherent Cross-Spectral Matrix
pdf	Probability density function
PSD	Power Spectral Density
SPL	Sound Pressure Level
TEENI	Turboshaft Engine Exhaust Noise Identification
The 3S method	The 3 signal measurement method
The 3S Array method	The 3 signal measurement method where the third signal is the output of a focussed beamformer.
The 3S PCCSM method	A measurement method based on the 3S method that can be used to create a Partially Coherent Cross-Spectral Matrix.

Chapter 1

Introduction

It is important for aircraft noise to be reduced as there are targets set by organisations such as ACARE [2] and government legislation which define acceptable levels of noise. If these are exceeded, airlines can face fines and some aircraft will not be allowed to fly. Heathrow airport, for example, is only allowed a limited number of arrivals and departures at night due to noise regulations. Between 11pm and 4:30am, there are no scheduled flights [3]. Noise is therefore an extremely important factor when it comes to the design of new engines. Combustion noise is becoming a more prominent noise source due to advances in the reduction of other jet engine noise sources. Development of methods to measure the combustion noise produced by a turbofan jet engine are required to isolate the combustion noise from the other noise produced by the engine.

The aviation industry is constantly striving to improve turbofan jet engine efficiency. Increasing efficiency reduces the amount of fuel required for the same journey which reduces the costs to airline operators. Companies such as Rolls-Royce are conducting research into 'lean burn' combustion technology designed to increase the fuel efficiency of their turbofan jet engines [4]. In addition to the increase in efficiency, lean burn combustors will also reduce the amount of pollution produced by the engine exhaust. It is currently unknown if lean burn combustors will produce more or less combustion noise. The development of techniques to measure the combustion noise in the far field of the engine is necessary in assessing it's importance to the total noise produced by the engine. In addition to this, these techniques allow comparisons of lean burn combustors and the current 'rich burn' combustors.

1.1 Jet engine noise sources

Combustion noise is a broadband noise phenomenon which radiates from the hot nozzle of a jet engine. Many other parts of a turbofan jet engine (Figure 1.1 is a diagram of a turbofan jet engine) contribute to the sound in the far field of a turbofan jet engine. Jet noise is also a broadband phenomenon which becomes a stronger contributor to the far field level at higher engine power conditions. Noise from the bypass duct is broadband in character and has tonal peaks at the blade passing frequency (and its harmonics) of the fan. Far field noise that propagated from the intake also has both broadband and tonal components. The presence of these

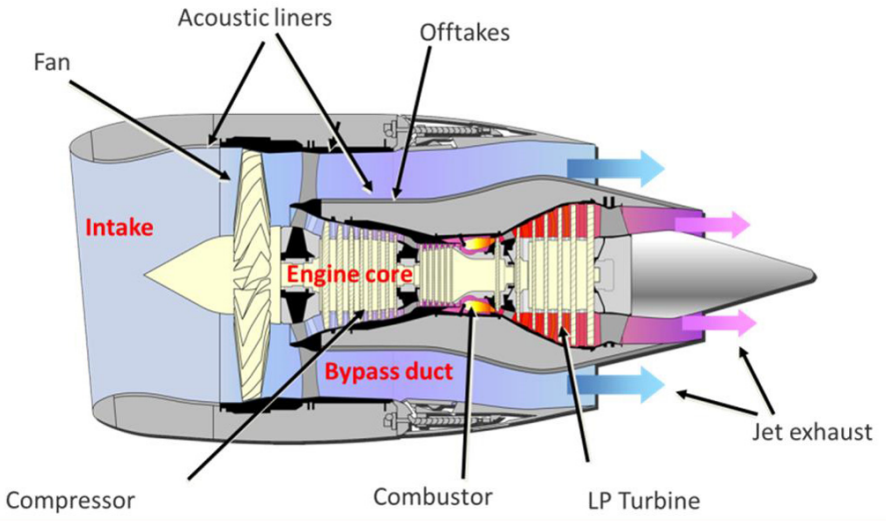

FIGURE 1.1: A diagram of a turbofan jet engine [1].

noise sources often masks the contribution of combustion noise that propagates to the far field. Noise generated by the combustion process therefore needs to be separated from the broadband noise of other sources to obtain an estimate of the combustion noise contribution. To add to the challenge, combustion noise is often a less prominent noise source than the other noise sources at higher engine power conditions.

1.1.1 Combustion noise

Combustion noise is produced in the combustor of a turbofan jet engine. Inside the combustion chamber are multiple fuel injectors, the number of which is dependent on the engine model. The fuel is ignited by a spark produced by an igniter plug resulting in a flame at each injector [5]. The unsteady heat release caused by the combustion of the fuel produces acoustic pressure waves [6]. The noise produced by this mechanism is known as the direct combustion noise as it is produced as a direct result of the combustion process. These waves then propagate through the turbine section and out of the core nozzle which will be referred to as the hot nozzle from here on.

The combustion process also produces entropy waves or 'hot spots' in the flow. These propagate through the combustor at the same velocity as the air passing through the combustor. The combustor narrows in cross-section close to the High Pressure (HP) turbine and the flow has to pass through the nozzle guide vanes (NGV). This narrowing of the cross-section causes the flow velocity to increase. As the entropy waves are accelerated through the NGV, they produce acoustic waves [6]. This is generally called indirect or entropy noise.

Another source of noise generated in the combustor is known as rumble. Dowling and Mahmoudi [6] state that rumble is caused by the entropy waves propagating downstream, being accelerated through the NGV and thus producing acoustic waves which then propagate upstream to the flame and interfere with the production of entropy waves. This feedback mechanism can produce a tonal sound with a sound pressure level high enough that it can damage the engine.

The sound produced in the combustor propagates along the duct, through the turbine sections and out into the far field. The ability to measure the individual contributions of direct and indirect combustion noise would provide insight into the combustion process. The production and propagation of combustion noise is examined in Chapter 2.

1.2 Notation for signals measured at specific engine positions

Figure 1.2 is a cross-sectional diagram of the core of a turbofan jet engine beginning at the combustor and ending at the hot exhaust nozzle. Between the combustor and the hot exhaust nozzle are the high pressure (HP) and low pressure (LP) turbines which are not drawn but the regions where they would be present are indicated on the diagram.

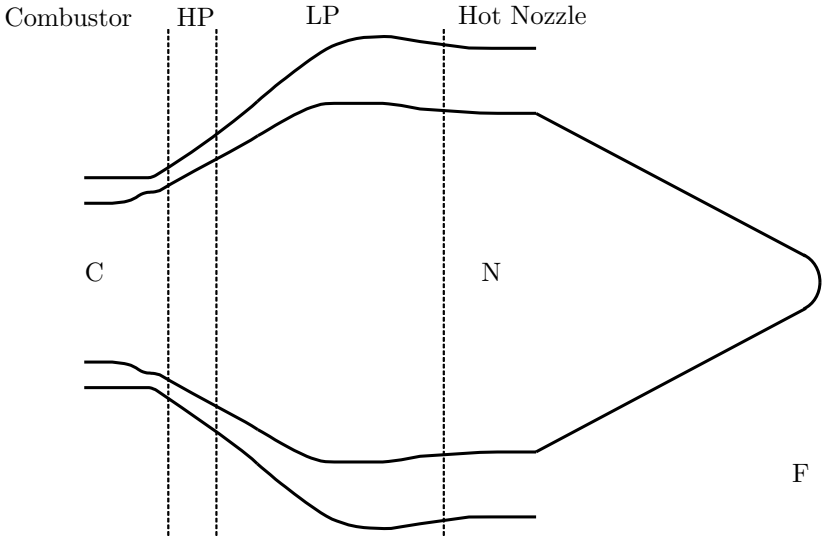

FIGURE 1.2: A cross-section of a commercial turbofan engine beginning at the combustor and ending at the hot nozzle.

Throughout this thesis, a convention for notation will be used to indicate the region the measurement took place. A pressure signal measured by a sensor in the combustor will be denoted by $C(t)$. The signals measured in the hot exhaust nozzle and the far field are denoted as $N(t)$ and $F(t)$. One-sided autospectral density of $C(t)$ is expressed as $G_{CC}(\omega)$ while the one-sided cross-spectral density of $C(t)$ and $N(t)$ is $G_{CN}(\omega)$. Only one-sided autospectral and cross-spectral densities will be used in this thesis so, for brevity, will simply be referred to as autospectral density or power spectral density (or PSD) and cross-spectral density (or CSD). Components of the signals will be indicated using subscripts so that the component of the combustor signal due to the combustion noise is noted as $\nu_C(t)$ where ν will represent combustion noise throughout this thesis.

1.3 Novel developments

During the course of this PhD project, several novel developments have been produced. These are:

- A method for isolating individual modes in an engine duct which can be combined with the combustion noise measurement method to provide a more accurate combustion noise estimate.
- The existing combustion noise measurement method is reformulated so that more advanced beamforming techniques can be used in combination with the method.
- Application of the combustion noise measurement with an advanced beamforming method on short cowl turbofan jet engine data.
- The identification of conditions which need to be met in order for the combustion noise measurement method to be valid.
- A method for calculating upper and lower confidence bounds for the combustion noise measurement method.
- Calculation of confidence intervals for combustion noise measurements of a short cowl turbofan jet engine.
- A method for separating direct and indirect combustion noise inside an annular combustor.
- Application of the combustion noise measurement method with modal isolation and the combustion noise measurement method with direct and indirect noise separation to no-flow laboratory test measurements.

1.4 Structure of Thesis

This thesis can effectively be divided into four sections which are:

1. A review of the combustion noise source mechanisms and coherence-based measurement methods.
2. Calculating limits and confidence intervals for a combustion noise measurement method and applying this to measured data.
3. Development of enhancements to the combustion noise measurement method.
4. Application of enhanced combustion noise measurement methods to experimental data.

The content of the thesis will be briefly summarised here.

1.4.1 A review of the combustion noise source mechanisms and coherence-based measurement methods

Chapter 2 describes the production of combustion noise in the combustor and how it propagates inside the engine duct. Chapter 3 is a literature review of different coherence-based measurement methods and the applications of these methods to turboshaft and turbofan jet engines. The derivation of a combustion noise measurement method called the 3S Array method, the method used and extended in this thesis, is presented in Chapter 4.

1.4.2 Calculating limits and confidence intervals for a combustion noise measurement method and applying this to measured data.

Statistical distributions of cross-spectral estimates and statistical distributions of the estimate obtained from the 3S Array method are examined in Chapter 5. Using these distributions, empirical methods for calculating confidence intervals are presented. Conditions that the signals need to meet in order for the estimate obtained from the 3S Array method to be valid are defined.

In Chapter 6, data acquired from measurements of a short cowl turbofan jet engine (provided by Rolls-Royce) is analysed. The 3S Array method is applied to the data including the newly developed confidence intervals. Two significant sources of coherence loss are identified which result in innacurate estimates of the combustion noise and limit the frequency range of the 3S Array technique.

1.4.3 Development of enhancements to the combustion noise measurement method.

A method for extending the effective frequency range of the 3S Array technique using a modal isolation method is presented in Chapter 7.

A method for measuring the direct and indirect noise that propagates to the far field is presented in Chapter 8.

A re-derivation of the 3S method is presented in Chapter 9 which provides a way of calculating partially coherent cross-spectral matricies (PCCSM). The PCCSM of an array of microphones can be calculated which is the part of the cross-spectral matrix (CSM) that is coherent with the signals from two other sensors.

1.4.4 Application of enhanced combustion noise measurement methods to experimental data.

The new methods presented in Chapters 7 and 8 are applied to no-flow laboratory experiments in Chapters 11 and 12 respectively. The configuration of the experiments is explained in Chapter 10.

The 3S PCCSM method is applied to the engine data that is introduced in Chapter 6 in Chapter 13. Final conclusions and potential avenues for future work are presented in Chapter 14.

Chapter 2

Production and propagation of combustion noise inside a turbofan jet engine

Before investigating methods for measuring combustion noise, it is useful to first understand the sources of combustion noise and it's propagation through the engine. The source mechanisms will be examined first before looking at the propagation through the engine and then out into the far field.

2.1 Combustion noise

In a modern turbofan jet engine, the combustor inlet is conneted to the outlet of a series of compressor fans. The compressor stages increase the energy potential of the air that is sucked in at the inlet of the engine. Fuel is sprayed into the combustor through many nozzles distributed around the combustor. The combination of compressed air and fuel is ignited which results in a very high temperature, high pressure air flow that is used to rotate the turbine stages. The turbines are connected to the compressor stages and the fan (which provides the thrust) by shafts in the hub of the engine.

The combustion process results in noise being produced by two sources which will be referred to as direct combustion noise and indirect combustion noise.

2.1.1 Direct combustion noise

In the combustor, there is an unsteady heat release caused by the combustion of the fuel. Dowling and Mahmoudi [6] state that this produces local volumetric expansions and contractions in the region of the flame. This results in pressure fluctuations which then propagate along the duct. This is referred to as direct combustion noise. These local volumetric expansions and contractions will occur at each of the fuel injector locations and so the number of unsteady heat

release source regions will be equal to the number of fuel injectors. As the source mechanism is localised volumetric expansions and contractions, it could be modelled as a number of incoherent monopole sources inside the combustor.

2.1.2 Indirect noise

The unsteady heat release also produces entropy waves. These convect downstream with the local mean flow velocity. When the waves reach the nozzle guide vanes (NGV) at the exit of the combustor, they are accelerated through the nozzle. As the waves pass through the nozzle, the acceleration of the entropy waves result in a pressure fluctuation at the NGV. This then propagates as an acoustic wave which is referred to as indirect combustion noise. Entropy waves will also convect through the nozzle and continue on to the turbine stages where they will undergo another acceleration, generating more indirect noise.

Marble and Candel [7] developed an approximate model for the generation of indirect combustion noise by replacing the nozzle with a discontinuity. The pressure up and downstream of the nozzle can be calculated analytically using this model. Marble and Candel's model indicates that there are both up and downstream acoustic waves produced even when the nozzle is choked.

Tam and Parrish [8] investigated the generation of indirect combustion noise. They formulated a Green's function which they solved numerically for a converging diverging nozzle. Using this they calculated both the up and downstream propagating acoustic pressure waves generated through the acceleration of the entropy waves for subsonic and supersonic flow velocities through the nozzle. They also investigated the generation of indirect noise at the turbine stages and show a numerical simulation of the generation of indirect noise when a line of entropy impinges on a turbine blade.

Tam et al. [9] use numerical simulations of indirect combustion noise generation to identify indirect combustion noise produced by a Honeywell Auxiliary Power Unit (APU) RE220. An APU is simpler than a jet engine in terms of the number of noise sources which is why Tam et al. used this to investigate indirect combustion noise. The model indicated the frequency ranges where indirect noise is likely to be present and far field measurements show two peaks (both above 2 kHz) which overlap these frequency ranges. They concluded that it is likely the peaks are caused by indirect combustion noise. Tam et al. state that it was not possible to identify indirect noise at low frequencies (below 1 kHz) which is predicted by the model due to the direct noise being dominant in this frequency range. They do show, however, that there is a peak in one of the signals measured by an in-duct probe a short distance downstream of the turbines in this frequency range.

One important difference between the direct and the indirect combustion noise is that if the combustion occurred in a free field, only direct combustion noise would be produced. This is because the indirect combustion noise can only be produced when the entropy waves undergo an acceleration.

2.2 Propagation of sound in an annular duct

The direct and the indirect combustion noise propagate through the engine. The engine core can be modelled as a hard-walled annular duct with a varying cross-section. The case of an infinite annular duct will now be examined.

An annular duct can easily be described using a cylindrical coordinate system where r is the radius of the duct, θ is the angular position around the duct cross-section and z is the position along the duct axis. The wave equation for a cylindrical coordinates system with a uniform fluid flow of U ms^{-1} along the duct is

$$\frac{\partial^2 p}{\partial r^2} + \frac{1}{r}\frac{\partial p}{\partial r} + \frac{1}{r^2}\frac{\partial^2 p}{\partial \theta^2} + \frac{\partial^2 p}{\partial z^2} - \frac{1}{{c_0}^2}\left(\frac{\partial p}{\partial t} + U\frac{\partial p}{\partial z}\right)^2 = 0 \tag{2.1}$$

where c_0 is the speed of sound in air. Assuming a separable solution of the form $p = R(r)\Theta(\theta)Z(z)T(t)$, a general solution of the wave equation in cylindrical coordinates is [10]

$$p(r, \theta, z, \omega) = [J_m(k_r r) + \beta Y_m(k_r r)]e^{jm\theta}e^{jk_z z}e^{-j\omega t} \tag{2.2}$$

where J_m and Y_m are the Bessel functions of the first and second kind respectively, m is an integer, ω is the angular frequency and

$$\frac{\omega}{c_0} = k = \pm\sqrt{{k_z}^2 + {k_r}^2} + k_z M. \tag{2.3}$$

where $M = U/c_0$ is the Mach number.

For an annular duct of infinite length, such as the one shown in Figure 2.1, there are boundaries at $r = a$ and $r = b$. For the case where the walls are hard, the particle velocity normal to the

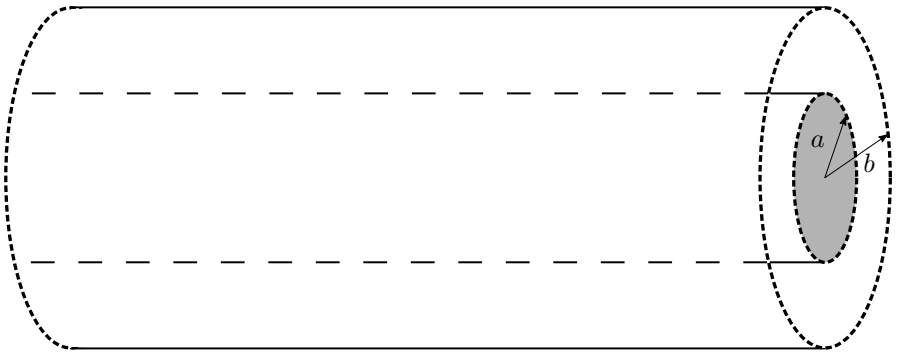

FIGURE 2.1: A diagram of an infinite hard-walled annular duct with inner radius a and outer radius b.

wall must be zero. The boundary conditions are therefore

$$\frac{\partial p}{\partial r} = \frac{\partial R}{\partial r} = 0 \quad \text{at} \quad r = a, b. \tag{2.4}$$

In this case, the function that describes the radial pressure can be expressed as

$$R(r) = J_m(k_r r) + \beta Y_m(k_r r) \tag{2.5}$$

where β is a constant. The boundary conditions are satisfied by

$$\left.\frac{\partial p}{\partial r}\right|_{r=a} = J'_m(k_r a) + \beta Y'_m(k_r a) = 0 \tag{2.6}$$

and

$$\left.\frac{\partial p}{\partial r}\right|_{r=b} = J'_m(k_r b) + \beta Y'_m(k_r b) = 0 \tag{2.7}$$

where J'_m and Y'_m are the derivatives of the Bessel functions of the first and second kind respectively. Here there are two unknowns, k_r and β that need to be found. Multiplying Equation (2.6) by $\beta Y'_m(k_r b)$ and Equation (2.7) by $\beta Y'_m(k_r a)$ and then subtracting the two equations yields

$$J'_m(k_r a)Y'_m(k_r b) - J'_m(k_r b)Y'_m(k_r a) = 0. \tag{2.8}$$

As the Bessel functions are oscillating functions, there will be an infinite number of values of k_r which satisfy this expression. We will therefore redefine the notation of k_r as $k_{r(m,n)}$ where n is the $(n-1)^{\text{th}}$ zero for a single m. The values of m and n represent the azimuthal and radial mode numbers and $k_{r(m,n)}$ is the radial wavenumber. The values of $k_{r(m,n)}$ can then be substituted into either Equation (2.6) or Equation (2.7) to obtain values of β which will be denoted by $\beta_{(m,n)}$ for a mode (m, n). Rearranging Equation (2.3) yields

$$k^{\pm}_{z(m,n)} = \frac{\pm\sqrt{k^2 - (1-M^2)k_{r(m,n)}{}^2} - Mk}{1-M^2} \tag{2.9}$$

where $k_{z(m,n)}$ is the axial wavenumber. As $k = \omega/c$, there will be frequencies where $k^2 < (1-M^2)k^2_{r(m,n)}$ which will result in an imaginary axial wavenumber. At these frequencies, the mode will not propagate along the duct but will instead exponentially decay and these are known as evanescent waves. There will therefore be a 'cut-on' frequency at which the mode will begin to propagate. These cut-on frequencies are defined as

$$\omega_{(m,n)} = c\sqrt{(1-M^2)}k_{r(m,n)}. \tag{2.10}$$

The pressure field inside the duct is equal to the sum of all of the modes and so can be expressed as

$$p^{\pm}(r,\theta,z,\omega) = \sum_{m,n} A^{\pm}_{(m,n)}\psi_{(m,n)}(r,\theta)e^{\pm jk^{\pm}_{z(m,n)}z}e^{-j\omega t} \tag{2.11}$$

where $(+)$ and $(-)$ represent waves travelling in the positive and negative z direction respectively and $A_{(m,n)}$ is the modal amplitude which is dependent on noise sources in the duct and $\psi_{(m,n)}(r,\theta)$ is the modeshape function. The modeshape function is defined as

$$\psi_{(m,n)}(r,\theta) = \frac{1}{\alpha_{(m,n)}}[J_m(k_{r(m,n)}r) + \beta_{(m,n)}Y_m(k_{r(m,n)}r)]e^{jm\theta} \tag{2.12}$$

where $\alpha_{(m,n)}$ is a normalisation factor chosen such that

$$\int_S \psi_{(m,n)}(r,\theta)\psi_{(m,n)}(r,\theta)\mathrm{d}S = 1 \tag{2.13}$$

where S is the area of the duct.

The core of a turbofan jet engine is an annular duct with a varying cross-section. In such a duct, modes which are cut-on in some regions may not be in others. Rienstra [11], has developed an analytical method for modelling sound propagation through a duct of slowly-varying arbitrary cross-section. Rienstra explains that modes can change from being cut-on to cut-off (where the mode exponentially decays) at locations in the duct where the geometry changes enough that the cut-on frequency becomes larger than the frequency of the mode that is propagating. At these locations, sound can be reflected as well as transmitted. The propagation path of the combustion noise inside the jet engine is additionally complicated by turbine blades as well as other pieces of structure. The calculations of the azimuthal and radial mode cut-on frequencies are important for identifying how the sound propagates in the jet engine and these calculations are still valid for a finite length duct.

Chapter 3

Literature Review

This chapter will review current measurement techniques for the measurement of combustion noise. This review will focus on methods which use a combination of sensors inside the engine and in the far field. There are several methods which use just far field measurements to measure core noise. Miles [12], for example, uses 4 microphones on a polar array in the far field of an engine to measure the core noise. These methods can provide inaccurate estimates due to noise from other sources (jet, bypass etc.). Tester et al. [13] and Tester [14] use a method called AFINDS to identify core noise, fan noise and jet noise. AFINDS requires data from a phased microphone array in the far field and coherence models of the separate sound sources. Using this information, the method applies a non-linear least-squares method to identify the separate sources and the source directivities from the measured data. AFINDS can provide a total core noise spectra. For long cowl engines the noise radiated from the single outlet nozzle will include other noise sources, such as fan noise, not just the combustion noise. AFINDS measurements have been used in conjunction with an analytic directivity model which accounts for radiation, convection and refraction effects through a jet to produce a new core noise prediction method for long cowl engines by Ekoule et al. [15].

Another method which uses an external microphone array, developed by DLR and Rolls-Royce Deutschland, called SODIX is applied to a BR700 series engine by Funke et al. [16]. SODIX is an inverse method which is applied to the signals from a microphone array external to the engine. SODIX calculates the equivalent strengths and directivities of sources along the centreline of the jet and on the casing of the engine which will produce a cross-spectral matrix that approximates the one measured. For long cowl engines the noise localised at the engine outlet nozzle will include noise sources other than the combustion noise.

In Chapter 6, data of a short cowl turbofan jet engine is analysed. The engine test takes place in an indoor test cell. Indoor test cells are reverberant and Böhning et al. [17] examine the reverberation characteristics of a test cell at Rolls-Royce Dahlewitz. Two methods are presented, one developed by DLR and the other by the ISVR, to take the effects of the reverberation in the test cell into account. The DLR method relies on a combination of microphone placement, absorbent material on the walls and a method called the Reflection Canceller. DLR define the best place for the microphones to be positioned is in the corner of the room between the floor and a side wall which has the effect of quadrupling the measured pressure when compared to the

same measurement performed under free field conditions. The positions of the microphones along the edge reduces the number of surfaces that will directly reflect sound towards the microphone array to two: the celling and the wall opposite to the array (measurements using this method are presented in Siller et al. [18]). They show that acoustic treatment on these walls significantly reduces the effect of reflections above low frequencies. At low frequencies the treatment is less effective and so the Reflection Canceller is used. The Reflection Canceller calculates where the image source location(s) for a given source will be and uses this information and standard delay-and-sum beamforming (discussed in Chapter 4) to calculate the sound propagating from a particular source more accurately. The ISVR method used the inverse beamforming technique with measured Green's functions that will include the reverberation in the test cell. This method is discussed in more detail in Chapter 9.

Coherence-based methods utilising sensors inside the engine allow for better isolation of the combustion noise from the other noise sources. These methods can be used to estimate the contribution to an autospectral estimate that is coherent between all of the measured spectra. For the application of measuring combustion noise, the contribution of the combustion noise to the autospectral estimate of a far field microphone can be estimated by using the estimated coherence function between pressure sensors in the duct and the external microphone. The benefit of using coherence-based measurement techniques (CBMT) is that CBMT do not require models of the sources. Therefore, as long as the required assumptions are met and the data is of good quality, the resulting estimate should be accurate. There are various methods which can be used to estimate the combustion noise in the far field and these will be examined in this review.

3.1 Analysis of sensors external to and inside jet engines

Siller et al. [19] examined the coherence between rumble probes mounted inside the combustor of a Rolls-Royce BR700 turbofan jet engine and a linear microphone array external to the engine which covers the angles ranging from 60° to 135°. The array was divided into a series of sub-arrays and the coherence between these sub-arrays and the combustor probe is high below 300 Hz for low engine powers. Siller et al. state that this indicates the combustion noise is a major contributor at low frequencies. As engine power increases, the coherence between the combustor probe and the external sub-arrays decreases, suggesting that other noise sources become dominant at higher engine powers.

Miles [20] presents a method for identifying direct and indirect combustion noise by analysing the delays between in-duct and external sensors. The method involves filtering the signals with low-pass filters which Miles gives the coefficients for. He applies the method to a Honeywell TECH977 jet engine and the results suggest that the indirect combustion noise is present in the 0 - 200 Hz frequency range while the direct combustion noise is present in the 200 - 400 Hz range. Rodríguez-García and Holland [21] examine the time delays between signals recorded by internal and external sensors in the ANTLE demonstrator engine. They use the same method as Miles but the results are inconclusive and thus, they are not able to identify frequency ranges where either the direct or indirect noise are definitely dominant. Rodríguez-García and Holland state that this could be due to the fact that they are applying the method to a different engine which is likely to have different noise characteristics.

3.2 Coherence output power spectrum

One of the simplest coherence-based measurement techniques is a two microphone method often called the coherence output power spectrum (COP) method. This technique was first presented by Halvorsen and Bendat [22]. The technique relies on the signal that needs to be measured (the 'wanted' signal) being the only coherent signal between the two microphones. Any other noise measured must be incoherent with the wanted signal and the noise measured at the other microphone. In the case of combustion noise measurements, one microphone would be located in the core of the engine and the other would be located in the far field. The signals measured at the microphones can be expressed as

$$C(t) = \nu_C(t) + n_C(t)$$
$$F(t) = \nu_F(t) + n_F(t)$$

where $C(t)$ and $F(t)$ represent the pressure signals measured using microphones located in the combustor and far field respectively. $\nu(t)$ and $n(t)$ represent the combustion noise signal and the unwanted noise signal (which can be acoustical, electrical and/or hydrodynamic) respectively. The coherence between these two signals can be expressed as

$$\gamma^2_{CF}(\omega) = \frac{|G_{CF}(\omega)|^2}{G_{CC}(\omega)G_{FF}(\omega)} = \frac{\gamma^2_{\nu_C\nu_F}(\omega)}{1 + \frac{G_{n_Cn_C}(\omega)}{G_{\nu_C\nu_C}(\omega)} + \frac{G_{n_Fn_F}(\omega)}{G_{\nu_F\nu_F}(\omega)} + \frac{G_{n_Cn_C}(\omega)G_{n_Fn_F}(\omega)}{G_{\nu_C\nu_C}(\omega)G_{\nu_F\nu_F}(\omega)}}.$$

For the case where the combustion noise is completely coherent between the combustor and far field sensors, $\gamma^2_{\nu_C\nu_F}(\omega) = 1$. The combustion noise measured at the far field location can be obtained provided that $G_{\nu_C\nu_C}(\omega) >> G_{n_Cn_C}(\omega)$ using

$$G_{FF}(\omega)\gamma^2_{CF}(\omega) \approx G_{\nu_F\nu_F}(\omega).$$

If the assumption above is not valid, the method will provide an underestimate of the combustion noise, the level of which is dependent on the level of incoherent noise present in both signals.

Initial work was done by Karchmer and Reshotko [23] looking at the coherence and cross-spectrum between in-engine measurements and far field measuements of a Lycoming YF-102 turbofan jet engine which has a reverse annular combustor. A reverse annular combustor is a combustor which has two 180° changes in flow direction. They concluded that core noise is a low frequency phenomenon. Karchmer et al. [24] continued this work, stating that core noise was present below 250 Hz with a peak near 125 Hz. It was also found that there was a peak in the core noise at 120° to the inlet axis. Reshotko and Karchmer [25] conducted measurements of a Pratt and Whitney JT15D turbofan jet engine which also has a reverse annular combustor. Again they find that there is high coherence below 250 Hz between the combustor and far field measurements. They also found a second region of high coherence between the probe after the turbine stage and the far field for the frequency range 250-500 Hz. They show that the coherence at low frequencies drops as engine speeds are increased, with the measurements taken at engine speeds above 65% of maximum being dominated by jet mixing noise. They compare the results of the JT15D to the YF-102 and state that at low engine powers and at frequencies below 250 Hz, there is good agreement between results. They suggest that this is likely due to the combustor design being similar.

This method has also been used for combustion noise measurements by Harper-Bourne et al [26] when conducting measurements of the Rolls-Royce ANTLE engine at the INTA facility in Spain. For this test, there were 6 rumble probes in the engine (2 in the combustor, 2 in the combustor outer casing and 2 slightly upstream of the hot nozzle) and 6 microphones on the floor of the test cell evenly spaced at angles 50° to 90° to the hot nozzle. They note that there is a difference in the output in the COP technique depending on whether the probes in the combustor or the probes in the hot nozzle are paired with the microphones to provide the combustion noise estimate. They state that this is due to direct noise being dominant in the signal measured in the combustor while both direct and indirect noise are present in the hot nozzle measurement as it is downstream of the turbines.

Miles [27] has also used COP to measure the combustion noise that propagates to the far field from a Honeywell TECH977 engine. The test set-up consisted of a far field polar array and a number of in duct sensors. To improve the coherence between the sensors, he used a method to calculate the phase delay of the cross spectra between the two microphones and used this to time align the signals. In doing this he noted that in the region of 0-200 Hz, a delay of 90.027 ms provided best coherence with the 130° microphone while 86.975 ms provided the best coherence for 200-400 Hz. These delays are dependent on the flow speed inside the engine, dimensions of the engine and the distance from the engine core nozzle to the far field microphone. Miles concluded that the difference in delay is due to the direct and indirect noise taking different amounts of time to propagate to the far field. He stated that the 0-200 Hz band must be where indirect combustion noise is dominant as the entropy waves will convect with the flow speed, which is slower than the sound speed, to the turbine stages.

Boyle et al. [28] investigated the core noise produced by a Price Induction DGEN 380 turbofan engine in the Aero-Acoustic Propulsion Laboratory at NASA Glenn Research Centre during the summer of 2017. They used a far field array of microphones as well as one microphone 10 ft from the hot nozzle exit which they refer to as the midfield microphone. Differential unsteady pressure transducers were also used in what the authors refer to as an infinite-tube-pressure (ITP) configuration. The ITP configuration is where the pressure transducer and a thermocouple are flush-mounted in the sides of a tube, one end of which is 1 ft from the transducer and was placed just inside the hot nozzle. The other end is approximately 50 ft away from the transducer and is connected to other ITP lines. Two ITP sensors were used in this experiment with one sensing at the 6 o'clock position of the not nozzle exit and the other at the 7 o'clock position.

Boyle et al. used the COP method in their investigation of the core noise to identify the components of the midfield and far field spectra that are due to the core noise. They present results at 60%, 70%, 80% and 90% power and there is a significant 'hump' in the core noise estimates produced using the COP method between 200 and 400 Hz far all engine powers in both the midfield and the far field. They also note that at 60% and 70% power there is a second hump in the estimate between 700 Hz and 1000 Hz when the IPT at the 7 o'clock position is used as the internal sensor. Boyle et al. provide estimates of the cut-on frequencies of the first azimuthal mode for different engine powers. They suggest that the second hump is associated with the cut-on of the first azimuthal mode although they were unsure why this hump only appears when the 7 o'clock sensor is used and plan further work to investigate this.

3.3 The 3S technique

The 3S technique is a 3 sensor technique originally developed by Chung [29] for the removal of flow noise from microphone measurements. It was later applied to jet engine core noise at NASA by Krejsa [30] [31]. For the application of measuring the combustion noise that propagates to the far field, two of the sensors are located in the engine core and one in the far field. As with the COP method, the 3S technique relies on the only coherent signal between the microphones being the wanted signal (in this case combustion noise) and any other noise being incoherent between microphones. Unlike the COP method, the 3S technique is not dependent on the uncorrelated noise sources and therefore, does not suffer from the bias that the COP technique suffers from. The 3S technique will be fully described in Chapter 4 but the estimate for the combustion noise present in the far field that can be obtained using this technique is given by

$$G_{\nu_F\nu_F}(\omega) = G_{FF}(\omega)\left(\frac{|\gamma_{CF}(\omega)||\gamma_{NF}(\omega)|}{|\gamma_{CN}(\omega)|}\right) = \frac{|G_{CF}(\omega)||G_{NF}(\omega)|}{|G_{CN}(\omega)|}.$$

where $G_{\nu_F\nu_F}(\omega)$ represents the estimated combustion noise autospectra in the far field. Note that the 3S technique is not dependent on the uncorrelated noise as long as the cross spectra have been calculated using a sufficient number of averages.

This technique was compared to the COP technique by Hultgren and Miles [32] on data obtained during the NASA/Honeywell EVNERT program. The sensors were located inside the combustor, the hot nozzle outlet and in the far field at 130° to the centreline of the hot nozzle. Hultgren and Miles also found the combustion noise estimate of COP was dependent on the location of the sensor inside the engine. They attributed the difference to the inherent bias in the COP method as the level of noise that does not propagate to the far field is significantly higher in the combustor than in the hot nozzle. Hultgren and Miles compared their results with the work Harper-Bourne et al. [26] did using the COP technique. They stated that the differences in the results obtained by Harper-Bourne et al. when using the combustor and hot nozzle sensors is not due to only having direct noise in the combustor and both direct and indirect in the hot nozzle. Instead, they attribute the differences to the significantly higher level of the unwanted noise in the combustor which adds bias to the results. They also cite the work done by Miles [27] on the aligned coherence method in which Miles states that the direct noise occurs at higher frequencies than the indirect noise which is the opposite to what Harper-Bourne found.

3.3.1 Comparison with Large Eddy Simulation

Livebardon et al. [33] have applied the 3S technique to a helicopter engine with a reverse annular combustor. There were a number of microphones in the combustor, just after the HP turbine, between the first and second power turbine stages and in the extended hot nozzle. There were also thermocouples in the hot nozzle and HP turbine to measure temperature fluctuations. They used the 3S technique to identify and locate the direct and the indirect noise. They state that the direct noise consists of a narrow broadband peak close to 200 Hz. Livebardon et al. also found significant broadband noise below 1500 Hz which is generated at the HP turbine and suggest that this could be the indirect noise.

Livebardon et al. then use Large Eddy Simulations (LES) and an analytical model of acoustic propagation and generation of core noise in a turbine which is called CHORUS. They call this combined technique CONOCHAIN. They found that the CONOCHAIN simulations underpredicted the contribution of direct noise when comparing to the 3S measurements. They also discovered that the technique provides a reasonable estimation of the broadband noise due to indirect noise below 1500 Hz. They show that a model for entropy wave attenuation is required as the method appears to over predict the level of the entropy noise. Overall, for this configuration of engine, they show that the direct noise is significantly lower in level than the indirect noise.

One important thing to note is that the measurements used do not appear to take into account the propagation of higher order modes inside the engine. This could have a significant effect on the measured results at higher frequencies. It is also possible that other coherent noise sources (such as indirect noise) were present in the 3S measurements of direct noise, resulting in higher measured levels than the simulated levels of direct noise.

3.3.2 Aligned and unaligned coherence

Miles fully describes his time alignment method in a 2006 paper [34] in which he applies it to far field, COP and 3S measurements of a Pratt and Whitney PW4098 turbofan jet engine. To implement this method, Miles uses the phase of the cross-spectra of pairs of microphones to estimate the time delay between the measured signals in the frequency range of interest. Miles then 'aligns' the measured signals by applying delays so that there will be zero delay between the measured signals and thus, maximising the coherence in the frequency range of interest. The unaligned coherence is calculated by delaying the signals such that, in the frequency range of interest, the phase delay will be longer than the time window so that the broadband signals are no longer coherent. With this information, it is possible to identify a coherence 'noise floor' which is useful for cases when the coherence between two sensors is low. This is very significant for combustion noise measurements as the magnitude squared coherence is often around and below 0.1. In addition to this, the unaligned coherence is also capable of isolating tones from broadband noise as tones will be coherent even with large phase delays. When Miles [27] examined the phase of the cross spectra for the Honeywell TECH977, he found two separate phase delays and could isolate the coherent part of one with the far field from the other by aligning the data using the different delays. He attributes the two different delays to the presence of direct and indirect noise in both measurements as stated earlier.

Miles further develops this method and applies it to more engine data [12, 20, 35, 36]. Miles has also applied the aligned and unaligned method to open rotor measurements to isolate tones from broadband noise [37].

3.3.3 Linear systems theory

Based on work done with his aligned and unaligned coherence technique, Miles [38] has used linear systems theory to calculate the autospectra at the turbine exit pressure and the cross-spectra between the combustor and the turbine exit. Miles has used measured data to inform

the calculation of a set of transfer functions which can be used to describe the propagation of the combustion noise. This is to aid in the identification of indirect noise in far field measurements. The model works at frequencies below 400 Hz for low engine power conditions but does not work for the entire frequency range in some cases. Miles states that indirect combustion noise dominates in the 0-50 Hz frequency range and that direct combustion noise is dominant up to 400 Hz. He also states that it is necessary to have two separate sets of parameters for the model, one for the region dominated by indirect noise and one for the direct noise. At 50 Hz this results in a discontinuity and between 0-50 Hz, the model has limited success. However, Miles states that as the indirect noise is known to be dominant in this region, it is of little consequence.

This was expanded by Miles [39] to include the ability to calculate the ratio of direct to indirect noise which, for the engine this method was applied to (Honeywell TECH977), was 26% for the lowest engine power and decreased to 5% for the highest engine power. Miles also describes measurements which might be useful for predicting NOx and soot levels inside the combustor. This is done by measuring the post-combustion residence time (the time taken for entropy waves to convect from the flame to the turbine entrance) in the combustor. Miles does not, however, describe the method for predicting NOx and soot levels.

3.4 The 3S Array method

Rodríguez-García et al. [40] adapted Chung's 3S method [29] by substituting the far field sensor for the output of a microphone array used as a time-domain beamformer. This new method is called 3S Array. The time-domain beamformer is used as a highly directional microphone and can be 'focused' on to the hot nozzle exit thus filtering out sound that arrives from other directions. This is to prevent other noise sources such as jet noise from being coherent between the hot nozzle and the far field measurement locations which would invalidate the assumptions of the 3S technique and result in an error in the combustion noise estimate. Rodríguez-García et al. use a delay-and-sum beamforming technique which will be described in Chapter 4.

In this paper, Rodríguez-García et al. use simulated data to compare the COP, 3S and 3S Array techniques for 3 cases which are:

1. Combustion noise only at each simulated microphone
2. Combustion noise plus uncorrelated noise at each simulated microphone
3. Combustion noise plus uncorrelated noise at each simulated microphone plus a noise from a source located away from the nozzle which contaminates both the nozzle and far field microphones.

For the first case, all three techniques produce accurate estimates of the combustion noise spectra. The second case shows the inherent bias in the COP technique, while the 3S and 3S Array methods produce estimates which are reasonably accurate ($\pm$ 3 dB) at most frequencies. The authors also show the bias error in these results which indicates that COP performs the worst (by a significant amount) and 3S Array has slightly less bias error than 3S. For the third case, the 3S Array technique obtains a very accurate estimate of the combustion noise source while

the estimate using the 3S method has significantly more error than the 3S Array estimate. This indicates that the 3S Array technique does provide the expected performance improvement over 3S.

Rodríguez-García et al. applied the 3S Array technique to the same ANTLE engine data that Harper-Bourne [26] applied the COP technique to. In these measurements, the microphone array is a spiral array made up of 52 microphones. Between 100 Hz and 300 Hz, which is the frequency range where Rodríguez-García et al. expected the combustion noise to be present, the 3S and 3S Array technique produce similar results. This is likely due to the beamformer having a very wide directivity lobe at low frequencies. This results in contributions from sounds arriving from directions other than the focus direction to be only attenuated by small amounts. At higher frequencies the estimates produced by the two techniques do differ.

The 3S Array technique was also applied to measurements of a Rolls-Royce BR700 which were taken at a Rolls-Royce indoor test cell in Dahlewitz, Germany in 2011. For these measurements, the microphone array is a linear microphone array. The 3S Array estimate of the combustion noise is generally lower than the 3S technique which suggests that the 3S is overestimating the combustion noise due to coherent noise between the nozzle and far field sensor. The two provide the same estimated combustion noise level at about 450 Hz. As both techniques agree, it is likely that this is due to a strong combustion noise signal present at this frequency. Rodríguez-García et al. also compare the output of the beamformer to measurements taken of the same engine at the Stennis. AFINDS was also applied to this data. The output of the beamformer in the Dahlewitz measurements agree closely with the AFINDS core noise source spectra. This indicates that the beamformer output is not affected by reflections in the test cell and is performing as expected.

The paper written by Rodríguez-García et al. was produced as part of Rodríguez-García's PhD project. His thesis [41] examines in further detail the implementation of the 3S Array method on the ANTLE and BR-700 engines and the importance of microphone array design on the performance of the time-domain beamformer. Rodríguez-García also investigates the use of cross-spectral estimates to measure combustion noise and investigate delays between the sensors. His results indicate that direct and indirect noise occupy the same frequency range.

The 3S Array technique is applied to measurements of a short cowl turbofan jet engine in Chapter 6.

3.5 Conditional spectral analysis in a coherence-based measurement technique

Hsu and Ahuja [42] developed a technique which utilises 5 microphones to separate ejector internal mixing noise which propagates to the far field of a mixer nozzle from background noise present in the far field. This utilises a combination of the 3S technique and conditional spectral analysis (CSA) to obtain estimates of these signals. Conditional spectral analysis is the term these authors use to describe a method of analysis where a signal is made 'conditional' on a specific sound source. This can be confusing as the term conditional does not indicate what has been done to the signal. CSA is essentially a partial coherence method (partial coherence is

described by Bendat [43]) which removes the part of a spectra that is coherent with one source from the original spectra so that the new spectra is only partially coherent with the original.

The CSA technique is used to obtain spectral estimates of two different 'wanted' signals which are not correlated with each other. The technique assumes that 3 of the microphones measure both wanted signals plus unwanted noise which is incoherent between microphones. The other 2 microphones measure only one of the wanted signals (the same one), plus unwanted noise that is incoherent between microphones.

Hsu and Ahuja apply this technique in an experiment to separate internal mixing noise and extraneous background noise in the far field of a mixer nozzle exhausting into an ejector duct. In the experiment there were 3 microphones in the far field (x_1, x_2 and x_3) and 2 in the ejector duct (x_4 and x_5). The internal mixing noise that propagates to the far field is present at (and coherent between) all 5 microphones. There is also correlated background noise which is assumed to be present only at the microphones in the far field. Other noise from various sources is assumed to be present at, but incoherent between, all 5 microphones. To obtain a spectral estimate of the noise in the ejector that propagates to the far field, ϕ, the 3S technique can be used as follows:

$$G_{\phi_1\phi_1}(\omega) = \frac{|G_{x_1x_4}(\omega)||G_{x_1x_5}(\omega)|}{|G_{x_4x_5}(\omega)|},$$
$$G_{\phi_2\phi_2}(\omega) = \frac{|G_{x_2x_4}(\omega)||G_{x_2x_5}(\omega)|}{|G_{x_4x_5}(\omega)|},$$
$$G_{\phi_3\phi_3}(\omega) = \frac{|G_{x_3x_4}(\omega)||G_{x_3x_5}(\omega)|}{|G_{x_4x_5}(\omega)|}.$$

To separate the background noise, θ, from the internal mixing noise that propagates to the far field, Hsu and Ahuja use conditional spectral analysis. In the case of this paper, conditional spectral analysis refers to the removal of one linear component (in this case ϕ) from the cross spectra of the far field microphones. The contribution of θ to the spectra of microphones 1, 2 and 3 is given by Hsu and Ahuja as

$$G_{\theta_1\theta_1}(\omega) = \frac{\left|G_{x_1x_2}(\omega) - \frac{G_{x_1x_4}(\omega)G_{x_5x_2}(\omega)}{G_{x_5x_4}(\omega)}\right| \left|G_{x_1x_3}(\omega) - \frac{G_{x_1x_4}(\omega)G_{x_5x_3}(\omega)}{G_{x_5x_4}(\omega)}\right|}{\left|G_{x_2x_3}(\omega) - \frac{G_{x_2x_4}(\omega)G_{x_5x_3}(\omega)}{G_{x_5x_4}(\omega)}\right|},$$
$$G_{\theta_2\theta_2}(\omega) = \frac{\left|G_{x_1x_2}(\omega) - \frac{G_{x_1x_4}(\omega)G_{x_5x_2}(\omega)}{G_{x_5x_4}(\omega)}\right| \left|G_{x_2x_3}(\omega) - \frac{G_{x_2x_4}(\omega)G_{x_5x_3}(\omega)}{G_{x_5x_4}(\omega)}\right|}{\left|G_{x_1x_3}(\omega) - \frac{G_{x_1x_4}(\omega)G_{x_5x_3}(\omega)}{G_{x_5x_4}(\omega)}\right|}$$

and

$$G_{\theta_3\theta_3}(\omega) = \frac{\left|G_{x_1x_3}(\omega) - \frac{G_{x_1x_4}(\omega)G_{x_5x_3}(\omega)}{G_{x_5x_4}(\omega)}\right| \left|G_{x_2x_3}(\omega) - \frac{G_{x_2x_4}(\omega)G_{x_5x_3}(\omega)}{G_{x_5x_4}(\omega)}\right|}{\left|G_{x_1x_2}(\omega) - \frac{G_{x_1x_4}(\omega)G_{x_5x_2}(\omega)}{G_{x_5x_4}(\omega)}\right|}.$$

These equations are of the same form as the 3S method but instead of the absolute value of three cross-spectra, there is the absolute value of three expressions. If we take the first expression in the first equation, the cross-spectrum between x_1 and x_2 is calculated which contains both ϕ and θ. The part of that cross spectra due to ϕ is calculated using an expression very similar to 3S and then is subtracted from the complete cross-spectra. If all of the assumptions are correct, this should leave just the part of the cross-spectra which is due to θ. The expressions within the modulus bars in each equation are, therefore, a partial cross spectra which can then be used as

inputs in the 3S technique. This will provide the part of the autospectra at each microphone which is due to the background noise in the far field. An important point to note is that this uses only measured signals and does not require any physical models to implement the technique.

The CSA method was applied to outdoor full-scale aero engine measurements along with the COP and 3S methods by Mendoza et al. [44]. A single sensor was located in the combustor, two sensors were located in the turbine stages and an array of microphones were arranged in the far field. Mendoza et al. state that the COP method does not perform adequately due to the presence of significant levels of hydrodynamic noise on the combustor measurement but that the 3S and CSA methods (called partial coherence method in the paper) provide good agreement over almost the entire frequency range. They state that the 3S method is not capable of providing accurate results when the turbine and combustion noise is produced at the same frequencies but also state that the overlap of frequency ranges of the sources is very small.

It is possible that this could be applied to combustion noise measurements for the removal of correlated noise sources between the hot nozzle and far field locations. This would require two probes inside the engine but sufficiently far apart that there is no unwanted coherent noise between them. Three probes would then be needed covering the positions of the hot nozzle and far field. This method would not necessarily work for separating direct and indirect noise as there is coherence between the combustor sensor and the indirect noise as Miles [27] has stated. There is, therefore, nowhere where the direct noise can be measured independently of the indirect or vice versa.

3.6 Virtual source analysis with coherence threshold

Leclére et al. [45] present a method which is a variation of the CSA method for multiple input multiple output (MIMO) systems. They use a method proposed by Price and Bernhard [46] called Virtual Source Analysis (VSA) which calculates the eigen decomposition of the cross-spectral matrix of their reference signals. The eigenvalues are treated as virtual sources which are incoherent with each other. The cross-spectral estimate between the ν^{th} virtual source and and an output microphone y is defined as

$$G_{\nu y} = \sum_{j=1}^{n} \Psi_{j\nu} G_{jy}$$

where n is the number of reference microphones and $\Psi_{j\nu}$ is the j^{th} value of the eigenvector corresponding to the ν^{th} eigenvalue. Using this, the coherence between the virtual source and the output microphone can be calculated and the COP method can be applied to obtain the part of G_{yy} due to the source ν. As the virtual sources are by definition incoherent, the part of G_{yy} due to all of the virtual sources can be obtained by taking the incoherent sum of all of the estimates for each of the virtual sources and the output microphone signal.

Leclère et al. define threshold values for the coherence for different statistical probabilities that the coherence of fully uncorrelated sources could be larger than the threshold value (essentially an upper confidence limit) for different numbers of segment averages and window overlaps. These threshold values are then used to define whether a virtual source is actually contributing to the

output signal or not. If the coherence value between the virtual source and the output is below the threshold, the contribution of that source is not included in the sum of the estimates as there is a reasonable likelihood that the source is not contributing significantly (or at all) to the output signal level.

Leclère et al. apply this method to measurements of an aircraft in flight with the reference microphones attached to the exterior of the fuselage of the aircraft along the same side, downstream of the wing. The output microphones were placed inside the cabin and the goal of the test was to obtain the noise level in the cabin due to the noise measured outside the aircraft. The experiments indicate that the noise in the cabin at low frequencies is due to the exterior noise. Above a certain frequency, the coherence drops sharply and only tones have significant levels of coherence.

This method is interesting and could be of use in the future although the method will still provide inaccurate estimates if significant levels of unwanted noise are present on the output microphone signals. In addition to this, multiple sensors will be needed inside the combustor. This can be a complex issue depending on combustor design and what other sensors are required for other measurement taken at the same time as the noise measurements.

3.7 5 microphone method for separating 3 separate signals

Minami and Ahuja [47] have developed a 5 microphone technique which is capable of separating 3 separate noise sources. Minami and Ahuja first derive the result of the 3S technique but using a different approach to Chung (the same method which is used in Chapter 4). Their method identifies the maximum number of equations associated with a particular number of microphones and the number of immeasurable quantities associated with the assumed number of sources. For a single source which is coherent between all microphones plus incoherent background noise at each microphone, there are 12 immeasurable quantities. Three microphones provide 12 equations in which these immeasurable quantities are present. As there are an equal number of equations and unknowns, it is possible to obtain estimates of the coherent noise at each of the microphones without the background noise present. The obtained equations are the same as the 3S equations derived by Chung. It is also possible to obtain the background noise by subtracting the separated coherent noise at one microphone from the measured autospectra of the same microphone.

Minami and Ahuja also show the error incurred if the 3S technique is used when two sources are coherent between all of the microphones. They found that if the level difference between the two sources is greater than 10 dB, the technique provides a reasonable estimate of the dominant source. If the difference is smaller than this, the error becomes large.

Minami and Ahuja describe a scenario with 2 wanted noise sources (u and v) assumed to be coherent at all microphones, but not with each other. Also present is extraneous background noise at each of the microphones which is not coherent between them. This scenario results in a total of 55 unknowns. They show that 5 microphones will provide 55 equations and will therefore be capable of separating the 3 signals. This method relies on the transfer functions between the sources and microphones being linear. The result is a number of non-linear equations which can

be solved numerically to obtain estimates of the two separate coherent noise sources and the background noise at each microphone.

The estimate does however, suffer from discontinuities. Minami and Ahuja express the real and imaginary parts of cross-spectra between the i^{th} and j^{th} microphone as

$$|G_{x_i x_j}(\omega)| \cos(\phi_{ij}(\omega)) = |G_{u_i u_j}(\omega)| \cos(\alpha_{ij}(\omega)) + |G_{v_i v_j}(\omega)| \cos(\beta_{ij}(\omega))$$

and

$$|G_{x_i x_j}(\omega)| \sin(\phi_{ij}(\omega)) = |G_{u_i u_j}(\omega)| \sin(\alpha_{ij}(\omega)) + |G_{v_i v_j}(\omega)| \sin(\beta_{ij}(\omega))$$

respectively where $i < j$ and $i, j = 1, 2, ..., 5$ and $\phi_{ij}(\omega)$ is the phase angle of the cross-spectrum between x_i and x_j. $\alpha_{ij}(\omega)$ and $\beta_{ij}(\omega)$ are the phase angles of the cross-spectra between u_i and u_j and v_i and v_j respectively. If $\alpha_{ij} - \beta_{ij} = n\pi$ where n is an integer, the real and imaginary parts of $G_{x_i x_j}(\omega)$ are equal which could result in the system becoming unstable. This occurs due to the spacing between the microphones. The closer the microphones are, the higher the frequency of the first discontinuity above 0 Hz.

This technique relies on knowing the location of each of the sources relative to the microphones and the transfer functions between sources and microphones. It also requires the microphones to be close together to increase the frequency of the first discontinuity. This means that all of the microphones would need to be in the far field for an engine test to obtain the contribution of combustion noise in the far field. The number and locations of all of the sources would need to be known and the maximum number of coherent sources would need to be no more than 2 for 5 microphones. Minami and Ahuja state that the jet mixing noise will not be coherent between microphone locations as long as the microphones are far enough apart. This is not possible if the first discontinuity is required to be at a high frequency. This would mean that jet noise, bypass noise, direct combustion noise and indirect combustion noise as well as other noise sources, will all be coherent between all of the microphones. 5 microphones will, therefore, not be enough for a full engine test.

Bennett and Fitzpatrick [48] conducted a review of coherence-based acoustic source identification techniques. This covers COP (called COS by Bennett and Fitzpatrick), 3S (called signal enhancement by Bennett and Fitzpatrick), the five microphone method which uses conditional spectral analysis by Hsu and Ahuja and the 5 microphone technique described by Minami and Ahuja [47]. In this review the benefits and limitations of the techniques are highlighted and Bennett and Fitzpatrick present a method for identifying the number of coherent sources present in the measured microphone signals. This can be used to identify whether there are enough microphones present to use Minami and Ahuja's technique.

Even if more microphones were added, there is still the complication of knowing exactly where the sources are relative to the far field positions, adding additional uncertainty to the estimates produced by this technique.

3.8 Application of COP, 3S and CSA to turboshaft engine data

Pardowitz et al [49] collects the COP, 3S and CSA techniques and applies them to measurements taken of a turbo-shaft engine as part of the TEENI (Turboshaft Engine Exhaust Noise Identification) European project. The measurements of an Ardiden 1H-1 turbo-shaft engine were taken at an outdoor test bed in Uzein, France. The in-duct measurements consisted of a combination of microphones and twin thermocouples in the combustor and at the HP turbine, two microphones at the power turbine and 4 azimuthal arrays in the engine exhaust. The first and last azimuthal arrays consisted of 3 microphones and the remaining two were made up of 12 microphones each. In the far field of the engine was a polar array made up of 18 microphones spaced at 10° increments with a radius of 19.2 m.

From the measurements made and techniques applied, five frequency bands of interest were identified. From the measurements it was deduced that:

- 100-260 Hz - consists of direct and indirect noise
- 260-600 Hz - either indirect noise or turbomachinery noise related to the HP turbine
- 600-1200 Hz - turbomachinery noise related to the HP turbine
- 1200-1750 Hz - not linked to any specific noise so far
- 1750-2400 Hz - turbomachinery noise related to the power turbine

The indirect noise was identified by examining the phase delay between the cross spectra of the combustor, HP turbine and power turbine probes. There were two distinct delays, one an order of magnitude larger than the other suggesting that the longer delay path was due to entropy waves convecting with the flow speed which is significantly slower than the sound speed. The COP and 3S techniques were used to identify the contribution of the combustion noise that propagates to the engine exhaust nozzle. The CSA technique was used to separate the combustion noise (which was coherent with all 5 probes) and anything that was only coherent with the remaining three probes located in the exhaust of the engine.

The techniques were then applied to examine the contribution of the combustion noise to each of the far field measurements. Directivity plots of the combustion noise were constructed from these measurements for two engine power states. It was noted that the combustion noise level peaked between 120° and 150°. Modal decomposition was also applied to the sound field in the exhaust and the modal contributions of different sources were examined.

3.9 Non-linear interactions with a turbine

Bennett and Fitzpatrick [50] investigated the effect of combustion noise propagation through a turbine stage. This investigation began with using an experimental rig with a duct that had a vane-axial fan mounted in it with 3 microphones downstream and 3 microphones upstream of

the fan. A loudspeaker was mounted upstream of the upstream microphones. The loudspeaker was used as a combustion source with the upstream microphones representing microphones in the combustor. They implemented the COP, 3S and Hsu and Ahuja's [42] CSA technique with the speaker producing tones with the fan off and then with the fan on. The CSA technique was also used when the speaker was used to produce band limited broadband noise. This was done as a comparison of the techniques and to demonstrate performance of the CSA technique when used to separate coherent noise sources.

Bennett and Fitzpatrick then state that it is generally believed that the reason for reduction in the coherence between combustor and far field measurements is the relative increase in level of other noise sources. They suggest that it is possible this is not the case but that the reduction in coherence could be due to non-linear interaction between the combustion noise and the turbines. Bennett and Fitzpatrick use a simulation that displays the effect of a relative increase in jet noise on the coherence between an upstream and a downstream microphone of the turbine is very similar to the effects of non-linear interaction between the combustion noise and the turbine. The non-linear interaction is assumed to be quadratic in nature and simulated by calculating $[com(t) + fan(t)]^2$ where $com(t)$ and $fan(t)$ are the time domain combustion and fan noise respectively. The simulation shows that if the coherence-based measurement techniques were used in this case, they would under predict the level of combustion noise.

Bennett and Fitzpatrick further investigated this by examining the autospectra of a microphone downstream of a fan where the speaker was producing single tones of increasing frequency. They found that there was no sign of non-linear interaction below 8.75 kHz. Above this frequency however, tones with a frequency of the blade passing frequency (BPF) of the fan plus the frequency of the speaker tone were present, along with the original speaker tone. The interaction tones were only present when the frequency of the interaction tones were above 11.2 kHz which is either the cut-on frequency of $(\pm 4, 1)$ or $(\pm 1, 2)$. They deduced that the non-linear interaction model needs to include the propagation effects of sound in a duct and suggest that modal decomposition of the sound in the duct would be useful for identifying the link.

Bennett and Fitzpatrick propose a method for decomposing the linear and non-linear parts of the signal. It uses partial coherence in the same way as Hsu and Ahuja [42] do for the CSA technique. The coherence between an upstream microphone signal squared with an downstream microphone results in the coherence between the non-linear components of the upstream signal with the downstream probe. This method showed high coherence at the frequencies of the tones assumed to be interaction tones.

They then applied the same method to a full scale engine test. They found that non-linear interaction tones were only present in the highest engine power tested and the separation method identified these tones. There were also strong combustion tones which had high coherence with the upstream signal squared. This suggests that the linearised wave equation does not apply in this region as the sound pressure level is high enough for non-linear propagation. This was also noticed at the cut-on frequencies in their experimental rig. The COP technique was applied to this data with the linear and non-linear parts separated. They show that the non-linear part of the combustion noise has a far greater frequency range of interest than the linear part. The level of the non-linear part, at certain frequencies, is higher than the linear part at the same frequency. This suggests that the coherence-based measurement techniques can be applied to

full engine tests for low engine powers but for higher engine powers, non-linear interactions with the turbines need to be taken into account.

Bennett et al. [51] displayed the results for the experimental test rig that Bennett and Fitzpatrick [50] used and then applied the same processing techniques to a small scale test rig, built by DLR, configured for the TEENI project. The rig consists of an azimuthal microphone array downstream of the inlet, followed by a rotor stator stage. Downstream of this is another azimuthal microphone array followed by an array of loudspeakers and then an anechoic termination. Sum and difference scattering is observed when a tone is played by the loudspeakers and, using the method developed by Bennett and Fitzpatrick, the linear and non-linear parts of the coherence are separated. It is clear from the results that the sum and difference tones are due to the non-linear scattering of the sound by the turbine. This is also observed when all of the loudspeakers are used to produce broadband noise.

Davis and Bennett [52] continue the investigation into non-linear interaction that Bennett and Fitzpatrick started. Their experiment consisted of a loudspeaker producing sound which travels along duct to a fan with one rotor and one stator stage and then to a semi-anechoic termination of the duct. There is a single microphone in the duct near the loudspeaker and an equally spaced azimuthal array of 25 microphones downstream of the rotor. The authors began their investigation by examining the signal measured by a single microphone in the array for the cases where the speaker was producing narrow band noise, the fan was operating, and both the fan and speaker were operating. They observed that scattering occurred at frequencies

$$f_{\text{scat}} = f_{\text{NBN}} + q \times f_{\text{BPF}}$$

where f_{NBN} are the frequencies that make up the narrow band noise produced by the speaker, q is a non zero integer indicating the scattering harmonic and f_{BPF} is the blade passing frequency of the fan. The authors use an equation which calculates the modal content of the scattered noise as

$$m_{\text{scat}} = m - (qB - kV)$$

where m is the propagating azimuthal mode of the noise produced by the speaker, B is the number of blades in the fan, k can take any integer value and V is the number of stator vanes. For their experiment, the dominant mode of the sound produced by the speaker is the plane wave mode, $m = 0$, and the fan has 5 blades and 8 stator vanes. For $q = 1$, the scattered noise will be propagating predominantly in the azimuthal modes $m_{\text{scat}} = -5$ and $m_{\text{scat}} = 3$. Davis and Bennett found that this was the case for their measurements by applying a modal decomposition technique using the azimuthal array.

The authors also investigated the case where the incident and scattered noise will spectrally overlap. This was performed using the same three test cases as before and scattering did indeed occur at $f_{\text{scat}} = f_{\text{NBN}} + f_{\text{BPF}}$. They applied the same method for decomposing linear and non-linear parts of the signal as presented by Bennett and Fitzpatrick [50] but with a slight change so that only the non-linear components that are quadratic in nature are used in the coherence. Interestingly, the scattered noise contains both linear and non-linear components which Davis and Bennett suggest is due to interactions which are both quadratic and linear. They suggest that this could be modelled using a time-varying boundary condition. They state it is possible that a combination of both models would best describe the system.

Davis and Bennett conclude that more experiments are required to further investigate this phenomenon, using multiple azimuthal arrays in a similar test to identify radial modes propagating along the duct.

3.10 Combining modal decomposition with 3S and CSA techniques

Davis and Bennett [53] have adapted the 3S technique (called SE by the authors) and Hsu and Ahuja's CSA method to identify the contribution of specific sources to specific modes. These adapted techniques have been called SE:Modal and CSA:Modal by the authors. These techniques replace the sensor at a single measurement position with the output from a modal decomposition technique where a single complex modal amplitude has been calculated. The complex modal amplitudes were calculated using a number of azimuthal arrays which were separated axially. This made it possible to decompose the signal into azimuthal and radial modes as well as the direction of propagation. The technique is fully described by Bennett [54]. In this instance, the complex modal amplitude was for the (2,0) mode travelling towards the duct inlet. The experiment consisted of a duct with a rotor-stator stage with the multiple azimuthal arrays upstream of this near the duct inlet, two sensors just downstream of the rotor and a loudspeaker some distance downstream with two microphones near it.

For the application of the SE:Modal technique it is required (as with the standard 3S method) that only one coherent noise source is present between the sensor locations. In this case the rotor was used as a source without the loudspeaker active. This made it possible to determine the contribution of the rotor noise to the (2,0) mode travelling towards the inlet without any flow noise present. This technique is used in combination with the CSA:Modal technique to separate out the contributions of the loudspeaker, rotor and any extraneous noise uncorrelated between sensors (electrical, hydrodynamic etc.).

Davis and Bennett found that their SE:Modal and CSA:Modal techniques provided good estimations of the contributions of each of the noise sources to the chosen mode of interest. One thing they noted, however, was that if the assumptions of CSA:Modal are violated (in particular that there are not two sensors measuring only one of the sources) then there will be errors in the estimation.

Chapter 4

3S Array Method

The 3S Array method discussed in Chapter 3 will be described in detail here as it is one of the most recently developed coherence-based measurement methods for measuring jet engine combustion noise and is the method this thesis will focus on developing further. Before developing potential improvements to the method, it is important to understand the limitations of the technique. To understand these limitations, a derivation of the 3S technique, which was developed by Chung [29], will be presented before examining the enhancements provided by the addition of the microphone array in the 3S Array technique.

4.1 Signal processing definitions

It is necessary to define some signal processing terms which will be used extensively throughout this thesis. To examine the spectral content of a signal $x(t)$, the one-sided autospectral density function (also called power spectral density or PSD) $G_{xx}(\omega)$ is defined as

$$G_{xx}(\omega) = \begin{cases} 2S_{xx}(\omega), & \omega > 0 \\ S_{xx}(\omega), & \omega = 0 \end{cases} \tag{4.1}$$

where S_{xx} is the two-sided autospectral density function and is defined as

$$S_{xx}(\omega) = \int_0^\infty R_{xx}(\tau) e^{-j\omega\tau} \mathrm{d}\tau \tag{4.2}$$

and $\omega = 2\pi f$ is the angular frequency. This equation relates the autospectral density function to the autocorrelation function $R_{xx}(\tau)$ of the signal $x(t)$ which is defined as

$$R_{xx}(\tau) = \lim_{T\to\infty} \frac{1}{T} \int_0^\infty x(t)x(t+\tau)\mathrm{d}t \tag{4.3}$$

where T is the observation time of the signal. The two-sided autospectral density function can also be defined as

$$S_{xx}(\omega) = \lim_{T\to\infty} \frac{E\left[X^*(\omega)X(\omega)\right]}{T} = \lim_{T\to\infty} \frac{E\left[|X(\omega)|^2\right]}{T} \tag{4.4}$$

where $X(\omega)$ is the Fourier transform of the signal $x(t)$ over time a time T, $E[\,]$ is the expectation operator and * denotes the complex conjugate. For a pressure signal, the units of autospectral density are Pa^2/Hz. Only the one-sided autospectral density will be used in this thesis and so, for brevity, the one-sided autospectral density function will simply be referred to as the autospectral density function.

For a signal of finite length, an estimate of the autospectral density function can be obtained by dividing the signal into N segments of length K samples. Each of these segments are then Fourier transformed and an estimate of the expected value of the product of the two frequency domain signals is calculated from all of the segments which makes it possible to obtain an estimate of the autospectral density function using Equation 4.4. This results in the estimate consisting of K frequency bins of equal width with the bin width being equal to F_s/K where F_s is the sampling frequency. The accuracy of the estimate is dependent on the frequency bin width and the length of the signal and will converge to the true value of the autospectral density when the window length and measurement length approach ∞. When calculating an estimate of $G_{xx}(\omega)$ using segment averaging, a windowing function is generally applied to each segment. The truncation of a measurement can result in the creation of sidelobes in the estimated autospectral density. These sidelobes result in a 'bleeding' of the measured signal at a particular frequency bin into other frequency bins which increases the error in the estimate and can result in high level tones 'masking' lower level broadband noise. To reduce the effect of these sidelobes, windowing functions can be applied that smoothly transition to 0 at the ends of the segment such as Hanning or Hamming windows.

The one-sided cross-spectral density (CSD) function describes the general dependence of one signal based on another and can be defined as

$$G_{xy}(\omega) = \begin{cases} 2S_{xy}(\omega), & \omega > 0 \\ S_{xy}(\omega), & \omega = 0 \end{cases} \tag{4.5}$$

where $S_{xy}(\omega)$ is the two-sided cross-spectral density function. The two-sided cross-spectral density function is defined as

$$\begin{aligned} S_{xy}(\omega) &= \int_0^\infty R_{xy}(\tau) e^{-j\omega\tau} \mathrm{d}\tau \\ &= \lim_{T\to\infty} \frac{E\left[X^*(\omega)Y(\omega)\right]}{T} \end{aligned}. \tag{4.6}$$

where $R_{xy}(\tau)$ is the cross-correlation function which is defined as

$$R_{xy}(\tau) = \lim_{T\to\infty} \frac{1}{T} \int_0^\infty x(t)y(t+\tau)\mathrm{d}t \tag{4.7}$$

and $Y(\omega)$ is the Fourier transform of a signal $y(t)$.

The coherence function is a measure of the linear causal relationship between two signals and is defined as

$$\gamma_{xy}^2(\omega) = \frac{|G_{xy}(\omega)|^2}{G_{xx}(\omega)G_{yy}(\omega)}. \tag{4.8}$$

where $\gamma_{xy}^2(\omega) = 1$ indicates a completely linear causal relationsip and $\gamma_{xy}^2(\omega) = 0$ indicates there is no linear causal relationsip between the two signals. As the measured signals will be finite,

the auto and cross-spectral density functions calculated from the signals will be estimates and therefore, the coherence function obtained from these values will also be estimates. The estimates will converge to the actual values as the measurement and window lengths both tend to ∞.

4.2 Derivation of the 3S technique

The purpose of the 3S technique is to obtain an estimate of the noise at one microphone that is coherent with the other two microphones (combustion noise in the case of this thesis) using only measurable quantities. The auto and cross-spectral densities of the microphone signals are measurable quantities. The goal is, therefore, to obtain the autospectral density function of the combustion noise that propagates to the far field microphone in terms of autospectral density functions, cross-spectral density functions and the coherence functions between the microphones.

The 3S method requires three separate microphone measurements which have been recorded simultaneously. For estimating combustion noise in the far field, the microphones are located in the combustor, the hot nozzle outlet and the far field. These sensor locations are used because the combustion noise that propagates to the far field will be present at all three locations but any unwanted noise (such as hydrodynamic noise) should not be. It is therefore assumed that the only correlated signal between the microphone signals is the combustion noise and that unwanted noise is present at each location which is incoherent with the combustion noise and is also incoherent between measurement positions. The combustor, hot nozzle and far field sensors will be designated as sensors 1, 2 and 3 respectively. Figure 4.1 is a block diagram of the signals.

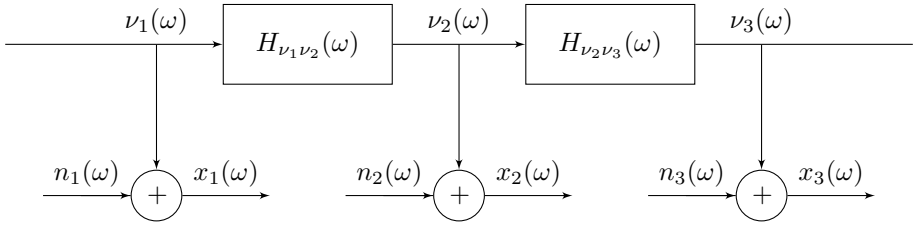

FIGURE 4.1: Block diagram of 3S technique.

The signal measured at the i^{th} microphone, for a single frequency, can be written as

$$x_i(\omega) = \nu_i(\omega) + n_i(\omega) \tag{4.9}$$

where $\nu_i(\omega)$ is the combustion noise and $n_i(\omega)$ is the unwanted noise measured at the i^{th} microphone. The one sided autospectral density function can be expressed as

$$G_{x_i x_i}(\omega) = G_{\nu_i \nu_i}(\omega) + G_{n_i n_i}(\omega) \tag{4.10}$$

assuming the unwanted noise is not correlated with the combustion noise. As the unwanted noise signals are assumed to be incoherent with the combustion noise as well as each other, over an infinite number of averages the cross-spectral density function between the i^{th} and j^{th} microphones (where $i \neq j$) is

$$G_{x_i x_j}(\omega) = G_{\nu_i \nu_j}(\omega). \tag{4.11}$$

As defined in equation (4.8), the coherence function between the i^{th} and j^{th} microphones is

$$\gamma^2_{x_i x_j}(\omega) = \frac{|G_{x_i x_j}(\omega)|^2}{G_{x_i x_i}(\omega) G_{x_j x_j}(\omega)}. \tag{4.12}$$

It is important to note that the combustion noise at the i^{th} microphone is assumed to be completely coherent with the combustion noise measured at the j^{th} microphone as the pressure-to-pressure transfer functions $H_{\nu_i \nu_j}(\omega)$ are assumed to be linear and time invariant. Therefore

$$\gamma^2_{\nu_i \nu_j}(\omega) = \frac{|G_{\nu_i \nu_j}(\omega)|^2}{G_{\nu_i \nu_i}(\omega) G_{\nu_j \nu_j}(\omega)} = 1. \tag{4.13}$$

Using the above expression and Equation (4.11), the cross-spectral density function between the measured signals in Equation (4.12) can be expressed as

$$|G_{x_i x_j}(\omega)|^2 = |G_{\nu_i \nu_j}(\omega)|^2 = G_{\nu_i \nu_i}(\omega) G_{\nu_j \nu_j}(\omega). \tag{4.14}$$

The coherence function between the measured signals can now be rewritten in terms of the autospectral densities of the combustion noise signals and the unwanted noise signals by substituting Equation (4.14) into Equation (4.12) and rearranging, which results in

$$\gamma^2_{x_i x_j}(\omega) = \frac{1}{1 + \frac{G_{n_j n_j}(\omega)}{G_{\nu_j \nu_j}(\omega)} + \frac{G_{n_i n_i}(\omega)}{G_{\nu_i \nu_i}(\omega)} + \frac{G_{n_i n_i}(\omega) G_{n_j n_j}(\omega)}{G_{\nu_i \nu_i}(\omega) G_{\nu_j \nu_j}(\omega)}}. \tag{4.15}$$

This expression can be simplified by defining a noise-to-signal ratio as

$$\alpha_{x_i}(\omega) = \frac{G_{n_i n_i}(\omega)}{G_{\nu_i \nu_i}(\omega)}. \tag{4.16}$$

Substituting Equation (4.16) into Equation (4.17) yields

$$\gamma^2_{x_i x_j}(\omega) = \frac{1}{(1 + \alpha_{x_i}(\omega))(1 + \alpha_{x_j}(\omega))}. \tag{4.17}$$

The definition of $\alpha_{x_i}(\omega)$ also allows the autospectral density function in Equation (4.10) to be simplified as

$$G_{x_i x_i}(\omega) = G_{\nu_i \nu_i}(\omega) \left(1 + \alpha_{x_i}(\omega)\right). \tag{4.18}$$

The measured autospectral density function and the measured coherence function are now in terms of the combustion noise and the $(1 + \alpha(\omega))$ terms. There are three different microphone positions in the 3S technique and so, three expressions of coherence and three different $(1+\alpha(\omega))$ terms. Each of the $(1 + \alpha(\omega))$ terms can be expressed in terms of the three measured coherence functions as there are an equal number of equations and unknowns. The three coherence functions can be used to eliminate two of the $(1 + \alpha(\omega))$ terms resulting in

$$(1 + \alpha_{x_i}(\omega)) = \sqrt{\frac{\gamma^2_{x_j x_k}(\omega)}{\gamma^2_{x_i x_j}(\omega) \gamma^2_{x_i x_k}(\omega)}} = \frac{|\gamma_{x_j x_k}(\omega)|}{|\gamma_{x_i x_j}(\omega)||\gamma_{x_i x_k}(\omega)|} \tag{4.19}$$

where k indicates a microphone location. The $(1+\alpha(\omega))$ terms can, therefore, all be obtained using measurable quantities from which combustion noise can be estimated. Substituting Equation

(4.19) into Equation (4.17) results in

$$G_{\nu_i\nu_i}(\omega) = G_{x_ix_i}(\omega)\left(\frac{|\gamma_{x_ix_j}(\omega)||\gamma_{x_ix_k}(\omega)|}{|\gamma_{x_jx_k}(\omega)|}\right). \tag{4.20}$$

This is the main result of the 3S technique and this section. It demonstrates that combustion noise can be obtained solely from measurable quantities.

Equation (4.20) can also be expressed in terms of cross-spectral density functions of the form

$$G_{\nu_i\nu_i}(\omega) = \frac{|G_{x_ix_j}(\omega)||G_{x_ix_k}(\omega)|}{|G_{x_jx_k}(\omega)|}. \tag{4.21}$$

The autospectral density function obtained from equations (4.20) and (4.21) when $i = 1, 2, 3$ are the components of the combustion noise present at the combustor, hot nozzle and the far field respectively. From here on, the microphone numbers will be replaced with letters indicating the location of the microphones so that $C(t)$, $N(t)$ and $F(t)$ are signals measured in the combustor, hot nozzle and far field respectively. The estimated combustion noise in the far field is now $\widehat{G}_{\nu_F\nu_F}(\omega)$ where the $\widehat{\ }$ symbol indicates the estimate is obtained from finite length measurements. Equation (4.20) indicates that the estimated combustion noise only depends on the autospectral density function of the far field signal and the coherence functions between each pair of sensors. Only the far field microphone therefore needs to be calibrated as errors in calibration will not affect the coherence functions between the measured signals.

4.3 Discussion of assumptions required for the 3S technique

There are several important assumptions that are made in the formulation of this technique. They are:

1) **The combustion noise is coherent between the three measurement locations.**

For combustion noise that propagates to the far field, the combustion noise will propagate through all three measurement locations.

2) **The unwanted noise (acoustic, hydrodynamic and electrical) is not coherent between measured signals.**

The measurement locations are selected so that there should not be any hydrodynamic noise which is coherent between measurement locations. Electrical noise should not be coherent between the measured signals provided there is sufficient shielding on the signal cables and isolation between the recorded channels. There should be no unwanted acoustic noise that is coherent between the combustor and the other two sensor locations but there may be between the hot nozzle and far field.

3) **The measured signal is long enough for a large number of averages to be used when calculating the cross-spectral density functions between signals.**

The effects of measurement length on the estimates of the cross-spectral density functions is discussed in Chapter 5.

4) **The transfer functions $H_{\nu_C\nu_N}(\omega)$ and $H_{\nu_N\nu_F}(\omega)$ are linear and time invariant.**

There are rotating turbine blades and a turbulent shear layer that the combustion noise must propagate through which have the potential to introduce non-linear phenomena in the propagation path and therefore the transfer functions. It is therefore assumed that, at low frequencies where combustion noise is present, the non-linear effects of propagation through the turbine stages and spectral broadening due to propagation through the turbulent shear layer are negligible.

5) **In the frequency range that combustion noise is present, only the plane wave mode of the duct is cut on.**

This is important as the 3S method does not take into account propagation inside a duct. Due to the source mechanism of direct combustion noise, when higher order modes become cut-on inside the duct they will be incoherent with all of the other propagating modes. This will result in a reduction in the coherence between two signals inside the duct which will result in error in the combustion noise estimate.

One of the more problematic assumptions when using the 3S technique to obtain an estimate of the combustion noise in the far field is the assumption that all 'unwanted' noise is incoherent between the hot nozzle and far field sensors. This is because noise from other sources (jet noise for example) can propagate to both measurement locations. If there is coherent unwanted noise between the hot nozzle and the far field measurements, the estimate obtained would be an overestimate of the combustion noise.

4.4 The 3S Array method

The 3S Array technique was developed by Rodríguez-García [41] as an attempt to reduce the error caused by coherent unwanted noise between the nozzle and far field. The technique uses a microphone array as a highly directional microphone using a processing technique called delay-and-sum beamforming to reduce noise arriving from directions other than the direction of the combustion noise.

Delay-and-sum beamforming (sometimes referred to as classical beamforming) is a technique for post-processing the signals from microphones in an array. By way of illustration, Figure 4.2 is a diagram of the sound arriving at a 1D microphone array from a point monopole source at a distance r_0 from the centre of the array and at an angle of θ to the normal of the array. The sound emitted from the source at $t = 0$ will arrive at the centre of the array at $t = c_0 r_0$ where c_0 is the speed of sound. Depending on the angle θ, the sound will arrive at each microphone in the

array at different times as the distance from each microphone to the source, r_i, will vary with microphone position. If all of the microphone signals are delayed such that the sound arrives at the same time from a sound source at a particular location, adding the signals together will result in the output of the array being relatively high for sound arriving from that direction due to wave superposition. For sound arriving from other source positions however, the microphones signals will not all be in phase and so, the output will be reduced. There are more advanced methods of beamforming, such as the inverse beamforming method [55], but for most of these it is not possible to obtain the cross-spectra between the in-duct microphones and the outputs of these methods which is necessary to then apply the 3S method.

For a microphone array consisting of M_n microphones, delay-and-sum beamforming in the time domain is implemented using:

$$F(\tau) = \frac{1}{M_n} \sum_{i=1}^{M_n} w_i F_i(t + \frac{r_i}{c_0}) \tag{4.22}$$

where $F_i(t)$ is the signal measured at the i^{th} microphone in the array and w_i is a weighting factor. The propagation from a monopole source to a microphone in free field conditions is described by the Green's function

$$g(r_i, t, \omega) = \frac{1}{4\pi r_i} e^{jkr} e^{-j\omega t}. \tag{4.23}$$

The amplitude of the pressure measured at a microphone is therefore dependent on the distance r_i. It is important to account for the effects of the spherical spreading in the delays and amplitudes as the application of the 3S Array method to an indoor engine test in Chapter 6 uses an array which will be in the near field of the engine. When these effects are accounted for, the beamformer is often known as a focussed beamformer. To correct for the amplitude differences, the weighting factor w_i is defined as

$$w_i = \frac{\frac{1}{4\pi r_0}}{\frac{1}{4\pi r_i}} = \frac{r_i}{r_0}. \tag{4.24}$$

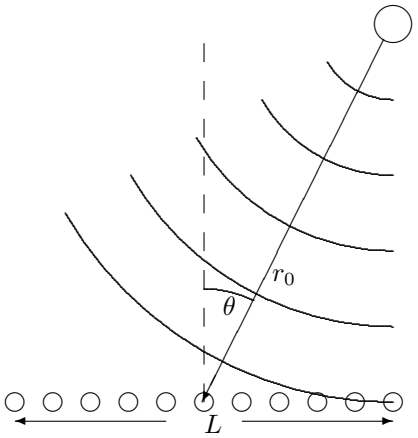

FIGURE 4.2: Diagram of a finite line array of finite length L with the centre of the array a distance r_0 from a monopole source with incident sound waves at an angle θ to the array.

The delay relative to the centre of the array can be expressed as

$$\tau_i = \frac{r_0 - r_i}{c_0}. \tag{4.25}$$

Another metric, other than array length and spacing, which can be used to characterise microphone arrays is called the aperture angle. This is the maximum angular coverage of the array for a source on a plane normal to the array. The aperture angle can be calculated using

$$\alpha_{\max} = 2 \arctan \frac{L}{2r_p} \tag{4.26}$$

where r_p is the distance between the centre of the array and the source plane normal to the array. If the source is on the plane but not directly over the centre of the array the angular coverage will be smaller and therefore the aperture angle is the maximum angular coverage rather than the actual angular coverage. This is a very useful metric, especially when examining the directivity of sources as it makes it possible to quantify the portion of the wavefront produced by the source that is measured by the microphone array.

By way of example, Figure 4.3 is the directivity of an 11 microphone linear array of length L for multiple discrete frequencies on a dB scale. It is clear that when the length of the microphone array is significantly smaller than the wavelength λ, the array directivity is close to omnidirectional. This is due to the array sampling only a small portion of the wavelength and so when the signals are all added together, the phase differences between microphones are small. When the wavelength is equal to the length of the array ($\lambda/10 = \Delta L$), there are clear nulls in the directivity pattern close to $90°$ and $-90°$ and two regions of high level called main lobes which are centred at $0°$ and $180°$. As the frequency increases, the width of the main lobe becomes narrower and other lobes, often called side lobes, begin to appear. When $\lambda = \Delta L$, the side lobes are now over half the strength of the main lobe. This effect, which is sometimes called spatial aliasing, is equivalent to the effect of frequency aliasing when there are fewer than two measurements per wavelength. The result of this is the level of the sound arriving from some directions other than the main lobe will not be reduced by the delay and sum beamforming algorithm.

From these directivity plots it is clear that a delay-and-sum beamformer only behaves like a highly directional microphone under certain conditions. The frequency range of interest needs to have a lower frequency limit which has a wavelength $\lambda < L$ and an upper limit where $\lambda > \Delta L$. The frequency range where the array is effective can be changed by using different array geometries. It is also important that the source that is being focussed on must be coherent between all of the microphones in the array otherwise the array will measure a lower level of that signal which could reduce the signal-to-noise ratio as well as provide an inaccurate estimate of the source strength. Mounting the array on hard wall or floor, a half-space assumption can be made. This will result in the the sound arriving at the 'rear' of the array (the rear arc being $90°$ to $-90°$ via $180°$) being equal to the sound arriving in the 'forward' arc ($90°$ to $-90°$ via $0°$). The measured pressure in this case will be equal to twice the amount that would be measured in a free field and effectively only one main lobe in the directivity of the array.

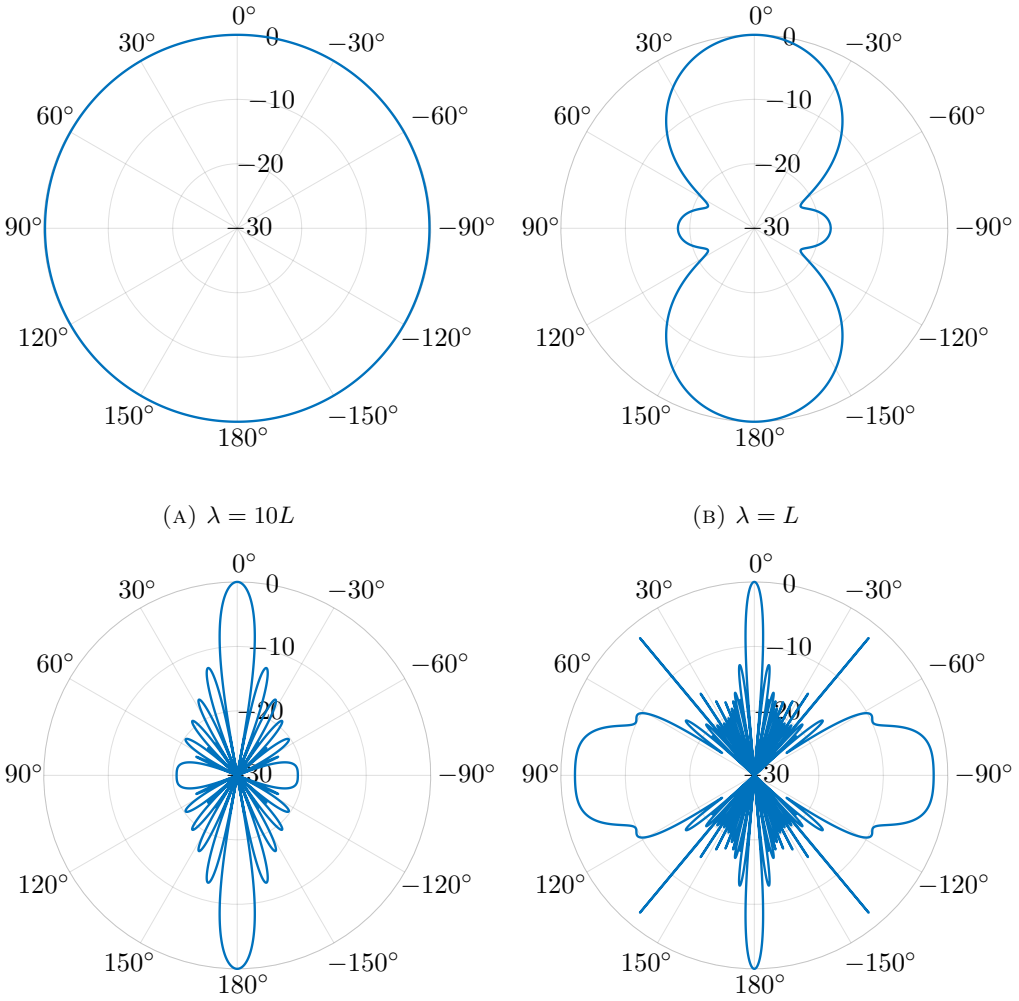

(A) $\lambda = 10L$ (B) $\lambda = L$

(C) $\lambda = 2\Delta L$ (D) $\lambda = \Delta L$

FIGURE 4.3: The directivity pattern in dB of an 11 microphone line array of length L with uniform spacing of ΔL for different frequencies. For a source normal to the array and 4 meters away the array aperture $\alpha_{\max} = 14.25°$.

4.4.1 2D Microphone Arrays

Figure 4.3 shows the azimuthal directivity for a line array in a single polar plane. Figure 4.4 shows the directivity plots for a range of azimuthal and polar angles. The line array lies along the dash-dot line. From these, it is clear that the line array directivity varies with azimuthal angle but not with polar angle. Figure 4.5 shows directivity plots for a 2D 11 by 11 square array with regular spacing ΔL and each side of the array L meters long. The array is on the plane indicated by the black mesh.

Here we can see that the 2D array can isolate sound in two dimensions (azimuth and polar). The square array is made up of 121 microphones as opposed to the 11 that made up the line array but it still has the same frequency limitations. This is a large number of microphones and channels for an effective frequency range of a decade.

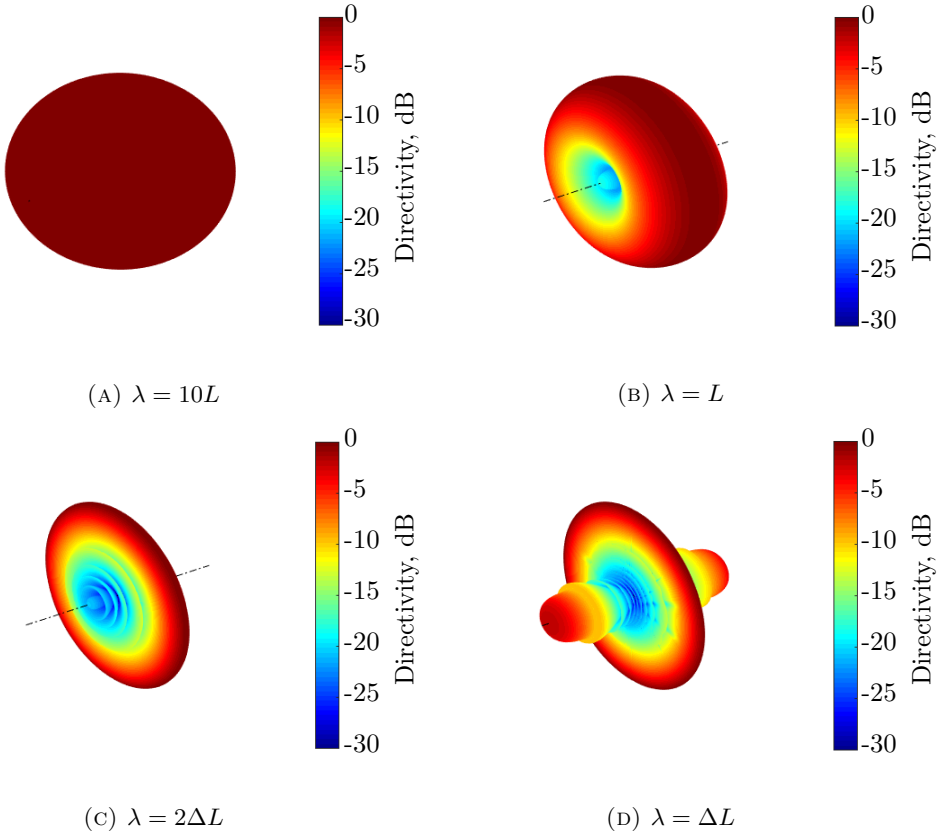

(A) $\lambda = 10L$ (B) $\lambda = L$

(C) $\lambda = 2\Delta L$ (D) $\lambda = \Delta L$

FIGURE 4.4: The directivity pattern in dB of an 11 microphone line array of length L with uniform spacing of ΔL for different frequencies in 3 dimensions. For a source normal to the array and 4 meters away the array aperture $\alpha_{\max} = 14.25°$ in the direction of the array and $0°$ in the other.

There are other array geometries that require fewer microphones to achieve high array directivity over a large frequency range with reduced side-lobe levels. Underbrink [56] examines the performance of several different types of microphone array and concludes that arrays with an aperiodic construction provide the best side-lobe suppression and frequency range. One such type of microphone array is a spiral array. This is made up of microphones placed on a spiral with an equal distance along the spiral separating the microphones. The result of this is a dense grouping of microphones in the centre of the array and a sparse grouping at the edges. The centre has a small ΔL thereby giving a higher upper frequency limit while still having a large overall length L which determines the lower frequency limit. This yields a large frequency range while using significantly fewer microphones than a square array. A spiral microphone array was used in the experiments that provided the measured data examined in Chapter 6 and Chapter 13 and the directivity plots of that array are provided in Chapter 6.

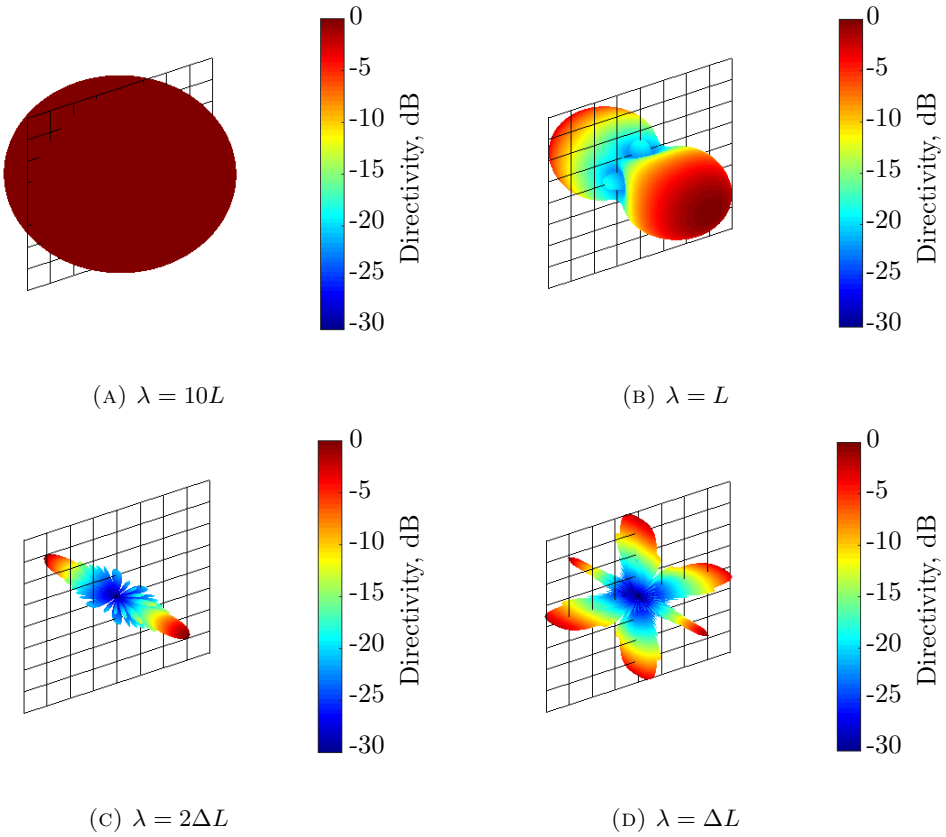

(A) $\lambda = 10L$ (B) $\lambda = L$

(C) $\lambda = 2\Delta L$ (D) $\lambda = \Delta L$

FIGURE 4.5: The directivity pattern in dB of an 121 microphone square array with a side length of L with uniform spacing of ΔL for different frequencies. For a source normal to the array and 4 meters away the array aperture $\alpha_{\max} = 14.25°$ in both directions of the array.

4.5 Assumptions required for the 3S Array method

The addition of the microphone array reduces the coherence of unwanted noise between the nozzle and far field microphones, increasing the validity of assumption 2) in Section 4.3. It does, however, add an additional assumption. For ease of reference, the list of assumptions for the 3S Array technique are:

1) The combustion noise is coherent between the three measurement locations.

2) The unwanted noise (acoustic, hydrodynamic and electrical) is not coherent between measured spectra.

3) The measured signal is long enough for a large number of averages to be used when calculating the cross-spectral density functions between signals.

4) The transfer functions $H_{\nu_C \nu_N}(\omega)$ and $H_{\nu_N \nu_F}(\omega)$ are linear and time invariant.

5) In the frequency range that combustion noise is present, only the plane wave mode of the duct is cut-on.

6) The combustion noise is coherent between all microphones in the microphone array.

4.6 Chapter Summary

In this chapter, a derivation of the 3S method developed by Chung [29] is presented. The assumptions of the 3S method are explained and, for the measurement of combustion noise, Rodríguez-García [41] noted that the assumption that the unwanted noise was incoherent between all measurement locations was not valid. To improve the validity of the 3S method, Rodríguez-García developed the 3S Array method which utilises the output of a delay-and-sum focussed beamformer as the far field measurement. An explanation of how a delay-and-sum beamformer can be implemented was presented as well as the design criteria for optimal performance of the beamformer for a given frequency range.

Chapter 5

Statistical analysis of the 3S technique

In general terms, the 3S method (and 3S Array method) can be used to obtain an estimate of the contribution of sound that is coherent between two spectral estimates to a third spectral estimate. To understand the validity of the estimate, confidence intervals of the estimate are required. As the 3S Array method is the product of two cross-spectra divided by a third, it is logical to first examine the probability distribution of a cross-spectral estimate. Whilst there is extensive literature on the probability distribution of estimates of γ^2_{xy} calculated from finite data, this author has not been able to find any literature concerning the probability distribution of a cross-spectral estimate.

5.1 Probability distribution of Cross-spectral estimate

As defined in Chapter 4, the equation for a one sided cross-spectral density estimate for two signals, $x(t)$ and $y(t)$, is defined as

$$G_{xy}(\omega) = \lim_{T\to\infty} \frac{E\left[X^*(\omega)Y(\omega)\right]}{T}. \tag{5.1}$$

If $x = y$, the cross-spectrum reduces to the autospectrum. The estimate itself will be a random variable with it's own probability distribution since it is computed from a finite time signal. The Fourier transform of a Gaussian noise signal will have both real and imaginary parts which will be independent Gaussian random variables. The autospectrum of a signal is the sum of the real part squared plus the sum of the imaginary part squared. Therefore, the probability distribution is equal to the square sum of two normal distributions which is the definition of a χ^2_n distribution with $n = 2$ degrees of freedom for a single segment of data. A χ^2_n distribution calculated from the sum of n square normal distributions with a mean of 0 and variance of 1 has a mean of $\mu = n$ and a variance of $\sigma^2 = 2n$. When using segment averaging to calculate a cross-spectral density estimate, the number of degrees of freedom is equal to $2\times$ the number of averages as each segment is the square sum of two normal distributions and all of the segments are summed when

taking the average. The number of averages can be expressed as BT where B is the bin width for each frequency bin and T is the length of the signal in seconds. The probability distribution of an autospectrum is well known and can be found in Bendat and Piersol [43].

The probability density function (pdf) of a χ^2_n distribution is given by

$$f(x|n) = \frac{1}{2^{\frac{n}{2}}\Gamma(\frac{n}{2})} x^{\frac{n}{2}-1} e^{\frac{-x}{2}} \tag{5.2}$$

where $\Gamma(\frac{n}{2})$ is the Gamma function. A χ^2_n distribution is a special case of the Gamma distribution. The pdf of a Gamma distribution is given by

$$f(x|a,b) = \frac{1}{b^a\Gamma(a)} x^{a-1} e^{\frac{-x}{b}} \tag{5.3}$$

where the parameters a and b can be defined by the mean μ and the variance σ^2 of the random variable x as

$$a = \frac{\mu^2}{\sigma^2}, \tag{5.4}$$

and

$$b = \frac{\mu}{a}. \tag{5.5}$$

As $\mu = n$ and $\sigma^2 = 2n$, the parameters $a = n/2$ and $b = 2$. Substituting these values into Equation (5.3) will result in the expression for a χ^2_n distribution given in Equation (5.2). For an autospectral density estimate calculated from a finite length Gausian signal with a mean of 0 and variance of 1, $\mu = n = 2BT$ and $\sigma^2 = 2n = 4BT$. Therefore, $a = BT$ and $b = \mu/BT$ and so the pdf of a measured autospectrum can be defined using the mean of the estimate and the number of averages.

The probability distribution of a cross-spectrum is more complicated to derive than that of an autospectrum as it can not necessarily be defined as the sum of the squares of two random variables. Defining the two signals as

$$x(t) = \nu(t) + n_x(t) \tag{5.6}$$

and

$$y(t) = \nu(t) + n_y(t) \tag{5.7}$$

where $\nu(t)$ is the part of the signals which is correlated between $x(t)$ and $y(t)$ and $n_x(t)$ and $n_y(t)$ are uncorrelated noise, the coherence between x and y can be expressed as

$$\gamma^2_{xy}(\omega) = \frac{|G_{xy}(\omega)|^2}{G_{xx}(\omega)G_{yy}(\omega)}. \tag{5.8}$$

Following a similar procedure to the beginning of the derivation of the 3S method in Chapter 4, the autospectum of x and y and the cross-spectrum between x and y are

$$G_{xx}(\omega) = G_{\nu\nu}(\omega) + G_{n_x n_y}(\omega), \tag{5.9}$$

$$G_{yy}(\omega) = G_{\nu\nu}(\omega) + G_{n_y n_y}(\omega), \tag{5.10}$$

and

$$G_{xy}(\omega) = G_{\nu\nu}(\omega). \tag{5.11}$$

Substituting equations (5.9), (5.10) and (5.11) into Equation (5.8) yields

$$\gamma_{xy}^2(\omega) = \frac{{G_{\nu\nu}}^2(\omega)}{(G_{\nu\nu}(\omega) + G_{n_x n_x}(\omega))(G_{\nu\nu}(\omega) + G_{n_y n_y}(\omega))}. \tag{5.12}$$

Dividing the numerator and denominator by ${G_{\nu\nu}}^2(\omega)$ allows the coherence to be expressed in terms of noise-to-signal ratios

$$\gamma_{xy}^2(\omega) = \frac{1}{\left(1 + \frac{G_{n_x n_x}(\omega)}{G_{\nu\nu}(\omega)}\right)\left(1 + \frac{G_{n_y n_y}(\omega)}{G_{\nu\nu}(\omega)}\right)}. \tag{5.13}$$

Defining $\alpha_x(\omega) = \frac{G_{n_x n_x}(\omega)}{G_{\nu\nu}(\omega)}$ and $\alpha_y(\omega) = \frac{G_{n_y n_y}(\omega)}{G_{\nu\nu}(\omega)}$, the coherence between the two signals can be expressed as

$$\gamma_{xy}^2(\omega) = \frac{1}{(1 + \alpha_x(\omega))(1 + \alpha_y(\omega))}. \tag{5.14}$$

The coherence between the two signals can therefore be expressed in terms of two signal to noise ratios. Note that for $\gamma_{xy}^2(\omega) = 1$, $\alpha_x(\omega) = \alpha_y(\omega) = 0$ and therefore $x(t) = y(t) = \nu(t)$. It is important to note that when using finite-length windows, coherence can be lost if there is a significant time delay between the two signals (if the signals are not tones) which is utilised by Miles' 'Aligned and Unaligned Coherence' technique [34]. For the rest of this chapter, it is assumed that any measured signals will have been simultaneously recorded and 'time aligned' to maximise coherence between signals so that the only mechanism for a loss of coherence is incoherent noise.

The relationship between the coherence of the two signals and the probability distribution of the cross-spectral estimate can be investigated using a Monte Carlo simulation. The Monte Carlo simulation is used to calculate 10000 different estimates of $G_{xy}(\omega)$ so that the pdf of $|G_{xy}(\omega)|$ for an arbitrarily selected frequency bin can be obtained. Note that when using Gaussian signals, the pdf of the estimate for each bin will be the same and therefore the selection of the bin is purely arbitrary. The work-flow for the simulation is as follows:

1) Fix a value of $\gamma_{xy}^2(\omega)$

2) Fix a value of β and define

$$\alpha_x(\omega) = \beta^2 \alpha_y(\omega) \tag{5.15}$$

3) Calculate $\alpha_y(\omega)$ by substituting Equation (5.15) into Equation (5.14) and using the values from 1) and 2)

4) Generate a normally distributed random signal to use as $\nu(t)$ using MATLABs 'randn' function with a mean of 0 and variance of 1 which is 32000 samples long (1000 seconds long with a sampling frequency of 32 samples per second).

5) Generate two different normally distributed random signals to use as $n_x(t)$ and $n_y(t)$ using MATLABs 'randn' function with a mean of 0 and variance of $\sqrt{\alpha_x(\omega)}$ and $\sqrt{\alpha_y(\omega)}$ respectively which are 32000 samples long.

6) Calculate an estimate of the $G_{xy}(\omega)$ using a rectangular window which is 32 samples long ($B = 1$) and has no overlap.

7) Repeat steps 4) - 6) 10000 times to obtain 10000 different estimates of $G_{xy}(\omega)$

Figure 5.1 is a plot of the pdf of the estimate of $|G_{xy}(\omega)|/\mu$ for an arbitrary frequency bin from the Monte Carlo simulation when $\gamma^2_{xy}(\omega) = 1$ and a $BT = 1000$. Also plotted is a Gamma

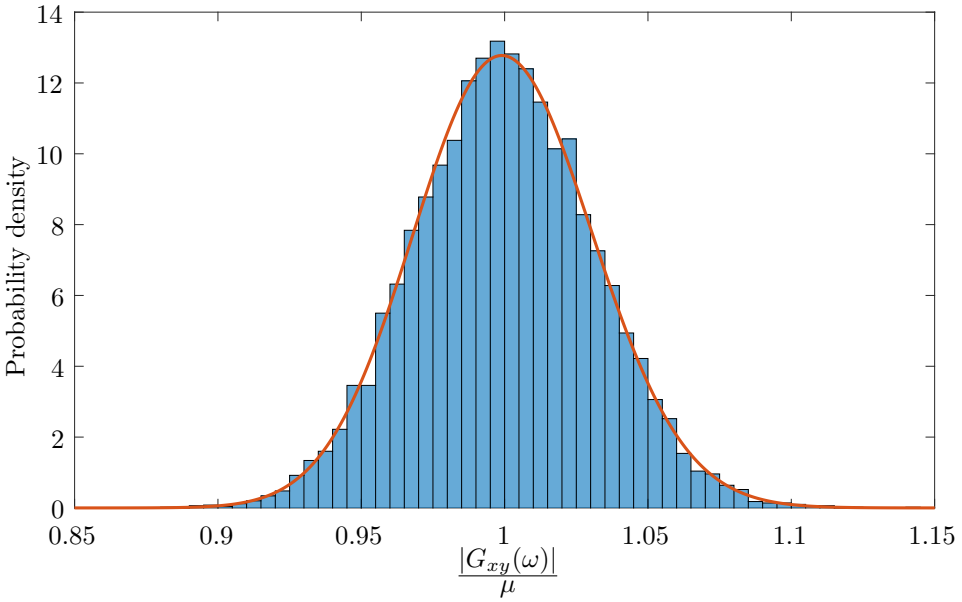

FIGURE 5.1: A histogram of the 10000 values of $|G_{xy}(\omega)|$ at an arbitrary frequency bin which has been normalised to the mean of the 10000 values when $\gamma^2_{xy}(\omega) = 1$. Also plotted in red is a Gamma distribution, where the parameters a and b have been defined using the mean and the variance of the data.

distribution which has been fitted to the data by using the mean and variance of the data to calculate a and b. For this data, $a = 1025$ and $b = \frac{1}{1025}$ which is as expected for an autospectrum as the values of a and b should be equal to BT and μ/BT respectively which they approximately are. It is clear that the Gamma distribution closely fits the simulated data which should not be surprising as the probability distribution of cross-spectrum with a coherence of 1 should provide the same probability distribution as an autospectrum of one of the signals for the same BT product.

Figure 5.2 is a plot of pdfs of $|G_{xy}(\omega)|/\mu$ for an arbitrary frequency bin from the Monte Carlo simulation with coherences of 0.9, 0.5, 0.2 and 0.1, $BT = 1000$ and $\beta = 1$ ($\alpha_x(\omega) = \alpha_y(\omega)$). Also plotted are the Gamma distributions, where the parameters a and b have been defined using the mean and the variance of $|G_{xy}(\omega)|/\mu$. From this plot it is clear that as the coherence decreases, the variance increases but the Gamma distributions still accurately describe the distribution of the data.

To understand how the parameters of the Gamma distribution vary with coherence, $\frac{\mu^2}{\sigma^2}$ is plotted against $\gamma^2_{xy}(\omega)$ in Figure 5.3. The estimates are calculated using coherence values between $x(t)$ and $y(t)$ ranging from 1 to 0.01 in steps of 0.1 and also the values of 0.001, 0.0001 and 0.00001. There are several sets of data plotted on the figure which represent estimates of $G_{xy}(\omega)$ calculated

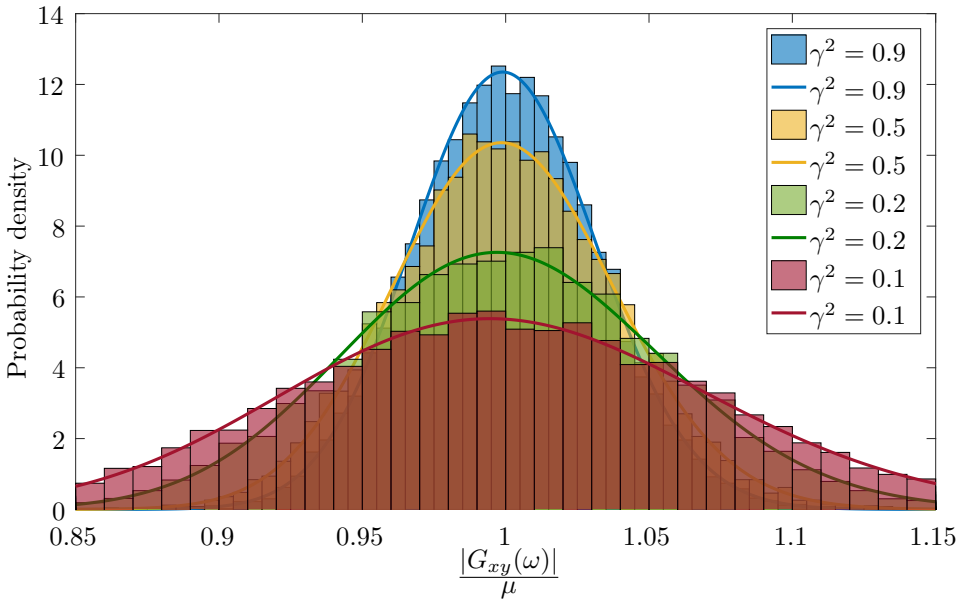

FIGURE 5.2: Probability density functions of estimates of $|G_{xy}(\omega)|/\mu$ at an arbitrary frequency bin when the spectra of $x(t)$ and $y(t)$ have a coherence values of 0.9, 0.5 0.2 and 0.1. Also plotted as line plots are Gamma distributions, where the parameters a and b have been defined using the mean and the variance of $|G_{xy}(\omega)|/\mu$.

using different values of β. From this plot it is clear that the relationship between $\frac{\mu^2}{\sigma^2}$ and γ_{xy}^2 is not dependent on β. Also shown in Figure 5.3 is a line graph of the empirically fitted curve

$$a = \frac{\mu^2}{\sigma^2} = BT\left(\frac{4}{3} - \frac{4}{3}4^{-\gamma_{xy}^2}\right) \tag{5.16}$$

which provides excellent agreement to the simulated data. This expression was obtained by means of trial and error. From this relationship the a parameter of the Gamma distribution can be calculated for different values of coherence for a signal with $BT = 1000$. The pdf of $|G_{xy}(\omega)|$ can therefore be estimated by a Gamma distribution using the measured coherence and BT product to calculate a using Equation (5.16) and the magnitude of the cross-spectral estimate as the mean of the distribution to estimate the b parameter.

The effect of the BT product on $\frac{\mu^2}{\sigma^2}$ can be observed in Figure 5.4. The values of $\frac{\mu^2}{\sigma^2}$ have been normalised by BT. The empirically fitted curve has also been normalised by BT. It is clear that the values of a obtained from the empirical fit curve accurately fit the simulated data. When the coherence drops below a value which is dependent on the value of BT, the values of $\frac{\mu^2}{BT\sigma^2}$ deviate slightly from the fitted curve. When the values of $\frac{\mu^2}{\sigma^2}$ deviate from those estimated from the empirical curve, the distribution of the data also deviates from that of a Gamma distribution. The coherences calculated from the simulated signals therefore each tend to a limit equal to $\frac{1}{BT}$ and so the measured coherence deviates from the actual coherence. It is therefore important to identify the minimum value of measured coherence at which the Gamma distribution still accurately describes the probability distribution of the absolute value of a cross-spectral estimate.

To identify the minimum value of measured coherence for which a Gamma distribution still accurately describes the pdf of $|G_{xy}(\omega)|$, the ratio the actual coherence, γ_{xy}^2 and the estimated

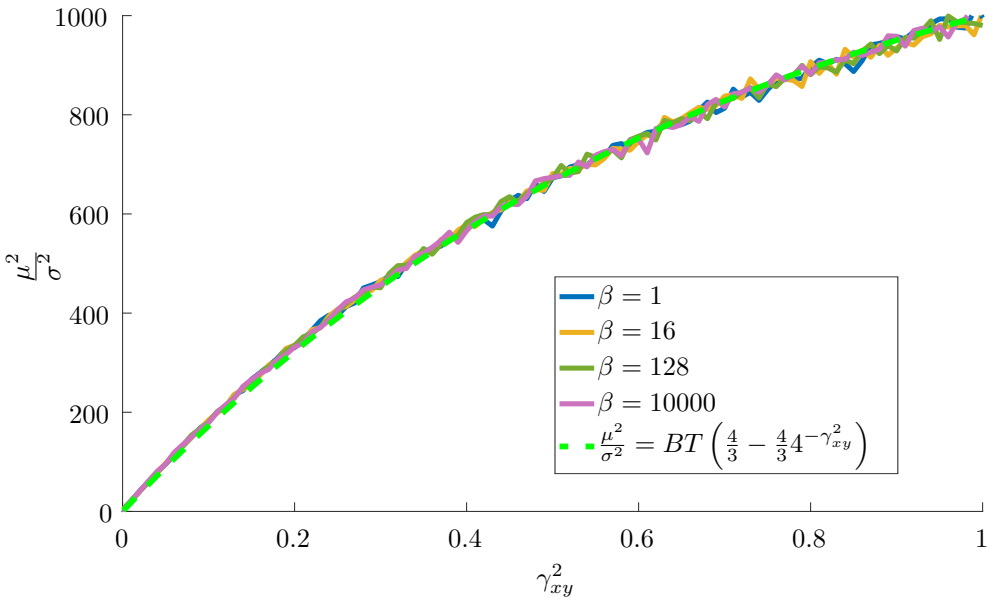

FIGURE 5.3: $\frac{\mu^2}{\sigma^2}$ of 10000 of $|G_{xy}(\omega)|$ plotted against $\gamma^2_{xy}(\omega)$ for estimates calculated using different values of β. Also plotted is an empirically fitted expression that describes relationship between $\frac{\mu^2}{\sigma^2}$ of 10000 of $|G_{xy}(\omega)|$ and $\gamma^2_{xy}(\omega)$.

coherence $\widehat{\gamma}^2_{xy}$ can be used. Figure 5.5 is a plot of $\gamma^2_{xy}/\widehat{\gamma}^2_{xy}$ against γ^2_{xy} for different values of BT. The values of $\widehat{\gamma}^2_{xy}$ for all values of BT is equal to the actual coherence when the coherence is high. Once the coherence drops below a threshold value (which is different for different values of BT) the measured coherence becomes greater than the actual coherence. It is at this value of coherence that the distribution of $|G_{xy}(\omega)|$ begins to deviate from the shape of a Gamma

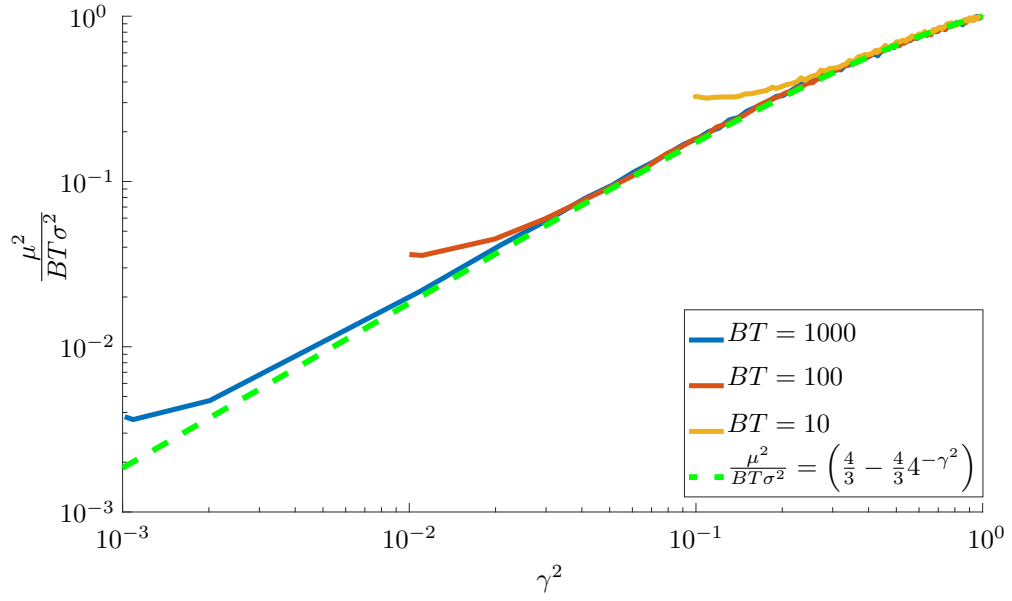

FIGURE 5.4: $\frac{\mu^2}{BT\sigma^2}$ of 10000 estimates of $|G_{xy}(\omega)|$ plotted against $\gamma^2_{xy}(\omega)$ for different values of BT. Also plotted is an empirically fitted expression that describes the relationship between $\frac{\mu^2}{BT\sigma^2}$ and $\gamma^2_{xy}(\omega)$.

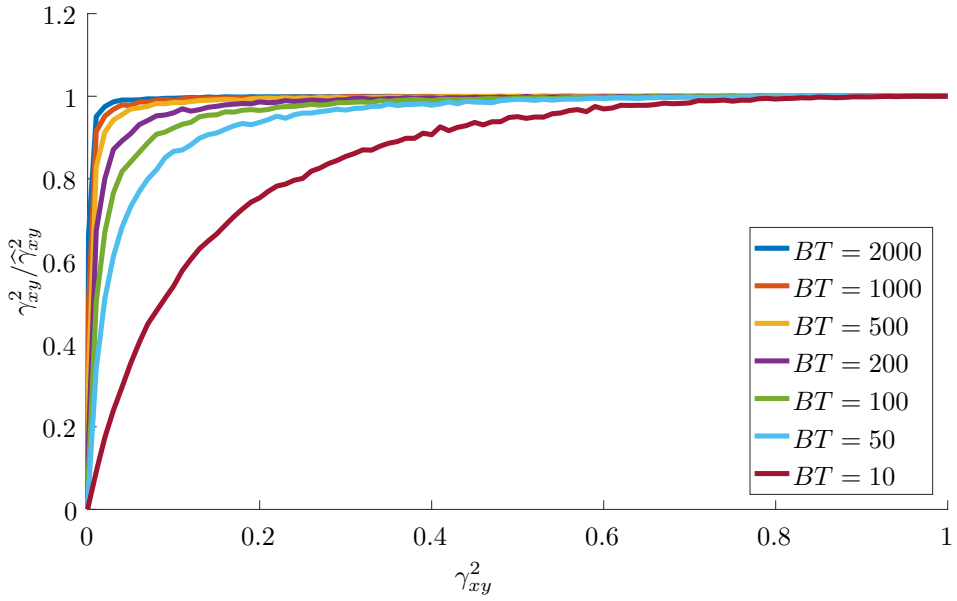

FIGURE 5.5: The actual coherence between x and y divided by the estimated coherence obtained from x and y for different values of BT plotted against the actual coherence.

distribution.

Examining the distributions of $|G_{xy}(\omega)|$ for different values of γ_{xy}^2 and BT has shown that the distribution of $|G_{xy}(\omega)|$ significantly deviates from the Gamma distribution when $\gamma_{xy}^2/\widehat{\gamma}_{xy}^2 < 0.95$. The range of measured coherence values over which $|G_{xy}(\omega)|$ can therefore be represented by a Gamma distribution is

$$\widehat{\gamma}_{xy}^2|_{\text{lower}} \leq \widehat{\gamma}_{xy}^2 \leq 1 \tag{5.17}$$

where

$$\widehat{\gamma}_{xy}^2|_{\text{lower}} = \frac{\gamma_{xy}^2}{0.95}. \tag{5.18}$$

The values of γ_{xy}^2 and $\widehat{\gamma}_{xy}^2$ where $\gamma_{xy}^2/\widehat{\gamma}_{xy}^2 = 0.95$ for different values of BT are given in Table 5.1.

BT	$\boldsymbol{\gamma_{xy}^2}$	**BT**$\times\boldsymbol{\gamma_{xy}^2}$	$\boldsymbol{\widehat{\gamma}_{xy}^2}$
10	0.55	5.5	0.58
50	0.25	12.5	0.26
100	0.14	14	0.15
200	0.1	20	0.11
500	0.04	20	0.042
1000	0.02	20	0.021
2000	0.01	20	0.011

TABLE 5.1: Values of γ_{xy}^2 and $\widehat{\gamma}_{xy}^2$ below which a gamma distribution no longer accurately describes the distribution of $|G_{xy}|$.

The coherence function multiplied by BT tends to a constant value of 20 when $BT \geq 200$. The coherence function when $\gamma_{xy}^2/\widehat{\gamma}_{xy}^2 = 0.95$ can be calculated using

$$\gamma_{xy}^2 = \frac{20}{BT} \qquad (BT \geq 200). \tag{5.19}$$

Substituting Equation (5.19) into Equation (5.18), the minimum estimated coherence value where a Gamma distribution is still an accurate fit of the distribution of $|G_{xy}(\omega)|$ can therefore be expressed as

$$\widehat{\gamma}_{xy}^2|_{\text{lower}} = \frac{20}{0.95BT}. \tag{5.20}$$

For values of $BT < 200$ the coherence can be calculated in the same way but using a numerator smaller than 20 with the values for $BT = 100$, 50 and 10 given in the table. From the table it is clear that for signals with low coherence, high values of BT are required. It is important to note that the deviation of $\frac{\mu^2}{BT\sigma^2}$ from the fit curve in Figure 5.5 is at lower values of coherence than the minimum coherence values defined in Table 5.1. Therefore, in the range of coherence values where a Gamma distribution is an accurate fit of the distribution of $|G_{xy}(\omega)|$, the fit curve given in Equation (5.16) is valid.

Miles [36] uses a method to calculate a lower limit of coherence which involves calculating the minimum coherence for a given number of averages and then calculates the upper limit of the 95% confidence interval for this value of coherence. Leclére et al. [45] uses a very similar method to Miles but includes different confidence limits. Any value of $\gamma_{xy}^2(\omega)$ below that limit could have a coherence of zero and can be disregarded. While using the lower limit of $\gamma_{xy}^2(\omega)$ that Miles uses results in a high likelihood that the coherence between sensors will not be zero, it does not account for the changing of the distribution of $|G_{xy}(\omega)|$ as this was not Miles' objective. The fact that the shape of the distribution of $|G_{xy}(\omega)|$ can no longer be expressed as a Gamma distribution means that the distribution of $|G_{xy}(\omega)|$ is no longer the sum of a number of squared Gaussian distributions even though $x(t)$ and $y(t)$ are Gaussian signals. This suggests that for coherence values below the threshold given in Equation (5.20), the estimate $|G_{xy}(\omega)|$ is likely to significantly deviate from the true value and confidence intervals will not be calculable from a Gamma distribution. The lower confidence intervals given by Miles are lower than those given in Table 5.1 and so, the limits calculated from Equation (5.20) will be used.

The above analysis and limits relate to cross-spectral estimates for which there is no overlapping of the window segments. Figure 5.6 is a plot of $\frac{\mu^2}{\sigma^2}$ calculated from 1000 estimates of $|G_{xy}(\omega)|$ for an arbitrary frequency bin which has been normalised by BT plotted against the percentage overlap of the segments for three diffreent window functions. With no overlap, the window has no effect on $\frac{\mu^2}{\sigma^2}$ since $\frac{\mu^2}{BT\sigma^2} \approx 1$. As the overlap increases, different windows provide different increases in $\frac{\mu^2}{\sigma^2}$ and therefore, the frequency window overlap reduces the variance in the spectral estimate. The variance tends to a constant value between 60% and 70% for the Hanning and Hamming windows and approximately at 80% for the rectangular window. The values from the plot can be used as a window correction factor, $w_c(\text{overlap}, \text{window})$, with which to obtain the equivalent value of BT, BT_{eqv}, which can be defined as

$$BT_{\text{eqv}} = BT \times w_c(\text{overlap}, \text{window}). \tag{5.21}$$

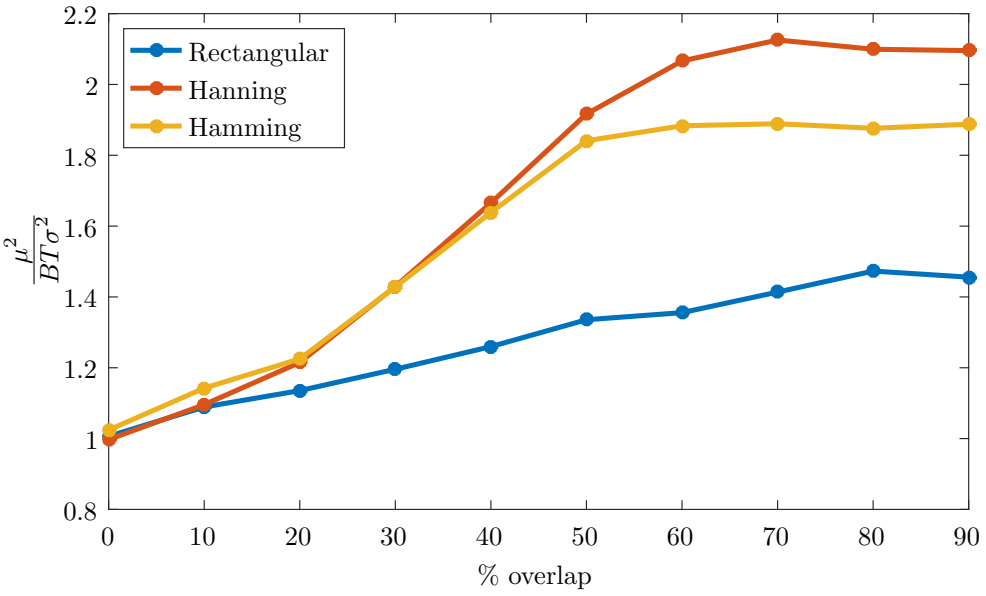

FIGURE 5.6: $\frac{\mu^2}{BT\sigma^2}$ of 1000 $|G_{xy}(\omega)|$ plotted against the % overlap of the segments used in segment averaging. The coherence between the two signals is 1. This is plotted for segments with rectangular, Hanning and Hamming windowing functions applied.

The empirical fit curve in Equation (5.16) can therefore be redefined as

$$\frac{\mu^2}{\sigma^2} = BT_{\text{eqv}}\left(\frac{4}{3} - \frac{4}{3}4^{-\gamma^2}\right). \tag{5.22}$$

The validity of this relationship is demonstrated in Figure 5.7 which is a plot of $\frac{\mu^2}{\sigma^2}$ calculated from 1000 estimates of $|G_{xy}(\omega)|$ normalised by BT_{eqv} against γ^2_{xy} for three different windows using a 70% overlap. As in Figure 5.4, the values of $\frac{\mu^2}{BT_{\text{eqv}}\sigma^2}$ follow the relationship given by the empirical fit curve until a threshold value is reached where the signals deviate. The distributions of the estimates obtained using different windows and overlap amounts can therefore be defined in terms of BT_{eqv} with no-overlap. The estimated coherence threashold defined in equation (5.20) can, therefore, be redefined as

$$\widehat{\gamma}^2_{xy}|_{\text{lower}} = \frac{20}{0.95BT_{\text{eqv}}}. \tag{5.23}$$

For clarity, the rest of the processing used in this chapter will use a rectangular window with no overlapping segments so that $BT_{\text{eqv}} = BT$. Equivalent results can be obtained using signals with different window and overlap such that a value BT_{eqv} is the same as the values used in this Chapter.

The uncertainty of the estimates of $|G_{xy}(\omega)|$ can be indicated by calculating it's confidence intervals. The confidence intervals can be calculated from the distribution of the data. Provided the required assumptions are valid and, therefore, the estimated coherence is above the minimum value for the value of BT, the confidence intervals can be calculated from a Gamma distribution. The parameters of the Gamma distribution can be calculated using the estimated coherence, the estimated value of $|G_{xy}(\omega)|$ and the value of $\frac{\mu^2}{\sigma^2}$ calculated from the fit curve in Equation (5.16).

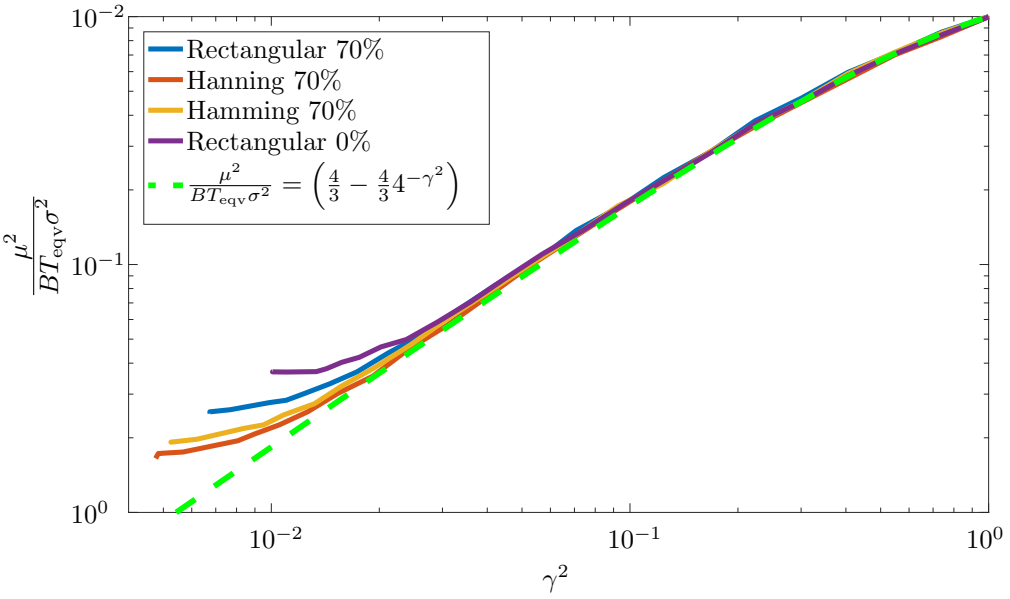

FIGURE 5.7: $\frac{\mu^2}{BT_{\mathrm{eqv}}\sigma^2}$ of 1000 $|G_{xy}(\omega)|$ plotted against γ^2 for different windows and overlaps. Also plotted is an empirically fitted expression that describes the relationship between $\frac{\mu^2}{BT_{\mathrm{eqv}}\sigma^2}$ and γ^2.

It is important to confirm the assumption that the signals $x(t)$ and $y(t)$ have Gaussian distributions is correct for combustion noise measurements as the pdf of $|G_{xy}(\omega)|$ changes depending on the distributions of $x(t)$ and $y(t)$. Figure 5.8 is a plot of the pdf of the time series normalised by the standard deviation, σ, for measurements in the combustor, hot nozzle outlet and the output of a focussed beamformer using a microphone array external to the engine for an engine running at a low power condition. All of the measured signals have had a high pass filter applied with

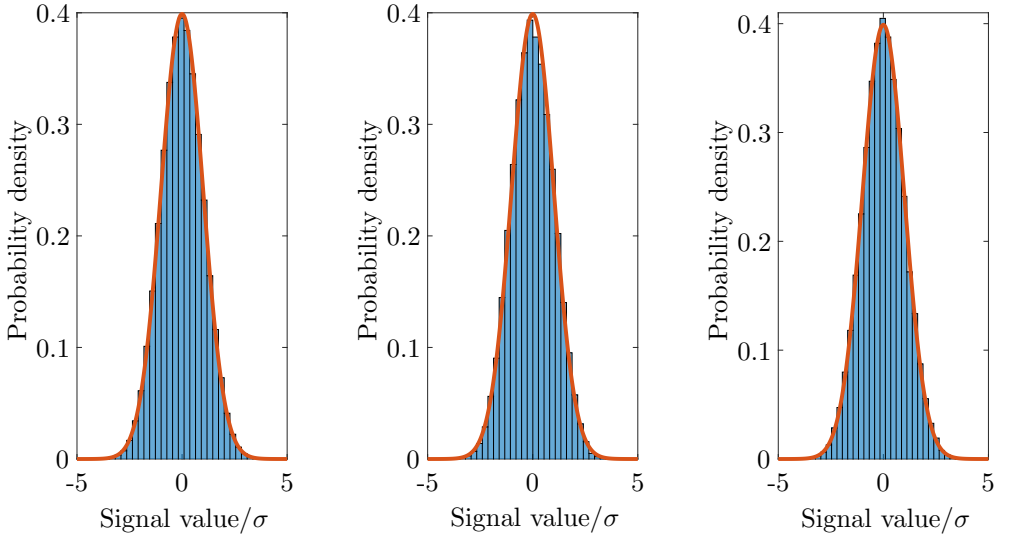

(A) Combustor (B) Hot nozzle (C) External microphone array

FIGURE 5.8: Histograms with fitted normal distributions of measured data inside and outside a jet engine at locations required for using the 3S Array method.

a cut-on frequency of 10 Hz applied to remove DC components present in the signals. Small sections of all of the signals have been removed due to an intermittent clicking noise, which is not due to the combustion process, present on the combustor signal. This data will be fully described and processed using the 3S Array method discussed in Chapter 6. Also plotted are pdfs of Gaussian distributions which have been fitted to the mean and standard deviation of the signal value/σ. From these three plots, it is clear that the measured signals appear to closely follow Gaussian distributions. Another two measures of the shape of a distribution are the skewness and kurtosis of the signal. The skewness and kurtosis are the third and fourth standardised moments of the data respectively and can be calculated using

$$\text{skewness} = \frac{E(x-\mu)^3}{\sigma^3} \tag{5.24}$$

and

$$\text{kurtosis} = \frac{E(x-\mu)^4}{\sigma^4}. \tag{5.25}$$

The value of the skewness describes the symmetry of the data with negative values representing data which has more data points below the mean than above and positive values represent more data points above the mean than below. A skewness of 0 represents data which is symmetric about the mean and a Gaussian distribution should have a skewness of 0. The kurtosis describes the relationship between the mean and the extreme values of the data. A normal distribution will have a kurtosis of 3 while distributions with a larger proportion of extreme values will have a smaller kurtosis and the opposite for a larger kurtosis. Rodríguez-García [41] used the kurtosis to identify whether sensors inside the engine duct had failed. Table 5.2 lists the kurtosis and skewness values for the combustor, hot nozzle outlet and a microphone array external to the engine measurements that were used in Figure 5.8. From these values, the distributions can be

Measurement location	Skewness	Kurtosis
Combustor	0.0208	2.93
Hot nozzle	0.0062	2.84
External Microphone Array	0.0141	2.92

TABLE 5.2: The skewness and kurtosis of measured signals from a low power engine test.

accurately described as Gaussian and therefore the assumptions required for the distributions and fit curves described in this section are accurate.

5.2 Generation of signals for simulating 3S output for different coherence values

To examine the probability distribution of the spectral estimates produced using the 3S Array method, another Monte Carlo simulation was performed. Instead of two signals being generated as in the previous section, three signals, $C(t)$, $N(t)$ and $F(t)$, will be generated which represent the combustor, hot nozzle and far field measurement locations and will be used as inputs to the 3S Array method. The signals will have one common signal $\nu(t)$ between them and each will

have an uncorrelated noise signal as in the previous section so that

$$C(t) = \nu(t) + n_C(t), \tag{5.26}$$

$$N(t) = \nu(t) + n_N(t) \tag{5.27}$$

and

$$F(t) = \nu(t) + n_F(t). \tag{5.28}$$

For simplicity, an array using one 'external microphone' signal, $F(t)$, will be generated and so, the spectral estimate of the 3S Array method will provide the same estimate as the 3S method. The pdf of the spectral estimate for the 3S Array method using an array of external microphones will be the same as that of the 3S method as long as the focussed beamformer output consists of correlated combustion noise and uncorrelated unwanted noise which both have a Gaussian distribution. The coherence functions between the three inputs can be defined using noise-to-signal ratios as in Equation (5.14) so that

$$\gamma^2_{CN}(\omega) = \frac{1}{(1+\alpha_C(\omega))(1+\alpha_N(\omega))}, \tag{5.29}$$

$$\gamma^2_{CF}(\omega) = \frac{1}{(1+\alpha_C(\omega))(1+\alpha_F(\omega))} \tag{5.30}$$

and

$$\gamma^2_{NF}(\omega) = \frac{1}{(1+\alpha_N(\omega))(1+\alpha_F\omega))} \tag{5.31}$$

where $\alpha_C(\omega) = \frac{G_{n_C n_C}(\omega)}{G_{\nu\nu}(\omega)}$, $\alpha_N(\omega) = \frac{G_{n_N n_N}(\omega)}{G_{\nu\nu}(\omega)}$ and $\alpha_F(\omega) = \frac{G_{n_F n_F}(\omega)}{G_{\nu\nu}(\omega)}$. To understand how the pdf of the spectral estimate obtained from the 3S method varies with the coherence between the three input cross spectra using a Monte Carlo simulation, the signals $C(t)$, $N(t)$ and $F(t)$ need to be generated which can be done using the noise-to-signal ratios as in the previous section. The noise-to-signal ratios will be dependent on each other, however, as the coherence function between one pair of generated signals will be dependent on the other two coherence functions. The three noise-to-signal ratios can be calculated by substituting equations (5.30) and (5.31) into Equation (5.29) to eliminate α_F and α_N to find

$$\alpha_C(\omega) = \sqrt{\frac{\gamma^2_{NF}(\omega)}{\gamma^2_{CN}(\omega)\gamma^2_{CF}(\omega)}} - 1. \tag{5.32}$$

Following a similar process

$$\alpha_N(\omega) = \sqrt{\frac{\gamma^2_{CF}(\omega)}{\gamma^2_{CN}(\omega)\gamma^2_{NF}(\omega)}} - 1 \tag{5.33}$$

and

$$\alpha_F(\omega) = \sqrt{\frac{\gamma^2_{CN}(\omega)}{\gamma^2_{CF}(\omega)\gamma^2_{NF}(\omega)}} - 1. \tag{5.34}$$

The signals can be generated using the noise-to-signal ratios in equations (5.32), (5.33) and (5.34) calculated from chosen coherence values. As with the Monte Carlo simulation described in the previous section, the signals were each generated 10000 times for each combination of the three coherence values. The lowest value of coherence squared used in the simulation is 0.05 and the increments between the coherence values is 0.05. The work-flow for the simulation is as follows:

1) Fix values of γ^2_{CN}, γ^2_{CF} and γ^2_{NF}.

2) Calculate the values of $\alpha_C(\omega)$, $\alpha_N(\omega)$ and $\alpha_F(\omega)$ by substituting the coherence function values into equations (5.32), (5.33) and (5.34).

3) Generate a normally distributed random signal to use as $\nu(t)$ using MATLABs 'randn' function with a mean of 0 and variance of 1 which is 32000 samples long (1000 seconds long with a sampling frequency of 32 samples per second).

4) Generate three different normally distributed random signals to use as $n_C(t)$, $n_N(t)$ and $n_F(t)$ using MATLAB's 'randn' function with a mean of 0 and variance of $\sqrt{\alpha_x(\omega)}$, $\sqrt{\alpha_y(\omega)}$ and $\sqrt{\alpha_z(\omega)}$ respectively which are 32000 samples long.

5) Calculate estimates of the $G_{CN}(\omega)$, $G_{CF}(\omega)$ and $G_{NF}(\omega)$ using a rectangular window which is 32 samples long ($B = 1$) and has no overlap.

6) Calculate an estimate of the spectrum of the 'combustion noise' using Equation (4.21) where $x_i = C$, $x_j = N$ and $x_k = F$.

7) Repeat steps 3) - 6) 10000 times to obtain 10000 different estimates of $\widehat{G}_{\nu\nu}(\omega)$.

5.2.1 Limitation on the possible coherence values between the three input signals

Since all of the noise-to-signal ratios in equations (5.32), (5.33) and (5.34) must have real positive values, there is a lower limit to the values of the third coherence given the other two values. Therefore, assuming the three signals consist of the combustion noise plus some unwanted noise and the signals are time aligned, the coherence values are limited to

$$\gamma^2_{NF}(\omega) \geq \gamma^2_{CN}(\omega)\gamma^2_{CF}(\omega), \tag{5.35}$$

$$\gamma^2_{CF}(\omega) \geq \gamma^2_{CN}(\omega)\gamma^2_{NF}(\omega) \tag{5.36}$$

and

$$\gamma^2_{CN}(\omega) \geq \gamma^2_{CF}(\omega)\gamma^2_{NF}(\omega). \tag{5.37}$$

If the estimated coherences from measurements do not fall within the range of limited values, it is therefore possible that the assumption that the signals consist of combustion noise plus uncorrelated unwanted noise which is made in the assumptions of the 3S method and in equations (5.26), (5.27) and (5.28) is incorrect. This is a useful test to identify whether there is unwanted coherent noise between two sensors as this would result in a larger coherence between one pair of signals and a reduced coherence between the other two pairs.

5.3 Probability distribution of the spectral estimate obtained using the 3S method

To acquire the probability distribution of the spectral estimate obtained from the 3S method (and the 3S Array method), the signals from the Monte Carlo simulation are used to calculate

an estimate of the contributions of $G_{\nu\nu}(\omega)$ present in $G_{FF}(\omega)$, using

$$\widehat{G}_{\nu\nu}(\omega) = \frac{|G_{CF}(\omega)||G_{NF}(\omega)|}{|G_{CN}(\omega)|}. \tag{5.38}$$

This estimate was obtained for an arbitrary frequency bin for each of the 10000 combinations of signals from the simulation. The pdf of $\widehat{G}_{\nu\nu}(\omega)$ with $BT = 1000$ and $BT = 100$ when $\gamma^2_{CN} = \gamma^2_{CF} = \gamma^2_{NF} = 1$ are shown in Figure 5.9. Also plotted are the fitted Gamma distributions

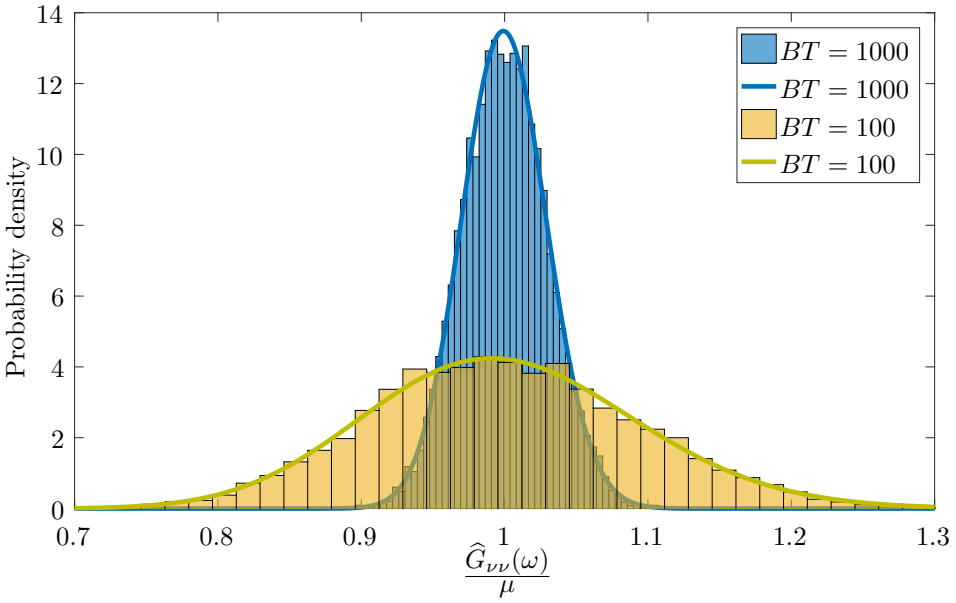

FIGURE 5.9: The distribution of $\widehat{G}_{\nu\nu}(\omega)$ with $\gamma^2_{CN} = \gamma^2_{CF} = \gamma^2_{NF} = 1$ for $BT = 1000$ and $BT = 100$. Also plotted are fitted gamma distributions.

to the data. It is clear that a Gamma distribution fits the distribution of $\widehat{G}_{\nu\nu}(\omega)$ accurately. For the 10000 estimates of $\widehat{G}_{\nu\nu}(\omega)$, $\frac{\mu^2}{\sigma^2} = 1142$ for $BT = 1000$ and $\frac{\mu^2}{\sigma^2} = 112$ for $BT = 100$, which are close to the actual value of $\frac{\mu^2}{\sigma^2}$ an autospectra has where $\frac{\mu^2}{\sigma^2} \approx BT$. The larger value indicates that the variance of the distribution of $\widehat{G}_{\nu\nu}(\omega)$ is smaller than that of an autospectra with the same value of BT. It is expected that the distribution of $\widehat{G}_{\nu\nu}(\omega)$ should be similar to that of an autospectrum given that

$$\widehat{G}_{\nu\nu}(\omega) = G_{FF}(\omega)\frac{|\gamma_{CF}(\omega)||\gamma_{NF}(\omega)|}{|\gamma_{CN}(\omega)|} \tag{5.39}$$

and each of the estimated coherences will have values very close to or equal to 1.

Having established that the distribution of $\widehat{G}_{\nu\nu}(\omega)$ is accurately described by a Gamma distribution, the distribution for different coherence combinations can be explored. Figure 5.10 is a plot of the pdf of $\widehat{G}_{\nu\nu}(\omega)$ for signals with $BT = 1000$ and coherence values of 0.9, 0.5, 0.3 and 0.1, where $\gamma^2_{CN} = \gamma^2_{CF} = \gamma^2_{NF}$. Also plotted are pdfs of Gamma distributions which have been fitted to the $\widehat{G}_{\nu\nu}(\omega)$ using the mean and the variance of the 10000 estimates for each of the coherence values. The distributions in this figure are all accurately described by the fitted Gamma distributions. To determine the effects on the pdf of $\widehat{G}_{\nu\nu}(\omega)$ when the three coherence functions do not all have the same value, Figure 5.11 is a plot of pdfs of $\widehat{G}_{\nu\nu}(\omega)$ where one of the values of coherence squared is 1 and the other two are 0.1. Also plotted are pdfs of Gamma distributions which have been fitted to the $\widehat{G}_{\nu\nu}(\omega)$ using the mean and the variance of the 10000 estimates

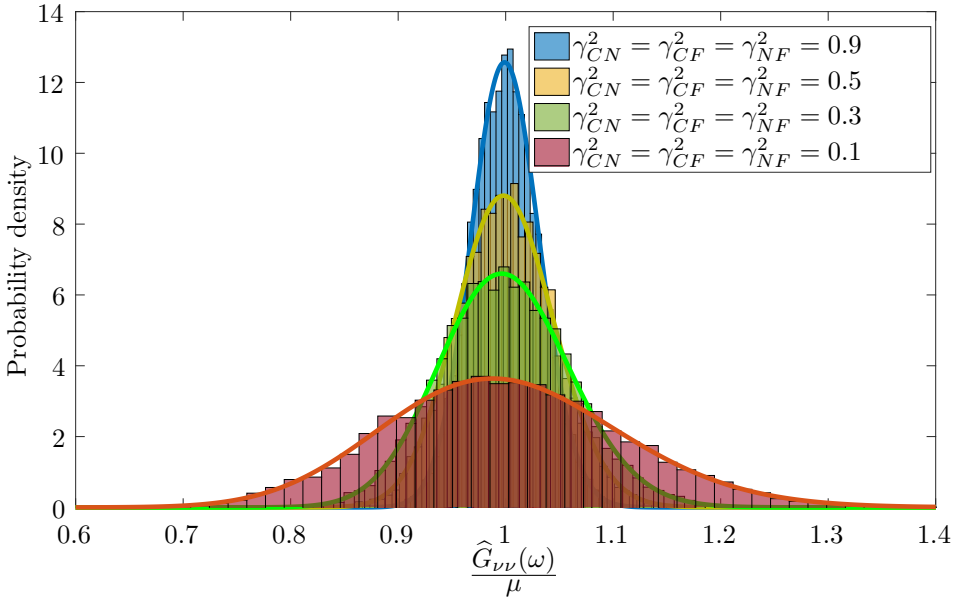

FIGURE 5.10: The distribution of $\widehat{G}_{\nu\nu}(\omega)$ with $BT = 1000$ and $\gamma^2_{CN} = 0.9, 0.5, 0.3$ and 0.1 where $\gamma^2_{CN} = \gamma^2_{CF} = \gamma^2_{NF}$. Also plotted are fitted gamma distributions.

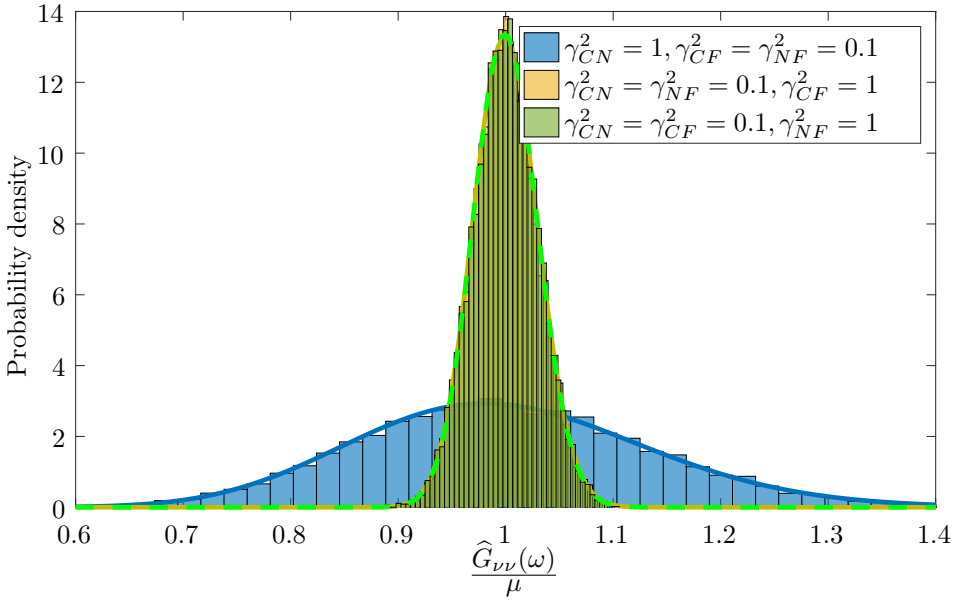

FIGURE 5.11: The distribution of $\widehat{G}_{\nu\nu}(\omega)$ with $BT = 1000$ where one value of coherence squared is 1 an the other two are 0.1. Also plotted are fitted gamma distributions.

for each of the coherence values. Again, the distributions for these values of coherence are also accurately described by Gamma distributions. It is of importance to note that the distributions for $\gamma^2_{CF} = 1, \gamma^2_{NF} = 0.1$ and $\gamma^2_{CF} = 0.1, \gamma^2_{NF} = 1$ are very similar. This is because $|G_{CF}(\omega)|$ and $|G_{NF}(\omega)|$ both appear on the numerator of Equation (5.38) and the distributions of the cross spectra will be the same for the same value of coherence. It is also important to note that the variance of the distribution is significantly higher with a cross-spectra with high coherence on the denominator and low coherence on the numerator than with low coherences on both the numerator and denominator. The confidence intervals of $\widehat{G}_{\nu\nu}(\omega)$ will therefore be largest when

the coherence value on the denominator is large and the two coherence values on the numerator are small. It is most likely that the cross-spectra on the denominator will a have higher coherence than cross-spectra on the numerator as there should be fewer sources of unwanted incoherent noise between the combustor and hot nozzle and the signal-to-noise ratio should be higher.

5.4 An analytic approach to defining confidence intervals of the 3S method

To calculate the confidence intervals of the 3S method (and the 3S Array method), the distribution of $\widehat{G}_{\nu\nu}(\omega)$ needs to be estimated. The distribution of the product and quotient of two continuous random variables, X and Y, can be calculated provided they are mutually independent of each other and expressions for this can be found in Mood et al. [57]. For continuous random variables X and Y, the product $\Xi = XY$ and the quotient $\Upsilon = X/Y$ can be calculated using

$$f_{\Xi}(\xi) = \int_{-\infty}^{\infty} \frac{1}{|x|} f_{X,Y}\left(x, \frac{\xi}{x}\right) \mathrm{d}x = \int_{-\infty}^{\infty} \frac{1}{|y|} f_{X,Y}\left(\frac{\xi}{y}, y\right) \mathrm{d}y \tag{5.40}$$

and

$$f_{\Upsilon}(\upsilon) = \int_{-\infty}^{\infty} |y| f_{X,Y}(\upsilon y, y) \mathrm{d}y. \tag{5.41}$$

In the above equations $f_{X,Y}(x, y)$ is the product of the pdfs of X and Y at the values of x and y respectively. The 3S and 3S Array methods assume that the three input spectra are at least partially coherent with each other. However, for the application of determining the contribution of combustion noise to the spectrum of either a single microphone or a focussed beamformer output, the coherences between the three spectra are often very small due to high levels of unwanted incoherent noise. For low values of coherence it is possible that equations (5.40) and (5.41) can be used to estimate the distribution of the combustion noise estimate obtained from the 3S and 3S Array methods.

The distribution of the spectral estimate, $\widehat{G}_{\nu\nu}(\omega)$, obtained using the 3S method where

$$\widehat{G}_{\nu\nu}(\omega) = \frac{|G_{CF}(\omega)||G_{NF}(\omega)|}{|G_{CN}(\omega)|},$$

as defined previously in Equation (5.38), can be calculated using equations (5.40) and (5.41) by calculating the distribution of $\frac{|G_{CF}(\omega)|}{|G_{CN}(\omega)|}$ using Equation (5.41) and then calculating the product of the distribution of $\frac{|G_{CF}(\omega)|}{|G_{CN}(\omega)|}$ and $|G_{NF}(\omega)|$ using Equation (5.40). As proven earlier in this Chapter, the distribution of $|G_{CF}(\omega)|$ where $C(t)$ and $N(t)$ are Gaussian signals can be described as Gamma distributions. Therefore, the distribution of the quotient of two Gamma distributions needs to be calculated and then the product of this new distribution and a Gamma distribution needs to be calculated to obtain the distribution of $\widehat{G}_{\nu\nu}(\omega)$ when the coherence values between the three input spectra are very small. Defining three continuous random variables as $X = |G_{CF}(\omega)|$, $Y = |G_{CN}(\omega)|$ and $Z = |G_{NF}(\omega)|$, the pdf of the spectral estimate obtained using the 3S method could therefore be calculated using Equation (5.41) to calculate $f_{\Upsilon}(\upsilon)$, which is the pdf of the

random variable $\Upsilon = \frac{|G_{CF}(\omega)|}{|G_{CN}(\omega)|}$, and

$$f_{\Xi}(\xi) = \int_{-\infty}^{\infty} \frac{1}{|\upsilon|} f_{\Upsilon,Z}\left(\upsilon, \frac{\xi}{\upsilon}\right) \mathrm{d}\upsilon \tag{5.42}$$

where $f_{\Xi}(\xi)$ is the pdf of $\widehat{G}_{\nu\nu}(\omega)$. To obtain the distributions of the magnitude of the cross-spectra the measured (estimated) coherence function and Equation (5.16) can be used.

Figure 5.12 is a plot of the pdf of $\widehat{G}_{\nu\nu}(\omega)$ evaluated from multiple combinations of coherence at an arbitrary frequency bin and the distributions obtained using equations (5.41) and (5.42) using the same values of coherence. It is clear that the distributions obtained using equations (5.41) and (5.42) do not fit the distributions of $\widehat{G}_{\nu\nu}(\omega)$ for high values of coherence. In fact, only the distribution for $\gamma_{CN}^2 = \gamma_{CF}^2 = \gamma_{NF}^2 = 0.05$ is close to the distribution of $\widehat{G}_{\nu\nu}(\omega)$. The pdfs obtained using equations (5.41) and (5.42) are similar to Gamma distributions and so, the distribution of $\widehat{G}_{\nu\nu}(\omega)$ and the distribution obtained from equations (5.41) and (5.42) can be compared using values of $\frac{\mu^2}{\sigma^2}$ calculated from $f_{\Xi}(\xi)$ and $\widehat{G}_{\nu\nu}(\omega)$. The mean, μ_{Ξ}, and variance, σ_{Ξ}^2 of $f_{\Xi}(\xi)$ can be calculated using

$$\mu_{\Xi} = \int_{-\infty}^{\infty} \xi f_{\Xi}(\xi) \mathrm{d}\xi \tag{5.43}$$

and

$$\sigma_{\Xi}^2 = \int_{-\infty}^{\infty} (\xi - \mu_{\Xi}) f_{\Xi}(\xi) \mathrm{d}\xi. \tag{5.44}$$

Figure 5.13 is a plot of the values of $\frac{\mu^2}{\sigma^2}$ for $\widehat{G}_{\nu\nu}(\omega)$ and for the distribution obtained from equations (5.41) and (5.42) for the combinations of coherence where $\gamma_{CN}^2 = \gamma_{CF}^2 = \gamma_{NF}^2$. The values of $\frac{\mu^2}{\sigma^2}$ of the estimated distribution using equations (5.41) and (5.42) are underestimates of those of $\widehat{G}_{\nu\nu}(\omega)$ and approach those of $\widehat{G}_{\nu\nu}(\omega)$ as $\gamma_{CN}^2 \to 0$.

To fully understand the range of coherence values where the estimated distribution using the integration method is valid, it is necessary to examine the variation of all of the combinations of coherence. For simplicity, as the mean of the distribution of the estimates obtained from the Monte Carlo simulation should be 1 as the variance of $C(t)$ is 1, $\frac{\mu^2}{\sigma^2}$ will be a measure of the variance of the distribution and can be expressed as

$$\frac{1}{\bar{\sigma}^2} = \frac{\mu^2}{\sigma^2} \tag{5.45}$$

and

$$\frac{1}{\widehat{\sigma}_{\Xi}^2} = \frac{\mu_{\Xi}^2}{\sigma_{\Xi}^2}. \tag{5.46}$$

Figure 5.14 is a plot of $\frac{\bar{\sigma}^2}{\widehat{\sigma}_{\Xi}^2}$ which describes the error in the the estimated distribution calculated using equations (5.41) and (5.42) against the three coherence functions. The closer the value of $\frac{\bar{\sigma}^2}{\widehat{\sigma}_{\Xi}^2}$ is to 1, the more accurately the $f_{\Xi}(\xi)$ fits the distribution of $\widehat{G}_{\nu\nu}(\omega)$. It is clear that for a large number of coherence combinations the estimated distribution is not a good fit as $\frac{1}{\widehat{\sigma}_{\Xi}^2} < \frac{1}{\bar{\sigma}^2}$. There is also a region where the fit is not good where $\frac{1}{\widehat{\sigma}_{\Xi}^2} > \frac{1}{\bar{\sigma}^2}$ which occurs when $\gamma_{CN}^2 > \gamma_{CF}^2$ and $\gamma_{CN}^2 > \gamma_{NF}^2$. When all three of the values of coherence are equal to 0.05, $\frac{1}{\widehat{\sigma}_{\Xi}^2}$ is an underestimate of $\frac{1}{\bar{\sigma}^2}$ but it is close to the correct value. An underestimate would result in a distribution with a larger variance which would mean the estimate of the confidence interval

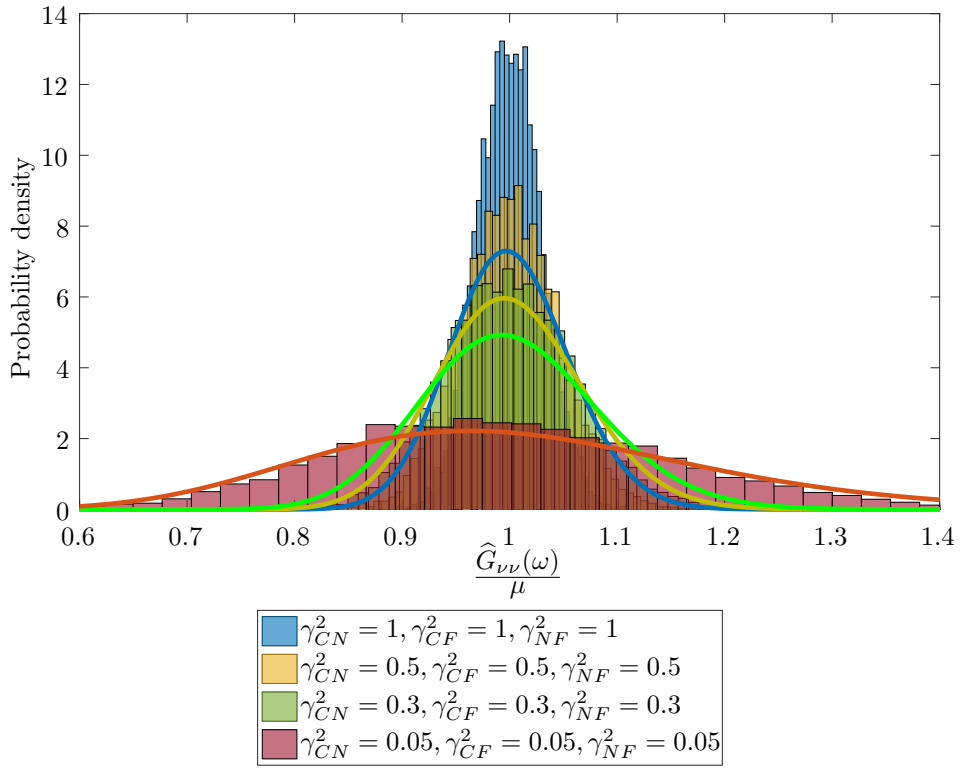

FIGURE 5.12: The distribution of $\widehat{G}_{\nu\nu}(\omega)$ with $BT = 1000$ for several values of coherence and the distributions obtained using the integration method.

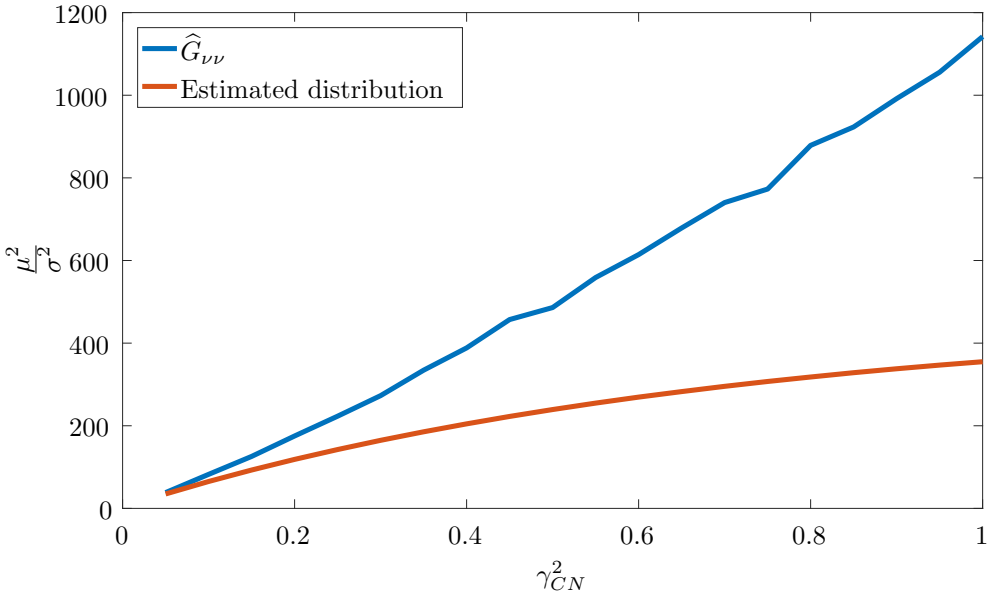

FIGURE 5.13: The values of $\frac{\mu^2}{\sigma^2}$ for $\widehat{G}_{\nu\nu}(\omega)$ and the estimated distribution using the integration method for different coherences where $\gamma^2_{CN} = \gamma^2_{CF} = \gamma^2_{NF}$.

would be wider than the true value of the confidence interval. There are other combinations of coherences where $\frac{\bar{\sigma}^2}{\widehat{\sigma}^2_{\Xi}}$ is close to 1 and these are displayed as Figure 5.15 for clarity. There is a small range of values of coherence where the estimated distribution is an approximately good fit

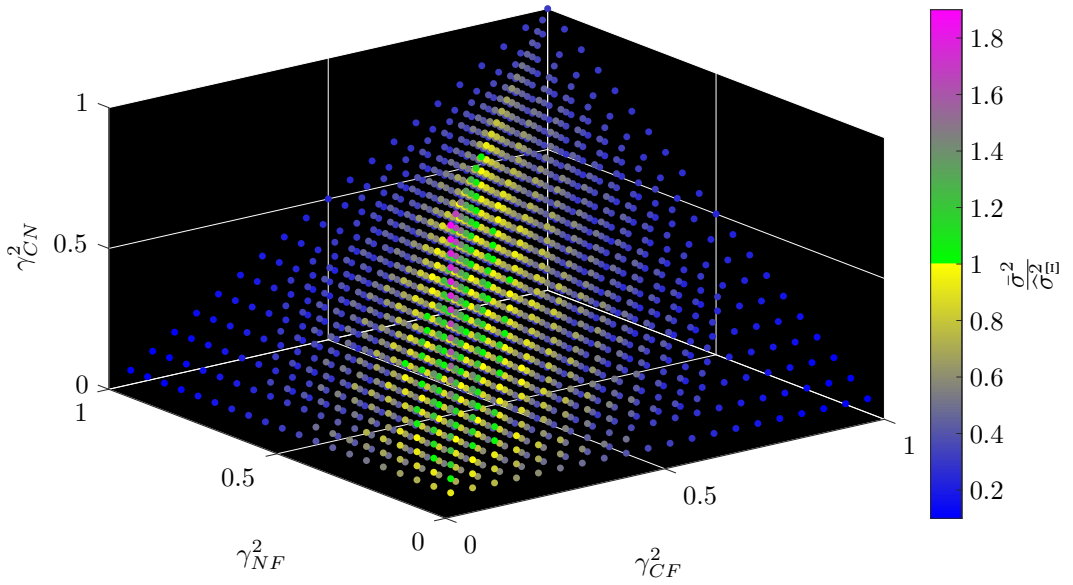

FIGURE 5.14: The values of $\frac{\hat{\sigma}^2}{\hat{\sigma}^{2[\mathrm{I}]}_{\Xi}}$ against the three coherence functions where $\frac{1}{\hat{\sigma}^2}$ is the mean squared divided by the variance of $\widehat{G}_{\nu\nu}(\omega)$ and $\frac{1}{\hat{\sigma}^{2[\mathrm{I}]}_{\Xi}}$ is the mean squared divided by the variance of the estimated distribution $f_{\Xi}(\xi)$.

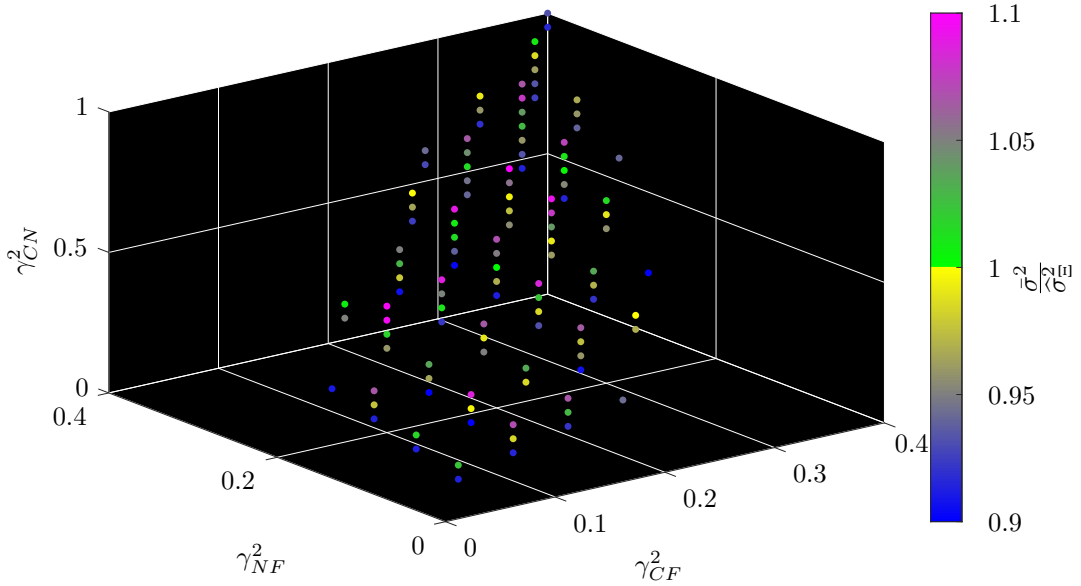

FIGURE 5.15: The values of $\frac{\hat{\sigma}^2}{\hat{\sigma}^{2[\mathrm{I}]}_{\Xi}}$ between 0.9 and 1.1 against the three coherence functions where $\frac{1}{\hat{\sigma}^2}$ is the mean squared divided by the variance of $\widehat{G}_{\nu\nu}(\omega)$ and $\frac{1}{\hat{\sigma}^{2[\mathrm{I}]}_{\Xi}}$ is the mean squared divided by the variance of the estimated distribution $f_{\Xi}(\xi)$.

to the actual distribution of the data. While this method could be used for values in this range it is only a very good fit for a small number of coherences and another method would need to be used for coherence values outside of this region.

5.5 Defining confidence intervals for 3S using an empirical approach

Previous sections have shown that the distribution of $\widehat{G}_{\nu\nu}(\omega)$ can be described as a Gamma distribution, fully defined by $\frac{\mu^2}{\sigma^2}$. The variation of $\frac{\mu^2}{\sigma^2}$ for different values of coherence of the three cross-spectra for signals with $BT = 1000$ is plotted in Figure 5.16. The variation of $\frac{\mu^2}{\sigma^2}$

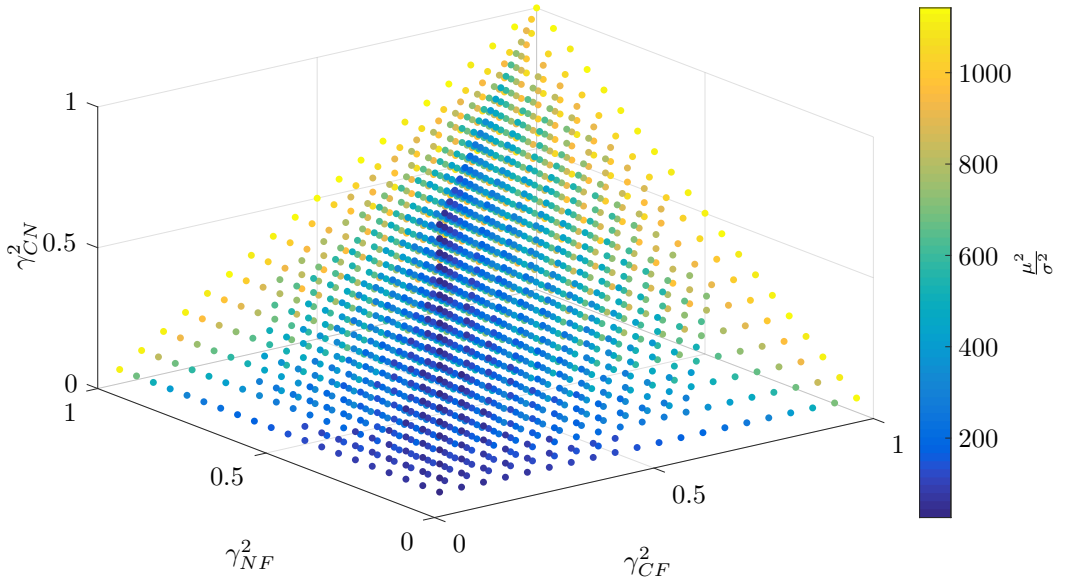

FIGURE 5.16: The values of $\frac{\mu^2}{\sigma^2}$ against the three values of coherence where μ^2 and σ^2 are the mean and the variance of $\widehat{G}_{\nu\nu}(\omega)$ respectively.

with the three coherence values does have a structure.

Using the MATLAB curve fitting application, functions can be fitted to the values of $\frac{\mu^2}{\sigma^2}$ for the different values of coherence. As the curve fitting application can only calculate a fit for three dimensions of data, curved were fitted to the data for fixed values of γ^2_{CN}. Through trial and error, it was found that an equation of the form

$$\frac{\mu^2}{\sigma^2} = Ae^{\Lambda(\gamma^2_{CF}+\gamma^2_{NF})} + C(\gamma^2_{CF} + \gamma^2_{NF}) + D \tag{5.47}$$

could provide an acceptable fit to the values in Figure 5.16 where A, Λ, C and D are constants. The fitting procedure was repeated for different values of γ^2_{CN} to obtain the coefficients for different values of γ^2_{CN} which are listed in Table 5.3. Also given in this table are parameters for the fit of the curves to the data. The R^2 parameter (known as the coefficient of determination) is a measure of how much of the variation in $\frac{\mu^2}{\sigma^2}$ is explained by variation in γ^2_{CF} and γ^2_{NF} in the fitted function. The value of R^2 will have a value between 0 which means the variation in $\frac{\mu^2}{\sigma^2}$ is not explained at all by the fitted function, and 1 where the variation in $\frac{\mu^2}{\sigma^2}$ is perfectly described by the fitted function (i.e. the function passes through all of the data points). The values of R^2 are all close to 1 with the highest values at high levels of γ^2_{CN}.

The fitted curve describes the variation in the values of $\frac{\mu^2}{\sigma^2}$ well when γ^2_{CN} is fixed. The coefficients vary however for different values of γ^2_{CN} as $\frac{\mu^2}{\sigma^2} = f(\gamma^2_{CN}, \gamma^2_{CF}, \gamma^2_{NF})$. To be able to estimate

γ^2_{CF}	A	Λ	C	D	R^2
0.05	0.00142	12.59	285.3	3.349	0.997
0.1	0.3312	6.804	472.8	-39.48	0.9869
0.15	14	3.56	277.4	-11.82	0.9863
0.2	128.7	1.91	-39.71	-107.6	0.9882
0.25	395.9	1.28	-372.3	-363.7	0.9895
0.3	123.8	1.756	24.53	-111.5	0.9932
0.35	318.8	1.249	-229.3	-291.1	0.9941
0.4	153.9	1.525	-17.78	-136.6	0.9953
0.45	84.11	1.746	113.5	-75.93	0.9968
0.5	166.8	1.372	-17.22	-147.6	0.9977
0.55	111.2	1.485	79.86	-101.1	0.9978
0.6	97.85	1.483	102.3	-86.56	0.9985
0.65	59.8	1.646	173.6	-56.35	0.9986
0.7	84.94	1.433	136.8	-80.25	0.9987
0.75	47.5	1.618	210.2	-51.92	0.999
0.8	64.3	1.442	179.6	-66.13	0.9992
0.85	51.51	1.493	193.3	-51.92	0.9996
0.9	89.68	1.224	147.9	-90.13	0.9997
0.95	38.81	1.571	227.2	-38.72	0.9996
1	51.9	1.377	188.1	-52.49	0.9998

TABLE 5.3: The values of the coefficients in $f(\gamma_{CF}, \gamma_{NF}) = Ae^{\Lambda(\gamma^2_{CF}+\gamma^2_{NF})}+C(\gamma^2_{CF}+\gamma^2_{NF})+D$ when fitted to the values of $\frac{\mu^2}{\sigma^2}$ for different values of γ^2_{CN}. The values of the coefficient of determination, R^2 are also given.

$\frac{\mu^2}{\sigma^2}$ for any valid combination of coherence values, the variation of the constants A, Λ, C and D with γ^2_{CN} needs to be defined. A simple method would be to use linear interpolation for values of γ^2_{CN} between the data points in Table 5.3. This provides coefficients for values of coherence over a large range but will not provide reliable coefficients below the lowest value of coherence given in the table. For $\gamma^2_{CN} < 0.05$ the values of the coherences are all similarly small and so the method given in Section 5.4 can be used to approximate the distribution of the data as the signals become close to being statistically independent. For a coherence value below 0.05 to be measured accurately, BT_{eqv} will need to be large enough so that a Gamma distribution still accurately describes the distribution of $|G_{CN}(\omega)|$ (the formula for which is given in Equation (5.23)). Due to the need for high frequency resolution to resolve the low frequency combustion noise, the only way to obtain large values of BT is to have long measurement times. For example, for $BT = 1000$ and $B = 4$ Hz, $T = 250$ s when no overlapping segments are used which means that, for a bin width of 4 Hz, the measurement will need to be taken over 250 seconds. This is extremely expensive to achieve during an engine test program as the engine will need to be kept at the same exact state for the entirety of that time. In addition, measurements will likely be needed for multiple engine conditions and so time available during a test program will be limited. It is therefore unlikely that a signal with a coherence squared below 0.05 could be accurately measured and have a distribution that can be approximated

with a Gamma distribution. Even with overlapping segments and using a Hanning window, the maximum window correction factor given in Figure 5.6 is 2.13 which will require a measurement length of 118 s to achieve $BT_{\text{eqv}} = 1000$. A table of measurement times for different values of BT with a bin width of 4 Hz is included in Table 5.4.

BT	B, Hz	T, s
10	4	2.5
100	4	25
200	4	50
500	4	125
1000	4	250
2000	4	500

TABLE 5.4: The measurement times required for different values of BT with a frequency resolution of 4 Hz per bin.

Figure 5.17 is a plot of the distributions of $\widehat{G}_{\nu\nu}(\omega)$ obtained from the mean and the variance of the 10000 values of $\widehat{G}_{\nu\nu}(\omega)$ and the empirically calculated distributions using the value of $\frac{\mu^2}{\sigma^2}$ calculated from Equation (5.47) using the coefficients from Table 5.3 for different combinations of coherence values. The empirically calculated distributions are very similar to the fitted distri-

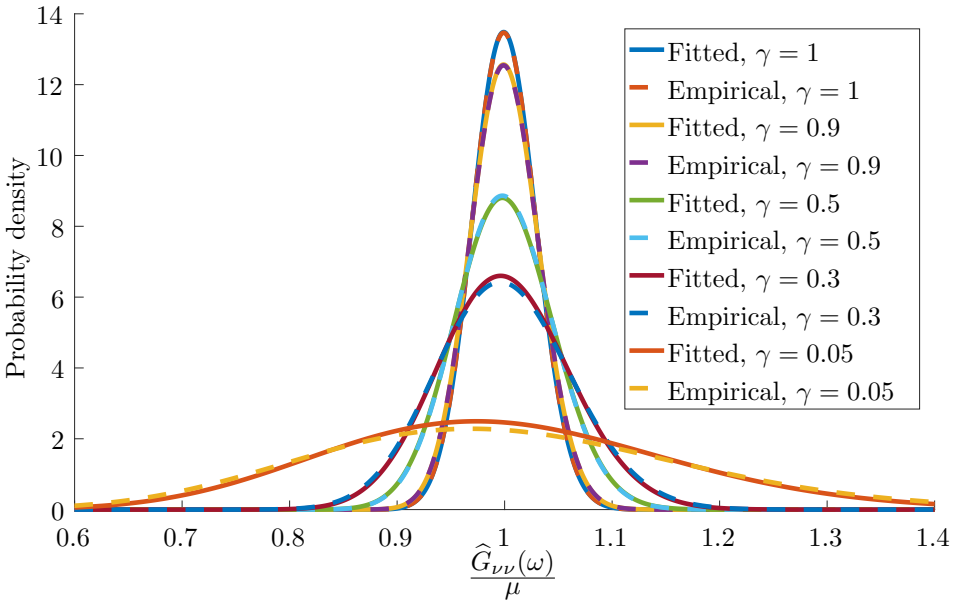

FIGURE 5.17: The gamma distributions fitted to the 10000 values of $\widehat{G}_{\nu\nu}(\omega)$ and the empirically calculated distributions for coherences $\gamma^2_{CN} = \gamma^2_{CF} = \gamma^2_{NF} = \gamma$.

butions, indicating that the empirical distributions are a good approximation for the distribution of $\widehat{G}_{\nu\nu}(\omega)$. As with the pdf calculated using equations (5.41) and (5.42) in the previous section, to fully assess the accuracy of the empirical distributions, Figure 5.18 shows the values of $\frac{\bar{\sigma}^2}{\widehat{\sigma}^2_e}$ plotted against coherence where

$$\frac{1}{\widehat{\sigma}^2_e} = \frac{\mu^2_e}{\sigma^2_e} \tag{5.48}$$

and μ^2_e and σ^2_e are the mean squared and variance of the empirical distribution. Comparing

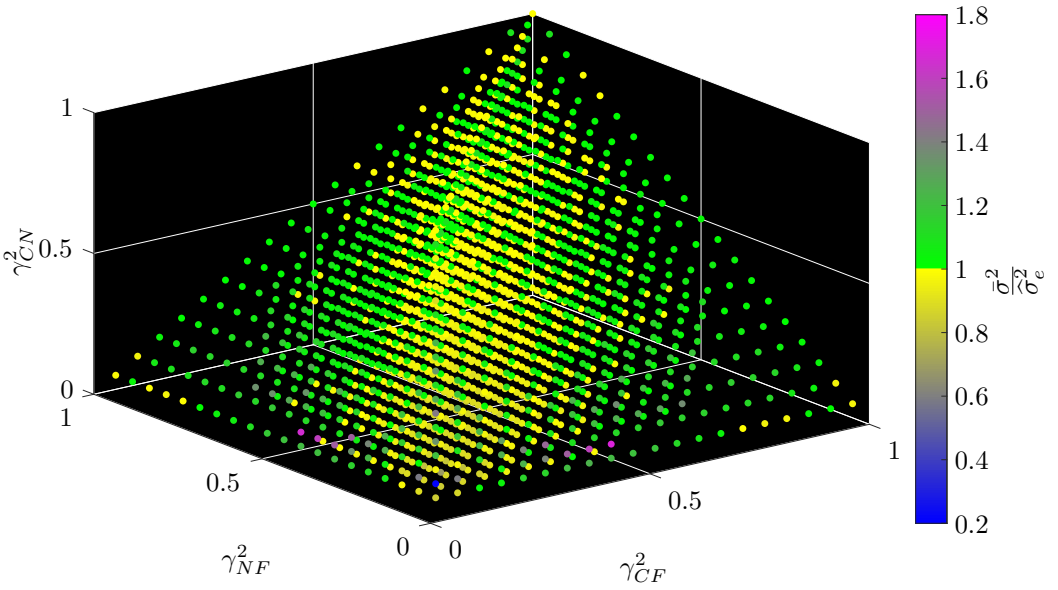

FIGURE 5.18: The values of $\frac{\bar{\sigma}^2}{\hat{\sigma}^2_e}$ against the three values of coherence where $\frac{1}{\bar{\sigma}^2}$ is the mean squared divided by the variance of $\widehat{G}_{\nu\nu}(\omega)$ and $\frac{1}{\hat{\sigma}^2_e}$ is the mean squared divided by the variance of the empirical distribution respectively.

Figure 5.18 to Figure 5.14 it is clear that the distributions calculated from the empirically fitted curves are a much better approximation of the actual distributions of $\widehat{G}_{\nu\nu}(\omega)$ for most of the coherence value combinations. There are, however, some combinations of coherence where the empirical distributions are not an accurate approximation of the the distribution of $\widehat{G}_{\nu\nu}(\omega)$. To make this clearer, Figure 5.19 is a plot of the values of $\frac{\bar{\sigma}^2}{\hat{\sigma}^2_e}$ which are close to 1. There are a large number of coherence combinations where the empirical distribution is a good fit. At lower values of coherence, there are some coherence combinations where there is significant error in the empirical distribution. Comparing Figure 5.19 to Figure 5.15 it is clear that the empirically-calculated distributions are in general a better fit. However, the coherence combinations for which the pdfs calculated using equations (5.41) and (5.42) are a good fit are combinations where the fit is not as good for the empirical method. Therefore the method with the best fit of the two methods for a particular combination of estimated coherence values can be chosen to obtain the most accurate estimates of the confidence intervals.

The distributions of the power spectral density estimates obtained using the empirical method are generally a good approximation of the distribution of $\widehat{G}_{\nu\nu}(\omega)$. The confidence intervals can be calculated from the empirically obtained Gamma distributions and compared to the confidence intervals of $\widehat{G}_{\nu\nu}(\omega)$, obtained from the Monte Carlo simulation, to identify the error in the estimated confidence interval. The confidence interval of the empirically obtained Gamma distribution can be calculated from the cumulative density function (cdf) of the Gamma distribution which is defined as

$$F(\widehat{G}_{\nu\nu}|a,b) = \frac{1}{b^a\Gamma(a)}\int_0^{\widehat{G}_{\nu\nu}} t^{a-1}e^{\frac{-t}{b}}\mathrm{d}t \tag{5.49}$$

where a and b are defined in equations (5.4) and (5.5) respectively. The value of a for the distribution is obtained from Equation (5.47) using the coefficient values from Table 5.3 and the

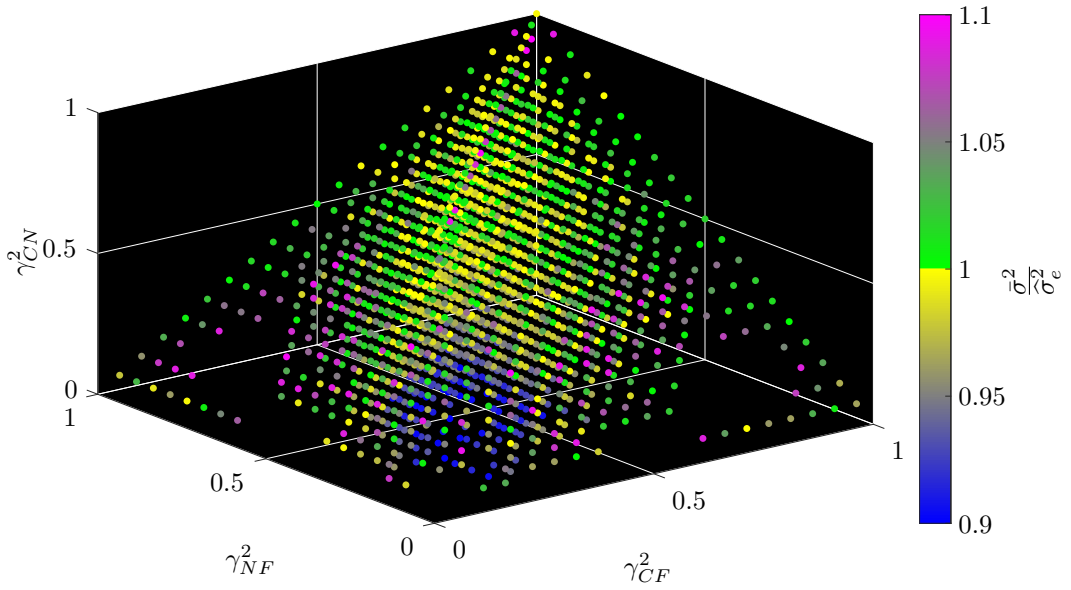

FIGURE 5.19: The values of $\frac{\bar{\sigma}^2}{\hat{\sigma}^2_e}$ between 0.9 and 1.1 against the three values of coherence where $\frac{1}{\bar{\sigma}^2}$ is the mean squared divided by the variance of $\widehat{G}_{\nu\nu}(\omega)$ and $\frac{1}{\hat{\sigma}^2_e}$ is the mean squared divided by the variance of the empirical distribution respectively.

combustion noise estimate obtained using the 3S method is used as the mean of the distribution. The 95% confidence intervals of the distribution will define the interval in which there is a 95% chance that the actual combustion noise is present. The 95% confidence interval can therefore be defined as $0.025 \leq F(\widehat{G}_{\nu\nu}(\omega)|a,b) \leq 0.975$ and the lower and upper bounds of the confidence interval are the values of the random variable $\widehat{G}_{\nu\nu}(\omega)$ at which the probability values $F(\widehat{G}_{\nu\nu}(\omega)|a,b) = 0.025$ and 0.975 respectively. The lower and upper limits of the 95% confidence interval were calculated using the MATLAB function 'gaminv' which takes a value of probability and a and b as inputs and outputs the value of $\widehat{G}_{\nu\nu}(\omega)$ for the chosen input parameters.

To obtain a direct comparison between the actual confidence interval from the Monte Carlo simulation and the estimated confidence interval for all coherence value combinations, the values of $\widehat{G}_{\nu\nu}(\omega)$ were divided by the mean so that all of the distributions would have a mean of 1. Figure 5.20 is a plot of the width of the 95% confidence interval of the empirically calculated distribution divided by the width of the 95% confidence interval of $\widehat{G}_{\nu\nu}(\omega)$ with the values plotted in dB. The confidence interval of the distribution of $\widehat{G}_{\nu\nu}(\omega)$ obtained from the Monte Carlo simulation was calculated using the MATLAB function 'prctile'. The majority of coherence value combinations produce only a small difference between the width of the empirical confidence interval and the width of the confidence interval of $\widehat{G}_{\nu\nu}(\omega)$ obtained from the Monte Carlo simulation. There is one point which is clearly an anomaly on the figure and that is when the $\gamma^2_{CN} = 0.1$ and $\gamma^2_{CF} = \gamma^2_{NF} = 0.05$ which is where the value of $\frac{\bar{\sigma}^2}{\hat{\sigma}^2_e}$ in Figure 5.18 is very small. For this combination of coherence values, the empirical fit is not accurate. This could be due to the empirical method not accurately fitting the distribution of $\widehat{G}_{\nu\nu}(\omega)$ but it is more likely that there is an anomaly in the Monte Carlo simulation for this combination of coherence values as this does not match the general trend in the plotted data. The width of the confidence interval obtained for the empirical distribution is significantly smaller than that of $\widehat{G}_{\nu\nu}(\omega)$ when γ^2_{CF} and

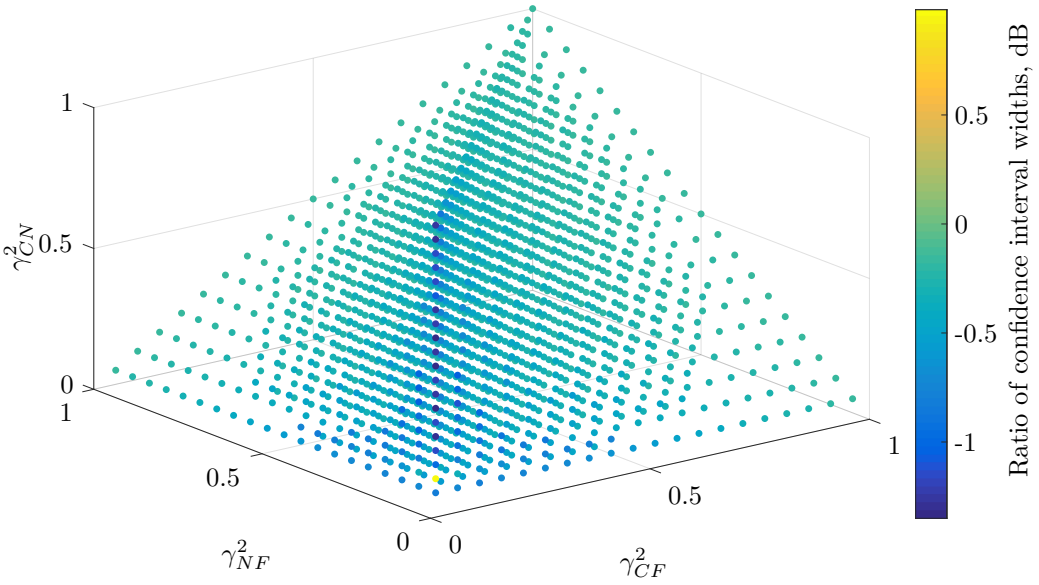

FIGURE 5.20: The ratio of the width of the 95% confidence interval of the empirically calculated distribution to the width of the 95% confidence interval of $\widehat{G}_{\nu\nu}(\omega)$.

γ^2_{NF} are small and γ^2_{CN} is larger than γ^2_{CF} and γ^2_{NF}. The error is largest when $\gamma^2_{CF} = \gamma^2_{NF} = 0.05$ and $\gamma^2_{CN} = 1$. To understand the reason for this, the ratio between the empirical and $\widehat{G}_{\nu\nu}(\omega)$ distributions for the lower and upper bounds of the interval are plotted separately and included as Figure 5.21 and Figure 5.22 respectively. The value corresponding to $\gamma^2_{CN} = 0.1$, $\gamma^2_{CF} = 0.05$, $\gamma^2_{NF} = 0.05$ has been omitted from both plots. From the scales on the figures it is clear that the

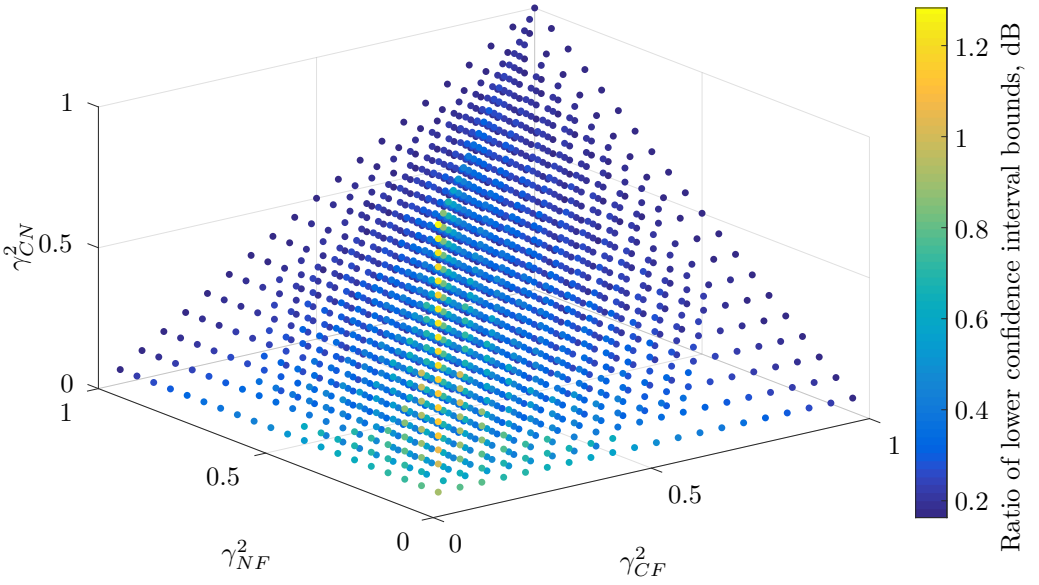

FIGURE 5.21: The ratio of the lower bound of the 95% confidence interval of the empirically calculated distribution and the 95% confidence interval of $\widehat{G}_{\nu\nu}(\omega)$ calculated from the Monte Carlo simulation.

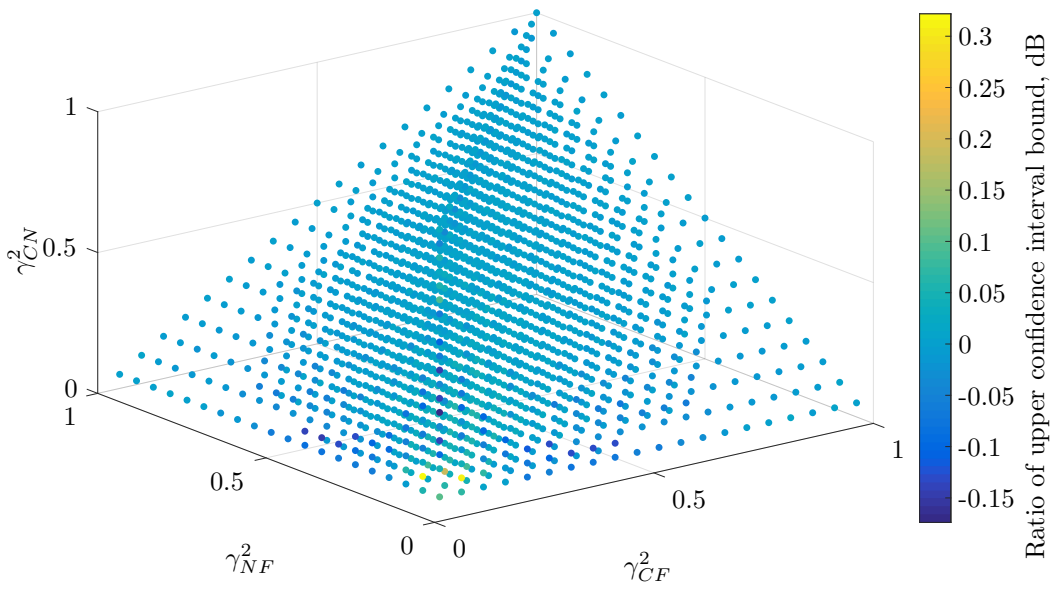

FIGURE 5.22: The ratio of the upper bound of the 95% confidence interval of the empirically calculated distribution and the 95% confidence interval of $\widehat{G}_{\nu\nu}(\omega)$ calculated from the Monte Carlo simulation.

error in the interval is almost entirely due to the lower bound of the confidence interval being incorrectly estimated. Since there is very little error on the upper coefficient, it is possible that the shape of the distribution is incorrect when $\gamma^2_{CF}\gamma^2_{NF} \ll \gamma^2_{CN}$.

The kurtosis of the empirically calculated distributions is approximately the same as the kurtosis of the distribution of $\widehat{G}_{\nu\nu}(\omega)$ obtained using the Monte Carlo simulation for all coherence values. The skewness of the empirical distribution does differ from that of the $\widehat{G}_{\nu\nu}(\omega)$ distribution which can be seen in Figure 5.23. The skewness of the empirically calculated distribution is generally larger than the skewness of the $\widehat{G}_{\nu\nu}(\omega)$ distribution. For the values of coherence where there is significant error in the lower bound estimate ($\gamma^2_{CF}\gamma^2_{NF} \ll \gamma^2_{CN}$), the skewness of the empirical distribution is slightly larger than that of the $\widehat{G}_{\nu\nu}(\omega)$ distribution. The error is more significant at these values of coherence as they have the smallest values of $\frac{\mu^2}{\sigma^2}$ and therefore, the largest variance. A small variation in skewness will therefore have a larger effect on the lower bound estimate. The confidence interval estimates produced using the empirical distribution are correct for the upper bound ± 0.3 dB. For the lower bound they are overestimates of the true value by between 0.18 and 1.3 dB with the larger overestimates occurring as $\gamma^2_{CF}\gamma^2_{NF}$ decreases. To ensure that there is at least a 95% chance that the confidence interval contains the true value of the combustion noise spectral value, the lower and upper bounds of the confidence interval calculated from Equation (5.49) need to be adjusted by decreasing the lower estimate by 1.3 dB and increasing the upper estimate by 0.16 dB. Defining the lower and upper bounds of the 95% confidence limit in dB, calculated from the empirically calculated distribution, as $EMP_{2.5}$ and $EMP_{97.5}$ respectively, the adjusted confidence intervals, $CI_{2.5}$ and $CI_{97.5}$, in dB can be defined as

$$CI_{2.5} = EMP_{2.5} - 1.3 \tag{5.50}$$

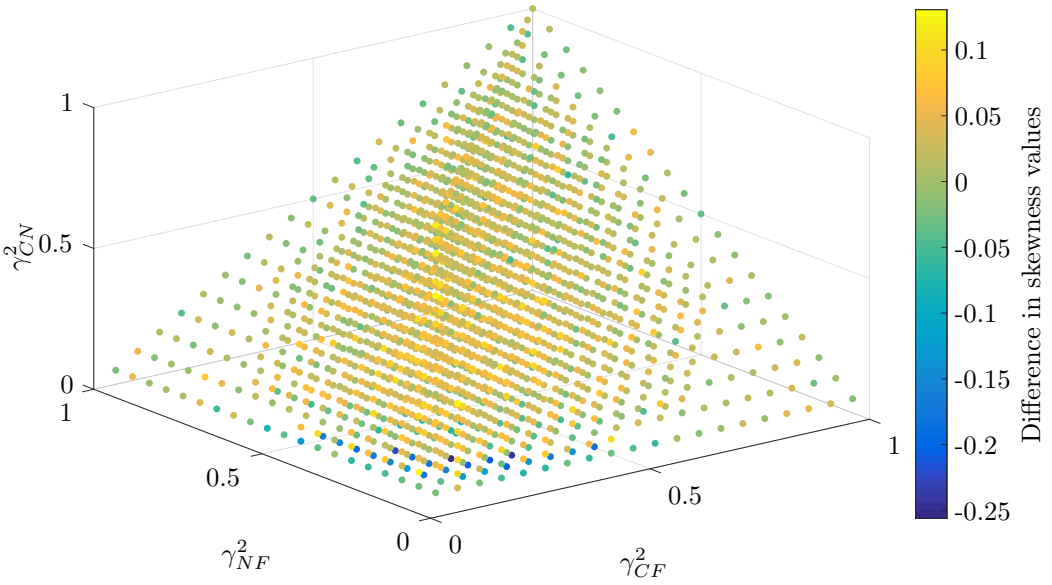

FIGURE 5.23: The difference between the skewness values of the empirically calculated distribution and the skewness values of the $\widehat{G}_{\nu\nu}(\omega)$ distribution.

and

$$CI_{97.5} = EMP_{97.5} + 0.16. \tag{5.51}$$

The values of $CI_{2.5}$ and $CI_{97.5}$ define an 'at least' 95% confidence interval for the estimate of the spectral density of the combustion noise.

5.6 Defining confidence intervals for lower values of BT

In sections 5.4 and 5.5, only signals with $BT = 1000$ have been when used when comparing the estimated distributions of $\widehat{G}_{\nu\nu}(\omega)$ to the distribution of $\widehat{G}_{\nu\nu}(\omega)$ calculated from the Monte Carlo simulation. The coefficients in Table 5.3 specifically relate to signals with $BT = 1000$. As stated earlier, it is expensive to perform a full scale engine test and keep the on condition for long enough to have estimates of $\widehat{G}_{\nu\nu}(\omega)$ with $BT = 1000$ that have sufficient frequency resolution and so it is likely that signals with values of BT smaller that 1000 will be used as inputs to the 3S method. To identify whether the empirical fit method will provide accurate estimates of the distribution of $\widehat{G}_{\nu\nu}(\omega)$ for different values of BT, a second set of simulated values of $\widehat{G}_{\nu\nu}(\omega)$ calculated using $BT = 100$ were produced using the Monte Carlo simulation.

From Figures 5.4 and 5.6, it is clear that for cross-spectral density estimates of two signals that have a correlated Gaussian component and an uncorrelated Gaussian component, the value of $\frac{\mu^2}{\sigma^2} \propto BT_{\text{eqv}}$ for a constant coherence value. It is therefore plausible that Equation (5.47) will also be a good fit for the values of $\frac{\mu^2}{\sigma^2}$ of $\widehat{G}_{\nu\nu}(\omega)$ for all values of BT_{eqv} where the coefficients A, C and D will all be proportional to BT_{eqv}. Figure 5.24 is a plot of $\frac{\bar{\sigma}^2}{\hat{\sigma}_e^2}$ for different combinations of coherence where $\frac{1}{\bar{\sigma}^2}$ the mean squared divided by the variance of the distribution of $\widehat{G}_{\nu\nu}(\omega)$ with $BT = 100$ and no overlapping segments calculated using the Monte Carlo simulation. The values

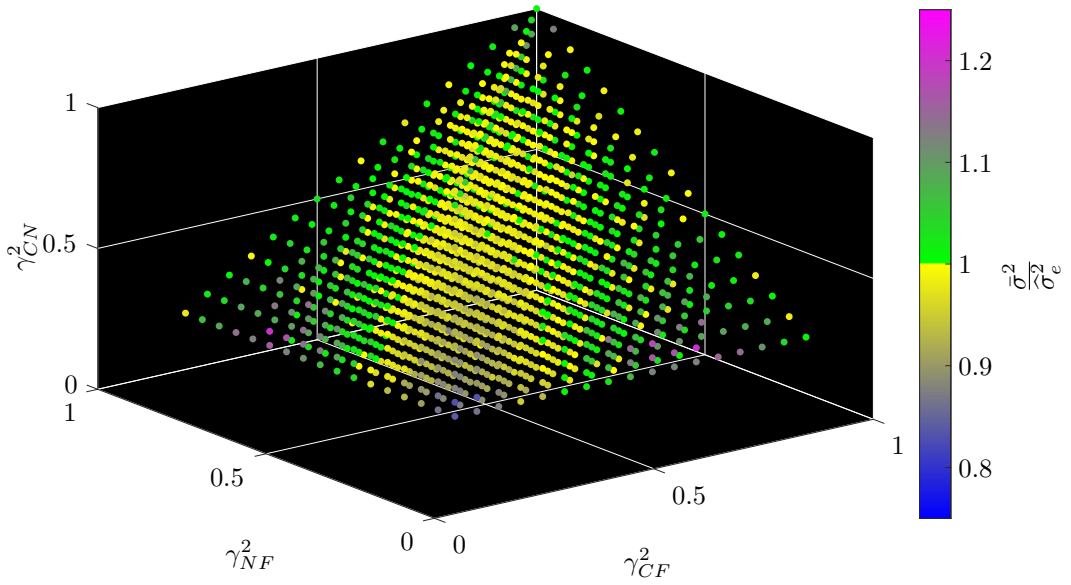

FIGURE 5.24: The values of $\frac{\bar{\sigma}^2}{\widehat{\sigma}^2_e}$ against the three values of coherence where $\frac{1}{\bar{\sigma}^2}$ is the mean squared divided by the variance of $\widehat{G}_{\nu\nu}(\omega)$ when $BT = 100$ and $\frac{1}{\widehat{\sigma}^2_e}$ is the mean squared divided by the variance of the empirical distribution respectively when $BT = 100$.

of $\frac{1}{\widehat{\sigma}^2_e}$ were calculated using Equation (5.47) with the same B coefficients as given in Table 5.3 and the values of A, C and D from the table multiplied by 0.1 as the BT product is a tenth of the BT product of the spectra from which the values in Table 5.3 were calculated. The lowest value of coherence plotted is 0.15 as for coherence values below 0.15 a Gamma distribution is not representative of the distribution of a cross-spectral density estimate (values given in Table 5.1). For the majority of coherence combinations, $\frac{1}{\widehat{\sigma}^2_e}$ is a good approximation of $\frac{1}{\bar{\sigma}^2}$. Comparing Figure 5.24 to Figure 5.18, the error in the values of $\frac{1}{\widehat{\sigma}^2_e}$ is smaller for the smaller value of BT. The empirical fitting function is therefore effective for different values of BT. The function can be rewritten as

$$\frac{\bar{\sigma}^2}{\widehat{\sigma}^2_e} = \frac{\mu^2_e}{\sigma^2_e} = BT_{\text{eqv}}\left(Ae^{\Lambda(\gamma^2_{CF}+\gamma^2_{NF})} + C(\gamma^2_{CF}+\gamma^2_{NF}) + D\right) \tag{5.52}$$

to accommodate different values of BT_{eqv} where the constants are given in Table 5.5.

The ratio of the width of the 95% confidence intervals of the empirically calculated distribution to the width of the 95% confidence intervals of distribution of $\widehat{G}_{\nu\nu}(\omega)$ calculated from the Monte Carlo simulation for $BT = 100$ is shown as Figure 5.25. As with the confidence interval for $BT = 1000$ (Figure 5.20) there is a large error in the confidence interval calculated using the empirically calculated distribution. Figures 5.26 and 5.27 are plots of the ratios of the empirically calculated values to the values calculated from the distribution of $\widehat{G}_{\nu\nu}(\omega)$ using the Monte Carlo simulation for $BT = 100$ of the lower and upper bounds of the 95% confidence interval respectively. As with the values for $BT = 1000$ there is only a small error in the empirically calculated upper bound of the interval but a significant error in the lower bound, which is in the same region for both values of BT. The error is, however, larger for $BT = 100$. The reason for the larger error

γ_{CF}^2	A	Λ	C	D
0.05	1.42×10^{-6}	12.59	0.2853	3.349×10^{-3}
0.1	3.312×10^{-4}	6.804	0.4728	-0.03948
0.15	0.014	3.56	0.2774	-0.01182
0.2	0.1287	1.91	-0.03971	-0.1076
0.25	0.3959	1.28	-0.3723	-0.3637
0.3	0.1238	1.756	0.02453	-0.1115
0.35	0.3188	1.249	-0.2293	-0.2911
0.4	0.1539	1.525	-0.01778	-0.1366
0.45	0.08411	1.746	0.1135	-0.07593
0.5	0.1668	1.372	-0.01722	-0.1476
0.55	0.1112	1.485	0.07986	-0.1011
0.6	0.09785	1.483	0.1023	-0.08656
0.65	0.0598	1.646	0.1736	-0.05635
0.7	0.08494	1.433	0.1368	-0.08025
0.75	0.0475	1.618	0.2102	-0.05192
0.8	0.0643	1.442	0.1796	-0.06613
0.85	0.05151	1.493	0.1933	-0.05192
0.9	0.08968	1.224	0.1479	-0.09013
0.95	0.03881	1.571	0.2272	-0.03872
1	0.0519	1.377	0.1881	-0.05249

TABLE 5.5: The values of A, Λ, C and D in $\frac{\mu_e^2}{\sigma_e^2} = BT_{\text{eqv}}\left(Ae^{\Lambda(\gamma_{CF}^2+\gamma_{NF}^2)} + C(\gamma_{CF}^2+\gamma_{NF}^2) + D\right)$ to fit the variation of $\frac{\mu^2}{\sigma^2}$ for the distribution of the values of $\widehat{G}_{\nu\nu}(\omega)$.

is that the smallest value of $\frac{1}{\widehat{\sigma}_e^2}$ for $BT = 100$ (this occurs at $\gamma_{CN}^2 = 1, \gamma_{CF}^2 = \gamma_{NF}^2 = 0.15$) is smaller than the smallest value for $BT = 1000$ ($\gamma_{CN}^2 = 1, \gamma_{CF}^2 = \gamma_{NF}^2 = 0.05$). Therefore, the variance in the estimated distribution for $BT = 100$ is larger than that of $BT = 1000$ for the same coherence value combination which amplifies the effect of the data having a generally larger value of skewness than a Gamma distribution for the same values of mean and variance. This is why the error in the confidence interval is small when $\frac{1}{\widehat{\sigma}_e^2}$ is large even when the absolute value of the difference in the skewness between the empirically calculated distribution and the distribution of $\widehat{G}_{\nu\nu}(\omega)$ is large. The variation in the skewness does not appear to be solely dependent on the combination of the three coherences. It is possible that the gamma distribution is an accurate model for the distribution and that the variation in the skewness values is due to an insufficient number of values of $\widehat{G}_{\nu\nu}(\omega)$ produced from the Monte Carlo simulation to accurately calculate the statistical parameters of the signals. If this was the case however, it would be very unlikely that the skewness would be consistently larger than the skewness of the empirically fitted Gamma distributions.

To ensure that there is at least a 95% chance that the calculated confidence interval contains the true value of the combustion noise for an estimate of $\widehat{G}_{\nu\nu}(\omega)$ with $BT = 100$, the confidence intervals calculated using the empirically calculated distribution will need to be adjusted as they

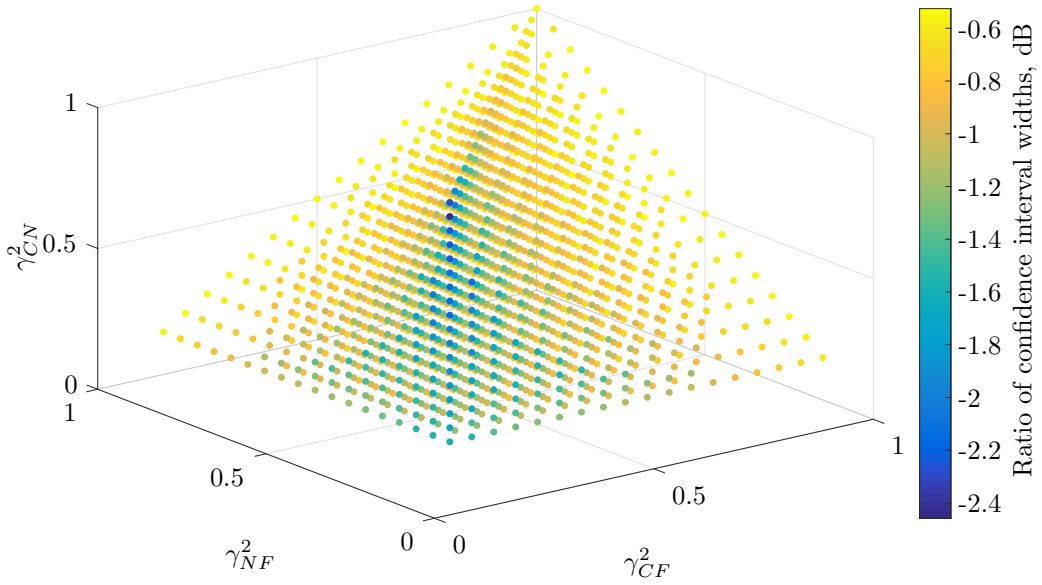

FIGURE 5.25: The ratio of the width of the 95% confidence interval of the empirically calculated distribution to the width of the 95% confidence interval of $\widehat{G}_{\nu\nu}(\omega)$ Calculated from the Monte Carlo simulation for $BT = 100$.

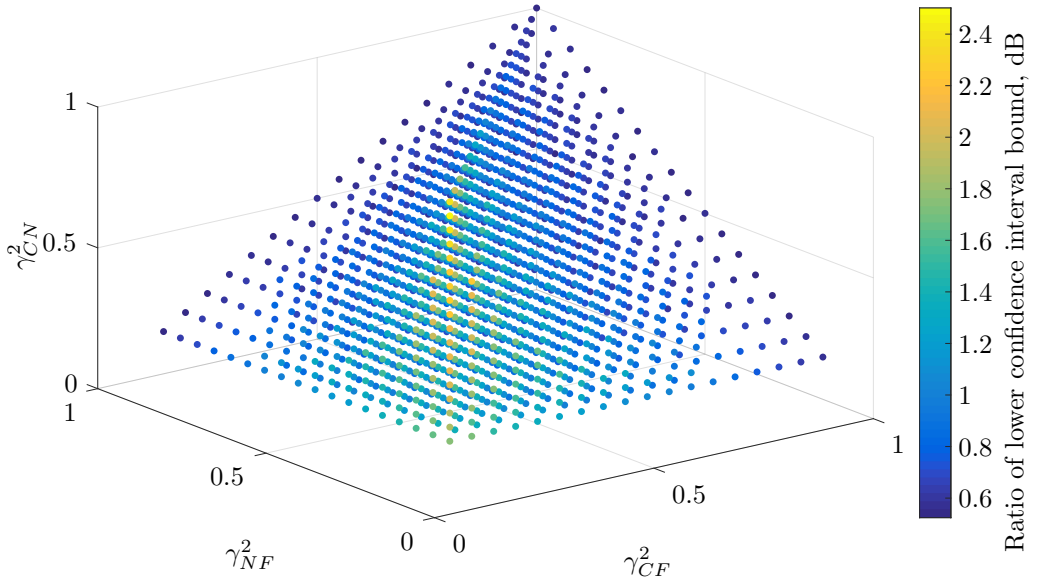

FIGURE 5.26: The ratio of the lower bound of the 95% confidence interval of the empirically calculated distribution to the lower bound of the 95% confidence interval of $\widehat{G}_{\nu\nu}(\omega)$ calculated from the Monte Carlo simulation for $BT = 100$.

were for when $BT = 1000$. The lower bound of the empirical confidence interval is 2.45 dB larger than the lower bound obtained from $\widehat{G}_{\nu\nu}(\omega)$ calculated using the Monte Carlo simulation for the worst case and the upper bound 0.1 dB smaller in the worst case. The adjusted lower and upper

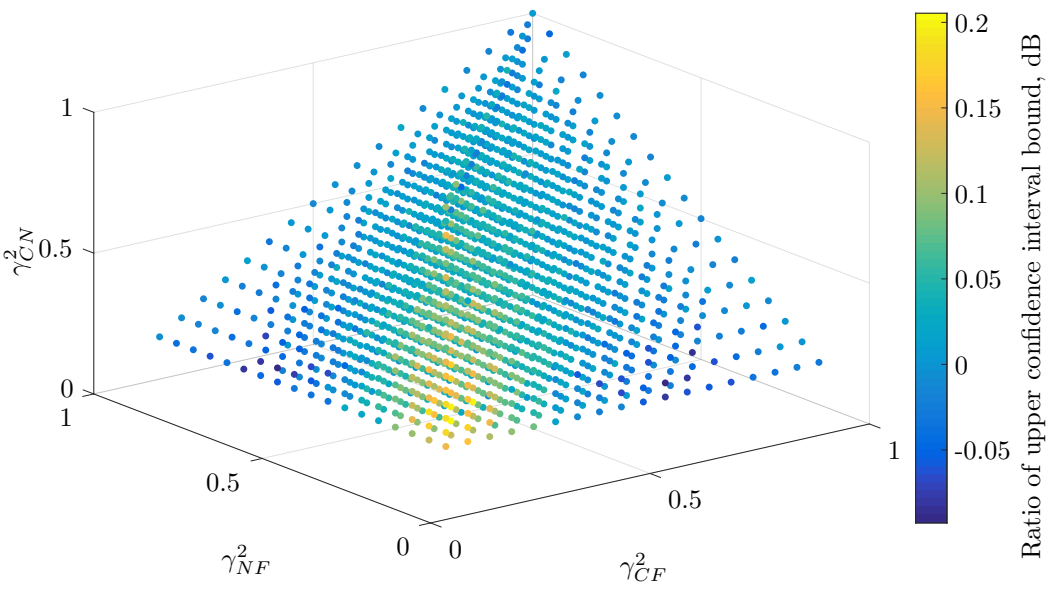

FIGURE 5.27: The ratio of the upper bound of the 95% confidence interval of the empirically calculated distribution to the upper bound of the 95% confidence interval of $\widehat{G}_{\nu\nu}(\omega)$ calculated from the Monte Carlo simulation for $BT = 100$.

bounds of the confidence interval in dB can be defined as

$$CI_{2.5} = EMP_{2.5} - 2.45 \tag{5.53}$$

and

$$CI_{97.5} = EMP_{97.5} + 0.1. \tag{5.54}$$

These corrections are different to those required for $BT = 1000$ and so, depending on the value of BT the correction will vary. To ensure that the confidence intervals calculated have at least a 95% chance of containing the true value of the combustion noise for signals with BT between 100 and 1000, the correction for the lower limit of $BT = 100$ and the correction for the upper limit of $BT = 1000$ should be used as these correct for the largest errors for the two cases.

5.7 Defining coefficients A, Λ, C and D using functions of γ^2_{CN}

The empirical method for calculating the distribution of $\widehat{G}_{\nu\nu}(\omega)$ used in Section 5.5 was also applied to 10000 values of $\widehat{G}_{\nu\nu}(\omega)$ produced using the Monte Carlo simulation where $BT = 2000$. From Equation (5.23), $\widehat{\gamma}^2_{xy}|_{\text{lower}} = 0.01$ for $BT = 2000$, so the coherence values were chosen to be logarithmically spaced between 1 and 0.01 to provide more information at the lower coherence combinations. MATLAB's curve fitting toolbox was applied in the same way as in Section 5.5 but to the values of $\frac{\mu^2}{BT\sigma^2}$ to obtain coefficients for use in Equation (5.52). The values of the coefficients A, Λ, C and D are plotted in Figure 5.28. Functions of γ^2_{CN} have been fitted to the

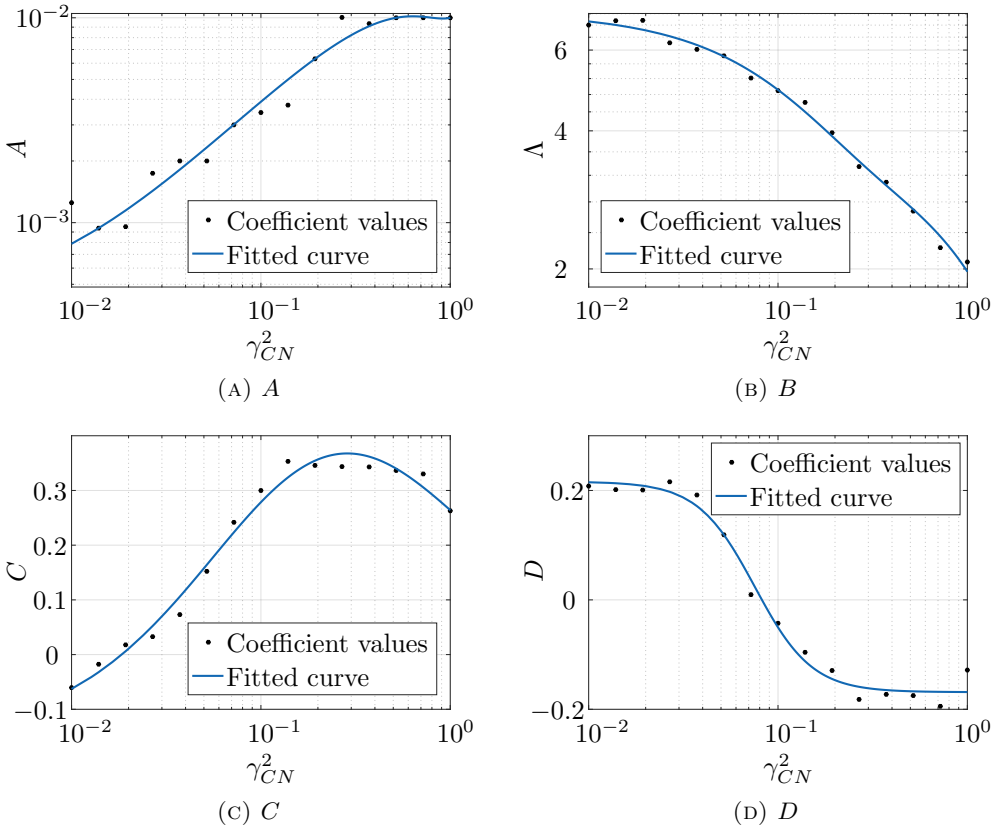

FIGURE 5.28: Coefficient values for Equation (5.52) calculated using MATLAB's curve fitting tool and curves fitted to the coefficient values.

coefficient values and are also plotted. It was not possible to fit relatively simple functions to coefficients obtained from the $BT = 1000$ or $BT = 100$ data as the coefficient values appeared to vary randomly with γ^2_{CN} which can be seen in Table 5.5. It is possible that this is because the MATLAB curve fitting toolbox uses an iterative optimisation method which will not necessary find the overall optimal solution but a local optimal solution instead. The equations for the curves fitted to the coefficient values are are

$$A = 0.02306(\gamma^2_{CN})^3 - 0.05355(\gamma^2_{CN})^2 + 0.04010\gamma^2_{CN} + 0.00039, \tag{5.55}$$

$$\Lambda = 3.582e^{-8.980\gamma^2_{CN}} + 3.677e^{-0.623\gamma^2_{CN}}, \tag{5.56}$$

$$C = \frac{0.48660\gamma^2_{CN} - 0.00895}{(\gamma^2_{CN})^2 + 0.75160\gamma^2_{CN} + 0.05743}, \tag{5.57}$$

and

$$D = \frac{-65.46}{(\gamma^2_{CN})^{-2.879} + 1701} + 0.02161. \tag{5.58}$$

There is some error in the functions as they do not reproduce the coefficient values perfectly resulting in a few outliers in Figure 5.28, especially at the larger values of γ^2_{CN} for the D coefficient. This is either because the functions are not quite accurate or because not enough values of $\widehat{G}_{\nu\nu}(\omega)$ have been calculated to provide values of $\frac{\mu^2}{\sigma^2}$ that have converged to the true value (with a reasonable level of accuracy).

The curve in Equation (5.52) with coefficients obtained from equations (5.55), (5.56), (5.57)

and (5.58) was used to obtain the empirically calculated values of $\frac{1}{\widehat{\sigma}_e^2}$ for $BT = 100, 1000$ and 2000. The values of $\frac{\bar{\sigma}^2}{\widehat{\sigma}_e^2}$ for $BT = 100, 1000$ and 2000 are plotted as Figures 5.29, 5.30 and 5.31 respectively. The empirically calculated value of $\frac{1}{\widehat{\sigma}_e^2}$ appears to be a good estimation of $\frac{1}{\bar{\sigma}^2}$ over

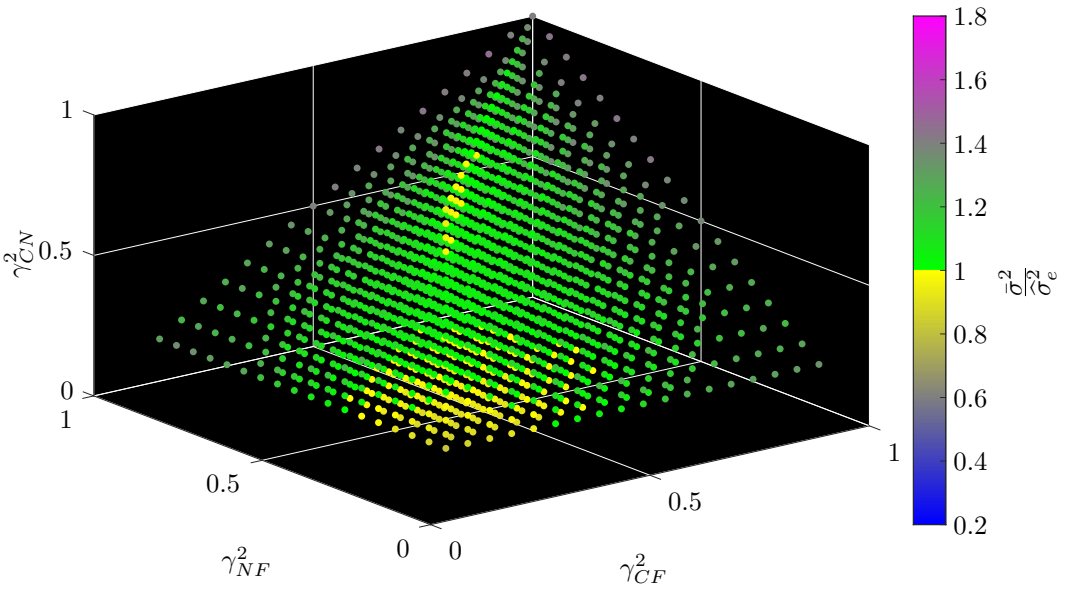

FIGURE 5.29: The values of $\frac{\bar{\sigma}^2}{\widehat{\sigma}_e^2}$ against the three values of coherence where $\frac{1}{\bar{\sigma}^2}$ is the mean squared divided by the variance of $\widehat{G}_{\nu\nu}(\omega)$ when $BT = 100$ and $\frac{1}{\widehat{\sigma}_e^2}$ is the mean squared divided by the variance of the empirical distribution respectively when $BT = 100$. $\frac{1}{\widehat{\sigma}_e^2}$ is calculated using the empirical equation with the coefficients calculated using equations (5.55), (5.56), (5.57) and (5.58).

a majority of the coherence value combinations for Figures 5.29 and 5.30. The values of $\frac{1}{\widehat{\sigma}_e^2}$ are not as good a fit for the $BT = 2000$ data, with significant overestimates when γ^2_{CF} is close to 1, γ^2_{NF} is close to 1 and γ^2_{CN}, γ^2_{CF} and γ^2_{NF} are all small. There are also significant underestimates when γ^2_{CN} is large while γ^2_{CF} and γ^2_{NF} are small. The reason for this has not been established. It is possible that this is due to an insufficient number of estimates of $\widehat{G}_{\nu\nu}(\omega)$ to obtain accurate distributions of $\widehat{G}_{\nu\nu}(\omega)$ or it could be that for large values of BT, Equation (5.52) is not a good fit for the variation of $\frac{1}{\bar{\sigma}^2}$ at the extremes of the range of coherence values. The fit is good when not at the extremes of the coherence value range.

To examine the accuracy of the empirically calculated values of $\frac{1}{\widehat{\sigma}_e^2}$, only the values of $\frac{\bar{\sigma}^2}{\widehat{\sigma}_e^2}$ that are between 0.75 and 1.25 are plotted as Figures 5.32, 5.33 and 5.34 for $BT = 100$, $BT = 1000$ and $BT = 2000$ respectively. For all three figures, $\frac{1}{\widehat{\sigma}_e^2}$ is an overestimate when either γ^2_{CF} or γ^2_{NF} is large. For Figures 5.32 and 5.33 $\frac{1}{\widehat{\sigma}_e^2}$ is an underestimate when all three coherences are small. For Figure 5.32, $\frac{1}{\widehat{\sigma}_e^2}$ is an overestimate when all three coherences are small and an underestimate when γ^2_{CF} and γ^2_{NF} are small and γ^2_{CN} is large. Underestimates of $\frac{1}{\bar{\sigma}^2}$ are generally preferable to overestimates as the calculated confidence interval will be wider and so, it is even more likely that the true value of $G_{\nu\nu}(\omega)$ will fall within the interval. However, underestimates or overestimates when $\frac{1}{\bar{\sigma}^2}$ is small will result in a more significant error in either the lower or upper bound as at

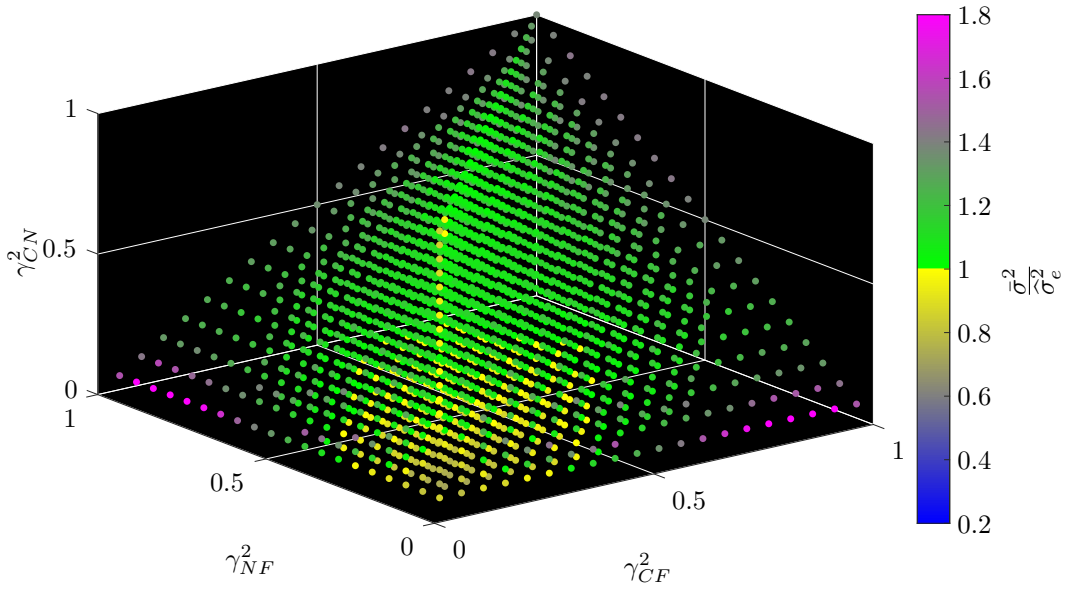

FIGURE 5.30: The values of $\frac{\bar{\sigma}^2}{\widehat{\sigma}^2_e}$ against the three values of coherence where $\frac{1}{\bar{\sigma}^2}$ is the mean squared divided by the variance of $\widehat{G}_{\nu\nu}(\omega)$ when $BT = 1000$ and $\frac{1}{\widehat{\sigma}^2_e}$ is the mean squared divided by the variance of the empirical distribution respectively when $BT = 1000$. $\frac{1}{\widehat{\sigma}^2_e}$ is calculated using the empirical equation with the coefficients calculated using equations (5.55), (5.56), (5.57) and (5.58).

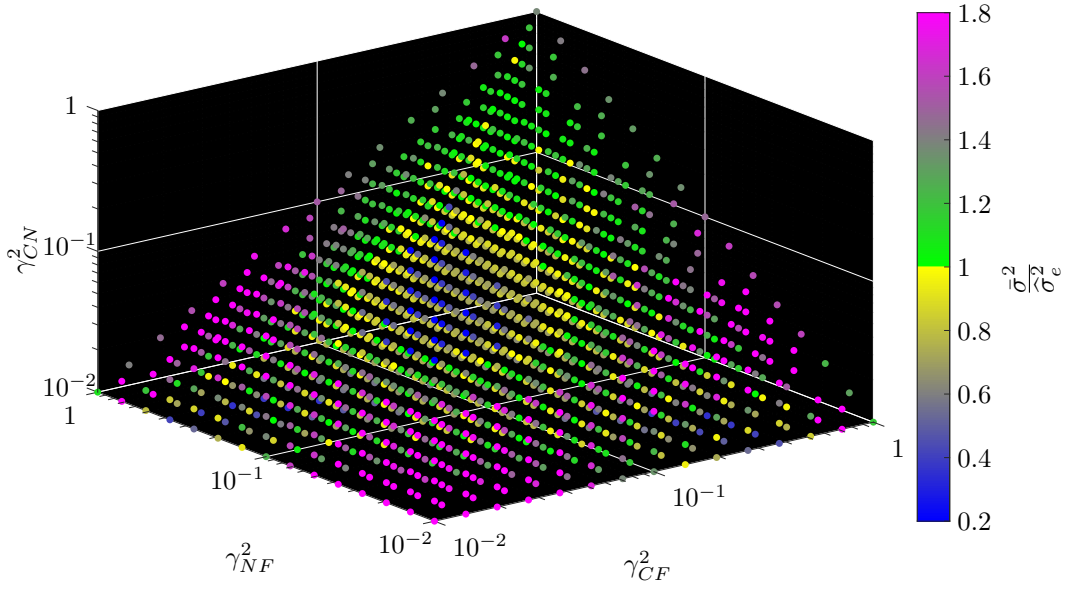

FIGURE 5.31: The values of $\frac{\bar{\sigma}^2}{\widehat{\sigma}^2_e}$ against the three values of coherence where $\frac{1}{\bar{\sigma}^2}$ is the mean squared divided by the variance of $\widehat{G}_{\nu\nu}(\omega)$ when $BT = 2000$ and $\frac{1}{\widehat{\sigma}^2_e}$ is the mean squared divided by the variance of the empirical distribution respectively when $BT = 2000$. $\frac{1}{\widehat{\sigma}^2_e}$ is calculated using the empirical equation with the coefficients calculated using equations (5.55), (5.56), (5.57) and (5.58).

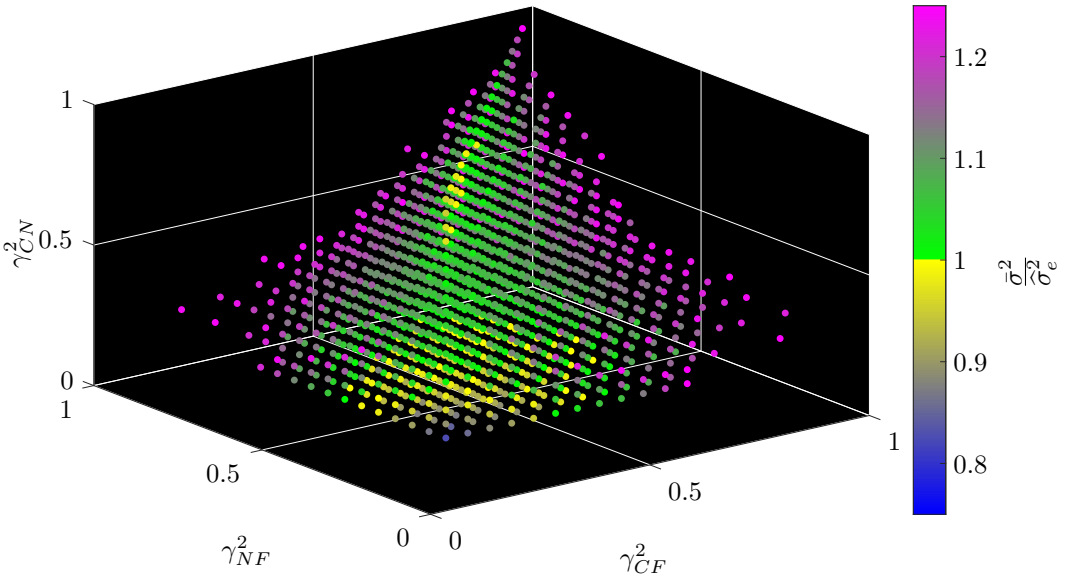

FIGURE 5.32: The values of $\frac{\bar{\sigma}^2}{\widehat{\sigma}^2_e}$ between 0.75 and 1.25 against the three values of coherence where $\frac{1}{\bar{\sigma}^2}$ is the mean squared divided by the variance of $\widehat{G}_{\nu\nu}(\omega)$ when $BT = 100$ and $\frac{1}{\widehat{\sigma}^2_e}$ is the mean squared divided by the variance of the empirical distribution respectively when $BT = 100$. $\frac{1}{\widehat{\sigma}^2_e}$ is calculated using the empirical equation with the coefficients calculated using equations (5.55), (5.56), (5.57) and (5.58).

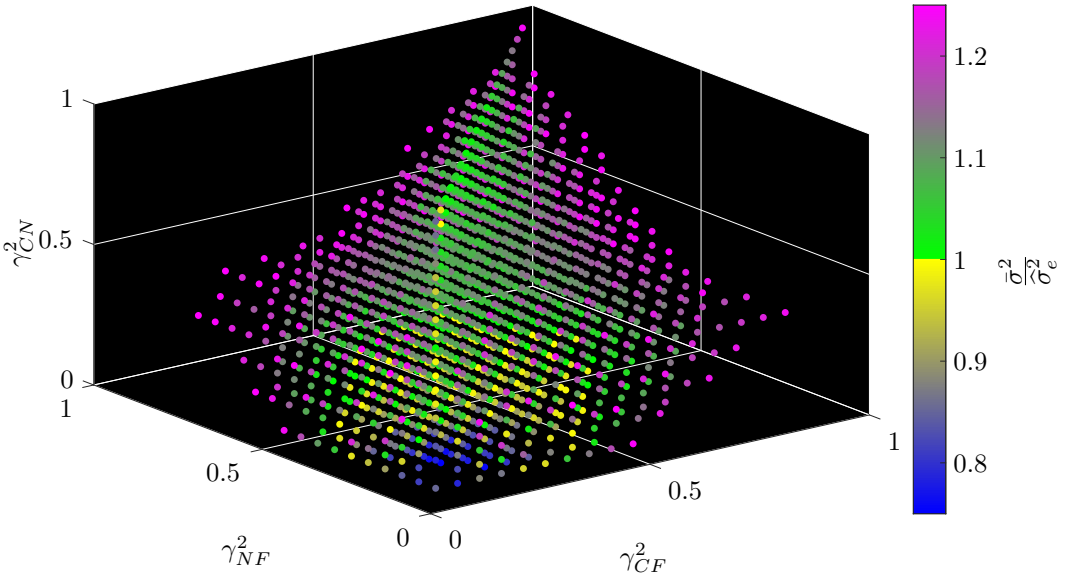

FIGURE 5.33: The values of $\frac{\bar{\sigma}^2}{\widehat{\sigma}^2_e}$ between 0.75 and 1.25 against the three values of coherence where $\frac{1}{\bar{\sigma}^2}$ is the mean squared divided by the variance of $\widehat{G}_{\nu\nu}(\omega)$ when $BT = 1000$ and $\frac{1}{\widehat{\sigma}^2_e}$ is the mean squared divided by the variance of the empirical distribution respectively when $BT = 1000$. $\frac{1}{\widehat{\sigma}^2_e}$ is calculated using the empirical equation with the coefficients calculated using equations (5.55), (5.56), (5.57) and (5.58).

small values, the gamma distribution has a positive skew which decreases as $\frac{1}{\bar{\sigma}^2}$ increases and

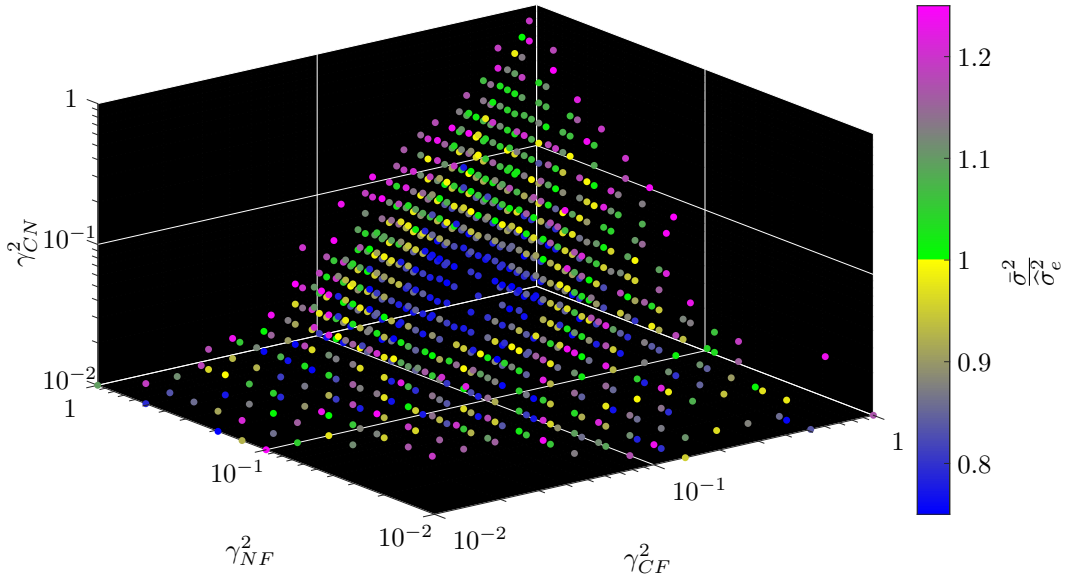

FIGURE 5.34: The values of $\frac{\bar{\sigma}^2}{\widehat{\sigma}^2_e}$ between 0.75 and 1.25 against the three values of coherence where $\frac{1}{\bar{\sigma}^2}$ is the mean squared divided by the variance of $\widehat{G}_{\nu\nu}(\omega)$ when $BT = 2000$ and $\frac{1}{\widehat{\sigma}^2_e}$ is the mean squared divided by the variance of the empirical distribution respectively when $BT = 2000$. $\frac{1}{\widehat{\sigma}^2_e}$ is calculated using the empirical equation with the coefficients calculated using equations (5.55), (5.56), (5.57) and (5.58).

tends to 0 as $\frac{1}{\bar{\sigma}^2}$ tends to infinity.

The ratio of the estimated values of the lower and upper bounds of the 95% to the values of the lower and upper bounds of the 95% confidence interval calculated using the Monte Carlo simulation for $BT = 1000$ are included as figures 5.35 and 5.36 respectively. Comparing these figures to figures 5.21 and 5.22 which used the values of the coefficients in Table 5.3, it is clear that the results are very similar. The method using the functions to calculate the coefficients does have a slightly smaller range of errors which can be seen when comparing the range of the colour axis. The adjustments required to obtain the at least 95% confidence interval are very similar to those given in Section 5.5 for $BT = 1000$ and Section 5.6 for $BT = 100$.

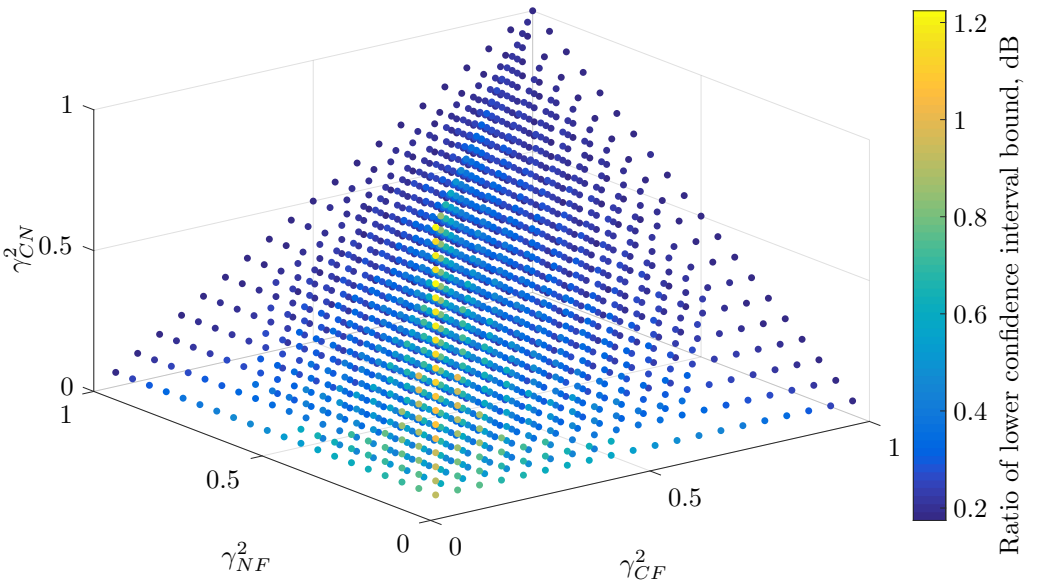

FIGURE 5.35: The ratio of the lower bound of the 95% confidence interval of the empirically calculated distribution using the coefficients obtained from functions to the lower bound of the 95% confidence interval of $\widehat{G}_{\nu\nu}(\omega)$ calculate from the Monte Carlo simulation for $BT = 1000$.

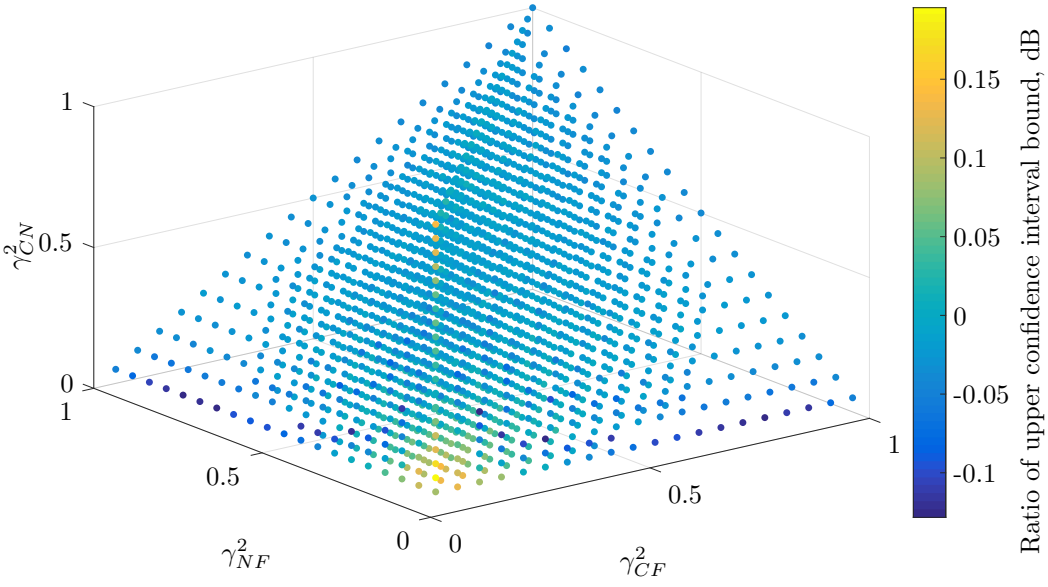

FIGURE 5.36: The ratio of the upper bound of the 95% confidence interval of the empirically calculated distribution using the coefficients obtained from functions to the upper bound of the 95% confidence interval of $\widehat{G}_{\nu\nu}(\omega)$ calculate from the Monte Carlo simulation for $BT = 1000$.

5.8 Selecting the best method for calculating confidence intervals

Three methods for estimating the distribution of $\widehat{G}_{\nu\nu}(\omega)$ and for determining the 95% confidence limits of $\widehat{G}_{\nu\nu}(\omega)$ have been presented in this chapter. To decide which method is most appropriate, the estimated coherence values need to be calculated from the measured data. Using the estimated coherences values, the methods can be selected by the coherence value combinations that each method provides the most accurate estimation of the distribution of $\widehat{G}_{\nu\nu}(\omega)$ which are:

- Analytic method - As the method makes the assumption that the three cross spectra are independent random variables, this method is most valid where all three coherence values are smaller than 0.1. Figure 5.15 indicates that the method only works well when all three coherence values are similar.
- Empirical equation (look up table) - This method cannot be used for coherence values below 0.05. The method uses linear interpolation to calculate the coefficient values between the values in the table. Therefore, the confidence intervals will be most accurate at coherence combinations which are in the table and may be less accurate between them.
- Empirical equation (coefficient functions) - This method produces values for the confidence interval limits which are similar to the values obtained from the lookup table method. As functions are used to calculate the coefficients rather than linear interpolation, the coefficient values should be accurate over the entire range of coherence values down to the threshold coherence value which can be calculated using Equation 5.23. The method overestimates the values of $\frac{\mu^2}{\sigma^2}$ when γ^2_{CF} and or γ^2_{NF} are close to 1 but this does not appear to have a significant effect on the values of the 95% confidence interval limits when compared to the lookup table method.

The integration method should therefore be used when all three coherence values are very small and have similar values. The lookup table method should be used when γ^2_{CF} and or γ^2_{NF} are close to 1. For all other coherence combinations, the method using the empirical equation with the coefficients obtained from equations (5.55), (5.56), (5.57) and (5.58) appears to be the most appropriate method to calculate the confidence intervals.

5.9 Requirements and recommendations for measured data

In this chapter, the distributions of cross-spectral estimates and the estimates obtained using the 3S Array method have been examined and methods for calculating their confidence intervals have been presented. There are, however, certain conditions which must be met if the 3S Array method is to produce a valid estimate of the combustion noise. All of these conditions have already been discussed in this chapter but are collected in Table 5.6 for ease of reference.

For the case when the coherence squared values are below the coherence threshold value, which can be calculated using Equation (5.23), it is possible to identify what the approximate value of BT_{eqv} that would be required to ensure the coherence values are above the coherence threshold

Condition	If data meets condition	If data does not meet condition
$\widehat{\gamma}^2_{xy}(\omega)\|_{\text{lower}} \geq \frac{20}{0.95BT_{\text{eqv}}}$ when $BT_{\text{eqv}} \geq 200$	The confidence interval method is valid as the estimate of $\|G_{xy}(\omega)\|$ will have a gamma distribution.	The confidence interval method is not valid as the estimate of $\|G_{xy}(\omega)\|$ will not have a gamma distribution. This is because there are not enough averages to isolate the coherent signal from the incoherent noise. The solution to this would be to use a larger value of BT_{eqv}
The time domain signals must be Gaussian.	The confidence interval method is valid as it assumes the input signals are Gaussian.	The confidence interval method is not valid as it assumes the input signals are not Gaussian. If only one of the signals is not Gaussian, it is likely that there is either incoherent unwanted noise (acoustic, hydrodynamic or electric) that is not Gaussian or that the sensor is faulty. If all three signals are not Gaussian, this suggests that either coherent noise (acoustic or electric) between all sensors is not Gaussian or that there was problem with the measurement system.
$\gamma^2_{NF}(\omega) \geq \gamma^2_{CN}(\omega)\gamma^2_{CF}(\omega)$, $\gamma^2_{CF}(\omega) \geq \gamma^2_{CN}(\omega)\gamma^2_{NF}(\omega)$, $\gamma^2_{CN}(\omega) \geq \gamma^2_{CF}(\omega)\gamma^2_{NF}(\omega)$	The signals may or may not be of the assumed signal structure where only the combustion noise is coherent between sensors.	The signals are not of the assumed signal structure where only the combustion noise is coherent between sensors. If only one of these conditions is not met, then it is likely that there is coherent unwanted noise between two of the sensors which will not be coherent with the third.

TABLE 5.6: The conditions that need to be met to apply the 3S Array method to data and calculate the confidence intervals for the method.

value. For example, for a cross-spectral density estimate with $BT_{\text{eqv}} = 100$ which has a smallest estimated value of coherence of $\widehat{\gamma}^2_{xy}(\omega) = 0.05$, it is possible to estimate what the actual value of coherence may be using the data from the Monte Carlo simulation in Section 5.1. Figure 5.37 is a plot of the actual coherence value, γ^2_{xy}, which is an input to the Monte Carlo simulation, divided by the estimated coherence value, $\widehat{\gamma}^2_{xy}$, obtained from the Mote Carlo simulation against $\widehat{\gamma}^2_{xy}$. This plot is similar to Figure 5.5 except the values are plotted against $\widehat{\gamma}^2_{xy}$ as opposed to γ^2_{xy}. The ratio of coherence values when the $\widehat{\gamma}^2_{xy} = 0.05$ is approximately 0.82 and so $\gamma^2_{xy} = 0.05 \times 0.82 = 0.041$. As is shown in Table 5.1, for $BT_{\text{eqv}} \geq 200$ the threshold value where $\frac{\gamma^2_{xy}}{\widehat{\gamma}^2_{xy}} = 0.95$ for a particular value of BT_{eqv} is equal to $20/\gamma^2_{xy}$. Therefore, for a minimum actual coherence value of $\gamma^2_{xy} = 0.041$ the value of BT_{eqv} required to make the condition valid is

$$BT_{\text{eqv}} \geq \frac{20}{\gamma^2_{xy}} = \frac{20}{0.041} = 488. \tag{5.59}$$

This is an approximate value of the required BT_{eqv} as $\widehat{\gamma}^2_{xy}$ is a random variable and so the estimated value obtained from the measurements may be larger or smaller than the true value of the measured coherence between the two signals. Therefore, it is advisable to use a value of BT_{eqv} larger than that obtained using the above method. As explained before, the value

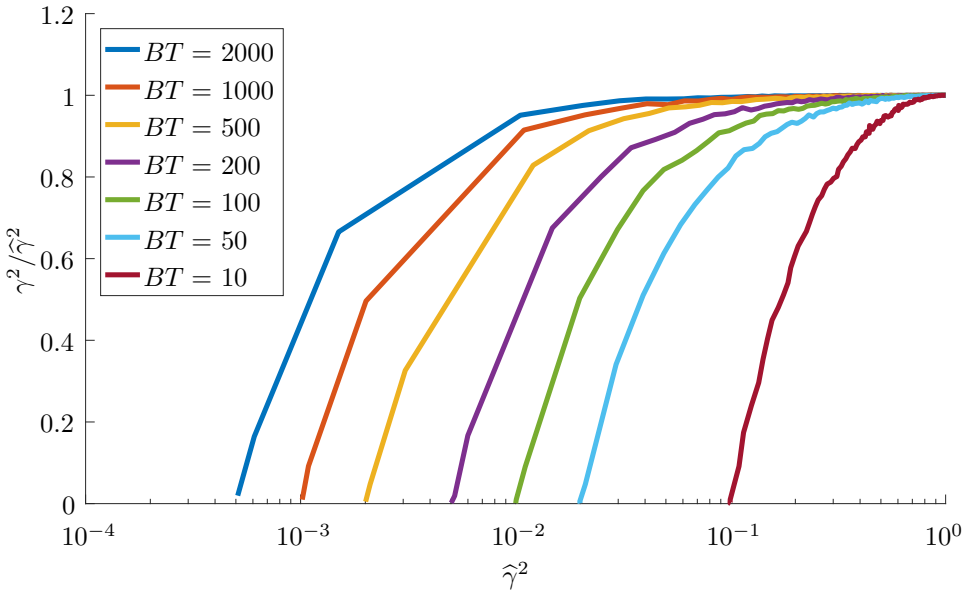

FIGURE 5.37: The actual coherence between two signals divided by the estimated coherence obtained from the signals for different values of BT plotted against the estimated coherence coherence. No overlapping segments were used to calculate these estimates.

of BT_{eqv} can be increased by either increasing the frequency bin width, B, which sacrifices frequency resolution, by increasing the measurement length, T, or by using different windows and amounts segment overlap to increase the window correction factor. Due to combustion noise being a low frequency noise source, increasing the window correction factor or the measurement length are the desired options as reducing frequency resolution will make it difficult to analyse the detail in the combustion noise estimate.

5.10 Chapter Summary

In this chapter, the statistical distributions of the absolute value of a cross spectrum and the estimate obtained from the 3S Array method have been examined. Empirical methods for finding the distributions of the estimates have been presented which use only quantities that can be obtained from the measured data. These distributions can be used to obtain confidence intervals for the spectral estimate obtained using the 3S Array method. The methods presented produce intervals within which there is at least a 95% chance that the true value falls within the interval. The methods for calculating confidence intervals and indeed the 3S Array method itself rely on the data meeting certain conditions which are given in Table 5.6

Chapter 6

Application of 3S Array to Short Cowl engine measurements

Acoustic measurements of a Rolls-Royce short cowl turbofan jet engine were taken at the Rolls-Royce indoor test facility in Derby. Dynamic pressure sensors were located in the combustor and hot nozzle and a microphone array external to the engine make it possible to apply the 3S Array method to the data to obtain an estimate of the combustion noise. This chapter contains an analysis of the data that has been acquired from these measurements. The validity of the assumptions required to implement the 3S Array technique is investigated and the data is assessed to see if the conditions required to calculate the confidence intervals of the estimate obtained using the 3S Array technique are met. The contribution of the combustion noise to the focussed beamformer spectrum is estimated using the 3S Array technique and the confidence intervals of the estimate are calculated.

6.1 Experiment configuration

Acoustic measurements of a short cowl turbofan jet engine were taken on the 12^{th} August 2011 in 55 bed at the Rolls-Royce indoor test facility in Derby. The data analysed in this chapter will be for the engine running at a low engine power condition. Figure 6.1 displays pictures of the engine in the test bed.

The instrumentation relevant to the application of the 3S Array technique consisted of three dynamic pressure sensors placed in the combustor (one of which was faulty), two dynamic pressure sensors in the hot nozzle and a spiral array of 32 microphones external to the engine. The precise location of the in-engine sensors are not known. Figure 6.2 is a diagram showing the hot nozzle location and the far field microphone array which is to scale. The microphone array is attached to a hand rail on a walkway and can be seen in Figure 6.1b. The array is 3.781 m from the nozzle in the y direction and approximately 1 m from the closest wall which is behind the array. Defining the origin of a Cartesian coordinate system as the center of the hot nozzle, the array is centred at (1.620 m, 3.781 m, -0.352 m). The positions of the microphones in the array are given in Appendix A.

(A) (B)

FIGURE 6.1: Photographs of 55 bed at the Rolls-Royce test facility in Derby with the equipment set up for the 12th August 2011 measurements.

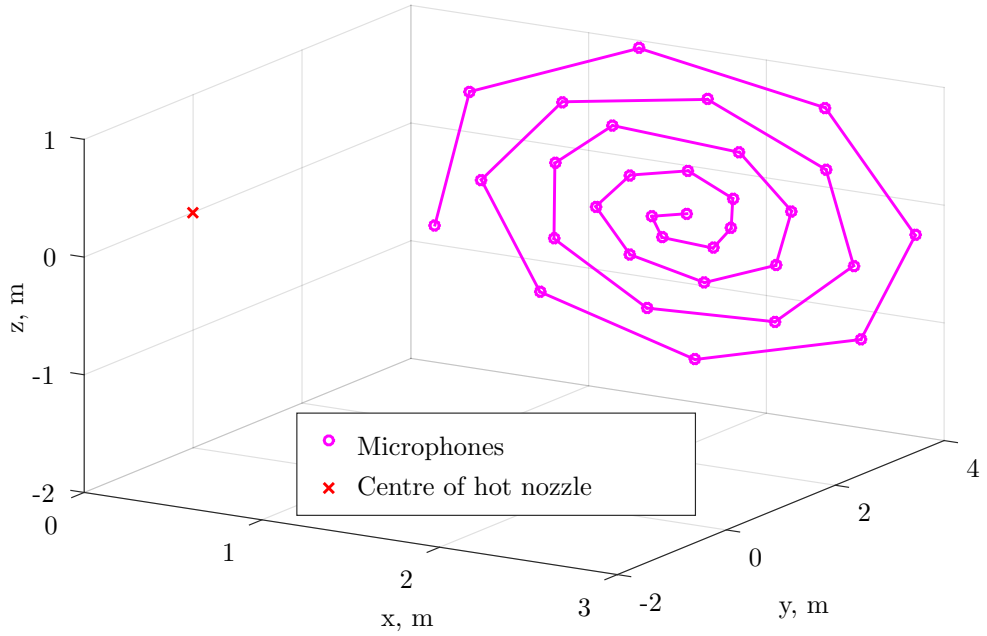

FIGURE 6.2: A diagram showing the hot nozzle and microphone array locations.

6.2 Evaluation of beamformer effectiveness

The array centre is not in the same plane as the hot nozzle of the jet engine. Using delay-and-sum beamforming to focus the array on the hot nozzle, 2D and 3D directivity plots of the focussed beamformer output are shown in figures 6.3 and 6.4 respectively. At low frequencies, the microphone array is almost omnidirectional. At 100 Hz there is limited reduction of noise from directions other than the focus direction. From 200 Hz, the array has a distinct main lobe and low level side-lobes.

The performance of a microphone array can be calculated using the Directivity Index of the array. The Directivity Index is the level of the array output when exposed to spatially white noise (noise that arrives at the array equally from all directions) relative to the response of

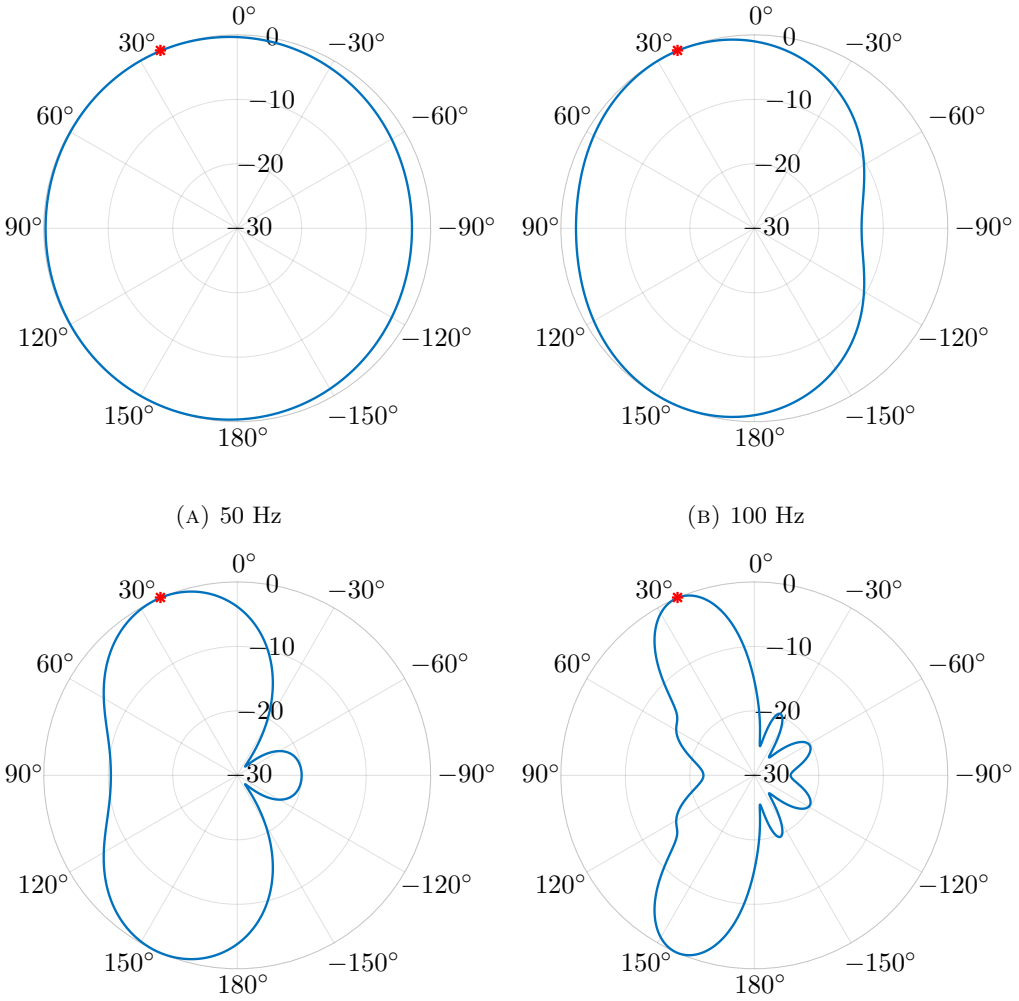

(A) 50 Hz

(B) 100 Hz

(C) 200 Hz

(D) 400 Hz

FIGURE 6.3: The directivity pattern in dB of the 32 microphone spiral array when focussed at the hot nozzle (indicated by the red star) for different frequencies.

an omnidirectional microphone to the same sound field in dB. The Directivity Index has been calculated by placing 40,000 monopole sources, evenly spaced, on a spherical surface centred on the centre of the array and calculating the output of the array. Figure 6.5 shows the Directivity Index of the microphone array when steered to focus on the hot nozzle. The beamformer signal will output a signal with a lower level than an omnidirectional microphone if there is any noise coming from a direction that the array is not focussed on. As the test bed has hard walls, there will be significant levels of reverberation. Therefore, sound will arrive at the array from directions other than that of the sound sources due to reflections. When comparing the output of the beamformer to a single omnidirectional microphone, the level difference between the two should be approximately equal to the directivity index.

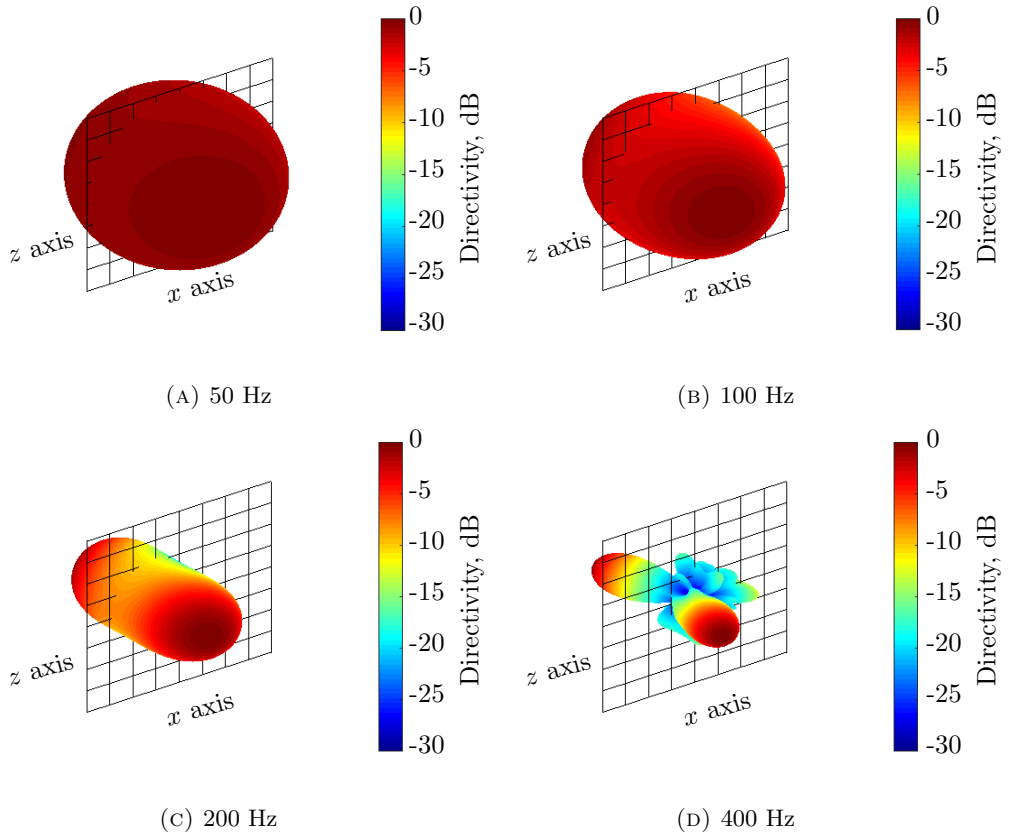

(A) 50 Hz (B) 100 Hz

(C) 200 Hz (D) 400 Hz

FIGURE 6.4: The directivity pattern of the 32 microphone spiral array when focused on the hot nozzle for different frequencies. The xz plane that the microphone array lies on is indicated by the black mesh grid and the y axis is purpendicular to this grid.

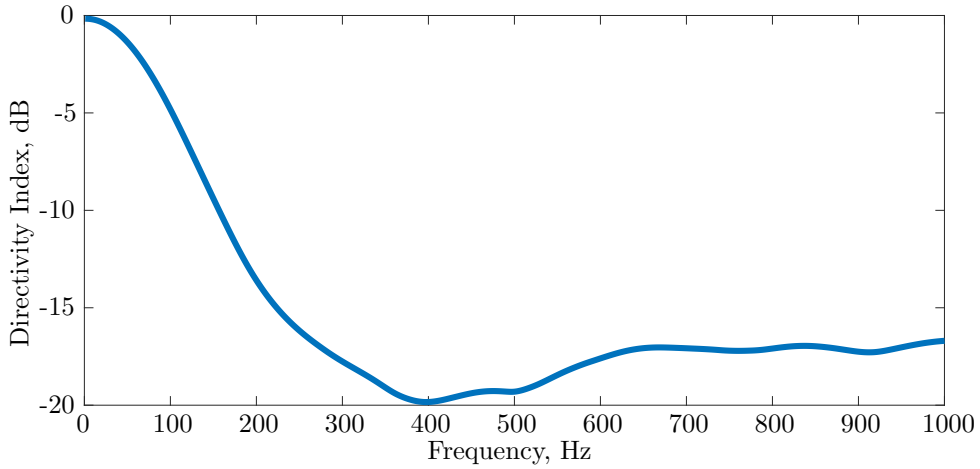

FIGURE 6.5: The directivity index of the spiral array used during the 12$^{\text{th}}$ August 2011 short cowl turbofan jet engine measurements.

6.3 Validity of the assumptions required for the 3S Array method

The 3S Array technique relies on the assumptions stated in Chapter 4. To satisfy assumption 1 (the combustion noise is coherent between all measurement locations), and thus provide the most accurate estimate, the combustor and nozzle sensors with the highest coherence with the far field microphone array are used. In this set of measurements these are the combustor sensor designated Z0301C1 and the nozzle sensor designated Z6924B1. The microphone array is used as a delay-and-sum beamformer which is focussed on the hot nozzle exit so that the amount of unwanted noise that reaches the far field array (such as jet and bypass noise) can be reduced. The reduction of jet and bypass noise reduces the coherent unwanted noise between the hot nozzle sensor and the far field array and makes assumption 2 (unwanted noise is not coherent between measured spectra) more reasonable.

All of the noise data recorded on the 12^{th} August 2011 had a sampling frequency of 24 kHz and there are 26 seconds of data for each channel for each test point. The channels were recorded synchronously as is required for the 3S array technique. A Hanning window 6000 samples long is used with a 70% overlap of segments so that there is good resolution at low frequencies with a bin width of 4 Hz. This results in $BT_{\text{eqv}} = 204$ ($B = 4$, $T = 26$ and a window correction factor of 2.126). Assumption 3 states that there need to be a 'large number' of averages when calculating the cross-spectra. In Chapter 5, the minimum value of BT_{eqv} for a measured coherence is defined and will be used to confirm whether or not BT is large enough to provide reasonable confidence in the estimate in the next section.

Assumption 5 states that for the frequency range of interest, only the plane wave mode of the duct is cut on. These cut on frequencies can be calculated using equations (2.8) and (2.9) to obtain

$$f_{m,n} = \frac{c_T \, k_{r(m,n)}}{2\pi} \sqrt{1 - M^2} \tag{6.1}$$

where c_T is the speed of sound at a total temperature T_{tot} and the Mach number $M = U/c_T$ where U is the average flow velocity. There is a large variation between the combustor cross-section and the hot nozzle cross-section where the nozzle cross-sectional area is approximately two times larger than the combustor, which will result in modes of the same order becoming cut-on at different frequencies.

There is also a large variation in temperature and average flow velocity. Information from Rolls-Royce gives the approximate average total temperature in the combustor of this particular engine as 1240 K and the approximate average flow velocity as 55 ms^{-1} for the low power condition that will be examined in this chapter. The speed of sound can be calculated using

$$c_T = \sqrt{\gamma R_s T_s} \tag{6.2}$$

where γ is the ratio of specific heats, R_s is the specific gas constant for dry air and T_s is the static temperature in Kelvin. The total temperature is related to the static temperature by

$$T_{\text{tot}} = T_s \left(1 + \frac{\gamma - 1}{2} \left(\frac{U}{c_T} \right)^2 \right). \tag{6.3}$$

Substituting Equation (6.2) into (6.3) and rearranging yields

$$T_s = T_{tot} - \frac{U^2(\gamma - 1)}{2\gamma R_s} \tag{6.4}$$

which results in $T_s = 1238.7$ K when $T_{tot} = 1240$ K and $U = 55$ ms^{-1}. The speed of sound inside the combustor is therefore 685.3 ms^{-1}. The cut-on frequency of the first cut-on higher order mode, (1,1), in the combustor is 347.8 Hz.

The average flow velocity and average total temperature were not provided for the hot nozzle outlet. To obtain an estimate of the range of frequencies within which the first azimuthal mode in the hot nozzle is likely to become cut-on, Table 6.1 contains estimates of the cut-on frequency of the first azimuthal mode in the hot nozzle for a range of total temperatures and average flow velocities. The temperatures used here are values centred on the temperature at the LP turbine

		Average velocity, ms^{-1}				
		210	235	260	285	310
Total temperature, K	700	125.6	121.8	117.5	112.5	106.8
	750	130.7	127.1	123.0	118.2	112.8
	800	135.7	132.2	128.2	123.7	118.6
	850	140.5	137.1	133.3	129.0	124.1
	900	145.1	141.8	138.2	134.0	129.3

TABLE 6.1: The first azimuthal mode cut-on frequency for a duct with the same dimensions as the hot nozzle on the short cowl turbofan jet engine for a range of total temperatures and average flow velocities.

outlet at a low power condition for the ANTLE turbofan jet engine that Rodríguez-García [41] quotes as 800.7 K. The bulk flow velocities are centred on 260 ms^{-1}, a value obtained from data from a Commercial Aviation Safety Team technical report [58] which was reproduced by Rodríguez-García [41]. The frequencies covered by these temperatures and velocities range from 106.8 Hz (low temperature, high velocity) to 145.1 Hz (high temperature, low velocity).

6.4 Analysis of signals

Before applying the 3S Array method, the noise data needs to be analysed to check it meets the conditions given at the end of Chapter 5 in Table 5.6. The measured combustor, hot nozzle and beamformer signals are assumed to be Gaussian in order to calculate confidence intervals using the methods defined in Chapter 5. Figure 6.6 is a plot of the probability density functions of the measured combustor, hot nozzle and external array beamformer signals which have been normalised by the standard deviation of each signal. Also plotted are Gaussian distributions which have been fitted to the data using the MATLAB 'histfit' function. The kurtosis and skewness of the signals are included as Table 6.2. All three signals have had a 2$^{\text{nd}}$ order high-pass Butterworth filter with a cut-off frequency of 20 Hz to remove DC offsets and a 2$^{\text{nd}}$ order low-pass Butterworth filter with a cut-off frequency of 2000 Hz applied to them. Combustion noise is a low frequency phenomenon and above 2000 Hz the measured noise will be due to other sources. The low pass filter was used to remove this noise to identify wheter the signals can be

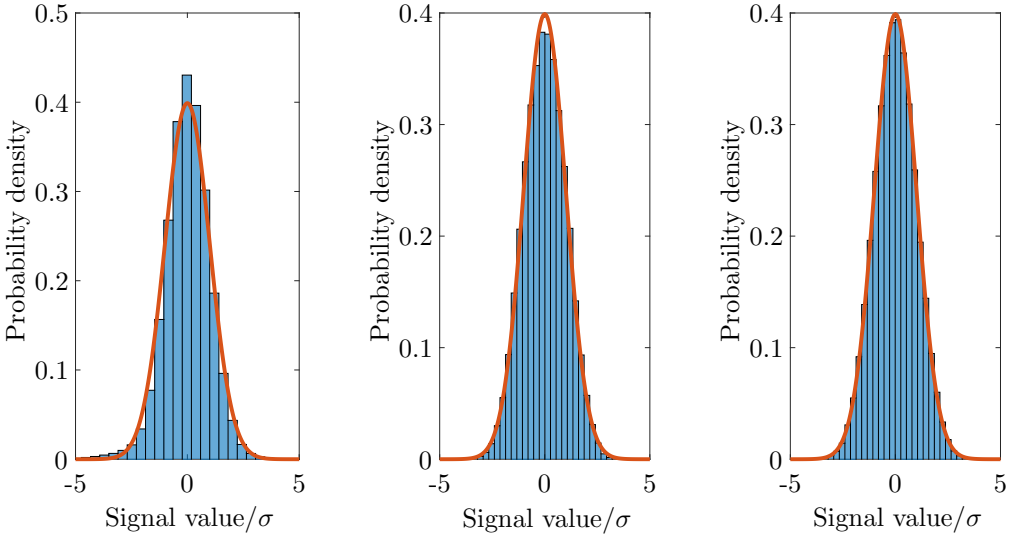

(A) Combustor (B) Hot nozzle (C) External microphone array

FIGURE 6.6: Probability density functions with fitted Gausian distributions of measured data inside and outside the short cowl turbofan jet engine at the locations required for using the 3S Array method. The data has been normalised by the standard deviation.

Measurement location	Skewness	Kurtosis
Combustor	-0.3641	4.50
Hot nozzle	-0.0122	2.78
External Microphone Array	0.0032	2.88

TABLE 6.2: The skewness and kurtosis of measured signals from a low power engine test.

accurately described as Gaussian in the frequency range of interest. The hot nozzle and focussed beamformer output signals are closely approximated by a Gaussian distribution. The distribution of the combustor signal is poorly approximated as Gaussian as the kurtosis is high for a Gaussian distribution and it is skewed to the left. To understand why this is, the time history of the two combustor signals is plotted as Figure 6.7. There is a periodic 'clicking noise' on the signals which is highlighted in yellow on the time histories. This 'clicking' is not present in the signals measured at the other locations. Each highlighted region encompasses several clicks which are short in time and therefore have a broad frequency content. This clicking will therefore affect the coherence between the combustor signal and signals at the other two measurement locations. This 'clicking noise' is either from electrical noise on the signals or potentially from the igniter inside the combustor as when listening to the measured combustor signal the 'click' sounds like a spark. One way to remove this noise source from the signal is to remove all of the highlighted sections from the time history. This is problematic as it reduces the length of the signal by almost half which will reduce the value of BT_{eqv} substantially. These sections also need to be removed from the hot nozzle and external beamformer signals as well.

To remove the same sections from the other two signals, the signals need to be aligned in time. The signals were measured simultaneously but the propagation of the sound from the combustor to the hot nozzle and external array needs to be taken into account. The combustor sensors and the hot nozzle sensors are separated by approximately 1.5 m and the centre of the array

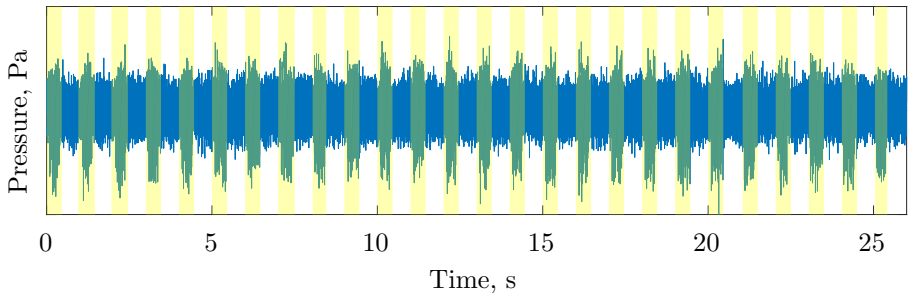

(A) Z0301C1

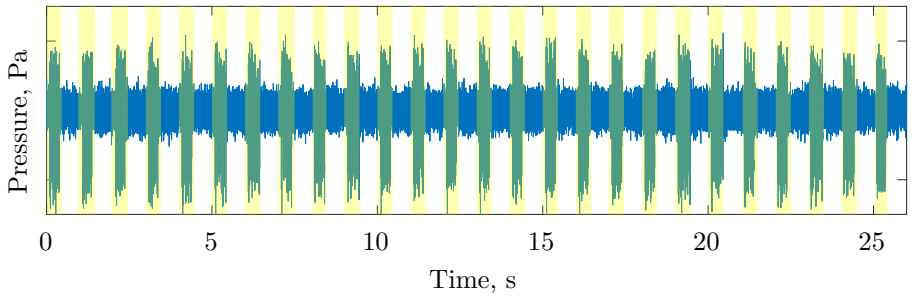

(B) Z0301F1

FIGURE 6.7: Time histroies of combustor probe Z0301C1 and Z0301F1 for a low power engine condition.

is 4.129 m from the centre of the hot nozzle. The speed of sound at 20°C with no flow is 343 ms^{-1} and using this, the propagation time in seconds and samples is included as Table 6.3. The

Probes	Distance, m	Travel time, s	Travel time, samples
Combustor to hot nozzle	1.500	0.0044	106
Combustor to external array	5.629	0.0164	394
Hot nozzle to external array	4.129	0.0120	289

TABLE 6.3: The distances between sensors and sound propagation times for no flow and speed of sound of 343 ms^{-1}.

speed of sound in the combustor is approximately double this and there is a mean flow velocity of approximately 55 ms^{-1}. At the hot nozzle, the temperature is lower but the flow speed is higher. The time it takes for sound to propagate from the combustor to the hot nozzle will be significantly lower (potentially half the time) than if the temperature was 20°C and there was no flow present. From the hot nozzle to the external array, the majority distance the sound travels is outside of the hot jet. The speed of sound will, therefore, be approximately 343 ms^{-1} and the direction of propagation is approximately perpendicular to the flow and so will not have a significant effect on the propagation time. The travel time from the combustor to the external array should be approximately 350 samples. This is over 5% of the 6000 sample window length that was defined in the previous section.

Assuming that the signals are all recorded simultaneously (which they were in these measurements) and that combustion noise is coherent between the signals, the delay between the signals should be equal to the propagation time of the combustion noise from one sensor to the other. The delay between the signals can be calculated using the phase of the cross-spectral estimates.

The phase delay, $\tau_{xy}(\omega)$, between the signals $x(t)$ and $y(t)$ is defined as

$$\tau_{xy}(\omega) = -\frac{\mathrm{d}\phi_{xy}(\omega)}{\mathrm{d}\omega} \tag{6.5}$$

where $\phi_{xy}(\omega)$ is the phase of the cross-spectra between x and y. The cross-spectral estimates, coherence function and phase between the combustor and nozzle, combustor and beamformer output and nozzle and beamformer output are shown in Figures 6.8, 6.9 and 6.10 respectively. Each of the signals are 26 seconds long and a bin width of 4 Hz was obtained using Hanning window and a 70% overlap resulting in $BT_{\mathrm{eqv}} = 221$. There is a region of broadband coherence

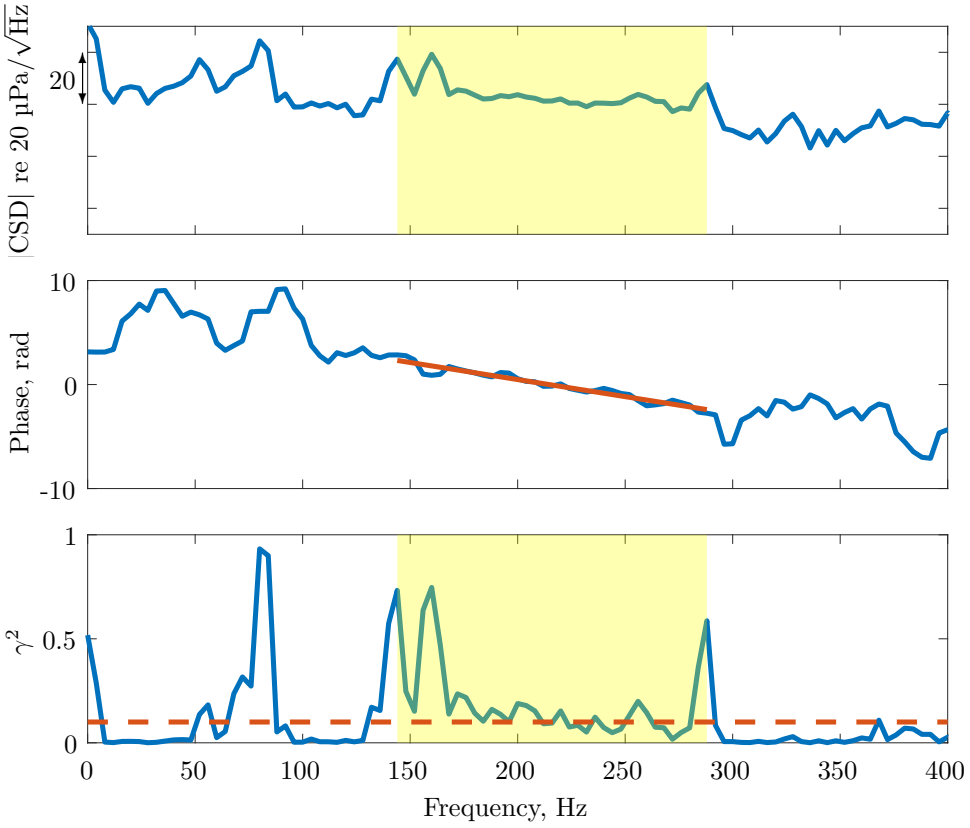

FIGURE 6.8: The magnitude and phase of the cross-spectral estimate and the estimated coherence function for the combustor and hot nozzle signals.

which is highlighted in yellow on the coherence and cross-spectral estimate plots where the phase delay is calculated. The red line on the phase plots is the fitted straight line with the gradient equal to $2\pi\tau_{xy}(\omega)$. The values of the phase delay for each combination of signals is displayed in Table 6.4. The sum of the combustor to nozzle and nozzle to beamformer output phase delays

Probes	Phase delay, s	Phase delay, samples
Combustor to hot nozzle	0.0052	125
Combustor to external array	0.0193	463
Hot nozzle to external array	0.0141	338

TABLE 6.4: The phase delay between measured signals calculated from the gradient of the phase between 146 Hz and 290 Hz.

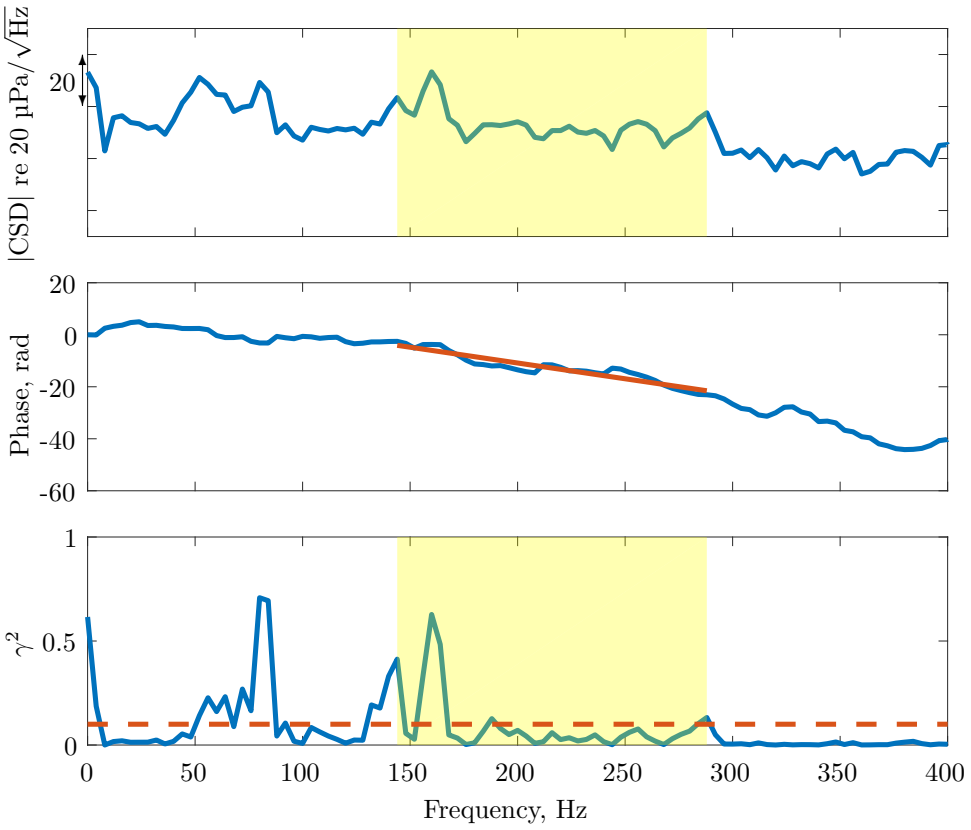

FIGURE 6.9: The magnitude and phase of the cross-spectral estimate and the estimated coherence function for the combustor and focussed beamformer signals.

is equal to the combustor to nozzle phase delay. The delays are all much larger than expected which suggests that the signals were not synchronised perfectly. Using these delays, the signals can be synchronised and the clicking noise removed from the combustor signal with the same sections removed from the other signals. A rectangular window is applied to all of the remaining sections before combining the sections to form the new signal. This procedure does have the effect of adding a discontinuity into the signal and thus altering the frequency content. One way of avoiding this would be to use a different windowing function, a Hanning window for example, which smoothly decreases to zero at the ends of the window so that when the sections are joined together there are no discontinuities. However, so much of the signals has already been removed that reducing the amount of information in the signal that is left by applying a windowing function will result in significant inaccuracies in the estimates obtained from the signals due to the significantly reduced BT_{eqv}. Applying a Hanning window to the entire section will also reduce the variance of the resulting signal which may make the assumption of a Gaussian distribution for the signal invalid. It was decided, therefore, that the rectangular windows would be used as the discontinuities would have a less detrimental effect on the overall estimate. The distributions of the new signals are displayed as Figure 6.11 and the kurtosis and skewness are given in Table 6.5.

The maximum frequency plotted is 400 Hz for Figures 6.8, 6.9 and 6.10 as the coherence values are very low above 400 Hz and so, the combustion noise is not coherent between all sensors. All three coherence function estimates meet the condition of $\gamma^2_{yz}(\omega) \geq \gamma^2_{xy}(\omega)\gamma^2_{xz}(\omega)$, $\gamma^2_{xz}(\omega) \geq \gamma^2_{xy}(\omega)\gamma^2_{yz}(\omega)$, $\gamma^2_{xy}(\omega) \geq \gamma^2_{xz}(\omega)\gamma^2_{yz}(\omega)$ and therefore, the coherence values fall within

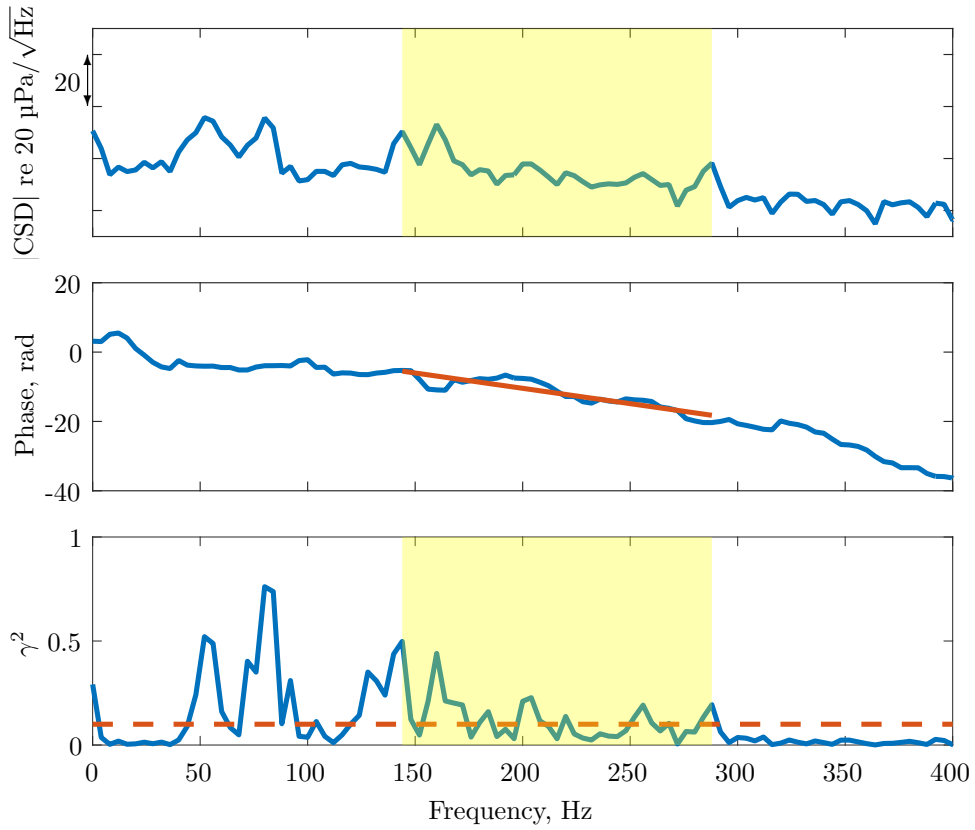

FIGURE 6.10: The magnitude and phase of the cross-spectral estimate and the estimated coherence function for the hot nozzle and focussed beamformer signals.

Measurement location	Skewness	Kurtosis
Combustor	0.0208	2.93
Hot nozzle	0.0062	2.84
External Microphone Array	0.0141	2.92

TABLE 6.5: The skewness and kurtosis of measured signals from a low power engine test with the clicking noise removed.

the range of valid values for the assumed signal content (defined in Section 5.2 as combustion noise plus uncorrelated unwanted noise). The minimum usable estimated value of coherence can be calculated using Equation 5.23 is

$$\widehat{\gamma}^2_{xy}(\omega)|_{\text{lower}} = \frac{20}{0.95BT_{\text{eqv}}w_c} = \frac{20}{0.95 \times 4 \times 26 \times 2.126} = 0.095 \tag{6.6}$$

and is indicated by the red line on the coherence function estimate plots in Figures 6.8, 6.9 and 6.10. It is clear that the majority of the coherence values are below this line. The lowest estimated coherence value in the highlighted section for the combustor and nozzle (where the coherence for all three plots indicates broadband combustion noise) is 0.017. Following the same procedure as in Section 5.9 and using the $BT = 200$ curve from Figure 5.37, the actual coherence value can be estimated as 0.012. Therefore using Equation (5.59),

$$BT_{\text{eqv}} \geq \frac{20}{\text{actual minimum}\,\gamma^2} = \frac{20}{0.01212} = 1650. \tag{6.7}$$

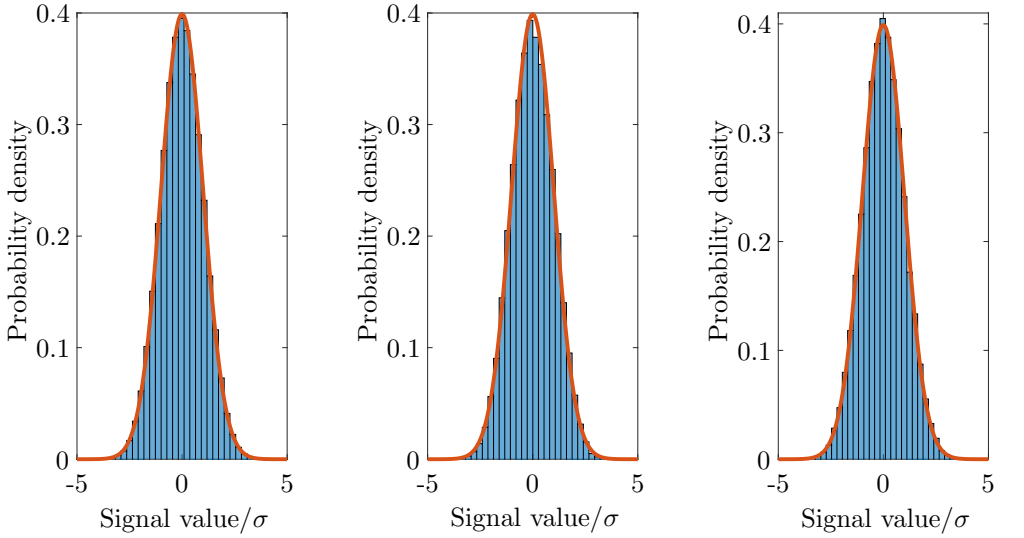

(A) Combustor (B) Hot nozzle (C) External microphone array

FIGURE 6.11: Histograms with fitted normal distributions of measured data inside and outside a jet engine at locations required for using the 3S Array method with the clicking noise removed. The data has been normalised by the standard deviation.

The low coherence values result in the need for a large BT_{eqv} which is an issue as for $T = 26$ s and window correction factor $w_c = 2.126$, $B \geq 1650/(26 \times 2.126) \approx 30$ Hz resulting in unsatisfactorily low resolution at low frequencies. To have a value of $B = 4$ Hz, the recorded signal length would need to be at least 194 s using a Hanning window with 70% overlap. Removing the 'clicking noise' shortens the signal substantially to 14 seconds and so, to achieve $BT_{\text{eqv}} = 1650$, B would need to be 55 Hz. The lowest coherence between the combustor and the hot nozzle would likely be not as low if the clicking noise was not present and so, a lower value of BT_{eqv} might be usable.

The window length required to achieve a bin width of 30 Hz would be approximately 800 samples which is 1/30 s. With a window of this short duration, the alignment of the signals becomes even more important as the estimated phase delay in Table 6.4 for the combustor to the external array and hot nozzle to external array is larger than the window length. However, the frequency resolution of the estimate will be so low that there will be very little information of use.

6.5 Reasons for low coherence

The low values of coherence shown in Figures 6.8, 6.9, 6.10 are likely to be caused by two factors:

- Unwanted incoherent noise present in the measured signals.
- Propagation of more than one mutually incoherent mode inside the engine duct.

Unwanted incoherent noise in the measured signals is accounted for by the 3S Array method but if the coherence is below the threshold value, the cross-spectral estimate is no longer representative of the true cross-spectra (as shown in Chapter 5). Therefore, further analysis is needed to ensure the unwanted noise is reduced as much as possible keep the coherence as high as possible. At low frequencies, the delay-and-sum beamformer is almost omnidirectional and so, other sources of noise (i.e. jet noise, bypass noise etc.) will be present on the beamformer output signal. To improve the coherence between the combustor sensor and the external array it would be beneficial if more advanced beamforming methods could be used to improve performance at low frequencies but this would require a reformulation of the 3S Array method. In addition, the test cell is highly reverberant and so, the sound arriving at the microphone array from the focus direction will likely also contain unwanted noise. The coherence between the hot nozzle and the external array is higher than between the combustor and the external array. This could be because noise other than combustion noise is coherent between the hot nozzle and external array which would result in an inaccurate estimate of the combustion noise. A method is presented in Chapter 9 which can be used to implement the 3S method with more advanced beamforming techniques. These advanced techniques reduce the level of noise arriving from directions other than that of the hot nozzle which will reduce the effect of coherent unwanted noise between the hot nozzle and the external array on the combustion noise estimate.

The propagation of multiple incoherent modes in the engine duct violates one of the key assumptions of the 3S Array method. From Table 6.1 it is clear that the first azimuthal mode in the hot nozzle likely becomes cut-on within the range of highlighted frequencies in Figures 6.8, 6.9 and 6.10. The propagation of multiple mutually incoherent modes in the hot nozzle result in a loss of coherence between the hot nozzle signal and the other two signals. The coherence loss due to the propagation of multiple mutually incoherent modes is not accounted for in the 3S Array method and so will result in an inaccurate combustion noise estimate. The coherence drops to a very low value close to 300 Hz and it is possible that this is the frequency where the first azimuthal mode in the combustor becomes cut-on as the coherence between all three sensors peaks just before the coherence reduces to zero. At the cut-on frequency of a specific mode, this mode will be dominant and so, the coherence will be higher as effectively only one mode will be present. The frequency range of the 3S Array method is severely limited by the cut-on frequency of the first higher order azimuthal mode in the hot nozzle and combustor. A method combining a mode isolation technique and the 3S Array method is presented in Chapter 7 which extends the frequency range of the 3S Array method.

6.6 Estimate of combustion noise contribution to the focussed beamformer spectrum using the 3S Array method

The combustion noise estimate using the 3S Array method for the full 26 s long signal with a bin width of 4 Hz (obtained using a Hanning window with 70% overlap) is shown in Figure 6.12. Also plotted is the output from the focussed beamformer and the PSD of the centre microphone

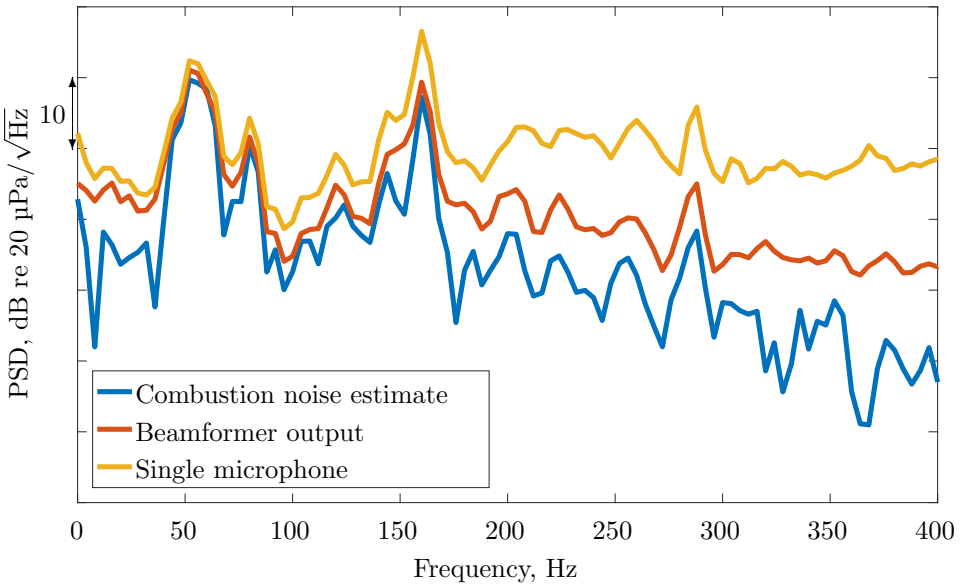

FIGURE 6.12: Combustion noise estimate obtained when $B = 4$ Hz, $T = 26$ s using a Hanning window with 70% overlap with the clicking noise present.

in the array. The combustion noise estimate is lower, or equal to, the beamformer estimate which is as expected given that the estimate is the contribution of the combustion noise in the beamformer signal. The noise estimate indicates that the combustion noise makes up a significant contribution of the total beamformer level between 50 Hz and 160 Hz. Between 160 Hz and 300 Hz, where the broadband coherence between the combustor and hot nozzle sensors is at a consistently higher level, the combustion noise estimate is lower. The lower estimate is due to the coherence between the nozzle and beamformer output and the combustor and beamformer output (which are on the numerator of the 3S Array equation) being lower than the coherence between the combustor and nozzle (which is on the denominator of the 3S Array equation). The low coherence of the combustor and nozzle sensors with the focussed beamformer suggests that the combustion noise in this frequency range is either not propagating strongly out of the hot nozzle or other noise sources are significantly stronger than the combustion noise. Above 300 Hz, the coherence between all three sensors is so low that the assumption that combustion noise is present at all three sensors is not valid.

To indicate the validity and accuracy of the combustion noise estimate, the at-least-95% confidence intervals of the combustion noise estimate (calculated using the method in Section 5.7) are plotted as Figure 6.13. There are significant bands of frequencies where the confidence interval is not plotted as the conditions required for the calculation of the confidence intervals (listed in Table 5.6) are not met. Therefore, the uncertainty in the combustion noise estimate can only

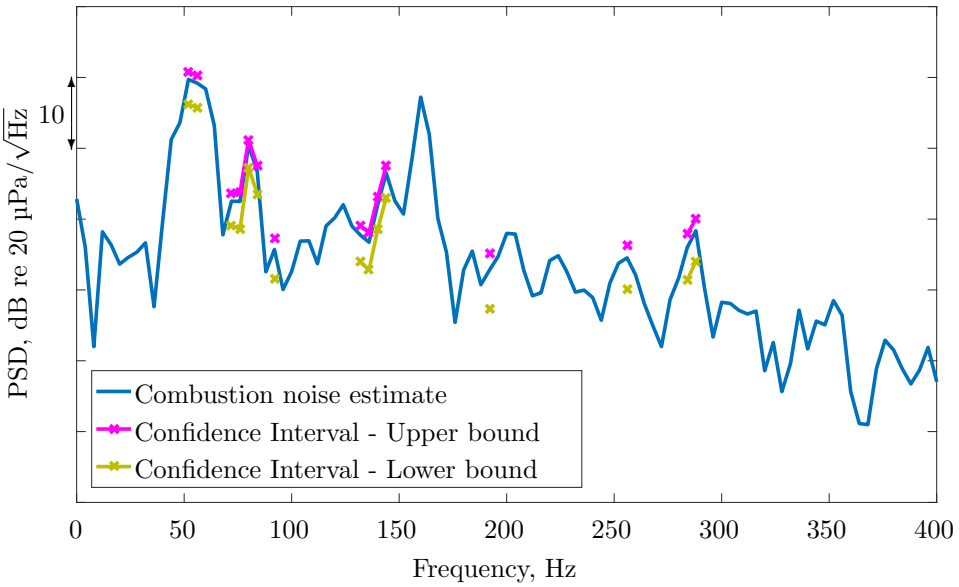

FIGURE 6.13: Combustion noise estimate with calculated confidence intervals obtained when $B = 4$ H $T = 26$ s using a Hanning window with 70% overlap with the clicking noise present.

be quantified where the confidence intervals are plotted. This does not necessary mean that the estimate is incorrect where the intervals are not plotted but it does mean that the accuracy of the estimate cannot be quantified and therefore, there cannot be a reasonable degree of confidence in the accuracy of the estimate.

As discussed in the previous section, the condition that the signals are Gaussian is not technically met as the combustor signal with the 'clicking noise' does not have a Gaussian distribution. Removing the clicking noise from the combustor signal results in the signal having a Gaussian distribution. Figure 6.14 is a plot of the combustion noise estimate with the clicking removed from the combustor signal and a bin width of 4 Hz. There are only two frequency bins where the conditions required to calculate the confidence intervals are met. This is not surprising given that the BT product has been almost halved due to the removal of the 'clicking noise'. When comparing this estimate to the one in Figure 6.13, it is clear that there are significant differences. This is likely due to the reduced number of averages as the coherence between the measured spectra is low.

To increase the value of BT_{eqv}, the window length can be decreased so that $B = 20$ Hz, giving $BT_{\text{eqv}} = 598$. The combustion noise estimate calculated using this BT product is shown in Figure 6.15. With this bin width it is hard to compare the variation of the estimate with frequency with the other two estimates as the resolution is so low. There is now a small bandwidth where the conditions required to calculate the confidence interval are now valid, which is a small improvement over Figure 6.14. When the bin width is increased above 20 Hz, the coherence between the signals is very small and the conditions are, again, not met. The low coherence is likely due to a combination of factors including the shortness of the window and the fact that a single bin will include some frequencies where the signals are coherent and a large number which are not, reducing the overall coherence of that frequency bin. To obtain a combustion noise estimate using the 3S Array method where the confidence of the estimate can be quantified, the

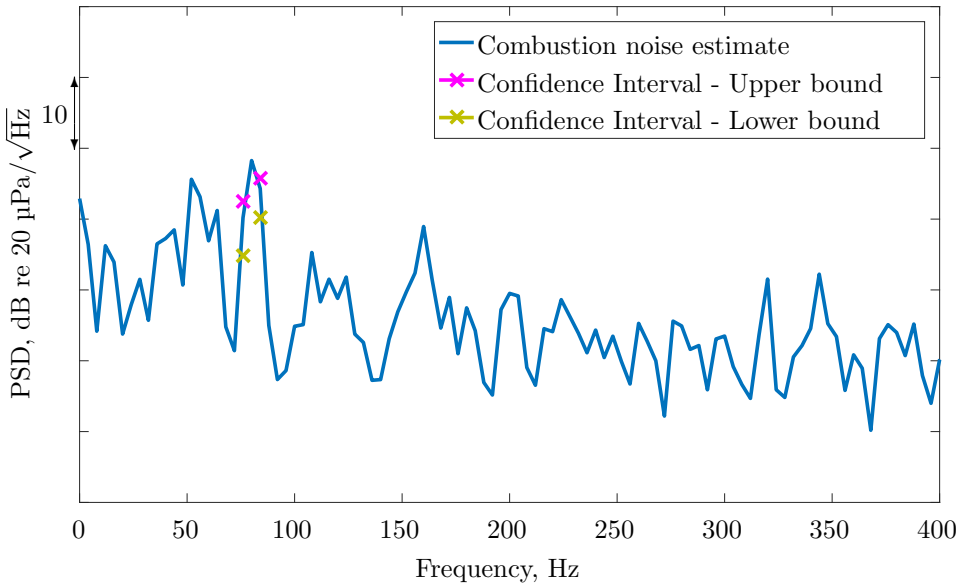

FIGURE 6.14: Combustion noise estimate with calculated confidence intervals obtained when $B = 4$ Hz using a Hanning window with 70% overlap with the clicking noise removed.

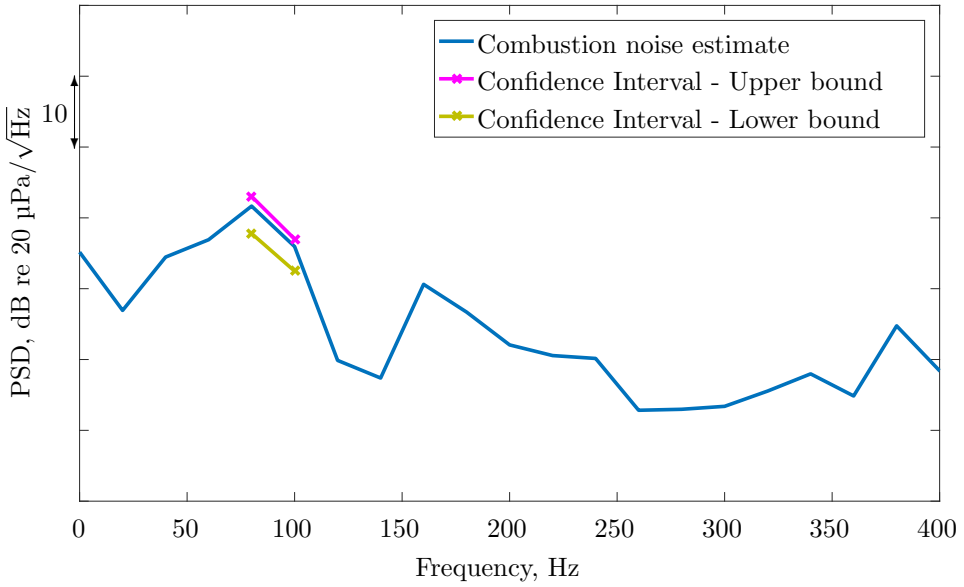

FIGURE 6.15: Combustion noise estimate with calculated confidence intervals obtained when $B = 20$ Hz using a Hanning window with 70% overlap with the clicking noise removed.

signal duration needs to be sufficiently long therefore, to provide a high value of BT_{eqv} with a sufficiently small frequency resolution B.

6.7 Chapter Summary

In this chapter the acoustic measurements acquired from a Rolls-Royce engine test at a low engine power condition is analysed and processed to obtain an estimate of the combustion noise

contribution to the focussed beamformer output. The coherence between the three spectra used to obtain the combustion noise estimate is low and, for the majority of the frequency range of interest, is below the threshold coherence. It is therefore not possible to quantify the confidence in the estimate and it is likely that the estimate will not be accurate.

To obtain estimates for which the confidence can be quantified, new methods need to be developed to improve the coherence between the measurement locations or the value of BT_{eqv} needs to be larger. As it is expensive to have the engine on condition for a long time, a combination of the two methods will likely provide the most beneficial solution. In addition to this, the loss of coherence due to multiple mutually incoherent modes propagating in the engine duct will result in inaccurate estimates of the combustion noise. Therefore, a method that can isolate individual modes and maintain the single mode propagation assumption will be beneficial to both the overall coherence and the accuracy of the estimate.

Chapter 7

Enhancement of 3S Array using a modal isolation method

In Chapter 6, the coherence between a combustor pressure probe and a hot nozzle pressure probe was seen to drop to close to zero near the estimated cut-on frequency of the first azimuthal mode in the combustor causing an upper frequency limit on the estimates obtained using the 3S Array method. The loss of coherence due to propagation effects is not accounted for in the 3S method leading to an incorrect estimate above the cut-on frequency of the first azimuthal mode. This limits the effective frequency range of the 3S method (and therefore the 3S Array method) to the cut-on frequency of the first azimuthal mode in the combustor. The cut-on frequency of the first azimuthal mode in the hot nozzle is lower than in the combustor due to the larger outer radius and lower average temperature. The propagation of higher order modes in the hot nozzle will also affect the estimate of the combustion noise as it violates the plane wave assumption.

To examine the effect of higher order modes on the coherence between the combustor and hot nozzle probes, a simple model of the engine duct will be developed and investigated.

7.1 Simplified model of coherence loss due to multi-mode propagation

To simplify the problem, an infinite annular duct of constant cross-section will be used to model the engine duct so that the issue of modal scattering due to variations in cross-section can be disregarded for now. Flow will also be disregarded. A ring of incoherent monopole sources will be used to represent the direct combustion noise sources produced by the unsteady heat release near each fuel injector. Indirect combustion noise will also be disregarded as it is not relevant to this investigation. Figure 7.1 is a diagram of the model of the engine duct.

At a single frequency the acoustic pressure, p, at a point in the duct for a distributed source volume Q_{vol}, the inhomogeneous Helmholtz equation is

$$(\nabla^2 + k^2)p = Q_{vol}. \tag{7.1}$$

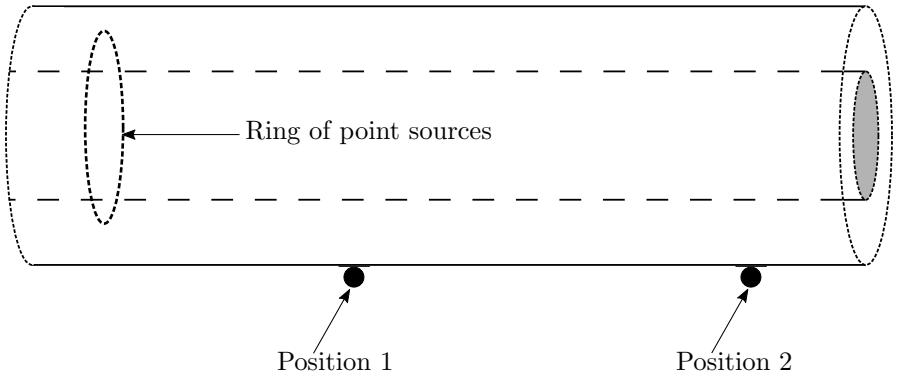

FIGURE 7.1: A diagram of an infinite hard-walled annular duct with a dashed ring indicating the line on which 16 point sources are positioned.

The solution may be expressed in terms of a Green's function $G(\mathbf{x}|\mathbf{y})$, defined by

$$(\nabla^2 + k^2)G(\mathbf{x}|\mathbf{y}) = -\delta(\mathbf{x} - \mathbf{y}) \tag{7.2}$$

where the Green's function describes the propagation between a point $\mathbf{x} = (r_x, \theta_x, z_x)$ and another location $\mathbf{y} = (r_y, \theta_y, z_y)$ inside the duct. The Green's function must also satisfy the boundary conditions on the duct wall. The Green's function for a hard walled annular duct is given by

$$G(\mathbf{x}|\mathbf{y}) = \sum_{m,n} \frac{-j}{2Sk_{z(m,n)}} \hat{\psi}_{mn}(r_x, \theta_x)\hat{\psi}^*_{mn}(r_y, \theta_y)e^{-jk_{z(m,n)}|z_x - z_y|}. \tag{7.3}$$

where S is the cross-sectional area of the duct and $\hat{\psi}_{mn}(r, \theta)$ are normalised modeshape functions with the ortho-normalisation property,

$$\frac{1}{S}\int_S \hat{\psi}_{mn}\hat{\psi}^*_{mn}\mathrm{d}S = 1. \tag{7.4}$$

Combining equations (7.1) and (7.2), the solution for the acoustic pressure inside the duct is of the form

$$p(\mathbf{x}) = \int_V G(\mathbf{x}|\mathbf{y})Q_{vol}(\mathbf{y})\mathrm{d}V \tag{7.5}$$

where V is a volume containing the source distribution. For a point monopole source located at $\mathbf{y}_s = (r_s, \theta_s, z_s)$,

$$Q_{vol} = \frac{j\omega\rho_0 q}{r}\delta(r_y - r_s)\delta(\theta_y - \theta_s)\delta(z_y - z_s) \tag{7.6}$$

where ρ_0 is the density of the fluid in the duct and q is the source strength. The volume integral in Equation (7.5) results in

$$p(\mathbf{x}) = -j\omega\rho_0 q G(\mathbf{x}|\mathbf{y}_s). \tag{7.7}$$

For multiple point sources in the duct, the pressure due to each source can be summed to produce the total acoustic pressure in the duct at a location $\mathbf{x}$. For N sources, the pressure at M measurement locations can be written as

$$\mathbf{p}(\mathbf{x}) = \mathbf{G}(\mathbf{x}|\mathbf{y})\mathbf{q}(\mathbf{y}) \tag{7.8}$$

where $\mathbf{p}$ is a column vector of the pressures, $\mathbf{G}$ is an $N \times M$ matrix of the Green's functions that describe the propagation from each source each measurement location and $\mathbf{q}$ is a column vector

containing the source strengths of the N sources.

Equation (7.8) is the pressure at a single frequency and so, if the pressure at $\mathbf{x}$ due to multiple sources is calculated and are summed together at this frequency, all of the pressures due to each source would be coherent as the phase difference between the signals will be constant. It is therefore not possible to use Equation (7.8) to obtain the pressure at $\mathbf{x}$ for incoherent sources producing broadband noise. For sources producing broadband noise, it is necessary to calculate the auto and cross spectra of the pressure signals. Using Equation (4.6), the Cross-Spectral Matrix (CSM) of the pressure signals is defined as

$$\mathbf{G}_{pp}(\omega) = \frac{1}{T} E\left[\mathcal{F}\{\mathbf{p}(\omega)\}^{\mathbf{H}} \mathcal{F}\{\mathbf{p}(\omega)\}\right] \tag{7.9}$$

where $\mathcal{F}\{\,\}$ denotes the Fourier transform. The diagonal terms of $\mathbf{G}_{pp}$ are the autospectra of the pressure signals and the off-diagonal terms are the cross spectra between pressure signals. Substituting Equation (7.8) into Equation (7.9) results in

$$\mathbf{G}_{pp}(\omega) = \mathbf{G}(\omega)\mathbf{G}_{qq}(\omega)\mathbf{G}^{\mathbf{H}}(\omega) \tag{7.10}$$

where $\mathbf{G}_{pp}(\omega)$ and $\mathbf{G}_{qq}(\omega)$ are the CSM of the pressure and source signals and $^{\mathbf{H}}$ is the Hermitian transpose operator. For incoherent sources, the off-diagonal terms in $\mathbf{G}_{qq}$ will be zero.

The coherence between the spectra of two microphones in an infinite annular duct can be calculated using the CSM of pressures, $\mathbf{G}_{pp}(\omega)$, from Equation (7.10) by defining the source strength CSM, $\mathbf{G}_{qq}(\omega)$, the source positions and the Green's function matrix, $\mathbf{G}(\omega)$ where the individual Green's functions can be calculated from Equation (7.3). To demonstrate the effect of multiple incoherent modes propagating in a duct on the coherence function between two microphone spectra, Figure 7.2 is the coherence function between two wall mounted microphones in a duct separated by 1 m in the axial direction, with 16 incoherent monopole sources of constant strength arranged in a ring inside the duct, plotted against ka. The black dashed lines indicate the values

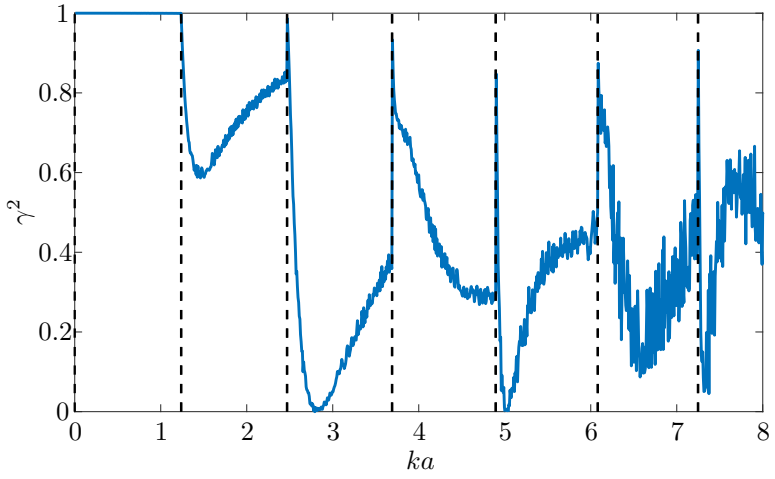

FIGURE 7.2: The coherence between two microphones at different axial locations in an infinite hard-walled annular duct with a ring of 16 monopole sources in the duct.

of ka that the azimuthal modes become cut-on at. The coherence in the plane wave region is 1. Above the cut-on frequency of mode (1,1), the coherence then fluctuates significantly. At the

cut-on frequencies of each mode, the coherence is high. This is because the mode which becomes cut-on at each of these frequencies is dominant. This can be seen in the Green's function as $k_{z(m,n)} = 0$ at the cut-on frequency of mode (m, n). In the frequency range between the cut-on frequency of mode m and mode $m+1$, there is a dip in the coherence values which is due to the presence of multiple incoherent modes. There is an overall trend of the coherence function decreasing as the frequency increases which is due to the number of incoherent modes propagating increasing.

There are two methods for mitigating against this coherence loss. One is to include the effects of multiple modes propagating along the duct into the formulation of the 3S Array technique. Including a model for multiple incoherent modes in the formulation of the 3S Array technique would require estimates of the temperature, flow speed, speed of sound and other parameters which cannot be easily measured inside the engine. The other is to use additional microphones to perform a modal decomposition at each in-duct measurement location so that individual modes can be isolated. A method for isolating individual mode amplitudes using in-duct microphone arrays will be presented in the following section.

7.2 Modal isolation method

This section introduces a method to isolate an individual azimuthal mode using an array of microphones and combine this method with the 3S Array technique to maintain the single mode propagation assumption. The pressure at a microphone in an annular duct can be expressed as

$$p(\theta, r, z, \omega) = \sum_{m=-\infty}^{\infty} \sum_{n=1}^{\infty} A_{(m,n)}(\omega) \hat{\psi}_{(m,n)}(\theta, r) e^{jk_{z(m,n)}z} \tag{7.11}$$

where $A_{(m,n)}(\omega)$ is the modal amplitude which includes all of the source terms. Restricting the microphone position to the wall of the duct results in $\hat{\psi}_{(m,n)}(\theta, a,) = Re^{jm\theta}$ where R is a constant. Redefining the modal amplitude to include this constant R, the pressure measured by a microphone at the hard wall of the duct is given by

$$p(\theta, r, z, \omega) = \sum_{m=-\infty}^{\infty} \sum_{n=1}^{\infty} A_{(m,n)}(\omega) e^{jm\theta} e^{jk_{z(m,n)}z}. \tag{7.12}$$

Modern turbofan jet engines have a large hub-to-tip ratio and so, in the frequency range in which combustion noise propagates, only the first radial mode is cut-on. At a single axial location $z = 0$, the above expression reduces to

$$p(\theta, z, \omega) = \sum_{m=-\infty}^{\infty} A_{(m,1)}(\omega) e^{jm\theta}. \tag{7.13}$$

For a number of microphones evenly spaced around the circumference of the duct, $\theta_i = \frac{2\pi i}{M}$ where θ_i represents the angular location of the i^{th} microphone and M is the total number of microphones in the array. The modal amplitude $A_{(m_{\text{iso}},1)}(z, \omega)$ of the mode to be isolated, m_{iso}, at an axial position z may therefore be obtained by a discrete Fourier transform (DFT) of the

pressure at the microphone locations so that

$$A_{(m_{\text{iso}},1)}(\omega) = \frac{1}{M}\sum_{i=1}^{M} p(\theta_i, z, \omega)e^{-jm_{\text{iso}}\theta_i} \tag{7.14}$$

where m_{iso} is the mode that is being isolated.

As with the DFT of a time signal, the DFT of the spatial pressures will suffer from aliasing when $|m_{\text{iso}}| \geq \frac{M}{2}$. So, for an array of 6 microphones, modes -2 to 2 can be isolated but when $m_{\text{iso}} = 3$ or -3, the modal amplitude obtained will contain contributions from both modes 3 and -3. Additionally, aliasing will also occur when

$$m = \kappa M + m_{\text{iso}} \tag{7.15}$$

is cut-on where κ is an integer and $\kappa \neq 0$. Therefore, for $M = 6$ and $m_{\text{iso}} = 2$, aliasing will occur when mode $m = -4$ becomes cut-on.

7.2.1 Simulation of modal isolation method

The modal isolation method can be applied at two axial locations inside a hard walled duct using two circular arrays of microphones. The coherence between the isolated mode amplitudes can be calculated by applying the modal isolation method using Equation (7.14) for each circular array. By way of example, Figure 7.3 is a plot of the coherence between two isolated mode amplitudes calculated using two circular arrays, each containing 6 microphones, separated by 1 m in the axial direction in a hard walled duct. There are 16 monopole sources arranged in a ring inside the duct. The black dashed lines indicate the cut-on frequencies of azimuthal modes. For $m_{\text{iso}} = 0, 1, 2$ the coherence drops at the modes which aliasing occurs at as described by Equation (7.15). For $m_{\text{iso}} = 3$, the coherence is high even though both modes -3 and 3 are cut-on which is due to the modes travelling along the duct at the same phase velocity and so the relative phase between the modes for a particular angular position does not change. Therefore, the coherence will be high until the cut-on frequency of mode 9. It is important to note that this is a simplified model and there may be factors in a physical example which result in phase differences between microphones in the same array which would result in a loss of coherence as individual modes would not be completely isolated. In all cases however, the coherence is high over a a much larger frequency range than for just a single microphone. The high coherence is due to the modal isolation method reducing the contribution of all modes other than m_{iso} and the amplitude of the same mode will be coherent at two different axial locations. Therefore, the modal isolation method maintains the assumption of single mode propagation required by the 3S Array method. The addition of the modal isolation method to obtain individual mode amplitudes at the in-duct measurement locations makes it possible to use the 3S Array method over a significantly wider range of frequencies, with the upper frequency limit dependent on the number of microphones in the circular array.

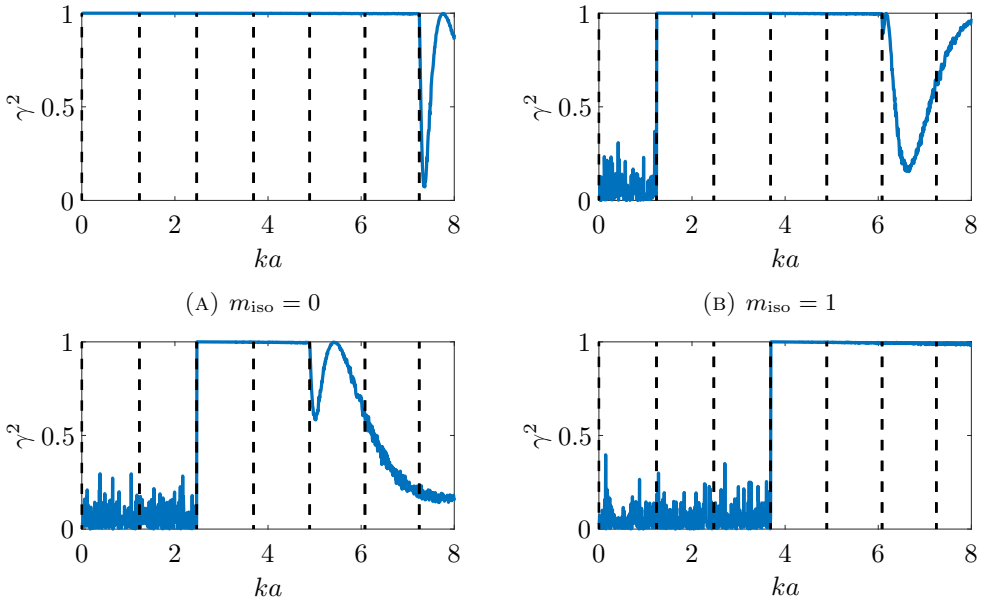

(A) $m_{\text{iso}} = 0$ (B) $m_{\text{iso}} = 1$

(C) $m_{\text{iso}} = 2$ (D) $m_{\text{iso}} = 3$

FIGURE 7.3: The coherence between two axial positions in an annular duct when modes 0 to 3 are isolated using a 6 microphone array.

7.2.2 Discussion of practical implementation of modal isolation

The above simulated coherences do not take into account any errors in the positioning of the microphones in the arrays which are likely to be present in practical applications. For a microphone, i, the true azimuthal position of the microphone can be expressed as

$$\hat{\theta}_i = \theta_i + \Delta\theta_i \tag{7.16}$$

where θ_i is the actual microphone position and $\Delta\theta_i$ is the difference between the true position and the expected position. Therefore, when the DFT is applied, there will be an error in the modal amplitude obtained because the microphones are no longer sampling the sound field at regular positions. The modal amplitudes obtained can be expressed as

$$\hat{A}_{(m_{\text{iso}},1)}(\hat{\theta}_i, \theta_i, \omega) = \frac{1}{M}\sum_{i=1}^{M} p(\hat{\theta}_i, z, \omega) e^{-jm_{\text{iso}}\theta_i} \tag{7.17}$$

which can be written as

$$\hat{A}_{(m_{\text{iso}},1)}(\hat{\theta}_i, \theta_i, \omega) = \frac{1}{M}\sum_{i=1}^{M}\sum_{m=-\infty}^{\infty} A_{(m,1)}(\omega) e^{j(m\hat{\theta}_i - m_{\text{iso}}\theta_i)}. \tag{7.18}$$

The contributions of each mode to the estimate of $\hat{A}_{(m_{\text{iso}},1)}(\hat{\theta}_i, \theta_i, \omega)$ can be defined as

$$\bar{A}_{(m,1)}(\hat{\theta}_i, \theta_i, \omega) = \frac{1}{M}\sum_{i=1}^{M} A_{(m,1)}(\omega) e^{j(m\hat{\theta}_i - m_{\text{iso}}\theta_i)}. \tag{7.19}$$

Equation (7.19) can be used to demonstrate the effect of azimuthal position error on the contribution of each mode $\bar{A}_{(m,1)}(\hat{\theta}_i, \theta_i, \omega)$ to the estimated modal amplitude $\hat{A}_{(m_{\text{iso}},1)}(\hat{\theta}_i, \theta_i, \omega)$. By way of example, a simulation using different values of the azimuthal position error, $\Delta\theta$, was performed. The simulation used 10000 values of $\Delta\theta$ for each microphone position which were generated using a normal distribution truncated at $\pm 2\sigma_{\Delta\theta}$ where $\sigma_{\Delta\theta}$ is the standard deviation of the distribution. The distribution of the values of $\bar{A}_{(m,1)}(\hat{\theta}_i, \theta_i, \omega)$ could therefore be obtained using the generated values of $\Delta\theta$. The standard deviation of $\bar{A}_{(m,1)}(\hat{\theta}_i, \theta_i, \omega)$, $\sigma_{\bar{A}_{(m,1)}}$, can be used as a measure of the error in the contribution of each mode due to the azimuthal position error. Figure 7.4 is the standard deviation of $\bar{A}_{(m,1)}(\hat{\theta}_i, \theta_i, \omega)$ normalised by $A_{(m,1)}(\omega)$ and multiplied by $\sqrt{M}$ for modes 1 and -1, with $m_{\text{iso}} = 1$, plotted against $\sigma_{\Delta\theta}$. The effect of the error

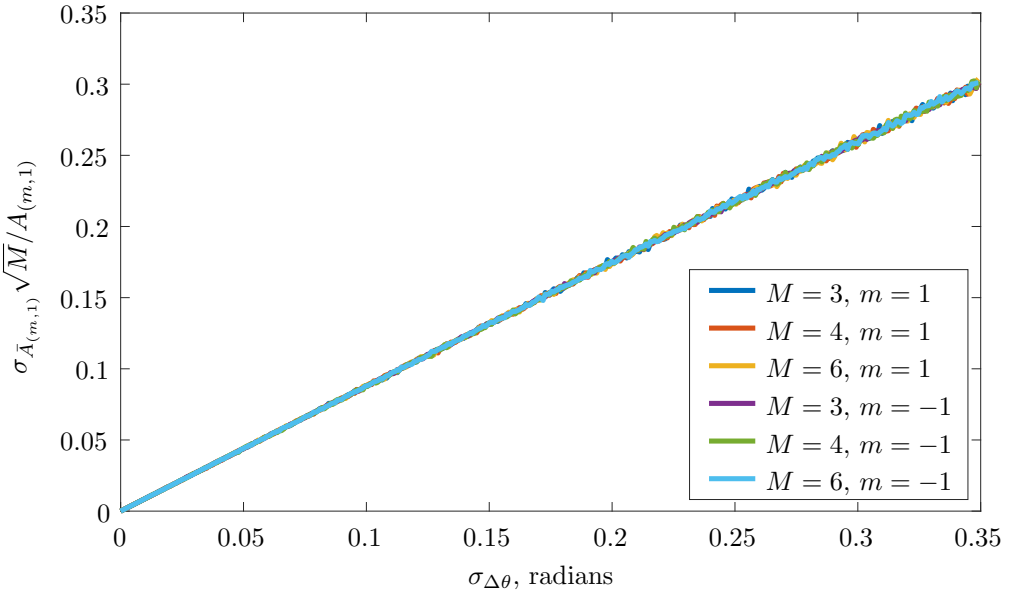

FIGURE 7.4: The standard deviation of $\bar{A}_{(m,1)}(\hat{\theta}_i, \theta_i, \omega)$ normalised by $A_{(m,1)}(\omega)$ and multiplied by the square root of the number of microphones for modes 1 and -1, with $m_{\text{iso}} = 1$, plotted against $\sigma_{\Delta\theta}$.

is shown for microphone arrays with 3, 4 and 6 microphones. When $\sigma_{\Delta\theta} = 0$, $\sigma_{\bar{A}_{(m,1)}} = 0$. As $\sigma_{\Delta\theta}$ increases, $\sigma_{\bar{A}_{(m,1)}}$ increases at a rate which is dependent on the number of microphones in the array and the rate of increase is the same for both $m = 1$ and $m = -1$. Arrays with more microphones are, therefore, affected less by the error in the microphone positions as there will be more microphones to average out any large position errors in a single microphone location. The error does not affect the contribution of $m = 0$ as there is no variation of pressure with θ. Therefore, if there is an error in the azimuthal position, the 'isolated' mode will be a combination of the desired mode plus other modes which are cut-on apart from the plane wave.

It is also possible that not all of the microphones will be in the same cross-sectional plane and so, there will be a frequency dependent phase error which will result in a frequency dependent error in the 'isolated' mode amplitude. The mode obtained from the isolation method for practical applications can be expressed as

$$\hat{A}_{(m_{\text{iso}},1)}(\hat{\theta}_i, \theta_i, \Delta z_i, \omega) = \frac{1}{M} \sum_{i=1}^{M} \sum_{m=-\infty}^{\infty} A_{(m,1)}(\omega) e^{j(m\hat{\theta}_i - m_{\text{iso}}\theta_i)} e^{jk_{z(m,1)}(z+\Delta z_i)} \tag{7.20}$$

where Δz_i is the difference between the microphones true location and the axial location the microphone is assumed to be at. Redefining the contributions of each mode to the estimate of $\hat{A}_{(m_{\text{iso}},1)}(\hat{\theta}_i, \theta_i, \omega)$ to include the effects of axial position error yields

$$\bar{A}_{(m,1)}(\hat{\theta}_i, \theta_i, \Delta z, \omega) = \frac{1}{M} \sum_{i=1}^{M} A_{(m,1)}(\omega) e^{j(m\hat{\theta}_i - m_{\text{iso}}\theta_i)} e^{jk_{z(m,1)}(z+\Delta z_i)}. \tag{7.21}$$

A similar simulation to the one used to investigate the effects of the azimuthal position error was used to demonstrate the effects of axial position error on the contribution of $\bar{A}_{(m,1)}(\hat{\theta}_i, \theta_i, \Delta z, \omega)$ to the estimate $\hat{A}_{(m_{\text{iso}},1)}(\hat{\theta}_i, \theta_i, \Delta z_i, \omega)$. Figure 7.5 is the standard deviation of $\bar{A}_{(m,1)}(\hat{\theta}_i, \theta_i, \Delta z, \omega)$ normalised by $A_{(m,1)}(\omega)$ and multiplied by $\sqrt{M}$ for modes 1, 0 and -1, with $m_{\text{iso}} = 1$. These results are plotted against $\sigma_{\Delta z}$ normalised by the axial wavelength $\lambda_{z(m,1)}$. A frequency was

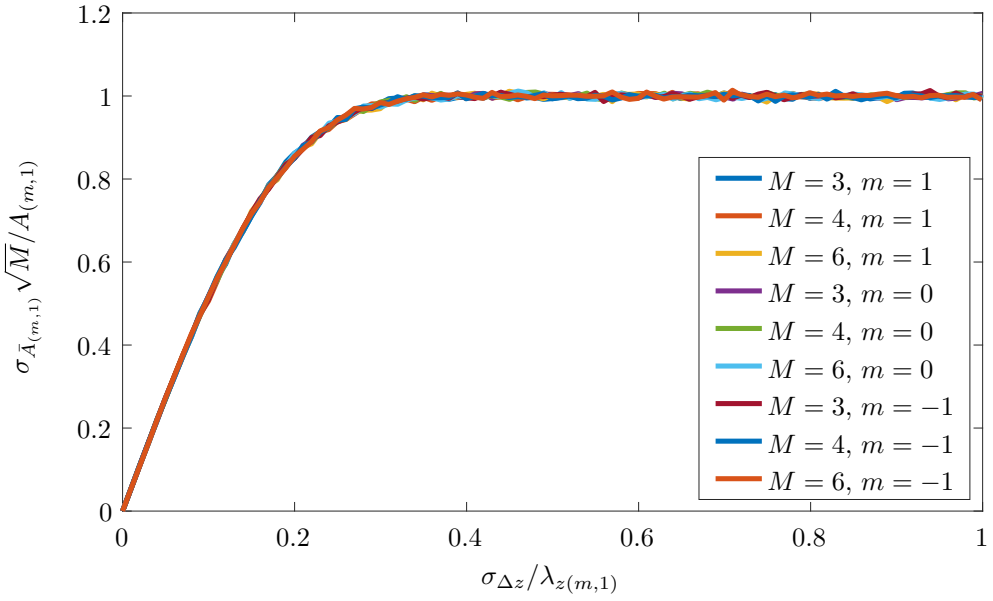

FIGURE 7.5: The standard deviation of $\bar{A}_{(m,1)}(\hat{\theta}_i, \theta_i, \Delta z, \omega)$ normalised by $A_{(m,1)}(\omega)$ and multiplied by the square root of the number of microphones for modes 1, 0 and -1, with $m_{\text{iso}} = 1$, plotted against $\sigma_{\Delta z}$ normalised by the axial wavelength $\lambda_{z(m,1)}$.

selected so that the axial wavenumbers $k_{z(1,1)} = k_{z(-1,1)} \approx k_{z(0,1)}$. As with the azimuthal error, $\sigma_{\bar{A}_{(m,1)}}$ increases with increasing $\sigma_{\Delta z}$ at a rate which is dependent on the number of microphones in the array and the rate of increase is the same regardless of azimuthal mode number m. The values of $\sigma_{\bar{A}_{(m,1)}}$ converge to a maximum at a value of $\sigma_{\Delta z}/\lambda_{z(m,1)} = 0.3$. The contribution of the plane wave mode is affected by the axial position error as the phase of the plane wave mode varies with z.

7.2.3 Combining modal isolation with 3S Array

The purpose of applying the modal isolation method to the in duct measurement positions is to improve the frequency range of the 3S Array technique. The pressure that propagates from the engine duct to a microphone in the far field will contain contributions of each of the modal amplitudes that are propagating along the duct. The pressure measured by a microphone in the

far field is

$$P_F(\mathbf{x},\omega) = \sum_{m=-\infty}^{\infty} A_{(m,1)}(\omega) H_{F(m,1)}(\mathbf{x},\omega) + N_F(\omega) \tag{7.22}$$

where $H_{F(m,1)}(\omega)$ is a pressure-to-pressure transfer function which describes the radiation of each modal amplitude from the nozzle to the far field microphone and $N_F(\omega)$ is noise which is uncorrelated between measurement positions. Replacing the individual sensors in the combustor and hot nozzle in the 3S Array method with circular microphone arrays with no errors in microphone positions, the individual mode amplitudes can be isolated in the combustor and hot nozzle. Assuming the propagating modes modes are incoherent, the cross-spectral density function between two isolated modal amplitudes using the in-duct arrays when isolating the same mode, m_{iso} is

$$G_{CN(m_{\text{iso}})}(\omega) = H^*_{C(m_{\text{iso}})}(\omega)|A_{(m_{\text{iso}})}(\omega)|^2 H_{N(m_{\text{iso}})}(\omega) \tag{7.23}$$

where

$$H_{C(m_{\text{iso}})}(\omega) = \frac{1}{S_C} e^{-jk_{z(m_{\text{iso}})}z_C}, \tag{7.24}$$

$$H_{N(m_{\text{iso}})}(\omega) = \frac{1}{S_N} e^{-jk_{z(m_{\text{iso}})}z_N}, \tag{7.25}$$

S_C and S_N are the cross-sectional areas of the duct at the combustor array and the hot nozzle array respectively and z_C and z_N are the axial positions of the combustor and hot nozzle arrays respectively. The cross-spectral density function between the isolated modal amplitude obtained using the combustor array and the far field microphone can be expressed as

$$G_{CF(m_{\text{iso}})}(\omega) = H^*_{C(m_{\text{iso}})}(\omega)|A_{(m_{\text{iso}})}(\omega)|^2 H_{F(m_{\text{iso}})}(\omega) \tag{7.26}$$

and a similar expression can be obtained for the cross-spectral density between the isolated modal amplitude using the hot nozzle array and the far field microphone.

The 3S Array method can be modified to use the two isolated mode amplitudes as the in-duct inputs. Assuming there is no error in the microphone positions inside the duct, applying the 3S Array method combined with the modal isolation method yields

$$\begin{aligned} G_{\nu_F\nu_F(m_{\text{iso}})}(\omega) &= \frac{|G_{CF}(\omega)||G_{NF}(\omega)|}{|G_{CN}(\omega)|} \\ &= \frac{|H^*_{C(m_{\text{iso}})}(\omega)|A_{(m_{\text{iso}})}(\omega)|^2 H_{F(m_{\text{iso}})}(\omega)||H^*_{N(m_{\text{iso}})}(\omega)|A_{(m_{\text{iso}})}(\omega)|^2 H_{F(m_{\text{iso}})}(\omega)|}{|H^*_{C(m_{\text{iso}})}(\omega)|A_{(m_{\text{iso}})}(\omega)|^2 H_{N(m_{\text{iso}})}(\omega)|} \\ &= |H_{F(m_{\text{iso}})}(\omega)|^2 |A_{(m_{\text{iso}})}(\omega)|^2, \end{aligned} \tag{7.27}$$

where the radial mode is omitted from the notation for brevity as it is assumed that only one radial mode is propagating. Therefore, the 3S Array method combined with the modal isolation method provides an estimate of the combustion noise that propagates in mode m_{iso} along the engine duct and out to the far field. In addition to extending the effective frequency range of the 3S Array method, it also makes it possible to assess which modes carry the most combustion noise. The total combustion noise that contributes to the far field microphone spectrum

$$G_{\nu_F\nu_F}(\omega) = \sum_{m_{\text{iso}}=1-M/2}^{M/2-1} G_{\nu_F\nu_F(m_{\text{iso}})}(\omega) \tag{7.28}$$

as the modes $m_{\text{iso}} = \pm(M/2-1)$ are the highest order modes that can be isolated before aliasing occurs. The cut-on frequency of modes $m_{\text{iso}} = \pm M/2$ are the upper frequency limit of the 3S Array method combined with the modal isolation method. However, if the cut-on frequency of a higher order radial mode is lower than the cut-on frequency of mode $m_{\text{iso}} = \pm M/2$, then the upper frequency limit is the cut-on frequency of the radial mode as it violates the assumption of only a single radial mode propagating in the duct.

7.2.4 Effects of microphone position error on the estimate obtained using the 3S Array method combined with the modal isolation method

The 3S Array method combined with the modal isolation method will be affected by errors in estimated mode amplitudes caused by errors in the in-duct microphone positions which were discussed in Section 7.2.2. The cross-spectral density function between the combustor array and a far field microphone can be expressed as

$$\begin{aligned} G_{CF(m_{\text{iso}})}(\omega) &= \lim_{T\to\infty} \frac{1}{T} E\left[(\hat{A}_{C(m_{\text{iso}})}(\hat{\theta}_i, \theta_i, \Delta z_i, \omega))^* (P_F(\mathbf{x}, \omega))\right] \\ &= \delta^*_{C(m_{\text{iso}})}(\omega) H^*_{C(m_{\text{iso}})}(\omega) |A_{(m_{\text{iso}})}(\omega)|^2 H_{F(m_{\text{iso}})}(\omega) + \epsilon_{CF}(\omega) \end{aligned} \tag{7.29}$$

where

$$\delta_{C(m_{\text{iso}})}(\omega) = \sum_{i=1}^{M} e^{j(m\Delta\theta_i + k_{z(m)}\Delta z_i)} \tag{7.30}$$

accounts for the error in the estimated modal amplitude for the mode m_{iso} and

$$\begin{aligned} \epsilon_{CF}(\omega) = \sum_{m=-\infty}^{\infty} &\left(\delta^*_{C(m)}(\omega) H^*_{C(m)}(\omega) |A_{(m)}(\omega)|^2 H_{F(m)}(\omega)\right) \\ &- \delta^*_{C(m_{\text{iso}})}(\omega) H^*_{C(m_{\text{iso}})}(\omega) |A_{(m_{\text{iso}})}(\omega)|^2 H_{F(m_{\text{iso}})}(\omega) \end{aligned} \tag{7.31}$$

accounts for the contribution of modes other than m_{iso} to the cross-spectral estimate due to the microphone position errors. A similar expression can be obtained for $G_{NF(m_{\text{iso}})}(\omega)$. The cross spectra between the combustor and nozzle can be expressed as

$$\begin{aligned} G_{CN(m_{\text{iso}})}(\omega) &= \lim_{T\to\infty} \frac{1}{T} E\left[(\hat{A}_{C(m_{\text{iso}})}(\hat{\theta}_i, \theta_i, \Delta z_i, \omega))^* (\hat{A}_{N(m_{\text{iso}})}(\hat{\theta}_i, \theta_i, \Delta z_i, \omega))\right] \\ &= \delta^*_{C(m_{\text{iso}})}(\omega) H^*_{C(m_{\text{iso}})}(\omega) |A_{(m_{\text{iso}})}(\omega)|^2 H_{N(m_{\text{iso}})}(\omega) \delta_{N(m_{\text{iso}})}(\omega) + \epsilon_{CN}(\omega) \end{aligned} \tag{7.32}$$

where

$$\begin{aligned} \epsilon_{CN}(\omega) = \sum_{m=-\infty}^{\infty} &\left(\delta^*_{C(m)}(\omega) H^*_{C(m)}(\omega) |A_{(m)}(\omega)|^2 H_{N(m)}(\omega) \delta_{N(m)}(\omega)\right) \\ &- \delta^*_{C(m_{\text{iso}})}(\omega) H^*_{C(m_{\text{iso}})}(\omega) |A_{(m_{\text{iso}})}(\omega)|^2 H_{N(m_{\text{iso}})}(\omega) \delta_{N(m_{\text{iso}})}(\omega) \end{aligned} \tag{7.33}$$

and again $\delta_{C(m)}(\omega)$ and $\delta_{N(m)}(\omega)$ are the effects of the position error on the contribution of the mode m to the estimates $\hat{A}_{C(m_{\text{iso}})}(\hat{\theta}_i, \theta_i, \Delta z_i, \omega)$ and $\hat{A}_{N(m_{\text{iso}})}(\hat{\theta}_i, \theta_i, \Delta z_i, \omega)$ respectively and ϵ_{CN} accounts for the contribution of modes other than m_{iso} to the cross-spectral estimate.

The estimate of the contribution of combustion noise that travels in mode m_{iso} to the far field microphone spectra obtained using the 3S Array method combined with the modal isolation method and, including in-duct microphone position errors, results in

$$G_{\nu_F\nu_F(m_{\text{iso}})}(\omega) = \frac{|\bar{G}_{CF(m_{\text{iso}})}(\omega) + \epsilon_{CF}(\omega)||\bar{G}_{NF(m_{\text{iso}})}(\omega) + \epsilon_{NF}(\omega)|}{|\bar{G}_{CN(m_{\text{iso}})}(\omega) + \epsilon_{CN}(\omega)|} \tag{7.34}$$

where

$$\bar{G}_{CF(m_{\text{iso}})}(\omega) = \delta^*_{C(m_{\text{iso}})}(\omega)H^*_{C(m_{\text{iso}})}(\omega)|A_{(m_{\text{iso}})}(\omega)|^2 H_{F(m_{\text{iso}})} \tag{7.35}$$

$$\bar{G}_{NF(m_{\text{iso}})}(\omega) = \delta^*_{N(m_{\text{iso}})}(\omega)H^*_{N(m_{\text{iso}})}(\omega)|A_{(m_{\text{iso}})}(\omega)|^2 H_{F(m_{\text{iso}})} \tag{7.36}$$

and

$$\bar{G}_{CN(m_{\text{iso}})}(\omega) = \delta^*_{C(m_{\text{iso}})}(\omega)H^*_{C(m_{\text{iso}})}(\omega)|A_{(m_{\text{iso}})}(\omega)|^2 H_{N(m_{\text{iso}})}\delta_{N(m_{\text{iso}})} \tag{7.37}$$

are the contributions of combustion noise that propagates in mode m_{iso} to the estimated combustion noise. Due to errors in microphone positions, the estimate of the combustion noise that travels in mode m_{iso} obtained using the 3S Array method combined with the modal isolation method will be an overestimate of the combustion noise that travels in mode m_{iso} in the engine duct and radiates to the far field. Using both the sum of the estimates and the estimate with the highest level, it is possible to obtain the interval which the actual level of the combustion noise that travels in mode m_{iso} falls between.

One important case to consider is the output of the 3S Array method combined with the modal isolation method when m_{iso} is cut-off. Assuming the arrays are not close to the sound source in the duct, the amplitude of the isolated mode will be very small. The combustion noise estimate in the far field when isolating a cut-off mode can be approximated as

$$G_{\nu_F\nu_F(m_{\text{iso}})}(\omega) \approx \frac{|\epsilon_{CF}(\omega)||\epsilon_{NF}(\omega)|}{|\epsilon_{CN}(\omega)|}. \tag{7.38}$$

For the case where only the plane wave mode is cut-on and $m_{\text{iso}} = 1$, the combustion noise estimate can be approximated as

$$\begin{aligned} G_{\nu_F\nu_F(1)}(\omega) &\approx \frac{|\delta^*_{C(0)}(\omega)H^*_{C(0)}(\omega)|A_{(0)}(\omega)|^2 H_{F(0)}(\omega)||\delta^*_{N(0)}(\omega)H^*_{N(0)}(\omega)|A_{(0)}(\omega)|^2 H_{F(0)}(\omega)|}{|\delta^*_{C(0)}(\omega)H^*_{C(0)}(\omega)|A_{(0)}(\omega)|^2 H_{N(0)}(\omega)\delta_{N(0)}(\omega)|} \\ &\approx |H_{F(0)}|^2|A_{(0)}|^2. \end{aligned} \tag{7.39}$$

Therefore, any estimate where m_{iso} is not cut-on will not be accurate but will instead be dependent on the position errors in the in-duct arrays. For the case where only the plane wave is cut-on, the estimate will approximately be equal to the estimate where $m_{\text{iso}} = 0$.

7.3 Chapter Summary

The 3S Array method requires the assumption that a single mode is propagating along the engine duct and so, the upper frequency limit of the 3S Array method is the cut-on of the first higher order mode in the duct. This chapter has introduced a modal isolation method that can be

used in combination with the 3S Array method to extend the effective frequency range of the 3S Array method. The 3S Array method combined with the modal isolation method requires:

- A circular array of evenly spaced microphones, the number of which needs to be equal to twice the highest mode that is to be isolated plus one.
- The estimate obtained from the 3S Array method combined with the modal isolation method is the combustion noise that propagates along the engine duct in mode m_{iso} and radiates to the far field.
- The total combustion noise that propagates to the far field is equal to the sum of the combustion noise estimates for all of the modes that are cut on.
- The microphones in each array need to be positioned as accurately as possible to avoid error in the combustion noise estimate. These errors will result in an overestimate of the combustion noise due to the loss of coherence between the estimates of the isolated modes.

This combined method is a significant improvement over the standard 3S Array technique as it makes it possible to increase the upper frequency limit by maintaining the assumption of single mode propagation. While errors due to position may result in an overestimate of the combustion noise, the ability to obtain an interval that the combustion noise falls between still makes it a viable method to estimate the combustion noise at higher frequencies.

Chapter 8

Separation of direct and indirect combustion noise

As described in Chapter 3, there have been several measurements of combustion noise where the direct and indirect noise has been examined. Harper-Bourne et al. [26] claimed that the differences in his measurements when using the combustor and far field microphones as opposed to the hot nozzle and far field were down to indirect combustion noise being present in the hot nozzle but not in the combustor. Miles [27] stated that the differences were more likely due to the inherent bias error in the COP method. Miles delayed his measured signals to align what he believed to be the direct and indirect noise and found a propagation time difference of 3.052 ms. He believes the signal that takes longer to propagate to the far field is the indirect noise as the entropy waves are convected with the flow until they undergo an acceleration, which generates the indirect noise. Tam et al. [9] used numerical simulations of indirect noise to identify contributions of indirect combustion noise to measurements of an APU.

As stated in Chapter 2, it is possible that the indirect noise is also present in the combustor. No method has attempted to separate the direct and indirect combustion noise in the combustor as it is believed that the largest source of indirect noise is at the turbines. Marble and Candel [7] and Tam [8] state that indirect noise propagates upstream as well as downstream of the location the entropy waves are accelerated. Inside the combustor, this would be indirect noise produced at the NGV and not any produced at the turbines as the flow through the NGV will be choked which will prevent noise produced downstream of the NGV to propagate upstream into the combustor.

If the entropy waves are propagating upstream from the NGV, then the combustor measurement will have both direct and indirect combustion noise present. Figure 8.1 is a simplified diagram of a section of an annular combustor assuming that the indirect noise does propagate upstream. It is assumed that the direct and indirect combustion noise propagate through the NGV without being reflected. The output of the 3S Array technique in this case would provide an estimate which is the combined direct and indirect combustion noise in the far field. To be able to gain a better understanding of the direct and indirect noise and their individual contributions to the far

field level, the direct and indirect noises need to be separated. The work presented in sections 8.1 to 8.4 inclusive in this chapter was published by Hart et. al. [59].

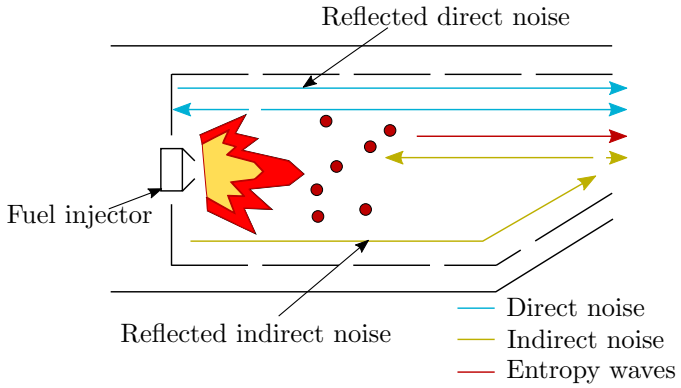

FIGURE 8.1: A simplified diagram of a section of an annular combustor.

8.1 Model for noise in the combustor

The sound field in the combustor will comprise the sum of direct and indirect noise. Pressure fluctuations in the combustor also contain contributions due to the hydrodynamic pressure field. The flow through the NGV can be expected to be choked which will result in an absence of reflections of sound from this end of the duct. There is a hard reflective surface near the fuel injector however, which will result in a single reflection of the direct and indirect noise.

Assuming that the only mode propagating in the combustor is the plane wave mode, the direct combustion noise can be modelled as a plane wave source at a position d_d and the indirect combustion noise can be modelled as a plane wave source at a position d_i. The assumption that the direct noise is all produced in a single plane is a significant simplification of the actual source mechanism as in reality the direct noise will be distributed throughout a significant volume of the combustor near the flame. However, this simplification is made to show that the direct and indirect noise can be separated if the two sources are not produced in the same plane. If a number of microphones are placed in the combustor downstream of d_d and upstream of d_i, at a single frequency, the pressure at the j^{th} microphone in the combustor can be expressed as

$$P_j(\omega) = H_{d,j}(\omega)P_d(\omega) + H_{i,j}(\omega)P_i(\omega) + N_j(\omega) \tag{8.1}$$

where $P_d(\omega)$ and $P_i(\omega)$ are the plane wave pressures of the direct noise at d_d and indirect noise at d_i respectively, $H_{d,j}(\omega)$ and $H_{i,j}(\omega)$ are pressure-to-pressure transfer functions that describe the propagation from the direct and indirect source locations to the microphone and $N_j(\omega)$ is the unwanted noise measured by the microphone. The transfer functions can be expressed as

$$H_{d,j}(\omega) = (\sigma_{d,j}\beta_{d,j})^{-\frac{1}{2}} \left(e^{jk^+(d_m - d_d)} + R(\omega)e^{j(k^- d_d + k^+ d_m)} \right) \tag{8.2}$$

and

$$H_{i,j}(\omega) = (\sigma_{i,j}\beta_{i,j})^{-\frac{1}{2}} e^{jk^-(d_i - d_m)} + (\sigma_{i,j}(1+M))^{-\frac{1}{2}} R(\omega)e^{j(k^- d_i + k^+ d_m)} \tag{8.3}$$

where $\sigma_{d,j}$ and $\sigma_{i,j}$ are ratios of the cross-sectional area at the source location to the cross-sectional area at the j^{th} microphone location, and $\beta_{d,j}$ and $\beta_{i,j}$ are ratios of the convective amplification at the source location to the convective amplification at the j^{th} microphone location which are defined as

$$\beta_{d,j} = \frac{1 + M_d}{1 + M_j} \tag{8.4}$$

and

$$\beta_{i,j} = \frac{1 - M_i}{1 - M_j}. \tag{8.5}$$

$M_d = U_d/c$ in which U_d is the flow speed at d_d and similar expressions hold for d_i and d_j and c represents the local speed of sound. $R(\omega)$ is the reflection coefficient of the wall and $k^{\pm}$ is the wavenumber depending on whether the sound is travelling upstream $(+)$ or downstream $(-)$. The wavenumber in a duct with only the plane wave mode cut on is

$$k^{\pm} = \frac{k_0}{(1 \pm M)} \tag{8.6}$$

where $k = \omega/c$.

For a number M_T of microphones, Equation (8.1) can be expressed in vector form

$$\mathbf{p}(\omega) = \mathbf{H}(\omega)\mathbf{s}(\omega) + \mathbf{n}(\omega) \tag{8.7}$$

where $\mathbf{s}^T(\omega) = \begin{pmatrix} P_d(\omega) & P_i(\omega) \end{pmatrix}$ with ^{T} representing the transpose operator and $\mathbf{H}(\omega)$ is a matrix of transfer functions between each microphone and each of the sources.

8.2 Separation method

Equation (8.7) is an expression for the acoustic pressure signal at a particular microphone location assuming the source signals, transfer functions and the noise signals are known. However, in practise $\mathbf{p}(\omega)$ can be measured and $\mathbf{s}(\omega)$ remains to be determined.

8.2.1 Single frequency source separation

For the case where there are two microphones inside the combustor, Equation (8.7) becomes

$$\begin{pmatrix} P_1(\omega) \\ P_2(\omega) \end{pmatrix} = \begin{pmatrix} H_{d,1}(\omega) & H_{i,1}(\omega) \\ H_{d,2}(\omega) & H_{i,2}(\omega) \end{pmatrix} \begin{pmatrix} P_d(\omega) \\ P_i(\omega) \end{pmatrix} + \begin{pmatrix} N_1(\omega) \\ N_2(\omega) \end{pmatrix}. \tag{8.8}$$

In this instance, assuming the transfer functions are known, there are four unknowns and two equations. Estimates of the direct and indirect noise can be deduced from

$$\begin{pmatrix} H_{d,1}(\omega) & H_{i,1}(\omega) \\ H_{d,2}(\omega) & H_{i,2}(\omega) \end{pmatrix}^{-1} \begin{pmatrix} P_1(\omega) \\ P_2(\omega) \end{pmatrix} = \begin{pmatrix} P_d(\omega) \\ P_i(\omega) \end{pmatrix} + \begin{pmatrix} H_{d,1}(\omega) & H_{i,1}(\omega) \\ H_{d,2}(\omega) & H_{i,2}(\omega) \end{pmatrix}^{-1} \begin{pmatrix} N_1(\omega) \\ N_2(\omega) \end{pmatrix}, \tag{8.9}$$

the accuracy of which is dependent on the level of unwanted noise present.

Obtaining an estimate of the direct and indirect combustion noise will be possible so long as the number of microphones is equal or greater than the number of source terms. Generalising Equation (8.9) to M_T microphones and writing in vector notation yields

$$\mathbf{s}(\omega) = \mathbf{H}^{-1}(\omega)\mathbf{p}(\omega) - \mathbf{H}^{-1}(\omega)\mathbf{n}(\omega). \tag{8.10}$$

For the case where there are more microphones than sources, the transfer function matrix will not be square and so the pseudo inverse

$$\mathbf{H}^{-1}(\omega) = (\mathbf{H}^{\mathbf{H}}(\omega)\mathbf{H}(\omega))^{-1}\mathbf{H}^{\mathbf{H}}(\omega) \tag{8.11}$$

will need to be calculated where $^{\mathbf{H}}$ is the Hermitian transpose.

8.2.2 Broadband source separation

The above single frequency source separation method can be rewritten for the more realistic case of random broadband noise. The CSM of the pressures in Equation (8.7) can be expressed as

$$\mathbf{G}_{pp}(\omega) = \mathbf{H}(\omega)\mathbf{G}_{ss}(\omega)\mathbf{H}^{\mathbf{H}}(\omega) + \mathbf{G}_{nn}(\omega) \tag{8.12}$$

where $\mathbf{G}_{ss}(\omega)$ is the CSM of source pressure signals and $\mathbf{G}_{nn}(\omega)$ is the CSM of unwanted noise which will be a diagonal matrix if all of the unwanted noise spectra are incoherent. To separate the direct and indirect noise for the broadband case, the same inverse method can be used which yields

$$\mathbf{G}_{ss}(\omega) = \mathbf{H}^{-1}(\omega)\mathbf{G}_{pp}(\omega)(\mathbf{H}^{\mathbf{H}}(\omega))^{-1} - \mathbf{H}^{-1}(\omega)\mathbf{G}_{nn}(\omega)(\mathbf{H}^{\mathbf{H}}(\omega))^{-1}. \tag{8.13}$$

8.3 Configuration of simulation

Equation (8.12) can be used to simulate a CSM of microphone pressures inside a combustor so that the effectiveness of the separation method can be investigated. Figure 8.2 is a diagram of the configuration that is used from here onwards to evaluate the separation method.

The simulated direct and indirect combustion noise will both consist of white noise with a level of 117 dB SPL. The indirect noise will be present between 0 - 200 Hz and the direct noise will be present between 100 - 400 Hz. Initially, the mean flow velocity is $v = 60$ ms^{-1} and the reflection coefficient $|R| = 1$. The speed of sound in the combustor was chosen to be 600 ms^{-1} due to the high average temperature in the combustor. The unwanted noise is uncorrelated between measurement locations and the direct and indirect noise. The uncorrelated noise signal for each microphone signal is white and has a level of 94 dB SPL.

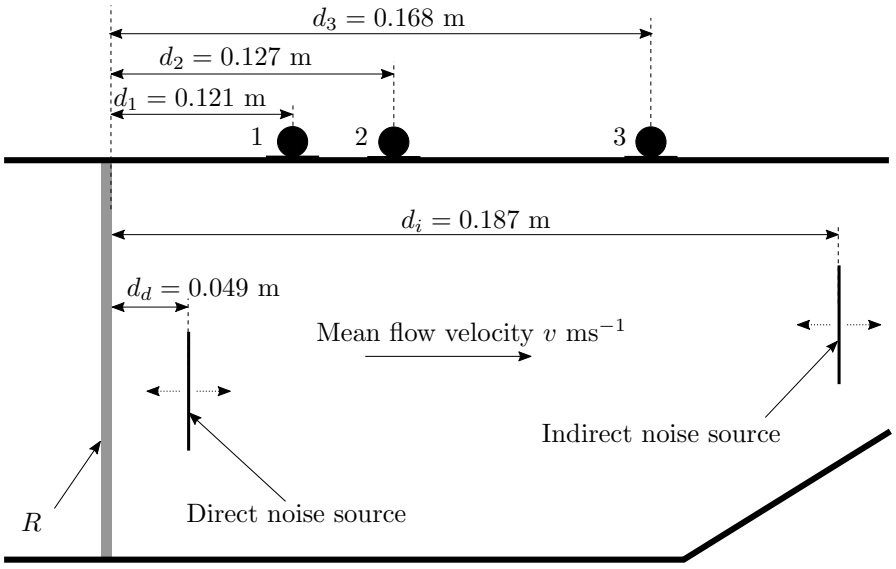

FIGURE 8.2: Configuration used to simulate microphone pressure signals and evaluate separation method.

8.4 Results

Figures 8.3 and 8.4 show the estimated direct and indirect combustion noise respectively using 2 microphones (1 and 3) without unwanted noise, 2 microphones with unwanted noise and 3 microphones with unwanted noise. The addition of the unwanted noise severely effects the

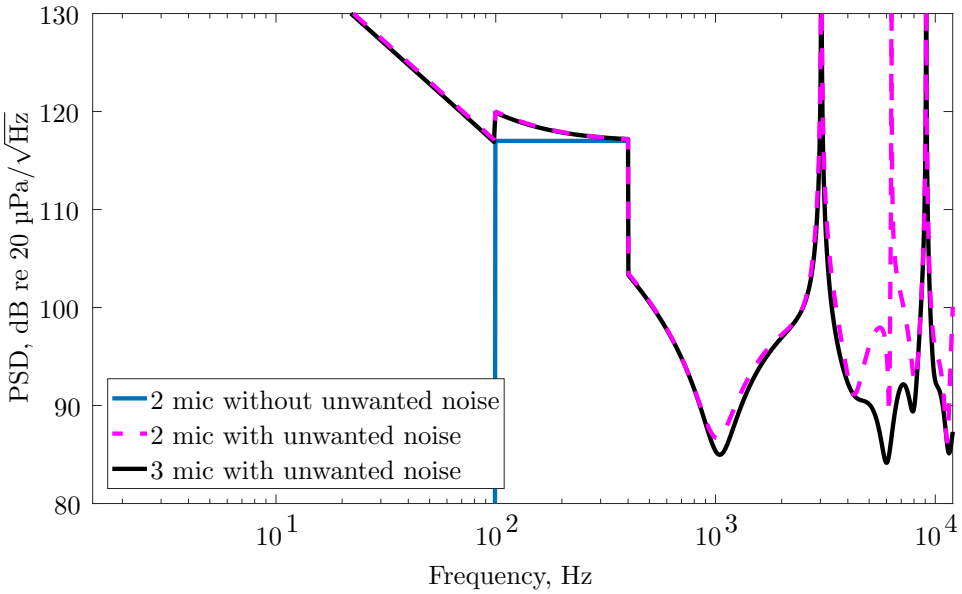

FIGURE 8.3: Estimated direct combustion noise using the separation method applied to data from the plane wave simulation, using 2 microphones without and with unwanted noise present and using 3 microphones with unwanted noise present.

estimate of the direct and indirect noise. At very low frequencies, the estimates provided by the 2 microphone and the 3 microphone separation with the unwanted noise are very similar. At higher frequencies the estimates begin to differ significantly, especially for the indirect noise

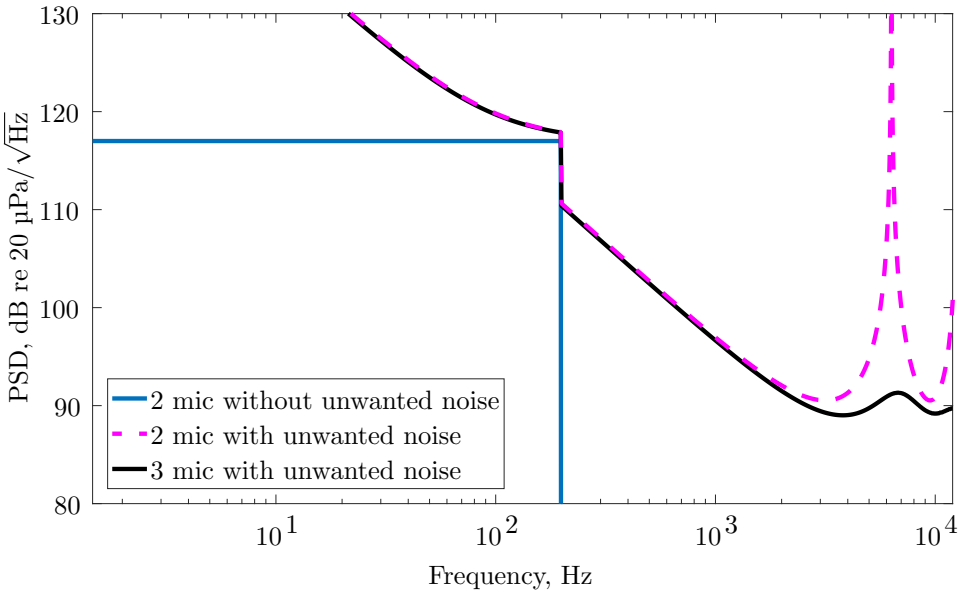

FIGURE 8.4: Estimated indirect combustion noise using the separation method applied to data from the plane wave simulation, using 2 microphones without and with unwanted noise present and using 3 microphones with unwanted noise present.

where there are two discontinuities in the 2 microphone separation which are not present in the 3 microphone separation.

The variation in the estimate where direct and indirect noise are not present (in this case above 400 Hz) is due to

$$\mathbf{H}^{-1}(\omega)\mathbf{G}_{pp}(\omega)(\mathbf{H}^{\mathbf{H}}(\omega))^{-1} = \mathbf{H}^{-1}(\omega)\mathbf{G}_{nn}(\omega)(\mathbf{H}^{\mathbf{H}}(\omega))^{-1}. \tag{8.14}$$

As all of the unwanted noise signals have flat autospectra with a level of 94 dB, the discontinuities and level variation in the estimate must be due to the inverse of the transfer function matrix. The inverse of the 2×2 transfer function matrix is defined as

$$\begin{pmatrix} H_{d1}(\omega) & H_{i1}(\omega) \\ H_{d2}(\omega) & H_{i2}(\omega) \end{pmatrix}^{-1} = \frac{1}{H_{d1}(\omega)H_{i2}(\omega) - H_{i1}(\omega)H_{d2}(\omega)} \begin{pmatrix} H_{i2}(\omega) & -H_{i1}(\omega) \\ -H_{d2}(\omega) & H_{d1}(\omega) \end{pmatrix}. \tag{8.15}$$

where $H_{d1}(\omega)H_{i2}(\omega) - H_{i1}(\omega)H_{d2}(\omega)$ is the determinant of the transfer function matrix. The inverse of the matrix is undefined for the case where

$$H_{d1}(\omega)H_{i2}(\omega) = H_{i1}(\omega)H_{d2}(\omega) \tag{8.16}$$

which results in the discontinuities in the estimate.

The 3 microphone method has fewer discontinuities in the direct estimate and no discontinuities in the indirect estimate. As there are 3 microphones, the pseudo inverse is calculated which results in many more terms in the determinant and therefore, fewer instances where the determinant is zero. Using 3 microphones to estimate the direct and indirect noise in the combustor results in a more accurate estimate than using 2 microphones.

Up to this point, it has been assumed that the transfer functions are known exactly. It is unlikely that this will be the case for measured data. The locations of the microphones may be known accurately, but there will be uncertainty in the estimates of mean flow velocity and reflection coefficient. It is therefore necessary to examine how sensitive the estimated direct and indirect combustion noise signals are to errors in the velocity and reflection coefficient estimates.

Figure 8.5 shows the estimates of the direct and indirect combustion noise for different estimated mean flow velocities with the actual velocity being 60 ms^{-1}. From this, it is clear that the estimate is not very sensitive to error in the velocity estimate.

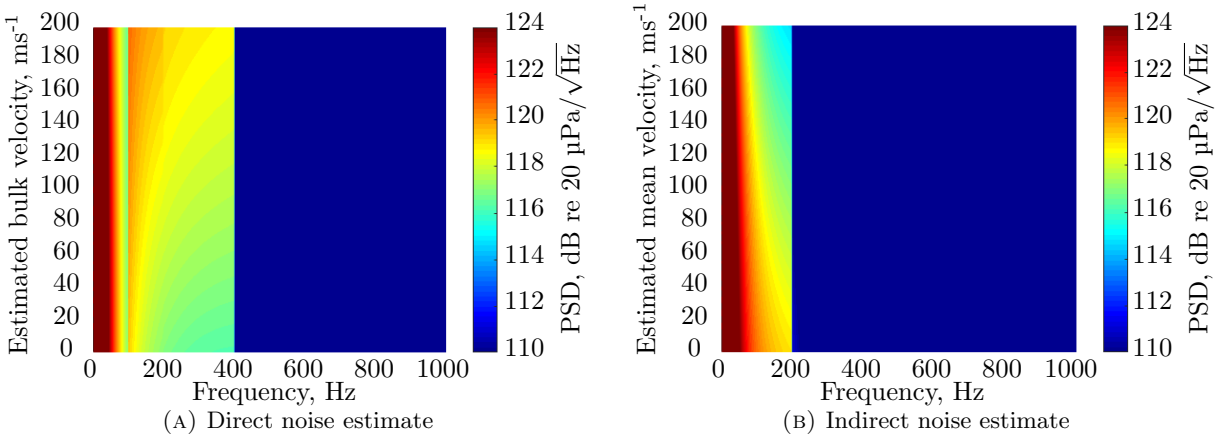

(A) Direct noise estimate (B) Indirect noise estimate

FIGURE 8.5: The direct and indirect noise estimates for different estimated velocities with the actual velocity being 60 ms^{-1}.

Figure 8.6 shows the estimates of the direct and indirect combustion noise for different estimated reflection coefficients with the actual reflection coefficient being 0.5. Again, while it does have an effect on the estimate, the estimate is only weakly sensitive to an error in the reflection coefficient.

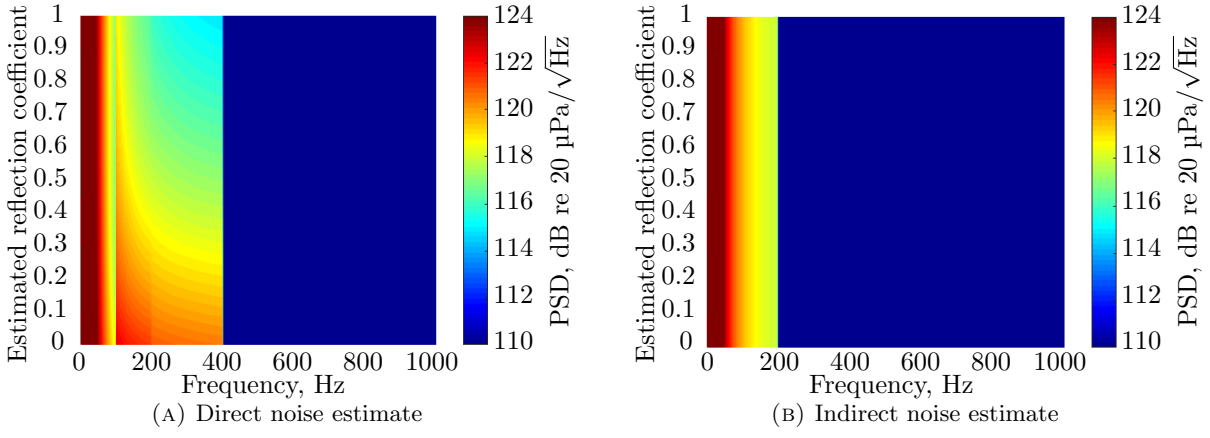

(A) Direct noise estimate (B) Indirect noise estimate

FIGURE 8.6: The direct and indirect noise estimates for different estimated reflection coefficients with the actual reflection coefficient being 0.5.

The main purpose of the separation technique is to use the estimated direct and indirect signals as inputs to a coherence-based measurement technique. As such, it is the coherence between the separated signal and a microphone in the far field of the turbofan jet engine that is of interest. The pressure measured by the far field microphone is assumed to consist of direct and indirect

combustion noise plus an unwanted noise signal which is not correlated with any other signal. For the purposes of a simple simulation, the far field microphone signal is simulated using

$$P_f(\omega) = H_{df}(\omega)P_d(\omega) + H_{if}(\omega)P_i(\omega) + N_f(\omega). \tag{8.17}$$

Figure 8.7 shows the coherence between the estimated separated signals and the far field microphone signal when the unwanted noise level is 94 dB SPL. From these coherences, it is clear that the estimated separated signals can be used in a coherence-based measurement technique to isolate the direct and indirect combustion noise in the far field. If indirect noise is not present

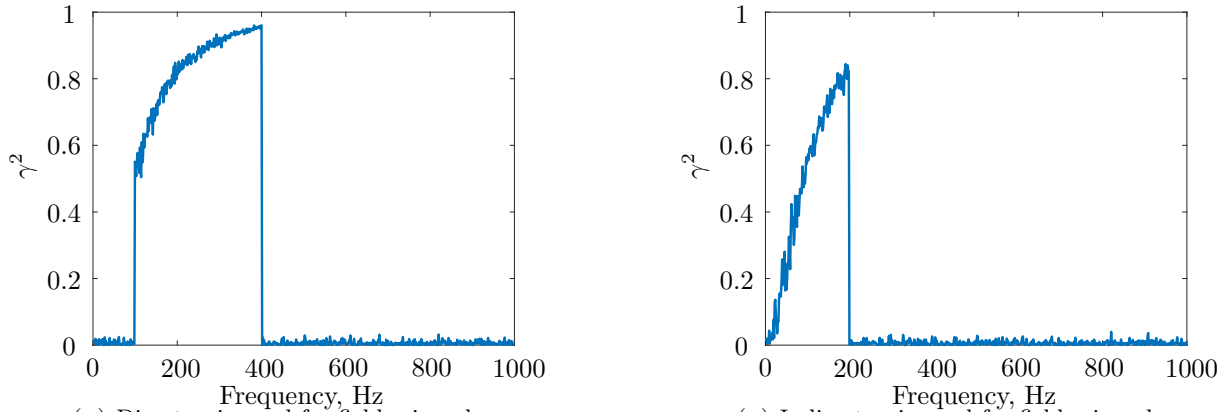

(A) Direct noise and far field microphone

(B) Indirect noise and far field microphone

FIGURE 8.7: The coherence between the far field microphone and the direct and indirect noise estimates respectively.

in the combustor, the separated signal will just be made up of the unwanted noise signals. The coherence with the far field should be 0 (assuming a large number of averages). This should confirm whether or not indirect noise is present in the combustor.

8.5 Combining direct and indirect noise separation with 3S Array

Combining the separation method with the 3S array method would make it possible to obtain the separate levels of direct and indirect noise in the far field. The 3S Array technique is implemented, from Equation (4.21), using

$$\widehat{G}_{\nu\nu}(\omega) = \frac{|G_{CF}(\omega)||G_{NF}(\omega)|}{|G_{CN}(\omega)|}. \tag{8.18}$$

The signals measured in the combustor, C, hot nozzle, N, and far field, F can be expressed as

$$\begin{aligned} C(\omega) &= D(\omega)H_{d,C}(\omega) + I(\omega)H_{I,C}(\omega) + N_C(\omega) \\ N(\omega) &= D(\omega)H_{d,N}(\omega) + I(\omega)H_{I,N}(\omega) + N_N(\omega) \\ F(\omega) &= D(\omega)H_{d,F}(\omega) + I(\omega)H_{I,F}(\omega) + N_F(\omega) \end{aligned} \tag{8.19}$$

where D and I are the pressure signals produced by the direct and indirect combustion noise respectively and N is unwanted noise. For the 3S Array method to be used to separate the indirect noise it is assumed that the indirect noise that propagates upstream into the combustor is coherent with the indirect noise that propagates downstream from the NGV. As the indirect noise that propagates upstream and downstream are produced via the same mechanism, it is plausible that this is the case. The direct and indirect combustion noise are assumed to not be coherent with each other due to the different source mechanisms and the unwanted noise is not coherent between any measurement location. The cross-spectral estimates of the three pairs of signals are

$$G_{CF}(\omega) = |{H_{d,C}}^{\mathbf{H}}(\omega)|D(\omega)|^2 H_{d,F}(\omega) + {H_{I,C}}^{\mathbf{H}}(\omega)|I(\omega)|^2 H_{I,F}(\omega)|, \tag{8.20}$$

$$G_{NF}(\omega) = |{H_{d,N}}^{\mathbf{H}}(\omega)|D(\omega)|^2 H_{d,F}(\omega) + {H_{I,N}}^{\mathbf{H}}(\omega)|I(\omega)|^2 H_{I,F}(\omega)|, \tag{8.21}$$

and

$$G_{CN}(\omega) = |{H_{d,C}}^{\mathbf{H}}(\omega)|D(\omega)|^2 H_{d,N}(\omega) + {H_{I,C}}^{\mathbf{H}}(\omega)|I(\omega)|^2 H_{I,N}(\omega)|. \tag{8.22}$$

The output of the 3S Array method will not, therefore, simply be the incoherent sum of the direct and indirect noise that propagates to the far field. The separation method can be combined with the 3S Array method by replacing the signal C with the direct noise in the combustor obtained using the separation method, which will be denoted as d_1. Assuming that the separation method has performed perfectly so that there is no incoherent noise present in the separated signal, the separated direct noise signal can be expressed as

$$d_1(\omega) = H_{d,1} D(\omega) + N_d. \tag{8.23}$$

The output of 3S Array with this new input signal is

$$\widehat{G}_{\nu\nu}(\omega) = \frac{|{H_{d,1}}^{\mathbf{H}}(\omega)|D(\omega)|^2 H_{d,F}(\omega)|(|{H_{d,N}}^{\mathbf{H}}(\omega)|D(\omega)|^2 H_{d,F}(\omega) + {H_{I,N}}^{\mathbf{H}}(\omega)|I(\omega)|^2 H_{I,F}(\omega)|)}{|{H_{d,1}}^{\mathbf{H}}(\omega)|D(\omega)|^2 H_{d,N}(\omega)|} \tag{8.24}$$

which is not the contribution of just the direct combstion noise to the far field but is instead still a combination of the direct and indirect combustion noise. To obtain just the contribution of the direct noise two of the inputs to the 3S Array method need to be signals obtained as the outputs from the separation method. Substituting the nozzle signal N with a separated direct signal d_2 which is obtained from a second array of microphones inside the combustor, the 3S Array technique output becomes

$$\begin{aligned} \widehat{G}_{\nu\nu}(\omega) &= \frac{|{H_{d,1}}^{\mathbf{H}}(\omega)|D(\omega)|^2 H_{d,F}(\omega)||{H_{d,2}}^{\mathbf{H}}(\omega)|D(\omega)|^2 H_{d,F}(\omega)|}{|{H_{d,1}}^{\mathbf{H}}(\omega)|D(\omega)|^2 H_{d,2}(\omega)|} \\ &= |H_{d,F}(\omega)|^2 |D(\omega)|^2 \end{aligned} \tag{8.25}$$

which is the contibution of direct combustion noise to the far field level. A similar expression can be obtained for the contribution of indirect combustion noise to the far field level when using the separated indirect signals as opposed to the separated direct signals. The assumptions of 3S Array still apply when using the separated signals as inputs to the 3S Array method. Therefore, if the separation is not perfect and some indirect noise is still present there will be errors in the estimate obtianed. Similarly, if the unwanted noise is coherent between the two arrays inside

the combustor the result will be an underestimate of the separated combustion noise source in the far field. The likelyhood of the unwanted noise being coherent between the two separated signals can be reduced by using two completely different microphone arrays in the combustor.

The separation method and the 3S Array combined with separation method are evaluated experimentally in Chapter 12.

8.6 Chapter summary

Combustion noise is comprised of two components: the direct and the indirect combustion noise. A 3 microphone separation technique has been presented in this chapter which can be used to provide estimates of the direct and indirect noise in the combustor. It has been found that:

- An estimate of the direct and indirect combustion noise using 3 microphones provides a significant improvement over using 2 microphones.
- The estimate of the direct and indirect combustion noise is only weakly sensitive to errors in the estimated mean flow velocity and reflection coefficient.
- The separated signals can be used in a coherence-based technique, even when the separated signals are significantly smaller than the unwanted noise.

To combine the separation method with the 3S Array method the combustor and hot nozzle signals need to be replaced with the separated combustion noise source. This requires the separation technique to be applied to two different microphone arrays to minimise the coherence of unwanted noise between the separated signals. The separation method cannot be applied in the hot nozzle as both the direct and indirect noise will arrive at sensors in the hot nozzle from the same direction and so, both in duct arrays need to be placed inside the combustor.

Chapter 9

3S PCCSM

The 3S Array method was developed by Rodríguez-García et al. [40] to reduce the coherence of unwanted noise between the external measurement signal and the hot nozzle signal as explained in Chapter 4. The 3S Array method utilises a microphone array and simple delay-and-sum beamforming to create a highly directional microphone to reduce the contribution of other noise sources to the external signal. The issue with delay-and-sum beamforming is that at low frequencies the beamformer has low resolution, as is shown in Chapter 6, and so does not reduce much of (or potentially any of) the sound produced by unwanted noise sources. The performance of the 3S Array method could be enhanced by applying more advanced frequency domain beamforming techniques such as the inverse beamforming method [55]. These methods use the CSM of the microphone array and produce either the PSD of a single source or the CSM of multiple sources. It is not possible to implement the 3S Array method using advanced frequency domain beamforming techniques as the coherence between the source(s) and the in-duct microphone cannot be calculated. To implement these more advanced methods, the 3S Array technique needs to be enhanced.

9.1 Reformulation of the 3S method

To use beamforming techniques that require a CSM, a variation of the 3S method needs to be used to obtain the part of the CSM that is coherent with the in-duct sensors. This partially coherent CSM (PCCSM) can then be used to implement the more advanced beamforming techniques. The 3S method in it's current form cannot be used to produce cross spectra because all of the phase information is lost as only the magnitudes of the cross spectra are used to obtain the estimate.

The stage at which the phase information is lost is when the square root of the three square coherences is calculated in Equation (4.19). The square coherence functions are used so that the substitution $|G_{x_i x_j}(\omega)|^2 = G_{\nu_i \nu_i}(\omega) G_{\nu_j \nu_j}(\omega)$ can be made in Equation (4.15). Starting from this

step but using the complex coherence instead of coherence squared,

$$\begin{aligned}\gamma_{x_i x_j}(\omega) &= \frac{G_{x_i x_j}(\omega)}{\sqrt{(G_{\nu_i\nu_i}(\omega)+G_{n_i n_i}(\omega))(G_{\nu_j\nu_j}(\omega)+G_{n_j n_j}(\omega))}} \\ &= \frac{G_{x_i x_j}(\omega)}{\sqrt{G_{\nu_i\nu_i}(\omega)G_{\nu_j\nu_j}(\omega)(1+\alpha_i(\omega))(1+\alpha_j(\omega))}}.\end{aligned} \tag{9.1}$$

Following the same procedure as the original derivation yields

$$\begin{aligned}1+\alpha_i(\omega) &= \frac{\gamma_{x_j x_k}(\omega)}{\gamma_{x_j x_i}(\omega)\gamma_{x_i x_k}(\omega)} \\ &= \frac{G_{x_j x_k}(\omega)G_{x_i x_i}(\omega)}{G_{x_j x_i}(\omega)G_{x_i x_k}(\omega)}.\end{aligned} \tag{9.2}$$

The combustion noise signal at i can be defined as

$$\nu_i(\omega) = H_i(\omega)\nu(\omega) \tag{9.3}$$

where $\nu(\omega)$ is the pressure of the combustion noise at the source and $H_i(\omega)$ is a pressure-to-pressure transfer function which describes the propagation from the source to i. Substituting

$$G_{x_i x_j}(\omega) = G_{\nu_i\nu_j}(\omega) = H_i^*(\omega)|\nu(\omega)|^2 H_j(\omega) \tag{9.4}$$

and

$$G_{\nu_i\nu_i}(\omega) = H_i^*(\omega)|\nu(\omega)|^2 H_i(\omega) \tag{9.5}$$

into Equation (9.2) yields

$$\begin{aligned}1+\alpha_i(\omega) &= \frac{H_j^*(\omega)|\nu(\omega)|^2 H_k(\omega)\left(H_i^*(\omega)|\nu(\omega)|^2 H_i(\omega)+G_{n_i n_i}(\omega)\right)}{H_j^*(\omega)|\nu(\omega)|^2 H_i(\omega)H_i^*(\omega)|\nu(\omega)|^2 H_k(\omega)} \\ &= 1+\frac{G_{n_i n_i}(\omega)}{G_{\nu_i\nu_i}(\omega)}.\end{aligned} \tag{9.6}$$

The PSD $G_{x_i x_i}(\omega)$ can therefore be expressed as

$$G_{x_i x_i}(\omega) = G_{\nu_i\nu_i}(\omega)(1+\alpha_i(\omega)) \tag{9.7}$$

which is identical to the expression in Equation (4.18). Substituting Equation (9.2) into (9.7), an estimate for the combustion noise that propagates to microphone i can therefore be obtained using

$$\begin{aligned}\widehat{G}_{\nu_i\nu_i}(\omega) &= G_{x_i x_i}(\omega)\frac{\gamma_{x_j x_i}(\omega)\gamma_{x_i x_k}(\omega)}{\gamma_{x_j x_k}(\omega)} \\ &= \frac{G_{x_j x_i}(\omega)G_{x_i x_k}(\omega)}{G_{x_j x_k}(\omega)}.\end{aligned} \tag{9.8}$$

This small modification to the 3S derivation removes the modulus signs and maintains the phase information. Adding a second external microphone $i2$, an estimate for the part of the cross spectra between the two external microphones that is coherent with the in duct microphones

can be obtained using

$$\widehat{G}_{\nu_i\nu_{i2}}(\omega) = \frac{G_{x_jx_{i2}}(\omega)G_{x_ix_k}(\omega)}{G_{x_jx_k}(\omega)}, \tag{9.9}$$

as

$$\frac{G_{x_jx_{i2}}(\omega)G_{x_ix_k}(\omega)}{G_{x_jx_k}(\omega)} = \frac{H_j^*(\omega)|\nu(\omega)|^2H_{i2}(\omega)H_i^*(\omega)|\nu(\omega)|^2H_k(\omega)}{H_j^*(\omega)|\nu(\omega)|^2H_k(\omega)} = H_i^*(\omega)|\nu(\omega)|^2H_{i2}(\omega). \tag{9.10}$$

Therefore, a partially coherent cross-spectral matrix (PCCSM) can be obtained for an array of external microphones using Equation (9.9). This subtle change to the 3S Array method provides a powerful new tool for the measurement of combustion noise as well as source location methods in general. This new method will be called the 3S PCCSM method from here on.

Taking the case where there is an additional coherent noise source ψ measured in the hot nozzle and at the external array (the case that the 3S Array and 3S PCCSM methods were designed for), the PSD and CSD for the hot nozzle and external array are

$$G_{NN}(\omega) = H_N^*(\omega)|\nu(\omega)|^2H_N(\omega) + H_{N_\psi}^*(\omega)|\psi(\omega)|^2H_{N_\psi}(\omega) + G_{n_Nn_N}, \tag{9.11}$$

$$G_{FF}(\omega) = H_F^*(\omega)|\nu(\omega)|^2H_F(\omega) + H_{F_\psi}^*(\omega)|\psi(\omega)|^2H_{F_\psi}(\omega) + G_{n_Fn_F} \tag{9.12}$$

and

$$G_{FN}(\omega) = H_F^*(\omega)|\nu(\omega)|^2H_N(\omega) + H_{F_\psi}^*(\omega)|\psi(\omega)|^2H_{N_\psi}(\omega) \tag{9.13}$$

assuming that ψ is not coherent with any other noise source. As the additional noise source is not coherent with the combustor signal the cross spectra between the combustor sensor and the other sensors will not be affected. Therefore, the combustion noise estimate for this case using the 3S PCCSM method is

$$\begin{aligned}\widehat{G}_{\nu_F\nu_{F2}}(\omega) &= \frac{H_C^*(\omega)|\nu(\omega)|^2H_{F2}(\omega)\left(H_F^*(\omega)|\nu(\omega)|^2H_N(\omega) + H_{F_\psi}^*(\omega)|\psi(\omega)|^2H_{N_\psi}(\omega)\right)}{H_C^*(\omega)|\nu(\omega)|^2H_N(\omega)} \\ &= G_{\nu_F\nu_{F2}}(\omega) + \frac{H_{F2}(\omega)}{H_N(\omega)}G_{\psi_F\psi_N}(\omega).\end{aligned} \tag{9.14}$$

The estimate will therefore contain an amount of the unwanted noise produced by a source ψ but the contribution of which is dependent on the pressure-to-pressure transfer functions $H_N(\omega)$ and $H_F(\omega)$ which are dependent on the locations of the sensors and the environment the sound needs to propagate through. If $H_N(\omega) \gg H_F(\omega)$, the combustion noise estimate could be approximated as

$$\widehat{G}_{\nu_F\nu_{F2}}(\omega) \approx G_{\nu_F\nu_{F2}}(\omega). \tag{9.15}$$

For an outdoor measurement it is possible that $H_N(\omega) \gg H_F(\omega)$ but for indoor measurements inside a test cell, it is likely that $H_N(\omega) > H_F(\omega)$ but not by a large amount and so, the 3S Array method incorporates a focussed beamformer using delay-and-sum beamforming to reduce the contribution of unwanted noise signals to the combustion noise estimate obtained. Combustion noise is a low frequency phenomenon and at low frequencies, the focussed beamformer used in Chapter 6 was close to omnidirectional (as shown in Figure 6.4) and so, the level of unwanted noise was not being significantly reduced. For measurements taken inside a test cell, reflections due to the hard walls will result in unwanted noise arriving from the direction of the hot nozzle even though the source could be either in the bypass duct or due to jet noise. More advanced

frequency domain bemforming methods are therefore required to significantly reduce the contribution of unwanted noise to the combustion noise estimate which cannot be implemented when using the 3S Array method but can be applied to the PCCSM obtained using the 3S PCCSM method.

9.2 Verification of 3S PCCSM

To verify that the 3S PCCSM method performs as theory suggests, the 3S PCCSM method can be applied to the measurements of the short cowl engine that are included in Chapter 6. Figure 9.1 is a plot of the combustion noise estimates obtained using the 3S Array and 3S PCCSM methods where both methods use delay-and-sum beamforming. The estimates produced are

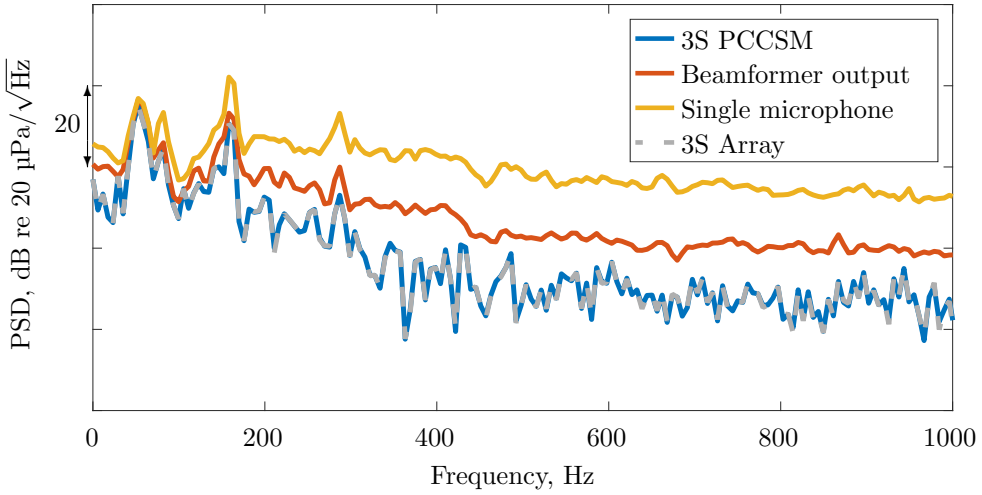

FIGURE 9.1: The 3S Array and 3S PCCSM using delay-and-sum beamforming methods applied to indoor measurements of a short cowl engine for an engine idle condition.

identical which is as expected given that the signal processing methods that have been applied are essentially the same but have just been implemented in different orders.

9.3 Application of the Inverse beamforming method to a PCCSM obtained using the 3S PCCSM method

Having established that the 3S Array and 3S PCCSM methods produce the same results when the same beamforming method is used, the use of more advanced beamforming methods can be investigated. One such method mentioned earlier in this chapter is the inverse beamforming technique.

The inverse beamforming technique relies on measuring or estimating the Green's functions between the array microphones and a source (or number of sources). The vector of microphone pressures can be defined as

$$\mathbf{p}(\omega) = \mathbf{G}(\omega)\mathbf{q}(\omega) + \mathbf{n}(\omega) \tag{9.16}$$

where $\mathbf{p}(\omega)$ is a vector of length M, $\mathbf{q}(\omega)$ is a vector of source strengths of length N, $\mathbf{G}(\omega)$ is an $M \times N$ matrix of Green's functions and $\mathbf{n}(\omega)$ is a vector of unwanted noise of length M. This is very similar to the pressure at microphones due to the direct and indirect combustion noise in Equation (8.7). Holland and Nelson [55] show that by applying an optimal set of filters, $\mathbf{w}_{\text{opt}}(\omega)$, to the measured spectral estimate, the source strengths can be obtained. They give the optimal set of filters as

$$\mathbf{w}^{\mathbf{H}}_{\text{opt}}(\omega) = (\alpha(\omega)\mathbf{I} + \mathbf{G}^{\mathbf{H}}(\omega)\mathbf{G}(\omega))^{-1}\mathbf{G}^{\mathbf{H}}(\omega) \tag{9.17}$$

where I is the identity matrix and $\alpha = G_{nn}(\omega)/G_{qq}(\omega)$ and so, when $G_{qq}(\omega) \gg G_{nn}(\omega)$

$$\mathbf{w}^{\mathbf{H}}_{\text{opt}}(\omega) \approx (\mathbf{G}^{\mathbf{H}}(\omega)\mathbf{G}(\omega))^{-1}\mathbf{G}^{\mathbf{H}}(\omega) = \mathbf{G}^{+}(\omega). \tag{9.18}$$

The CSM of the sources can therefore be obtained from

$$\mathbf{G}_{qq}(\omega) = \mathbf{w}^{\mathbf{H}}_{\text{opt}}(\omega)\mathbf{G}_{pp}(\omega)\mathbf{w}_{\text{opt}}(\omega) \tag{9.19}$$

assuming $G_{qq}(\omega) \gg G_{nn}(\omega)$. By applying the inverse beamforming technique to the PCCSM obtained from the 3S PCCSM method, the validity of the assumption that the sources are greater than the unwanted noise is improved as they are not likely to be coherent with the combustor probe. The inverse method is a least squares solution for a set of source strengths calculated from a set of pressure measurements. If Green's functions for sources in the bypass duct are defined as well as for the core nozzle, the method will be able to separate the two noise sources much more effectively than standard delay-and-sum beamforming. For indoor measurements inside test cells, the Green's function can be measured prior to testing. The measured Green's functions will include the reverberation inside the test cell. When the inverse method is applied, the reflections are effectively removed from the estimates of the source strengths which makes it possible to obtain a much more accurate source strength estimate than using standard beamforming.

A simulation to demonstrate the benefits of using the inverse method on the PCCSM obtained using 3S PCCSM is described here. The simulation consists of a spiral array of microphones with the same geometry of the one used in Chapter 6 with a spherically spreading combustion noise source located at $(0, 0, 0)$, the same position as the hot nozzle centre in that test. The combustion noise is limited to produce frequencies up to 500 Hz. A single monopole source located at $(-0.75, 1.5, 0)$ is used as a sound source being emitted from a bypass duct. Two unwanted noise sources are positioned on the 'jet axis' 0.5 m and 1 m downstream respectively. Two in-duct measured signals are simulated with the combustor signal containing only combustion noise while the nozzle signal contains both combustion noise and bypass noise. Figure 9.2 shows the source locations relative to the external microphone array. For simplicity, the simulation is free field with no fluid flow and the Green's functions that are used for the inverse method are exact. Figure 9.3 shows the combustion and bypass noise estimates when the inverse method is applied to the PCCSM and the CSM without any unwanted noise present. Both estimates of the combustion noise do obtain the correct level. The estimate of the bypass noise is correct for the estimate using the CSM. The estimate using the PCCSM underestimates the bypass by more than 100 dB and the shape of the spectra is not correct. This is because the bypass noise is only coherent between the nozzle and far field locations.

From Equation (9.14), the contribution of the bypass noise is dependent on the the pressure-to-pressure transfer functions $H_{F2}(\omega)$ and $H_N(\omega)$ which describe the changes in level and phase

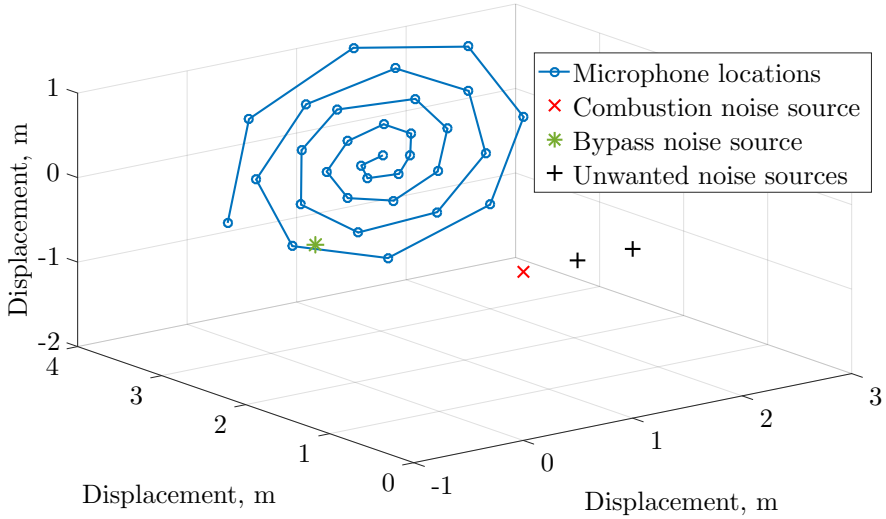

FIGURE 9.2: A diagram of the external microphone locations and source positions for the 3S PCCSM with inverse method validation simulation.

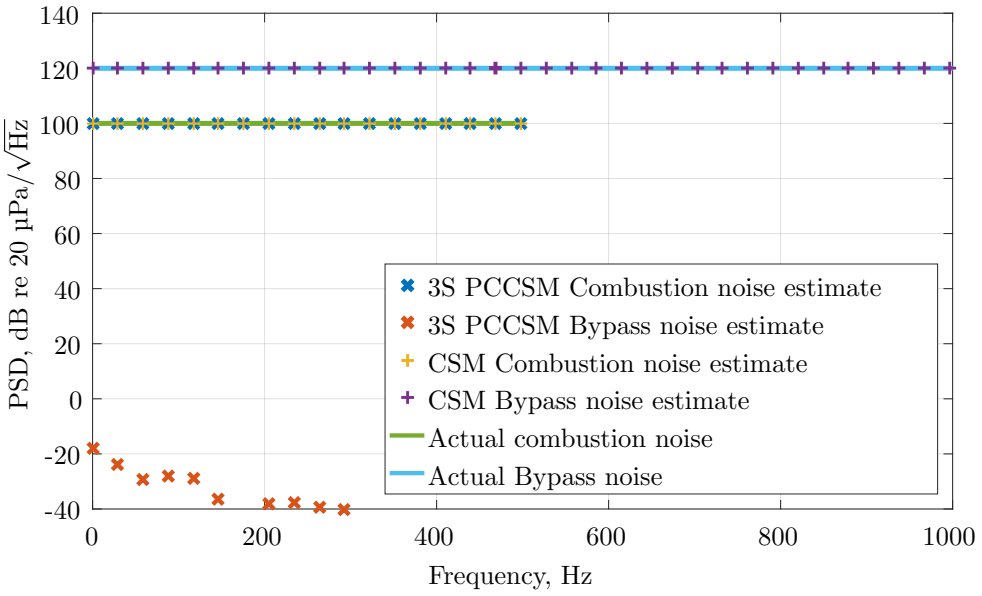

FIGURE 9.3: The estimates of simulated combustion noise and bypass noise using the inverse method on the PCCSM obtained using 3S PCCSM and the CSM of a spiral microphone array. There are no unwanted noise sources present.

of the measured combustion noise due to microphone position. This will result in significant phase and level variations of the bypass noise between the microphones in the array. When the inverse method is implemented, the delays and level differences between the microphones will not necessarily be representative of a single source at the location of the bypass noise which further reduces the level of the bypass noise. As the goal is to obtain an accurate estimate of the combustion noise, this is a benefit as the signal to unwanted noise ratio has been improved.

Figure 9.4 is a plot of the combustion and bypass noise estimates but with the unwanted noise sources now producing 110 dB each. The bypass estimates are very similar to those in Figure 9.3.

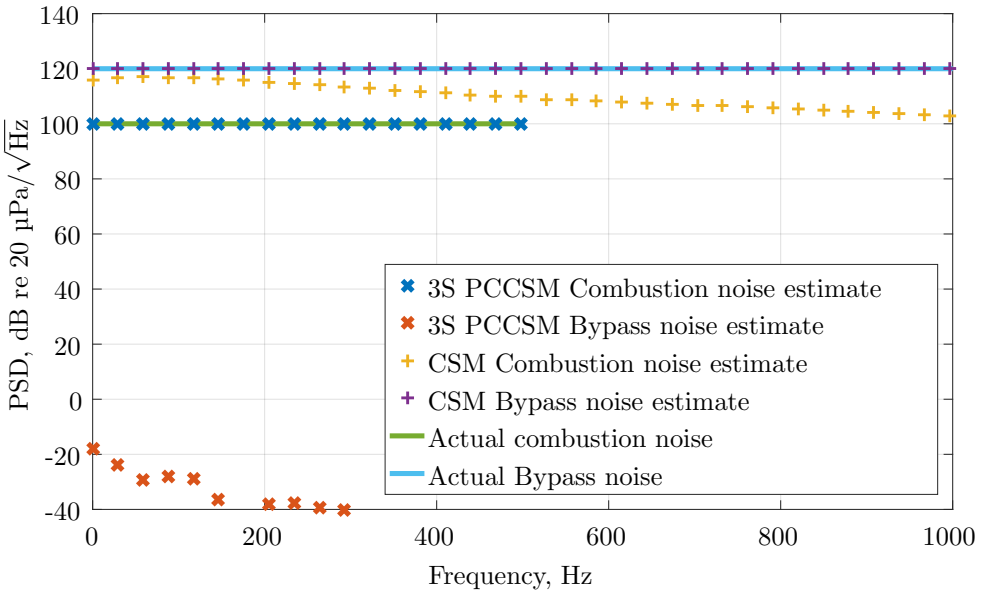

FIGURE 9.4: The estimates of simulated combustion noise and bypass noise using the inverse method on the PCCSM obtained using 3S PCCSM and the CSM of a spiral microphone array. Two unwanted noise sources are present producing 110 dB each.

The combustion noise estimate using the CSM is overestimating the combustion noise. This is due to the combustion noise source and the unwanted noise sources being close together and so, the inverse method is struggling to identify what is coming from the combustor. In addition to this the optimal filter can no longer be given by Equation (9.18) as the assumption that $G_{qq}(\omega) \gg G_{nn}(\omega)$ is no longer valid as the level of the combustion noise source is 10 dB lower. The combustion noise estimate using 3S PCCSM does produce an accurate estimate of the combustion noise level as the assumption $G_{qq}(\omega) \gg G_{nn}(\omega)$ is valid as the unwanted noise sources are not coherent between the 'in-duct' sensors and the external array and so, are not present in the PCCSM.

9.4 Comparison of the 3S Array method and the Inverse beamforming method applied to a PCCSM obtained using the 3S PCCSM method

The 3S Array method can be compared to the Inverse beamforming method applied to a PCCSM using the same simulation configuration as described in the previous section. Figure 9.5 is a plot of the Combustion and bypass noise estimates obtained using the 3S PCCSM method with the Inverse beamforming method and the combustion noise estimate obtained using the 3S Array method without any unwanted noise present. Also plotted are the actual source strengths of the combustion and bypass noise and the level of the focussed beamformer output (FBO), which is focussed on the combustion noise source, used as the external sensor in the 3S Array method. As in Figure 9.3, the combustion noise estimate using the 3S PCCSM with the Inverse beamforming method accurately estimates the actual combustion noise level. The combustion noise estimate

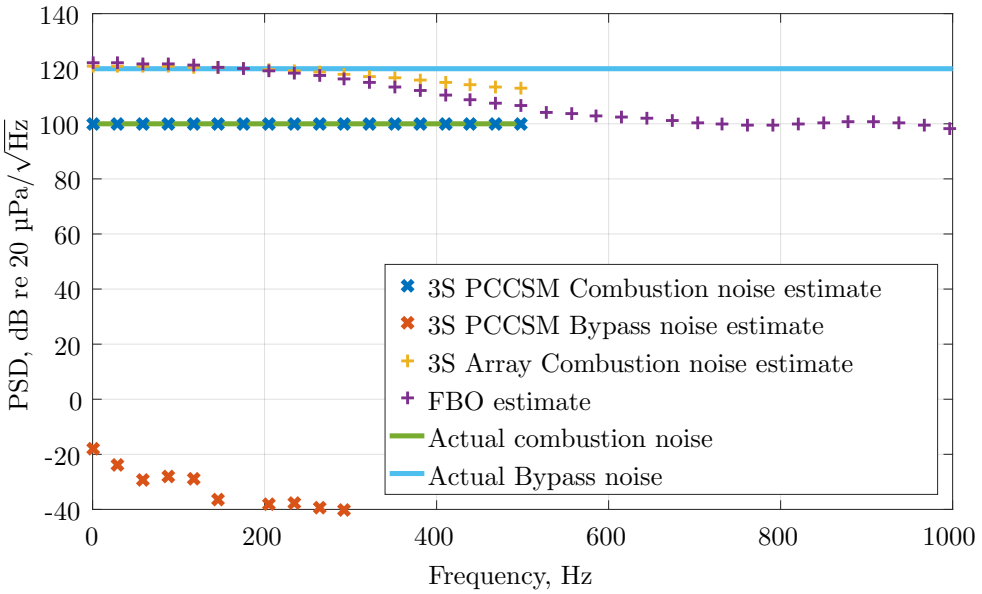

FIGURE 9.5: The estimates of simulated combustion noise and bypass noise using the inverse method on the PCCSM obtained using 3S PCCSM and the combustion noise estimate obtained using the 3S Array method.

obtained using the 3S Array method is significantly larger than the actual combustion noise level. This is due to the beamformer behaving close to omnidirectional at low frequencies and the bypass noise being coherent between the nozzle and FBO spectra. The combustion noise estimate is larger than the FBO estimate above 220 Hz. This is because the coherence between the combustor and nozzle spectra is very low due to the bypass noise on the nozzle signal but the coherence between the nozzle and FBO is large as both combustion and bypass noise are present in both signals. The presence of the bypass noise in the nozzle and FBO signals violates the assumption that only combustion noise is coherent between measurement locations resulting in an incorrect estimate. The application of the Inverse beamforming method to the PCCSM makes it possible to adequately separate the combustion and bypass noise which represents a significant improvement to the accuracy of the combustion noise estimate obtained.

9.5 Chapter Summary

A new coherence-based measurement method for measuring combustion noise was presented called 3S PCCSM. This method is similar to the 3S Array method except that it can be used to produce a PCCSM which can then have advanced source location methods applied to it to better isolate the combustion noise source from other noise sources. The 3S Array and 3S PCCSM methods were both applied to short cowl engine test data and both, when both use the same standard beamforming method, produced the same result. A simulation was used to show the benefit of using the inverse beamforming method on a PCCSM as opposed to a CSM for combustion noise measurements and it was shown that it is possible to maintain the validity of a key assumption in the inverse method by applying the method to a PCCSM instead of a CSM. The advantage of using the 3S PCCSM with the Inverse beamforming method over the 3S Array method was also demonstrated using the same simulation.

Chapter 10

Experimental validation: Configuration and calibration

The 3S method combined with the modal isolation method and the 3S method combined with the direct and indirect combustion noise separation method are applied to no-flow measurements in Chapter 11 and Chapter 12 respectively. This chapter will describe the equipment, configuration and calibration procedures for the validation experiments. There are significant similarities between the test configurations used for validating the modal isolation method and the separation method which is why both are explained in this chapter. Two separate tests were conducted, one in April 2018 to validate the modal isolation method and one in July 2017 to validate the separation method.

10.1 No-flow experiment configurations

Both validation tests used a 2.83 m long circular duct with one end closed and the other open and is made up of sections of the 'ISVR No-flow Rig'. The duct has a diameter of 0.4 m and is mounted on stands so that the centre of the duct is 1.712 m above the floor. The duct is constructed from stainless steel. The in-duct microphones are 1/4" electret microphones located at different positions for each of the experiments. Both experiments use a single Brüel & Kjær Type 4189 1/2" measurement microphone mounted on the floor of the chamber to measure the sound that propagates out of the open end of the duct. The in-duct sound sources are produced by compression drivers, the arrangement of which changes depending on the experiment. All of the microphones are connected to pre-amplifiers, which are connected to a single data acquisition system and are recorded synchronously. In the following two sections, the details of each of the two experiments are outlined.

10.1.1 Specific to the 3S method combined with the modal isolation method validation experiment

The 3S method combined with the modal isolation method validation experiment was conducted in April 2018 in the ISVR's Small Anechoic Chamber at the University of Southampton. A photograph of the experiment is shown in Figure 10.1. The microphones inside the duct are arranged in two circular arrays with the microphones equally spaced around the circumference of the duct. One array is placed 0.09 m from the open end of the duct and is referred to as the 'Nozzle' array, the other array is placed 0.66 m from the open end of the duct and is referred to as the 'Combustor' array as sketched in Figure 10.2. Combustion noise is simulated by driving four compression drivers with white noise. The compression drivers are evenly spaced around the circumference of the duct 0.3 m from the closed end. The signals produced by the compression drivers are uncorrelated with each other to simulate the unsteady heat release that produces the direct combustion noise.

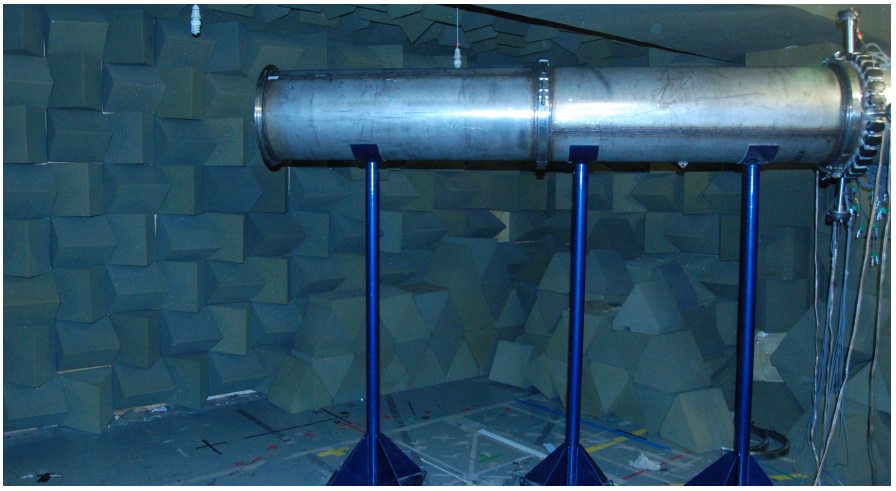

FIGURE 10.1: Photograph of the April 2018 the 3S method combined with the modal isolation method validation experiment.

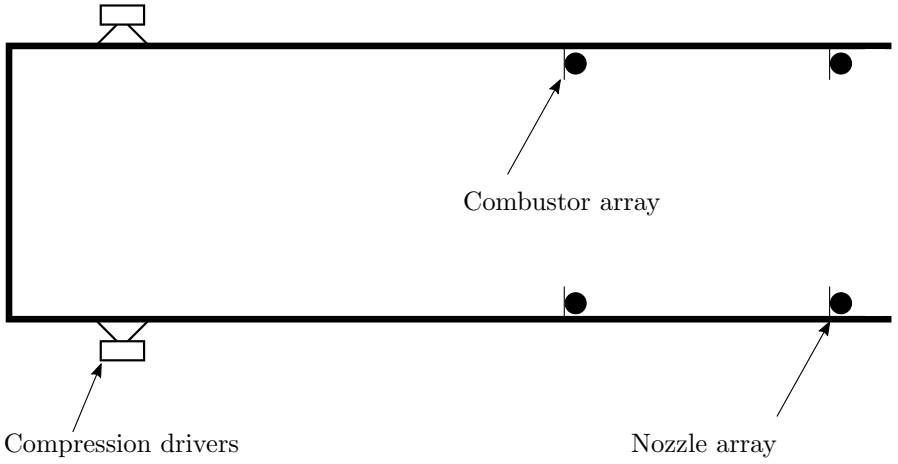

FIGURE 10.2: Configuration of in-duct microphones and compression drivers for the April 2018 3S method combined with the modal isolation method experiment.

10.1.2 Specific to the 3S method combined with the direct and indirect combustion noise separation method validation experiment

The 3S method combined with the direct and indirect combustion noise separation method validation experiment was conducted in July 2017 in the ISVR's Large Anechoic Chamber at the University of Southampton. A photograph of the experiment is shown in Figure 10.3 and a diagram of the layout of the equipment in the duct as shown in Figure 10.4. The 12 microphones

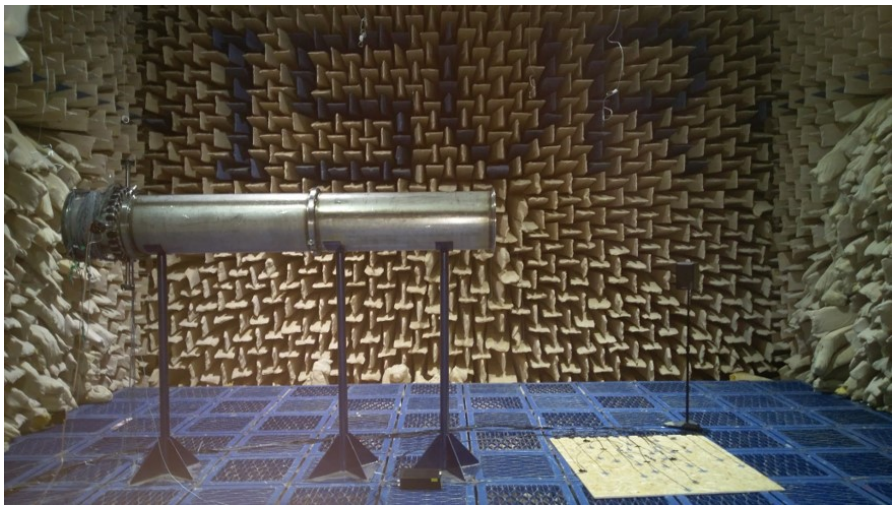

FIGURE 10.3: Photograph of the July 2017 3S method combined with the direct and indirect combustion noise separation method validation experiment.

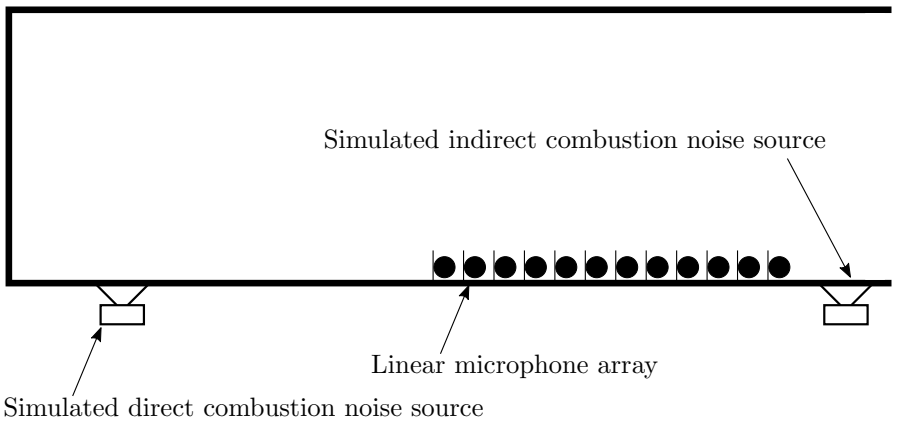

FIGURE 10.4: Configuration of in-duct microphones and compression drivers for the July 2017 3S method combined with the direct and indirect combustion noise separation method validation experiment.

inside the duct are arranged axially with a non-uniform separation in distance along the duct wall. The locations of the microphones relative to the open end of the duct are given in Table 10.1. The simulated direct noise is produced by a compression driver 0.3 m from the closed end of the duct. The simulated indirect combustion noise is produced by a compression driver in two configurations. In configuration 1 the compression driver producing the indirect noise is 0.07 m from the open end. In configuration 2 the compression driver is 0.22 m from the open end. Two combinations of signals were produced by the compression drivers and are listed in Table 10.2.

Microphone	Distance from open end, mm
1	1220
2	1170
3	1120
4	1070
5	1020
6	970
7	820
8	720
9	620
10	520
11	270
12	170

TABLE 10.1: The locations of the 12 microphones inside the duct for the 3S method combined with the direct and indirect combustion noise separation method validation experiment.

	Simulated direct noise signal	**Simulated indirect noise signal**
Combination 1	White noise with low pass filter cut-off frequency of 450 Hz	White noise with low pass filter cut-off frequency of 450 Hz
Combination 2	White noise with a high pass filter cut-on at 250 Hz and a low pass filter cut-off at 550 Hz	White noise with a low pass filter cut-off at 250 Hz

TABLE 10.2: Signals used in validation experiment of the 3S method combined with the direct and indirect combustion noise separation method.

10.2 Calibration

The external microphone was calibrated using a Brüel & Kjær 1 kHz Type 4230 calibrator. The electret microphones were calibrated using a tweeter with a coupler attached that has a mounting point for a measurement microphone and seals around the electret microphone against the duct wall. A photograph of the calibrator is shown in Figure 10.5 and a diagram showing the calibration of an electret microphone is shown in Figure 10.6. The electret microphone's

FIGURE 10.5: Photograph of the calibrator used to calibrate the in-duct electret microphones.

frequency response was calibrated using the measurement microphone as the calibrated reference signal. The tweeter produced white noise and the transfer function, $H_1(\omega)$ between the two microphones was calculated, which is defined as

$$H_1(\omega) = \frac{G_{xy}(\omega)}{G_{xx}(\omega)} \tag{10.1}$$

where $G_{xy}(\omega)$ is the PSD estimate of the measurement microphone signal and $G_{xy}(\omega)$ is the CSD estimate between the two signals. The electret microphone signal was then calibrated by multiplying the frequency response of the electret microphone signal by $\frac{1}{H_1(\omega)}$ prior to applying any of the processing methods presented in Chapters 7 and 8.

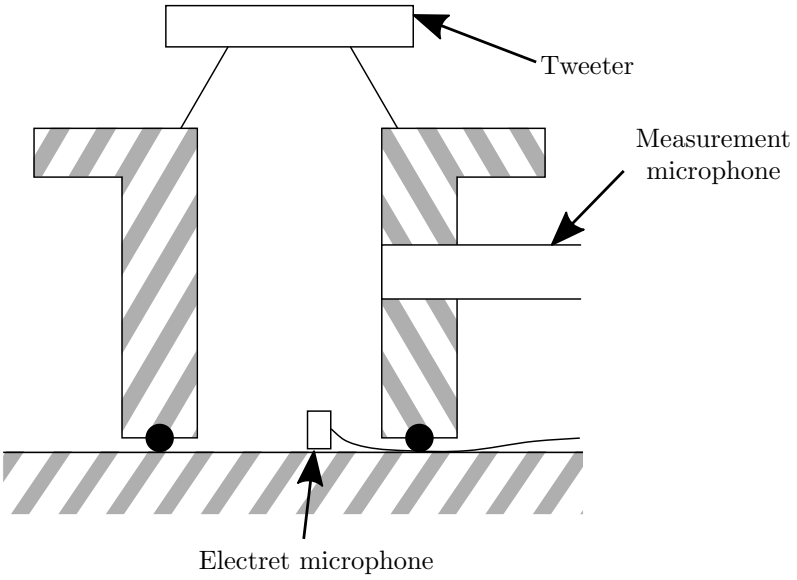

FIGURE 10.6: A diagram showing the calibration of an electret microphone.

Chapter 11

Experimental validation: Modal isolation method

This chapter focuses on validating the 3S Array method combined with the modal isolation method on the data acquired from controlled, no-flow laboratory measurements taken in the ISVR Small Anechoic Chamber. The experimental configuration is described in Chapter 10. A ring of compression drivers each producing incoherent white noise was used to simulate combustion noise. The 6-microphone circular-array furthest from the open end of the duct simulates an array in the combustor of a jet engine and will be referred to as the combustor array. The 6 microphone array closest to the open end of the duct simulates an array in the nozzle of a jet engine and will referred to as the nozzle array. A single measurement microphone mounted on the floor of the chamber is used instead of a microphone array as there are no unwanted noise sources and so, no need to reduce the contribution of sound arriving from directions other than from the open end of the duct.

11.1 Implementation of the modal isolation method

The modal isolation method described in Chapter 7 was applied to the measured pressure data from the two combustor and nozzle microphone arrays inside the duct. To examine the effectiveness of the modal isolation, the autospectra of each array and the coherence between the arrays can be used.

Figure 11.1 shows the autospectra of the estimates of the isolated modes obtained using the modal isolation method on the nozzle array pressure data when $m_{\text{iso}} = 0$ to 3 are plotted against ka where a is the radius of the duct. The black dashed lines indicate the estimated cut-on frequencies of the of azimuthal modes in the duct calculated from the duct radius. At frequencies below the modal cut-on frequency, each mode has a significantly lower level than above the modal cut-on frequency. This indicates that the modal isolation method is isolating individual modes and the level of isolation provided between the cut-on and cut-off modes is between 20 and 25 dB. Figure 11.2 is the autospectra of the estimates of the isolated modes obtained using the modal isolation method on the nozzle array pressure data when $m_{\text{iso}} = 0$ to

-3 plotted against ka. The isolation is equally effective for the negative modes with an isolation between the cut-on and cut-off modes of between 20 and 25 dB. It is important to note that, for a 6 microphone array, it is not possible to isolate modes 3 and -3 from each other due to spatial aliasing and therefore, $m_{\text{iso}} = 3$ and $m_{\text{iso}} = -3$ in these these plots are the same and contain contributions from both modes.

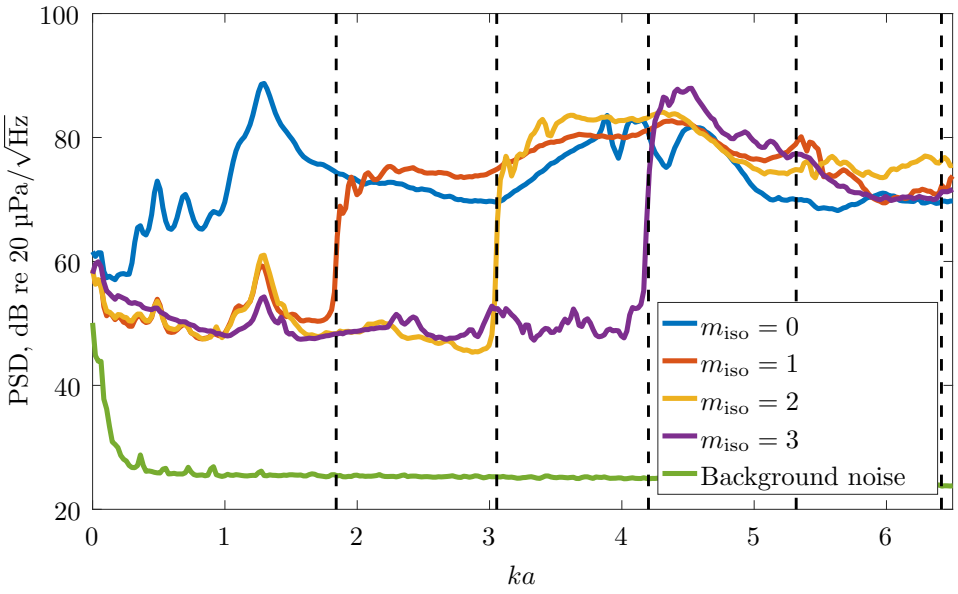

FIGURE 11.1: The autospectra of isolated modes 0 to 3 at the nozzle array location.

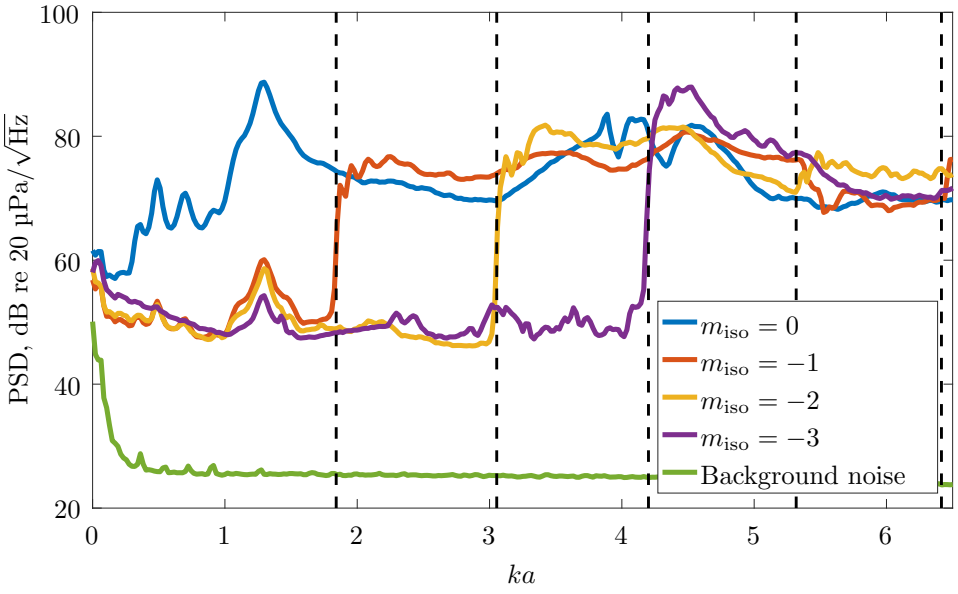

FIGURE 11.2: The autospectra of isolated modes 0 to -3 at the nozzle array location.

Furthering the application of the modal isolation method, the amplitude of the mode should be equal to the background noise when the mode that is being isolated is cut-off. As the level of the modes when cut-off is higher than the background noise, errors must be present in the measurement. These errors will be either due to the microphones not being positioned

perfectly or unwanted noise present in the measurement. As the experiment was conducted under controlled laboratory conditions, and no unwanted noise was added to the measurement, the error is most likely due to an error in the microphone positions, the effect of which is described in Chapter 7. A circular template was used to mark the locations of the microphones. The locations of the microphones in the nozzle array will have an error of $\Delta z \approx \pm 0.003$ m and $\Delta\theta \approx \pm 2°$. The error in the positions of the microphones in the combustor array are potentially much larger with $\Delta z \approx \pm 0.01$ m and $\Delta\theta \approx \pm 5°$ due to the array being positioned much further inside the duct which made marking the microphone locations and fixing the microphones to the inside of the duct difficult.

Figure 11.3 shows the autospectra of the estimates of the isolated modes obtained using the modal isolation method on the combustor array pressure data when $m_{\text{iso}} = 0$ to 3 are plotted against ka. The isolation is effective using the pressure signals from the combustor array but there is significant variation in the levels with frequency when compared to the isolated modes at the nozzle array. The oscillations in the level of each isolated mode decay with increasing frequency. The period of the oscillation in level decreases with a higher value of m_{iso}. This suggests that the issue could be due to an error in the microphone placement as a variation due to axial resonances would not vary with m_{iso}. As the variation of the estimated modal amplitude of mode m_{iso} is frequency dependent, it is likely that one or more microphones are not in the same plane as the rest of the array as an axial position error results in a frequency dependent phase error as can be seen in Equation (7.20).

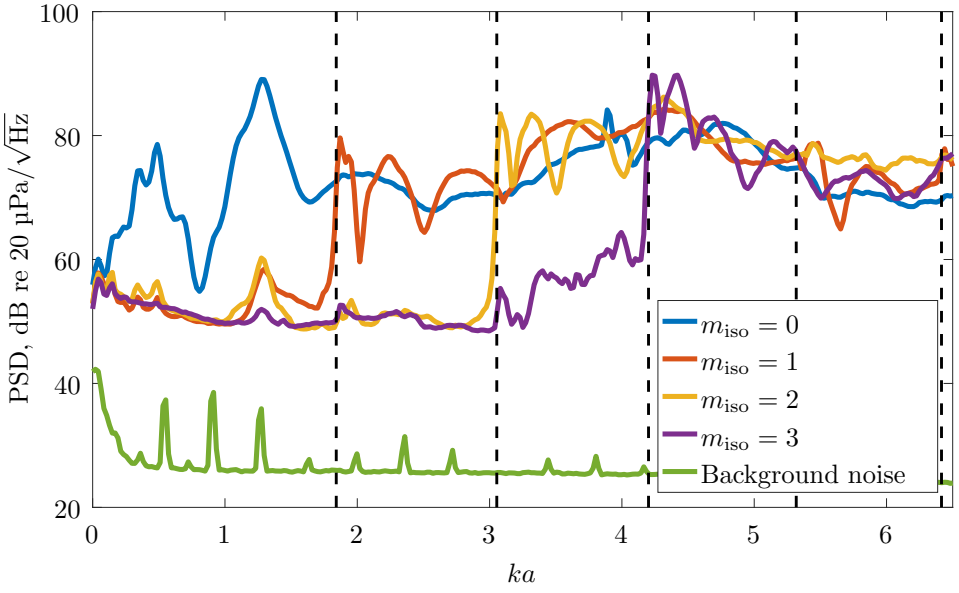

FIGURE 11.3: The autospectra of isolated modes 0 to 3 at the combustor array location.

The purpose of incorporating the modal isolation method into the 3S Array method is to maintain the validity of the single mode propagation assumption over a wider frequency range. When the cut-on modes are mutually incoherent, the coherence values between two microphones in the duct will be low as shown in Figure 7.2. The coherence between the estimated modal amplitudes obtained using the modal isolation method can be used as a measure of the effectiveness of the modal isolation method. The coherence between single microphones in each array and between the arrays with the plane wave mode isolated are shown in Figure 11.4. In addition to the

azimuthal mode cut-on frequencies marked as black dashed lines, the radial modes are also indicated with magenta dash-dot lines. The coherence is significantly improved by the modal isolation method compared to the single microphones with a coherence near 1 over most of the frequency range. There is a drop in the coherence at $ka = 0.78$ which is approximately 216 Hz. The resonance frequencies of a closed-open cylindrical duct can be calculated using

$$f_n = \frac{c_0(2n+1)}{4(L+\delta_L)} \tag{11.1}$$

where c_0 is the speed of sound, L is the length of the duct, δ_L is the end correction for an unflanged duct (which can be foung in Levine and Schwinger [60]) and n is an integer greater than or equal to zero. The frequency of the drop in coherence is close to $f_3 = 203$ Hz. A Disk of Rockwool 0.15 m thick was placed against the closed end of the duct to reduce the effect of the resonances of the duct on the measurement. Shortening the length of the duct by 0.15 m in Equation (11.1) results in $f_3 = 214$ Hz. The drop in coherence at 216 Hz is therefore likely to be due to a resonance in the duct. The coherence values in Figure 11.4 also drops at the cut-on frequency of the first radial mode as there is no circumferential pressure variation for this mode and so the method cannot separate it from the plane wave mode. When the modal isolation method is combined with the 3S Array method, the assumption that the signals only contain a single propagating mode is not valid if a higher ordar radial mode is propagating. However, even with the additional radial mode propagating, the coherence is still significantly higher than that of the single microphones.

Figure 11.5 is a plot of the coherence function between the two arrays when modes 0 to 3 are isolated. The coherence is high when each of the modes become cut-on with the exception of some oscillations similar to that seen in the combustor autospectra. Mode $m_{\text{iso}} = 3$ does not reach as high a level of coherence as the other modes when it becomes cut-on and this is due to having too few microphones to isolate the positive mode from the negative mode. The inability

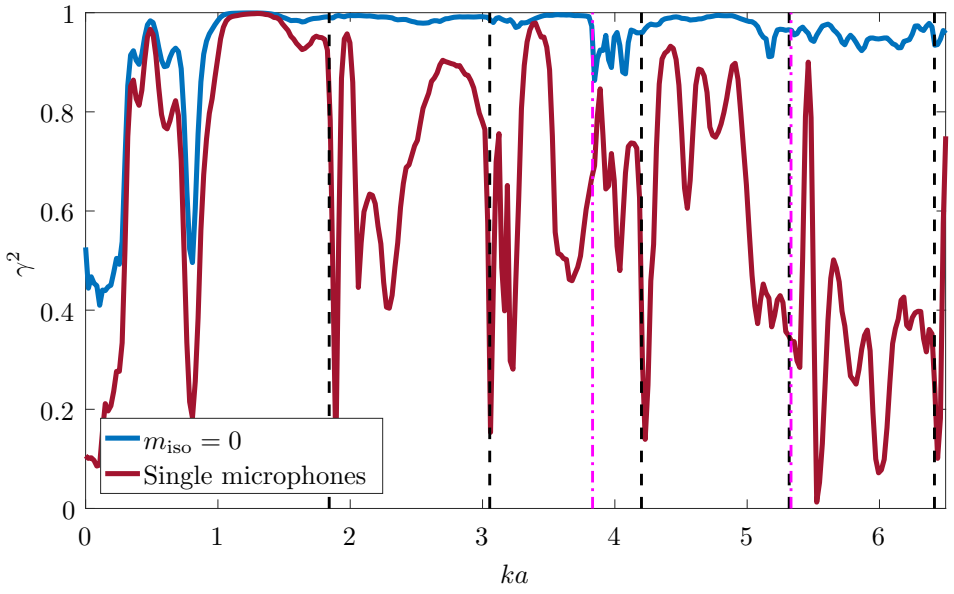

FIGURE 11.4: The coherence between single microphones in each array and the coherence between mode 0 isolated at each array.

to separate $m = 3$ and $m = -3$ results in a loss of coherence as the two modes are not coherent with each other. In the frequency range where only the plane wave mode is propagating, the coherence between the two arrays for the cut-off modes is high at certain frequencies.

The coherence function between two mode amplitude estimates obtained using the modal isolation method on the combustor and hot nozzle pressure signals when a single mode is isolated can be expressed as

$$\gamma^2_{CN(m_{\text{iso}})}(\omega) = \frac{|G_{CN(m_{\text{iso}})}(\omega)|^2}{G_{CC(m_{\text{iso}})}(\omega)G_{NN(m_{\text{iso}})}(\omega)} \tag{11.2}$$

where the cross-spectra is defined in Equation (7.32). The autospectra of the estimated modal amplitude using the combustor array can be defined similarly as

$$\begin{aligned} G_{CC(m_{\text{iso}})}(\omega) &= \lim_{T\to\infty}\frac{1}{T}E\left[(\hat{A}_{C(m_{\text{iso}})}(\hat{\theta}_i,\theta_i,\Delta z_i,\omega))^*(\hat{A}_{C(m_{\text{iso}})}(\hat{\theta}_i,\theta_i,\Delta z_i,\omega))\right] \\ &= |\delta_{C(m_{\text{iso}})}(\omega)|^2|H_{C(m_{\text{iso}})}(\omega)|^2|A_{(m_{\text{iso}})}(\omega)|^2 + \epsilon_{CC}(\omega) + G_{n_Cn_C}(\omega) \end{aligned} \tag{11.3}$$

where $\delta_{C(m_{\text{iso}})}(\omega)$ is as defined in Equation (7.30), $H_{C(m_{\text{iso}})}(\omega)$ is as defined in Equation (7.24), $G_{n_Cn_C}(\omega)$ is unwanted noise and

$$\begin{aligned} \epsilon_{CC}(\omega) = \sum_{m=-\infty}^{\infty} &\left(|\delta_{C(m)}(\omega)|^2|H_{C(m)}(\omega)|^2|A_{(m)}(\omega)|^2\right) \\ &- |\delta_{C(m_{\text{iso}})}(\omega)|^2|H_{C(m_{\text{iso}})}(\omega)|^2|A_{(m_{\text{iso}})}(\omega)|^2. \end{aligned} \tag{11.4}$$

A similar expression of the autospectra of the estimated mode amplitude obtained from the modal isolation method using the nozzle array pressure signals can be obtained in the same way. When a mode is isolated that is cut-off, $|A_{(m_{\text{iso}})}|$ is significantly smaller than the cut-on modes. Substituting equations (7.32), (11.3) and a similar expression to Equation (11.3) but for the estimate obtained using the nozzle array into Equation (11.2) when $|A_{(m_{\text{iso}})}|$ is cut off yields

$$\gamma^2_{x_Cx_N(m_{\text{iso}})}(\omega) \approx \frac{|\epsilon_{CN}(\omega)|^2}{(\epsilon_{CC}(\omega) + G_{n_Cn_C}(\omega))(\epsilon_{NN}(\omega) + G_{n_Nn_N}(\omega))}. \tag{11.5}$$

If the unwanted noise is small and the modal isolation is not perfect, the coherence will be larger than zero. If the isolation is working perfectly, the coherence will be zero if there is some unwanted noise present or 1 if there is not.

The highest levels of coherence in the cut-off modes is in the frequency range when only the plane wave mode is propagating. This is because, while the isolation method appears to work well, it is not perfect and so the isolated modes at both array locations contain small amounts of the plane wave mode. Since no other modes are propagating and the level in the cut-off region is above the background noise level, these small levels will be coherent with the external measurement. Above the cut-on frequency of mode 1, there are effectively two additional incoherent noise signals which effectively behave like unwanted noise and so the coherence is reduced. The coherence between the two arrays for $m_{\text{iso}} = 3$ peaks at 0.4 between the cut-on frequencies of mode 2 and mode 3. This is due to 'leakage' of other modes into $m_{\text{iso}} = 3$. Leakage from the other modes can clearly be seen in Figure 11.3 where the level of $m_{\text{iso}} = 3$ is significantly higher between the cut-on frequencies of modes 2 and 3 than it was between the cut-on frequencies of modes 1 and 2 and is also significantly higher than in for the nozzle array as shown in Figure 11.1.

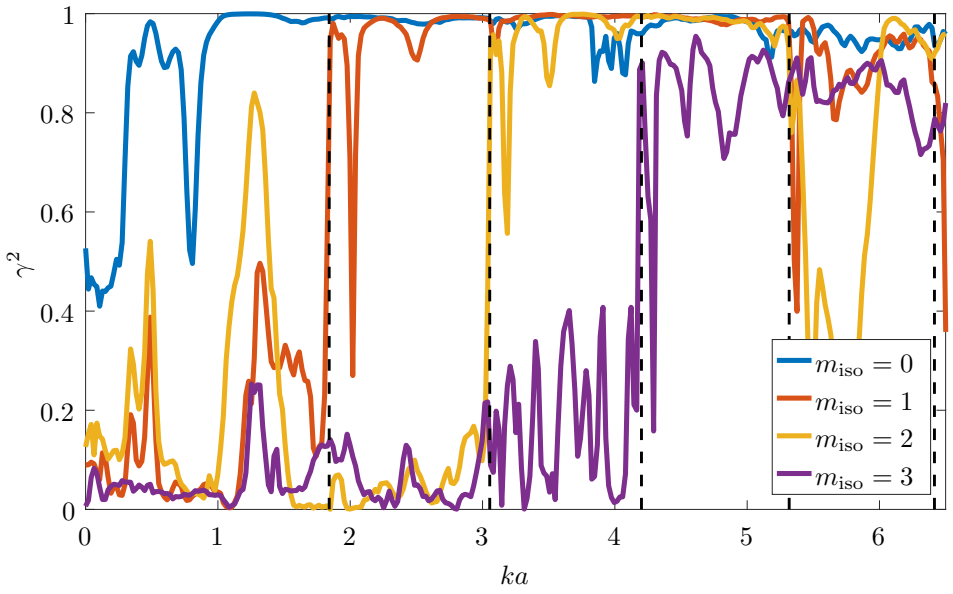

FIGURE 11.5: The coherence between modes 0 to 3 isolated at each array.

11.2 Validating the 3S Array method combined with the modal isolation method

The previous section indicated that the modal isolation method worked well under controlled laboratory conditions for a cylindrical duct with constant cross-section. This section combines the modal isolation method with the 3S Array method to validate the combined method.

Figure 11.6 is a plot of the contributions of the simulated combustion noise to the external microphone spectra which travel along the duct in modes -2 to 2. As modes 3 and -3 cannot be individually isolated due to the number of microphones used, the estimates have been plotted up to the value of ka where modes 3 and -3 become cut-on. The PSD of the external microphone signal is also plotted. As there are no noise sources other than the simulated combustion noise, the PSD of the external microphone signal represents the total simulated combustion noise propagating to the external microphone. The estimates using the 3S method combined with the modal isolation method are plotted from the value of ka where the mode that is being isolated becomes cut-on. In the frequency range where only the plane wave is propagating, the 3S method with mode 0 isolated is very similar to the total simulated combustion noise that propagates to the external microphone. It is expected that mode 0 should be equal to the PSD of the microphone signal as it is the only mode that is propagating in the duct in this frequency range. When mode 1 becomes cut-on, the level of the estimate with mode 0 isolated drops below the total level of combustion noise at the external microphone. The estimates using $m_{\text{iso}} = -1, 0, 1$ are similar in level from $ka = 1.9$ to 2.45. From $ka = 2.45$ to 2.7, the sound that propagates as mode -1 in the duct is dominant at the external microphone. Above $ka = 2.7$ the level of the mode -1 estimate drops below the levels of the other two propagating modes. When modes 2 and -2 begin to propagate in the duct, the estimates using $m_{\text{iso}} = -1$ and -2 become dominant at the external microphone with the estimate using the isolated plane wave mode having the next highest level. Above $ka = 3.55$, the estimates using $m_{\text{iso}} = -2$ and -1

drop rapidly with ka, while the levels of the other estimates increase and all have similar levels. From this plot it is clear that the 3S method combined with the mode isolation method is clearly able to isolate the contributions of individual modes propagating in the duct to the pressure measured at the external microphone.

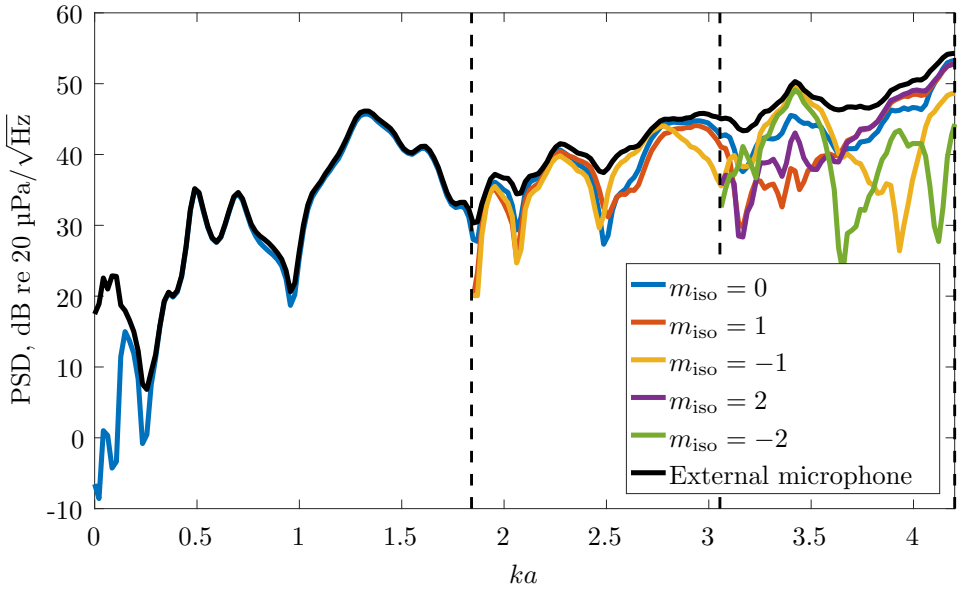

FIGURE 11.6: Estimates of the simulated combustion noise that propagates to the external array using the combined 3S array and modal isolation techniques for $m_{\text{iso}} = 0$ to 3. Also shown on the plot is the autospectra of the external microphone.

As stated in Chapter 7, the total combustion noise contribution to an external microphone spectrum can be expressed as

$$G_{\nu_F\nu_F}(\omega) = \sum_{m_{\text{iso}}=1-M/2}^{M/2-1} G_{\nu_F\nu_F(m_{\text{iso}})}(\omega) \tag{11.6}$$

where $G_{\nu_F\nu_F(m_{\text{iso}})}(\omega)$ is the contribution of the combustion noise that travels in mode m_{iso} to the external microphone spectrum. Figure 11.7 is a plot of the estimated total simulated combustion noise contribution to the external microphone spectrum using the 3S method combined with the modal isolation method as well as the estimate of the contribution obtained using the standard 3S method and the PSD of the external microphone signal. The total estimate using the 3S method combined with with the modal isolation method is identical to the standard 3S method in the frequency range where only the plane wave mode is propagating. For values of ka above the cut-on of mode 1, the sum of the estimates using the 3S method combined with the modal isolation method has a higher level than the standard 3S method. The estimate of the contribution of the combustion noise to the external microphone spectrum using the combined method does exceed the level of the external microphone spectrum at a number of values of ka by up to 1.5 dB. These overestimates in the total combustion noise level are likely due other modes 'leaking' into the modes that are being isolated due to inaccurate placement of the microphones inside the duct. The leaking of other modes into the estimate of the amplitude of mode m_{iso} results in the assumption of a single mode being inaccurate and so, the level of the individual isolated modes will be higher than the actual levels and so, the sum is an overestimate. While the sum

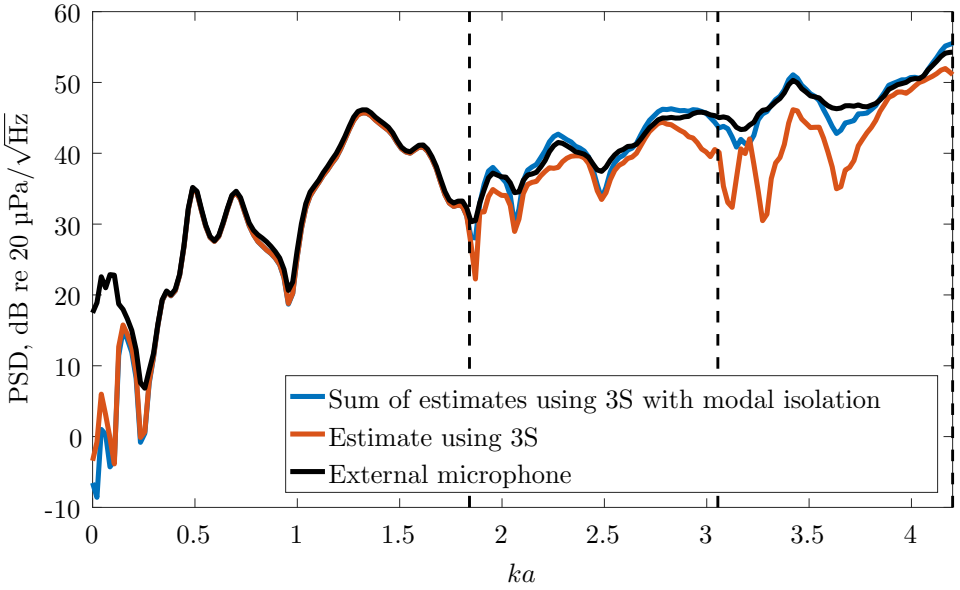

FIGURE 11.7: The sum of estimates of the simulated combustion noise measured at the external microphone which propagated inside the duct as modes -2 to 2 calculated using the 3S method combined with the modal isolation method. The black dashed lines indicate the values of ka where azimuthal modes become cut-on.

of estimates using the 3S method combined with the modal isolation method is subject to errors which result in a small overestimate, it is a significant improvement over the standard 3S method.

11.3 Chapter Summary

In this chapter, the 3S method combined with the modal isolation method that was presented in Chapter 7 was applied to controlled no-flow laboratory measurements. It was found that the modal isolation method using a 6 microphone circular array is capable of isolating azimuthal modes 0 to ± 2 as expected. The coherence between two measurement locations when multiple incoherent modes are propagating is significantly improved when individual modes are isolated. It was shown that combining the modal isolation method and the 3S method makes it possible to identify the contributions of specific in-duct modes to the external microphone level. An estimate of the total combustion noise that propagates to the external microphone can be obtained by taking the incoherent sum of the individual mode contributions. Comparing the estimates of the total combustion noise using the 3S method and the 3S method combined with the modal isolation method, the combined method provides a much more accurate estimate above the cut-on frequency of the first higher order azimuthal mode.

Chapter 12

Experimental validation: Direct and indirect combustion noise separation

A method to separate direct and indirect combustion noise is presented in Chapter 8. In this chapter, the separation method is applied to a no-flow laboratory experiment. The experimental configuration is described in Chapter 10. The 12 microphones arranged in a linear array along the axis of the duct are used for the separation. While 3 microphones were used to simulate the separation method in Chapter 8, the method can use any number of microphones as long as there are more than two. Using more microphones will reduce the effect of errors in a single transfer function on the separated combustion noise obtained from the method. A single compression driver is used as the simulated direct noise source positioned 0.3 m from the closed end of the duct. The indirect noise is simulated using another compression driver positioned 0.07 m from the open end of the duct for the first configuration and 0.22 m for the second. A diagram of the equipment inside the duct is shown as Figure 12.1 which is a reproduction Figure 10.4 and is included here for convenience.

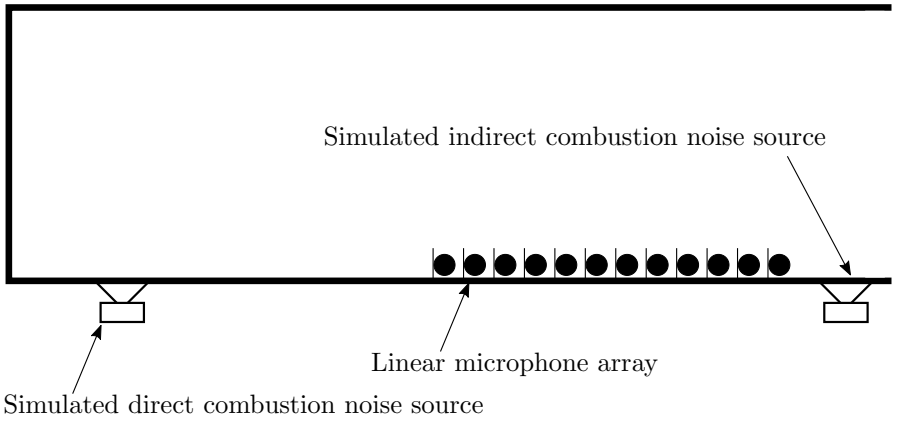

FIGURE 12.1: Configuration of in-duct microphones and compression drivers for the July 2017 the 3S method combined with the direct and indirect combustion noise separation method validation experiment.

The signals used for the direct and indirect noise consisted of filtered white noise generated in MATLAB. The signals produced by the two sources were incoherent with each other as, in reality, the source mechanisms for direct and indirect combustion noise are different. The signals used are listed in Table 12.1 (this is a reproduction of Table 10.2 for ease of reference).

	Simulated direct noise signal	**Simulated indirect noise signal**
Combination 1	White noise with low pass filter cut-off frequency of 450 Hz	White noise with low pass filter cut-off frequency of 450 Hz
Combination 2	White noise with a high pass filter cut-on at 250 Hz and a low pass filter cut-off at 550 Hz	White noise with a low pass filter cut-off at 250 Hz

TABLE 12.1: Signals used in validation experiment of the 3S method combined with the direct and indirect combustion noise separation method.

12.1 Implementing the separation method

To implement the separation method, estimated pressure to pressure transfer functions are required. Assuming plane wave propagation, the transfer function from the direct source to a microphone m can be written as

$$H_{(d,m)}(\omega) = \frac{e^{jk(d_m-d_d)} + R_c(\omega)e^{jk(d_d+d_m)} + R_o(\omega)e^{jk(2L-d_d-d_m)} + R_c(\omega)R_o(\omega)e^{jk(2L+d_d-d_m)}}{1 - R_c(\omega)R_o(\omega)e^{2jkL}} \tag{12.1}$$

where $R_c(\omega)$ is the reflection coefficient of the closed end of the duct, $R_o(\omega)$ is the reflection coefficient of the open end of the duct, d_d is the distance of the direct source from the closed end, d_m is the distance of the microphone m from the closed end, and L is the length of the duct. The Transfer function from the indirect source can be written as

$$H_{(i,m)}(\omega) = \frac{e^{jk(d_i-d_m)} + R_c(\omega)e^{jk(d_i+d_m)} + R_o(\omega)e^{jk(2L-d_i-d_m)} + R_c(\omega)R_o(\omega)e^{jk(2L+d_m-d_i)}}{1 - R_c(\omega)R_o(\omega)e^{2jkL}} \tag{12.2}$$

where d_i is the distance from the closed end to the indirect source. These transfer functions are of a more generalised form than those in Chapter 8 as they include the reflections from the open end. The transfer functions in Chapter 8 can be obtained by choosing $R_o(\omega)$ to be zero (making the open end anechoic).

The open end cannot be assumed to be anechoic in the case of the validation experiment. The reflection coefficient at the open end of an unflanged circular pipe for plane wave propagation is defined by Levine and Schwinger [60] as

$$R_o(\omega) = -|R(\omega)|e^{2jkl}, \tag{12.3}$$

where

$$|R(\omega)| = \exp\left\{-\frac{2ka}{\pi}\int_0^{ka}\frac{\arctan\left(-J_1(x)/N_1(x)\right)}{x[(ka)^2 - x^2]^{\frac{1}{2}}}\mathrm{d}x\right\}, \tag{12.4}$$

and

$$\frac{l}{a} = \frac{1}{\pi}\int_0^{ka} \frac{\log_e\{\pi J_1(x)[(J_1(x))^2 + (N_1(x))^2]^{\frac{1}{2}}\}}{x[(ka)^2 - x^2]^{\frac{1}{2}}}\mathrm{d}x + \frac{1}{\pi}\int_0^{\infty} \frac{\log_e[1/(2I_1(x)K_1(x))]}{x[x^2 + (ka)^2]^{\frac{1}{2}}}\mathrm{d}x. \quad (12.5)$$

In the above equations, a is the radius of the duct, J and N are the Bessel functions of the first and second kind respectively and I and K are modified Bessel functions of the first and second kind respectively. These equations were solved numerically using MATLAB to obtain the reflection coefficient for the open end of the duct.

The closed end of the duct poses more of a challenge as the sound absorption material used to dampen the axial resonances in the duct changed the reflection coefficient from that of a rigid wall to something more complex. When only the indirect source is producing sound, the open end of the duct can be treated as part of the source as none of the microphones detect the sound coming directly from the indirect source without this reflection. Therefore, any sound travelling towards the closed end can be treated as sound coming directly from the source while any sound travelling away from the closed end is equal to the sound that travelled towards it modified by the reflection coefficient of the closed end. Therefore, the reflection coefficient of the closed end can be calculated using

$$R_c(\omega) = \frac{B(\omega)}{A(\omega)} \quad (12.6)$$

where $A(\omega)$ and $B(\omega)$ represent the sound travelling towards and away from the closed end respectively. At a microphone m the pressure can be expressed as

$$P_m(\omega) = A(\omega) + B(\omega) \quad (12.7)$$

while the pressure at a microphone, n, further from the wall

$$P_n(\omega) = A(\omega)e^{-jkd_\Delta} + B(\omega)e^{jkd_\Delta} \quad (12.8)$$

where d_Δ is the displacement between the microphones. Rearranging the above equations yields

$$A(\omega) = \frac{P_n(\omega) - P_m(\omega)e^{jkd_\Delta}}{e^{-jkd_\Delta} - e^{jkd_\Delta}} \quad (12.9)$$

and

$$B(\omega) = P_m(\omega) - A(\omega). \quad (12.10)$$

The reflection coefficient was calculated using multiple pairs made up of all 12 microphones in configuration 1 and an average taken of $R_c(\omega)$.

All of the components required to perform the separation of the direct and indirect noise can be calculated/estimated as described above. However, when the separation was performed using the reflection coefficients above, the separation method did not produce the expected results. One of the reasons for this are the fiberglass wedges placed inside the duct between the direct source location and the microphones to reduce the effect of axial resonances. A diagram indicating the positions of the sound absorption material relative to the source and microphone positions is shown in Figure 12.2. The calculated reflection coefficient for the closed end takes the wedges into account but the sound from the direct source that is not reflected off of the closed end does

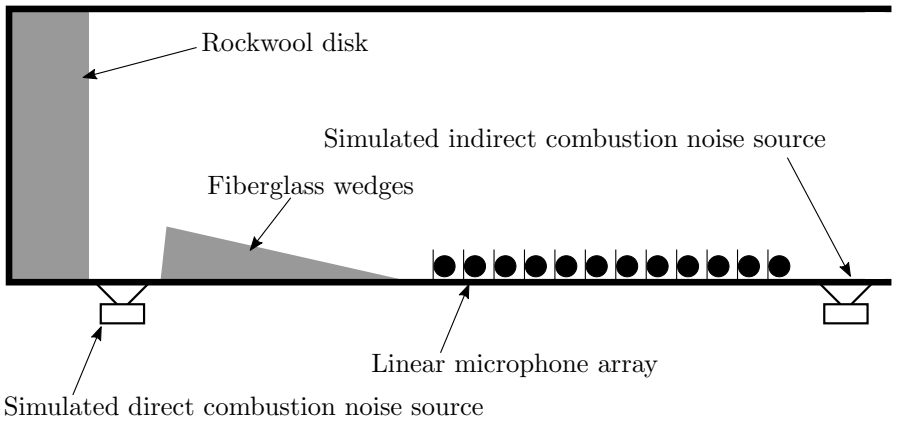

FIGURE 12.2: Configuration of in-duct microphones and compression drivers and positions of sound absorption material for the July 2017 3S with direct and indirect combustion noise separation validation experiment.

not take this into account. The direct noise source transfer function can be altered to be

$$H_{(d,m)}(\omega) =$$

$$\frac{G_a e^{jk(d_m-d_d)} + R_c(\omega)e^{jk(d_d+d_m)} + G_a R_o(\omega)(\omega)e^{jk(2L-d_d-d_m)} + R_c(\omega)R_o(\omega)e^{jk(2L+d_d-d_m)}}{1 - R_c(\omega)R_o(\omega)e^{2jkL}} \tag{12.11}$$

where G_a is the attenuation caused by the fiberglass wedges. After trying several values, it was found that $G_a = 0.8$ provided the most effective separation of the signals.

The other reason for the separation not performing correctly is that the open end reflection coefficient is not correct for the indirect source. This is due to the proximity of the indirect source to the open end of the duct resulting in the plane wave assumption for the open end reflection coefficient not being valid. To take these effects into account, the same method that was used to calculate $R_c(\omega)$ can be used to calculated $R_o(\omega)$ for the indirect source (which we will now call $R_{o,i}(\omega)$ to distinguish it from $R_o(\omega)$). This is possible as in configuration 2, there are two microphones between the indirect source and the open end of the duct. The two transfer functions that are used to produce the results in the rest of the chapter are

$$H_{(d,m)}(\omega) =$$

$$\frac{G_a e^{jk(d_m-d_d)} + R_c(\omega)e^{jk(d_d+d_m)} + G_a R_o(\omega)(\omega)e^{jk(2L-d_d-d_m)} + R_c(\omega)R_o(\omega)e^{jk(2L+d_d-d_m)}}{1 - R_c(\omega)R_o(\omega)e^{2jkL}} \tag{12.12}$$

and

$$H_{(i,m)}(\omega) = \frac{e^{jk(d_i-d_m)} + R_c(\omega)e^{jk(d_i+d_m)} + R_{o,i}(\omega)e^{jk(2L-d_i-d_m)} + R_c(\omega)R_{o,i}(\omega)e^{jk(2L+d_m-d_i)}}{1 - R_c(\omega)R_{o,i}(\omega)e^{2jkL}}. \tag{12.13}$$

12.1.1 Test Configuration 1

12.1.1.1 Signal combination 1

Applying the separation method to test configuration 1, signal combination 1 yields the results shown in Figure 12.3. The solid lines are the results from the separation method. The blue and red dashed lines are the pressure at microphone 1 when only the direct noise and only the indirect noise sources are active respectively. If the separation is successful the separated signals should be similar to the microphone 1 pressure signals. It is clear that the separated signals are generally similar to the microphone 1 signals but are also similar to each other. There are differences at some frequencies of up to 10 dB between the separated spectra and the microphone 1 spectra which is due to axial resonances in the duct affecting the level of the microphone 1 spectra and the effectiveness of the separation method. To obtain a better understanding of how

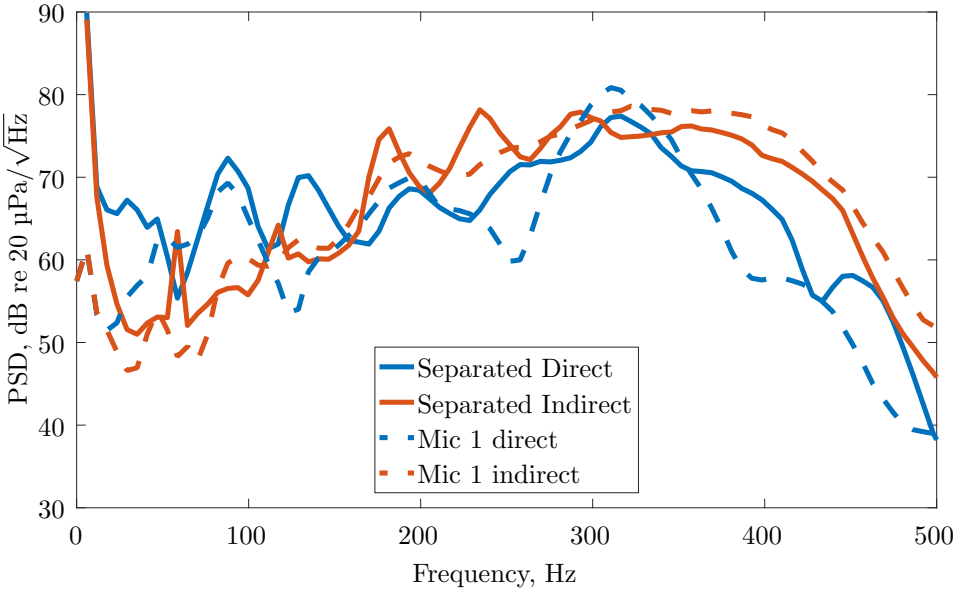

FIGURE 12.3: The separated simulated direct and indirect signals for test configuration 1: signal combination 1.

effective the separation has been, the coherence between the separated signals can be examined. If the separation has been effective the coherence between the separated signals should be very low as the signals the sources were driven with are mutually incoherent. Figure 12.4 shows the coherence between the separated signals. From the coherence it is clear that the separation has not been completely successful. Between 250 Hz and 370 Hz the coherence is low which suggests that the separation was successful for these frequencies. At these frequencies, the separated signals in Figure 12.3 are reasonably similar to the microphone 1 signals (there is some variation which could be due to axial modes affecting the microphone 1 signals). The coherence increases above 370 Hz (apart from a drop in coherence at 420 Hz) and peaks below but close to the cut on frequency of the first circumferential mode. Below 220 Hz there are regular peaks in the coherence separated by approximately 60 Hz which is equal to the interval between axial modes in the 2.83 m duct. Between the peaks, the coherence is low and the separated signals are similar to the microphone 1 signals.

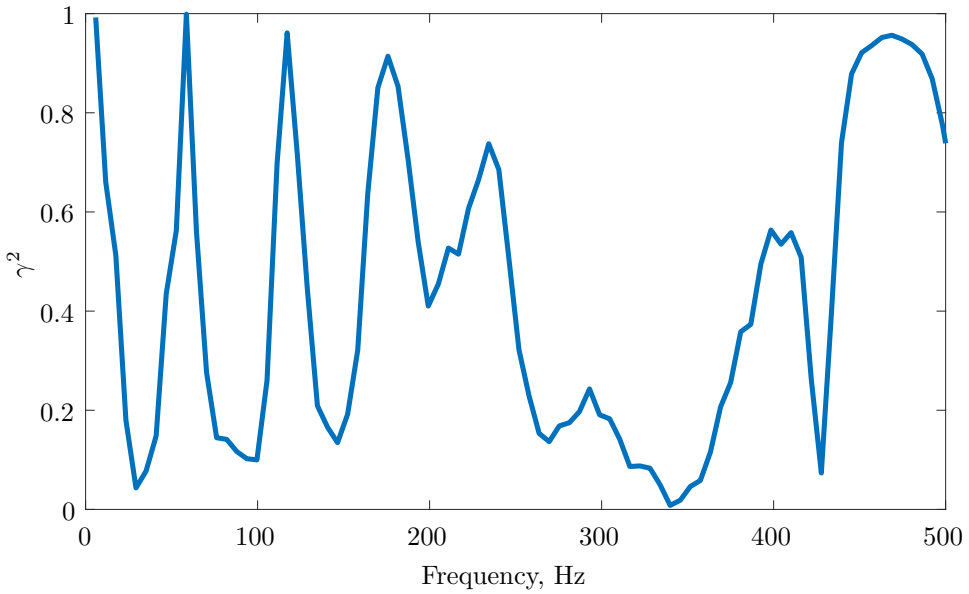

FIGURE 12.4: The coherence between separated simulated direct and indirect signals for test configuration 1: signal combination 1.

12.1.1.2 Signal combination 2

Applying the separation method to the second combination of signals results in the signals displayed in Figure 12.5 and the coherence between the separated signals is shown as Figure 12.6. From the coherence between the separated signals, it is clear that the separation is not effective below 240 Hz as the separated signals are highly coherent. Above 240 Hz however, the coherence is low up to approximately 430 Hz. In this region the separated signals in Figure 12.5 are close matches to the target signals and the separation is effective. Above 430 Hz, the coherence between the separated signals is high, suggesting the separation method is no longer effective. Both the PSD estimates of the direct and indirect noise measured by microphone 1 are 40 dB in the frequency ranges where the direct and indirect sources are not producing sound respectively. 40 dB is the noise floor of the microphones. The fact that the separation method is successful when only the direct combustion noise is present and is not successful when only the indirect noise is present suggests that the transfer functions for the indirect noise do not describe the propagation from the indirect source to the microphones correctly.

12.1.2 Test Configuration 2

For test configuration 2, only 10 of the 12 in-duct microphones were used as 2 of the microphones were between the indirect noise source and the open end of the duct.

12.1.2.1 Signal combination 1

Figure 12.7 shows the separated signals for test configuration 2, signal combination 1 and Figure 12.8 shows the coherence between the separated signals.

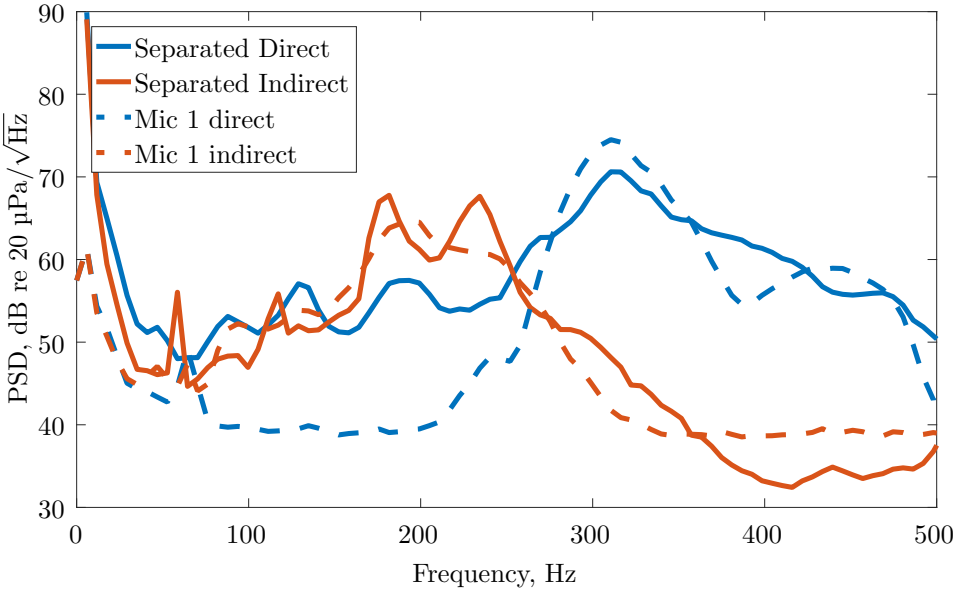

FIGURE 12.5: The separated simulated direct and indirect signals for test configuration 1: signal combination 2.

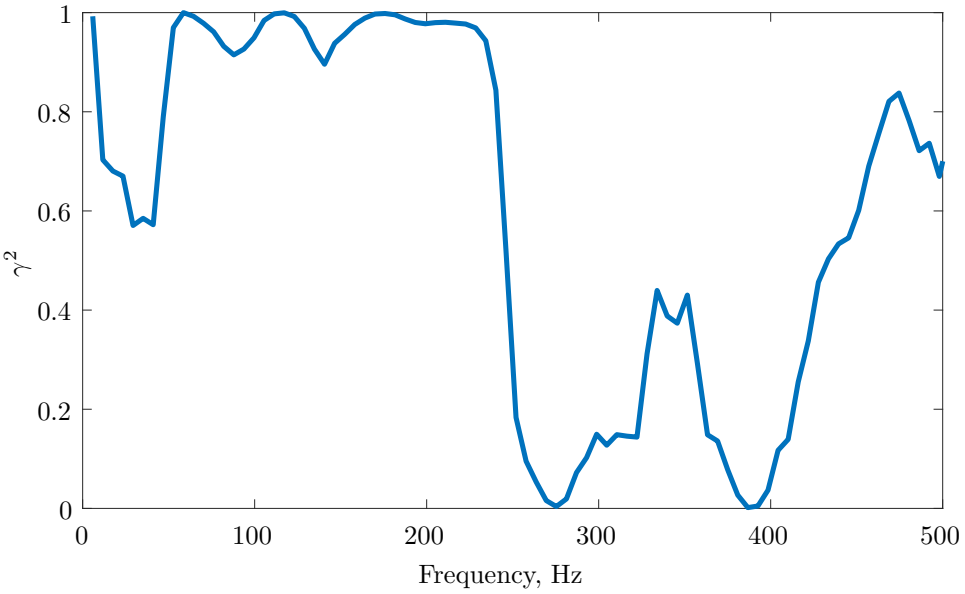

FIGURE 12.6: The coherence between separated simulated direct and indirect signals for test configuration 1: signal combination 2.

The separated noise signals are similar to the microphone 1 signals as they were for test configuration 1, combination 1. The coherence for the separated signals is higher below 200 Hz between the peaks in coherence than it was for configuration 1. This could be due to the reduction in number of microphones or it could be due to the change in the indirect source location.

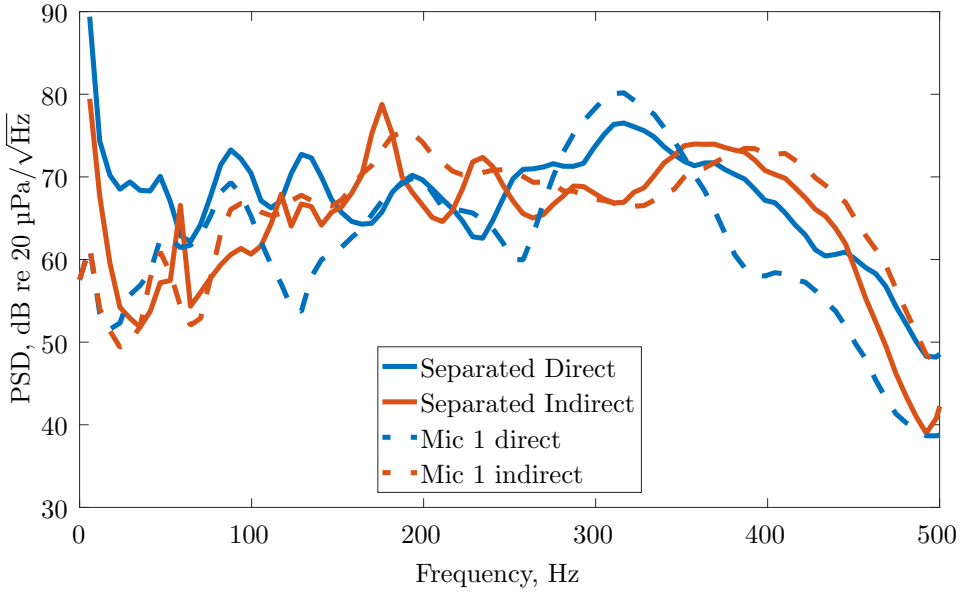

FIGURE 12.7: The separated simulated direct and indirect signals for test configuration 2: signal combination 1.

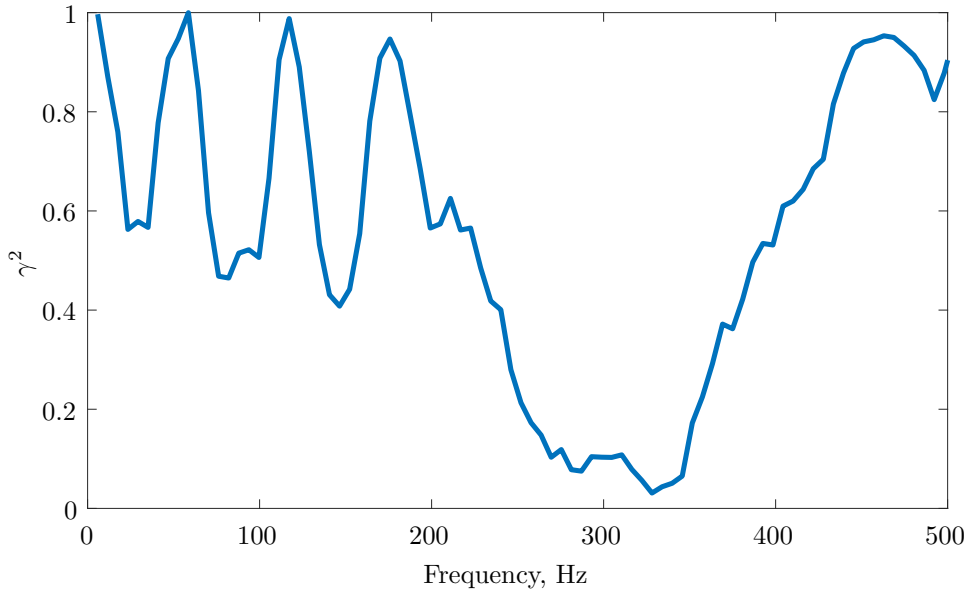

FIGURE 12.8: The coherence between separated simulated direct and indirect signals for test configuration 2: signal combination 1.

12.1.2.2 Signal combination 2

Figure 12.9 shows the separated signals for test configuration 2, signal combination 2 and Figure 12.10 shows the coherence between the separated signals. The separation is again similar to that of test configuration 1, combination 2 except for some stronger peaks in the indirect signal below 200 Hz. The coherence is also similar except for the 'hump' in the coherence between 280 Hz and 400 Hz is larger for the configuration 2 signals.

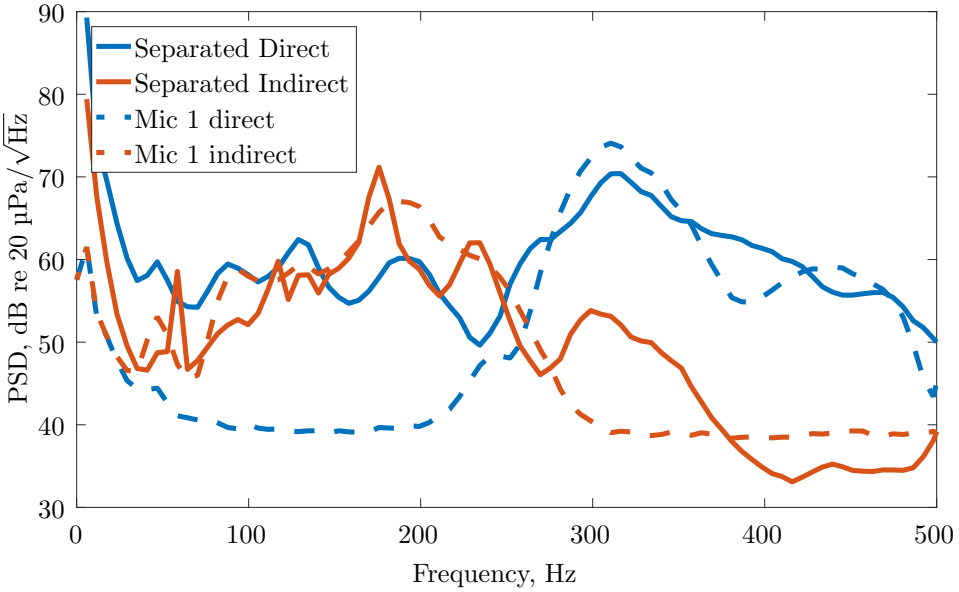

FIGURE 12.9: The separated simulated direct and indirect signals for test configuration 2: signal combination 2.

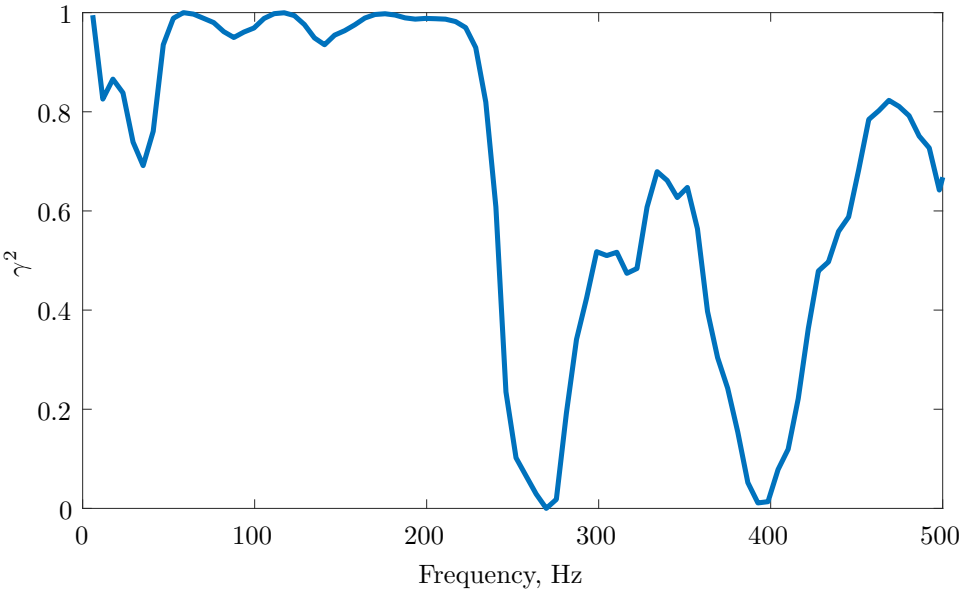

FIGURE 12.10: The coherence between separated simulated direct and indirect signals for test configuration 2: signal combination 2.

12.2 Regularisation

The solution to inverse problems is often unreliable due to poor conditioning of the matrix that is to be inverted. Conditioning refers to how sensitive the result is to small changes in the matrix to be inverted. A poorly conditioned matrix will be very sensitive to small changes. The condition of the matrix can be determined by calculating the condition number of the matrix. This can be calculated by dividing the largest singular value of the matrix by the smallest. A

large condition number indicates an ill-conditioned matrix whereas a condition number close to 1 indicates a well conditioned matrix.

Using MATLAB's 'cond' function the condition number of the Transfer function matrix for configuration 2 was calculated and is displayed as Figure 12.11. It is clear that the matrix is poorly conditioned at a number of frequencies which are approximately multiples of 60 Hz which are also the frequencies where the coherence peaks in Figures 12.4 and 12.8. It makes sense that the matrix will be poorly conditioned at these frequencies as the denominator of the transfer functions will $\rightarrow 0$.

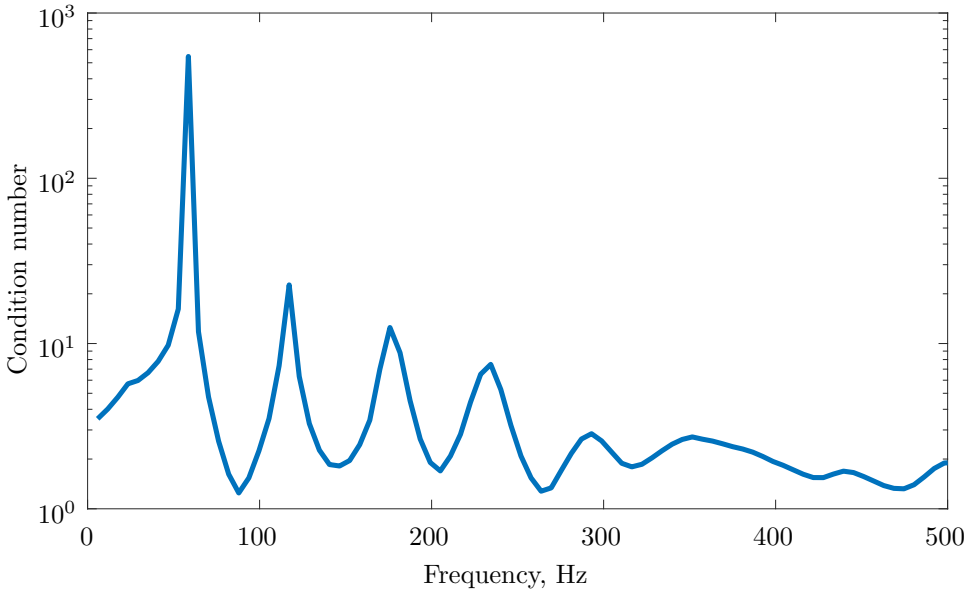

FIGURE 12.11: Condition number of the configuration 2 transfer function matrix.

To improve the conditioning of a matrix, a regularisation method can be applied. One type of regularisation is a method developed by Tikhonov and Arsenin and is widely used for ill-conditioned problems such as the separation of multiple acoustic sources using microphone arrays [61]. When separating the direct and indirect combustion noise using the method described in Chapter 8, the expression

$$||\mathbf{H}(\omega)\mathbf{p}(\omega) - \mathbf{s}(\omega)||^2 \tag{12.14}$$

is minimised. When Tikhonov regularisation is applied, the expression that is to be minimised becomes

$$||\mathbf{H}(\omega)\mathbf{p}(\omega) - \mathbf{s}(\omega)||^2 + \lambda_r^2||\mathbf{p}(\omega)|| \tag{12.15}$$

where λ_r^2 is a regularisation parameter. The addition of the regularisation parameter makes the system less sensitive to small changes and 'smooths' the solutions.

To implement Tikhonov regularisation, the regularisation parameter needs to be added to the diagonal of the matrix $\mathbf{H^H}(\omega)\mathbf{H}(\omega)$. The pseudo inverse therefore becomes

$$\mathbf{H}^{-1}(\omega) = (\mathbf{H^H}(\omega)\mathbf{H}(\omega) + \lambda_r^2\mathbf{I})^{-1}\mathbf{H^H}(\omega) \tag{12.16}$$

where **I** is the identity matrix. The regularisation parameter needs to be chosen to improve the condition number of the transfer function matrix when the conditioning is poor. The value of the regularisation parameter is important as too small a value will not improve the conditioning significantly while too large a value will result in the separated signals being 'smoothed' together until they are the same and the separation will not be successful. Figure 12.11 shows that the conditioning of the transfer function matrix is generally good except at frequencies with wavelengths that are multiples of $2L$.

A good measure of the amount of regularisation to apply is the coherence function between the separated signals as an increase in coherence indicates the regularisation parameter is too large while no reduction in coherence indicates the regularisation is not having a beneficial effect. To highlight the effect regularisation has on the separated signals, Tikhonov regularisation was applied to configuration 2, signal combination 2. Figure 12.12 is the PSD of and coherence between the separated signals and the condition number of the transfer function matrix for multiple values of regularisation parameter. The regularisation parameter has been calculated for each frequency as

$$\lambda_r(\omega) = 10^{\alpha} \log_{10}(\text{condition number}(\omega)) \tag{12.17}$$

where α takes values from -1 to 1 in steps of 0.5 which results in the frequencies with poorer conditioning having more regularisation applied. The regularisation parameter was defined in this way to display the effect of a wide range of regularisation values. It is clear that for negative values of α there is only a small reduction in coherence between the separated signals and condition number of the transfer function matrix below 70 Hz. The changes in the PSD of the separated signals is also minimal for negative values of α with the only significant change being a strong reduction in level at 60 Hz. For $\alpha = 0$ there is a reduction in the level of the separated direct noise below 250 Hz, mainly at the frequencies with a high condition number, but there is also a reduction in the indirect noise over the same frequency range which is not desired. The coherence between the separated signals is reduced by a small amount below 250 Hz but is increased between 250 Hz and 400 Hz. This increase in coherence will result in additional error in the estimates of direct and indirect noise which propagates to the external microphone obtained using the 3S with separation method. For positive values of α, there is a significant increase in the coherence between the separated signals between 250 Hz and 500 Hz. Over the same frequency range there is a reduction in the level of the separated direct noise and an increase in the separated indirect noise. Below 250 Hz both the separated direct and indirect noise reduce in level while the coherence between the signals does increase at some frequencies. The condition number reduces to almost 1 across the frequency range but this does not result in better separation as it reduces the variation between the separated signals and effectively blends them together. While at some frequencies small amounts of regularisation have had limited beneficial effects, for most of the frequency range regularisation has had no effect for small values of λ_r and detrimental effect for larger values. This is due to the transfer function matrix being well conditioned over most of the frequency range. Therefore, regularisation is not useful for this inverse problem.

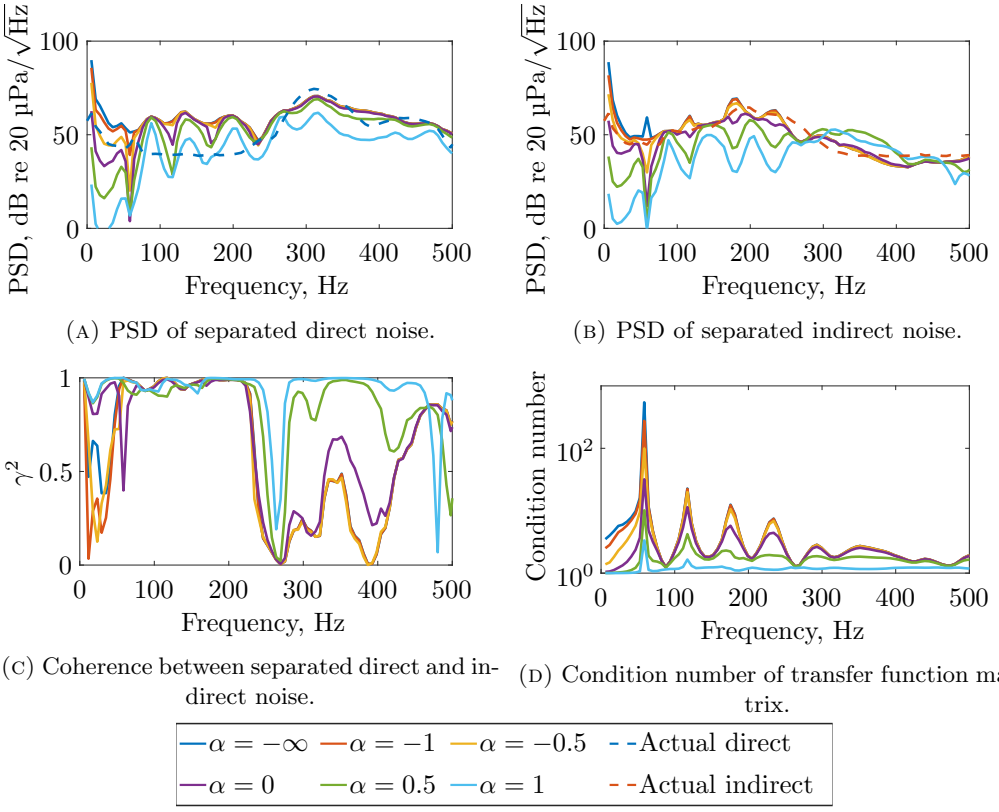

(A) PSD of separated direct noise.

(B) PSD of separated indirect noise.

(C) Coherence between separated direct and indirect noise.

(D) Condition number of transfer function matrix.

FIGURE 12.12: The PSD and coherence between the separated direct and indirect noise and the condition number of the transfer function matrix for different amounts of regularisation. The regularisation is given by $\lambda_r(\omega) = 10^{\alpha} \log_{10}(\text{condition number}(\omega))$ and the actual direct and indirect noise was measured at the microphone 1.61 m from the closed end of the duct.

12.3 Plane wave model of experiment

A simple, plane wave model of the experiment was used to try and explain why the separation was not performing well over the entire frequency range where only plane waves propagate. A diagram of the model used is displayed as Figure 12.13. The plane wave sources representing the direct and indirect noise sources are in the same locations as in configuration 1. The 3 microphones are in the same locations as microphones 1-3 in the experiment. The direct and indirect source signals are incoherent white noise. The coherence between the separated signals is 0 when the separation is successful (as in the experiment). For the separation to be successful, the transfer functions need to accurately describe the propagation of the sound in the duct. This simple model can be used to identify how accurate the microphone and source locations used in the transfer functions need to be. The pressure signals at each microphone will be created with the transfer functions in equations (12.1) and (12.2) using the open end reflection coefficient for plane waves and a reflection coefficient of 0.8 at the close end.

The effect of position error in the source locations was first investigated by varying the 'estimated' position of a single source while keeping all of the other parameters the same. It was found that errors in the estimated source position had no effect on the coherence between the separated signals even with large errors of plus or minus 0.1 m.

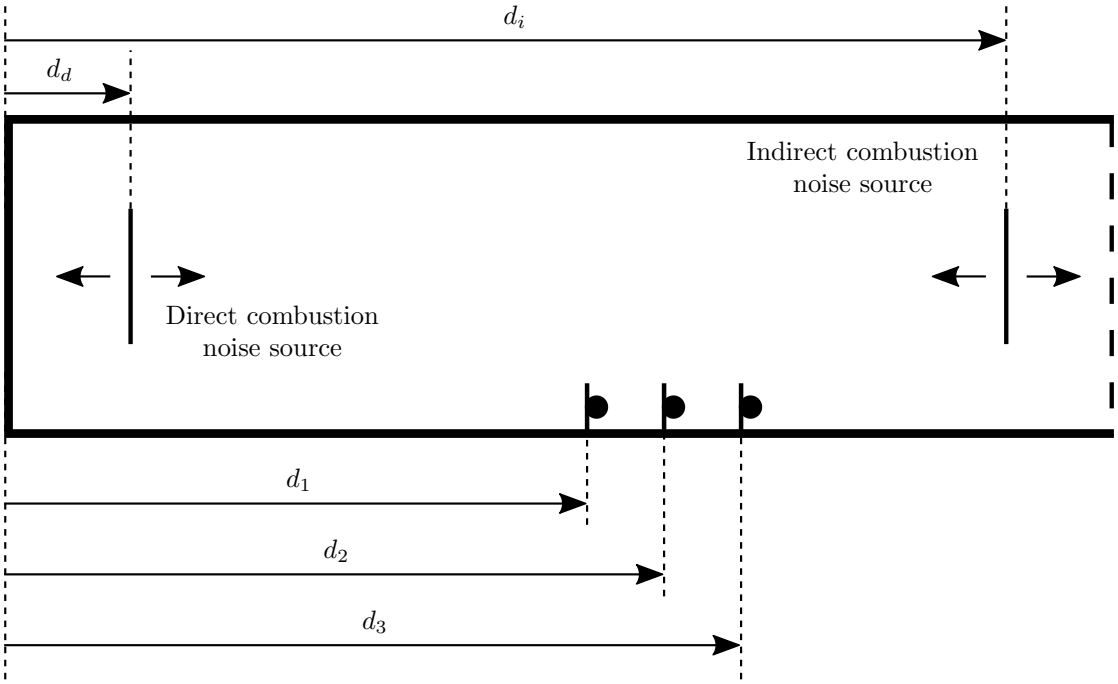

FIGURE 12.13: Diagram of a simple model used to identify sources of error in direct and indirect combustion noise separation method in the validation experiment.

The effect of position error in the microphone locations was also investigated by varying the 'estimated' position of a single microphone while keeping all of the other parameters the same. Figure 12.14 is a plot of the effect of error in the microphone 1 location on the coherence between the separated signals. It is clear that error in the microphone 1 location has a significant effect on the separation of the signals. The coherence becomes high at frequencies equal to the axial resonances in the duct. This makes sense as the pressure amplitude will vary significantly with axial location at the axial resonance frequencies. Therefore, an incorrect estimate of the microphone location will have a significant impact on the separation method at these frequencies. The error has a stronger effect on the coherence at certain frequencies which is likely due to the position of the microphone relative to the nodes and antinodes in the duct. Figures 12.15 and 12.16 show the effect of the microphone position error on the coherence for microphones 2 and 3 respectively. Again, there is an increase in the coherence at the same frequencies as in Figure 12.14 but the strength of the effect differs between microphones for each frequency as expected.

The frequencies of the peaks in the coherence in the plane wave model are different from those in the experiment. The peaks in coherence in the experiment occur at approximately twice the frequency of those in the plane wave model. As reflection coefficients have needed to be measured in several cases for the experiment due to the theoretical ones not resulting in a successful separation, it is likely the boundary conditions in the experiment do not match the ideal case that was used in the plane wave model.

The peaks in coherence in the experimental results shown in Figures 12.4 and 12.8 are probably due to errors in the microphone locations used in the transfer functions. The microphone locations in the experiment have a tolerance of approximately ± 1 mm. It may be possible to

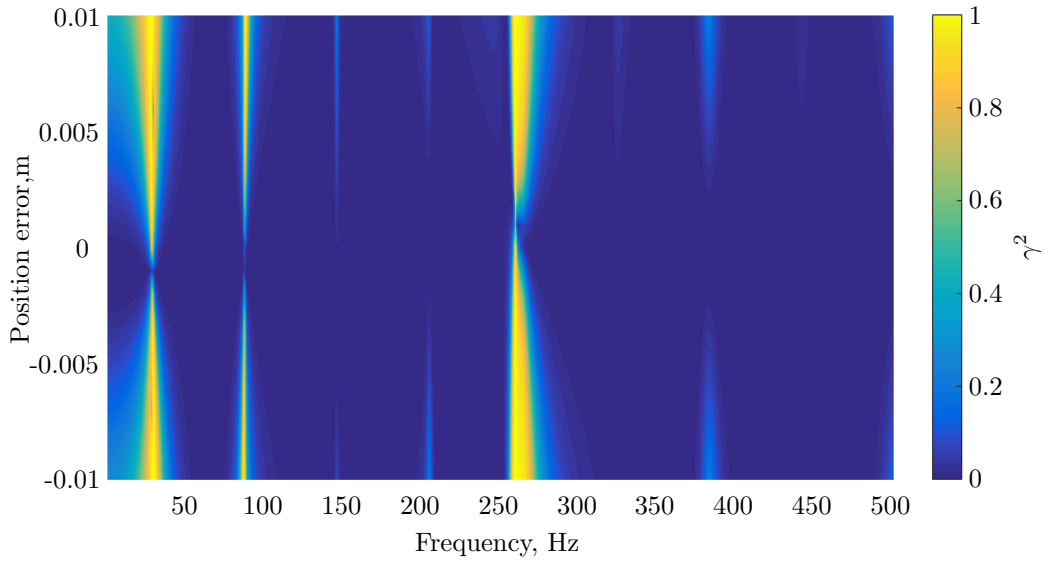

FIGURE 12.14: Effect of position error in the microphone 1 location on the coherence between separated signals.

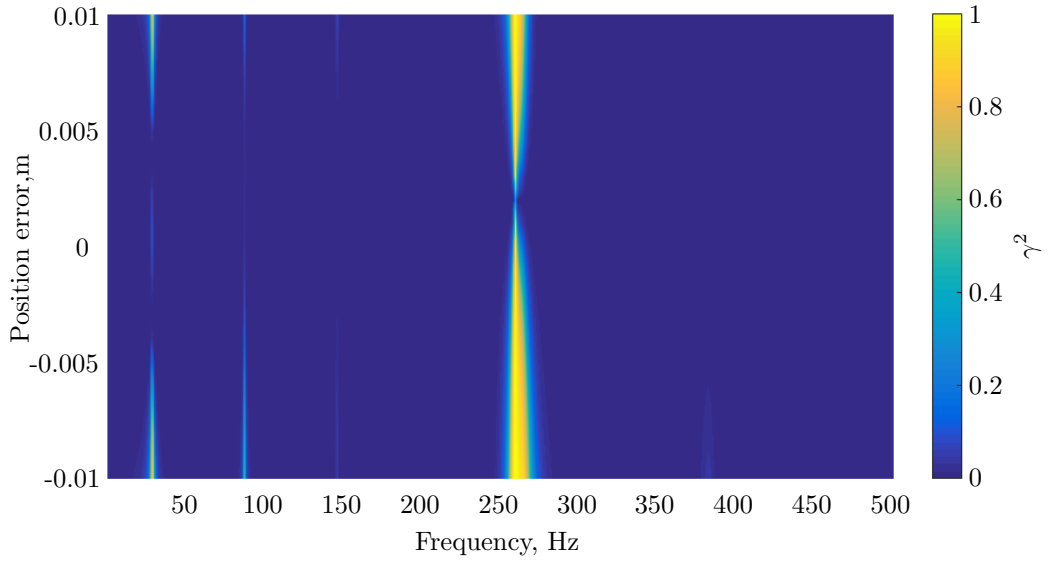

FIGURE 12.15: Effect of position error in the microphone 2 location on the coherence between separated signals.

formulate a cost function to minimise for a gradient decent method to isolate the correct microphone locations. This will potentially be dependent on the signals produced by the sources (the coherence peaks are not present when signal combination 2 is used) and so is potentially not practical to implement on an engine test.

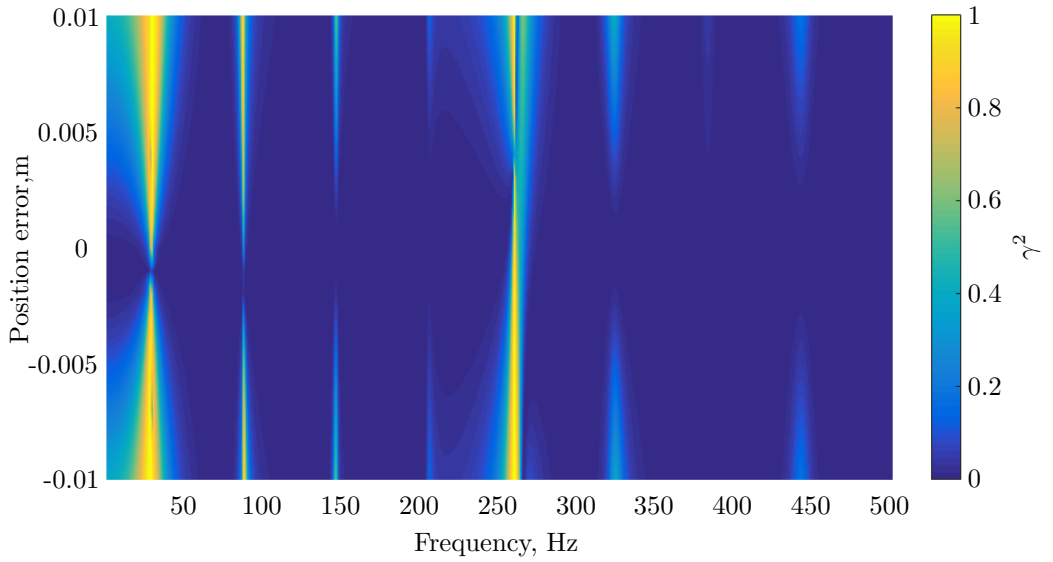

FIGURE 12.16: Effect of position error in the microphone 3 location on the coherence between separated signals.

12.4 The 3S method combined with the direct and indirect combustion noise separation method

The purpose of the separation method is to use it as an input for the 3S Array method to isolate the individual contributions of direct and indirect combustion noise to the measured far field level. As explained in Chapter 8 to isolate the direct and indirect combustion noise in the far field using the 3S method, the separation needs to be performed twice (similar to the 3S method combined with the modal isolation method introduced in Chapter 7). The 3S combined with the separation method was implemented on the test configuration 2, signal combination 2 data with the level of the indirect noise increased by 30 dB. This level increase was to improve the signal-to-noise ratio in the external microphone signal. The 10 microphones used in test configuration 2 have been divided into two 5 microphone arrays, the locations of which are listed in Table 12.2. The effectiveness of the 3S method combined with the separation method

Array	Microphone position relative to closed end of the duct, m				
1	1.61	1.66	1.71	1.76	1.81
2	1.86	2.01	2.11	2.21	2.31

TABLE 12.2: Microphone positions for the two 5 microphone arrays used for implementing the 3S method combined with the separation method.

is dependent on the separation of the direct and indirect noise achieved with each of the 5 microphone arrays. Figures 12.17 and 12.18 are plots of the separated direct and indirect signals at arrays 1 and 2 respectively. Also plotted is the actual direct and indirect noise measured at the first microphone in array 1. Below 150 Hz the level of the separated direct noise is higher than the actual direct and indirect noise for both plots. Between 150 Hz and 250 Hz the level of the separated indirect noise is, for the most part, higher than the separated direct noise for both

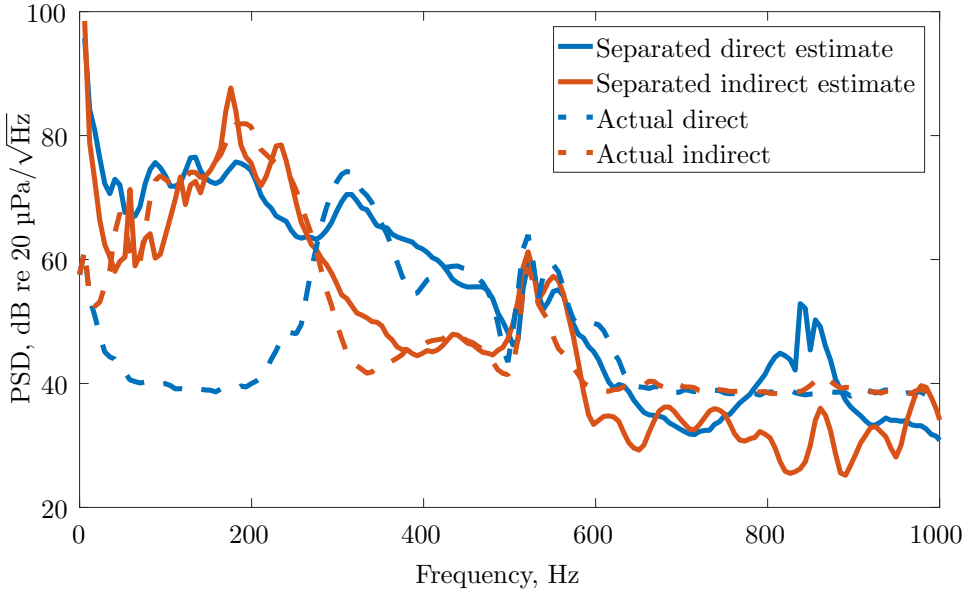

FIGURE 12.17: Direct and indirect noise separated using array 1 with the actual direct and indirect noise measured at microphone 1 in array 1.

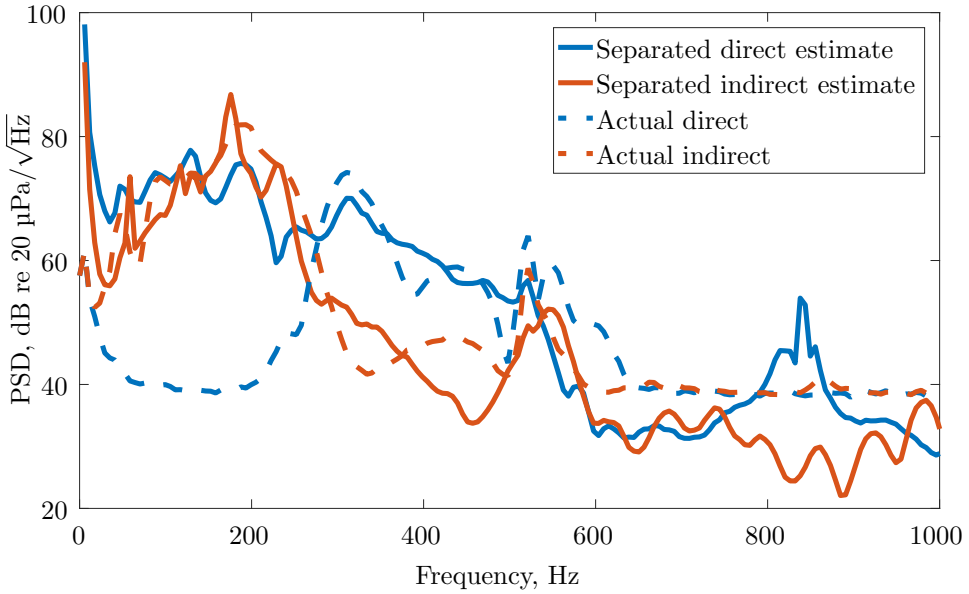

FIGURE 12.18: Direct and indirect noise separated using array 2 with the actual direct and indirect noise measured at microphone 1 in array 1.

arrays. In this frequency range, the separated indirect noise approximately follows the shape of the actual indirect noise. From 250 Hz to 500 Hz, the sound measured in the duct is dominated by the direct noise. In this frequency range, the separated direct noise closely matches the actual direct noise while the separated indirect noise drops to the level of the background noise. The separated direct noise does not exactly match the actual direct noise but the variation in the actual direct and indirect levels is due to the axial resonances inside the duct. The separated direct and indirect noise is not affected as strongly by the axial resonances due to the microphones

being distributed axially in the duct. The separation method is most successful between 150 Hz and 500 Hz (approximately the cut-on frequency of the first azimuthal mode).

The 3S method combined with the separation method was implemented using arrays 1 and 2 as the in-duct sensors and a single external microphone. The results of the 3S method with the separation method for this configuration is shown in Figure 12.19. Up to 250 Hz the separated

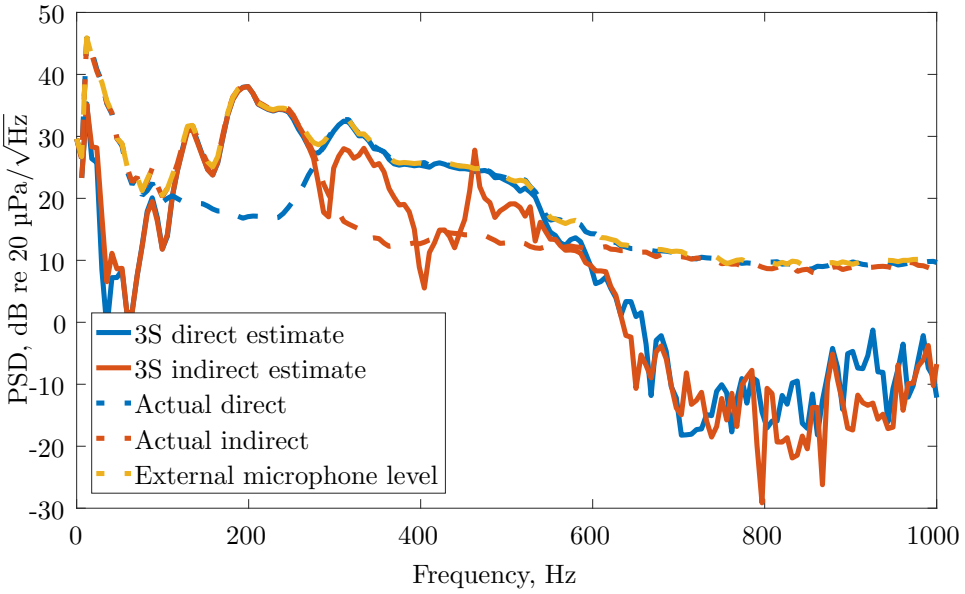

FIGURE 12.19: Direct and indirect noise at the external microphone estimated using the 3S method combined with the separation method with the actual direct and indirect noise measured at the external microphone.

direct and indirect noise are both the same level as the actual indirect noise at the external microphone. From 250 Hz the direct noise becomes dominant and the separated direct noise closely follows the actual direct noise while the indirect noise level is below the direct noise level except for at 462 Hz. Therefore the 3S method combined with the separation method does work between 250 and 500 Hz. Below 250 Hz the coherence between the separated signals is high as it was for the combination 2 signals in Figures 12.6 and 12.10 which results in high coherence with the external microphone for both separated signals below 250 Hz. This is likely due to the estimated transfer functions for the indirect noise having significant differences to the actual transfer functions. While these results do not show the combined method working perfectly, they do show that it is possible to implement the method on measured data with estimated transfer functions and obtain approximately correct results. Further work is needed before this method can be applied to real engine tests and that work would need to be primarily focussed on the estimation of the transfer functions.

12.5 Chapter Summary

The direct and indirect noise separation method combined with the 3S method was applied to no-flow laboratory measurements. The separation method is moderately successful in separating the direct and indirect noise in the duct when only the direct noise is being produced by the

compression drivers. When only the indirect noise is being produced, the direct noise cannot be separated from the indirect noise. This is likely due to the estimated pressure-to-pressure transfer functions from the source to the microphone and the actual transfer functions differing significantly. Combining the separation and 3S methods was moderately successful in separating the direct and indirect noise that propagates to the external microphone. This indicates that the two methods could be used together in the future to obtain estimates of the direct and indirect noise that propagates to the external microphones in an engine test. However, to apply the separation method to an engine test, the transfer functions between the sources and the microphones will need to be calculated. The calculation of the transfer functions will require the propagation of sound in the combustor to be accurately known (probably using finite element simulations). There will also be additional complications as the level of hydrodynamic noise will be high due to annular combustors having a cross-sectional area which varies with axial position.

Chapter 13

Application of the 3S PCCSM and inverse beamforming methods to short cowl engine data

To demonstrate the benefits of the 3S PCCSM method, the 3S PCCSM method and the inverse beamforming method will be applied to the short cowl engine data introduced in Chapter 6. The full 26 seconds of data (including the clicking noise) are used in this chapter. The combustion noise estimates obtained using the 3S PCCSM method and the inverse bemforming method will be compared with the estimate obtained using the 3S Array method for the same data. As explained in Chapter 6, the short cowl engine test was conducted inside a test cell. The measured pressure signals in the external microphone array is made up of the pressure waves that travelled directly from the hot nozzle to the array microphones plus the reverberated pressure waves that originated from the hot nozzle as well as the waves from unwanted noise sources (both direct and reverberated). One method to extract the combustion noise would be to estimate the effective source strengths of the combustion noise that radiates from the hot nozzle. The inverse beamforming method can be used to do this by inverting Green's functions that account for the reverberation inside the test cell. By applying the inverse method to a PCCSM obtained using the 3S PCCSM technique, only the part of the CSM which is coherent with the measured spectra inside the engine will be used to calculate the equivalent source strengths. Combining the two methods can therefore make it possible to obtain the equivalent combustion noise sources at the hot nozzle exit plane.

13.1 Estimating Green's functions

There are two methods that can be used to estimate the Green's functions in a space with many reflective surfaces and complicated geometries. One of these methods is to use computational

methods such as finite-element or boundary-element models. These methods require the precise geometry and reflection coefficients of all of the surfaces to be known and can be computationally expensive, especially when calculating the Green's functions at high frequencies. Another method to obtain the Green's functions is to measure them in-situ. This can be done by applying known input signals to calibrated sources at the nozzle and recording the pressure signals at each of the microphones in the microphone array for each source in turn. The Green's functions can then be calculated from the transfer function between the input signal and each microphone for each source.

Before estimates of the Green's functions can be calculated, the equivalent source distribution needs to be defined. Combustion noise radiates from the hot nozzle outlet to the far field. Therefore, the equivalent source region can be defined as the hot nozzle outlet. For this engine test the Green's functions of sound radiating from 12 loudspeakers, which radiate as monopole sources in the frequency range of interest, to the microphones in the external array were measured. The loudspeakers were evenly distributed around the hot nozzle as shown in Figure 13.1 and were mounted on a baffle which blocked the hot nozzle outlet. These Green's functions could only

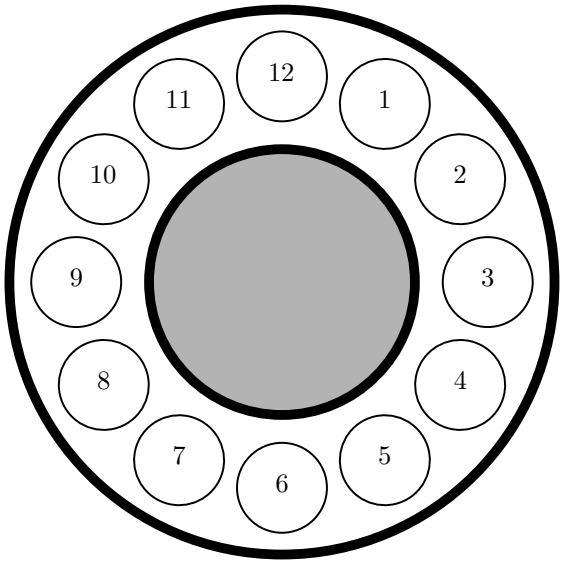

FIGURE 13.1: A diagram of the loudspeaker positions used for the Green's function measurements.

be measured when the engine was not running and so, do not account for the effects of the jet flow on the sound radiated to the microphone array. The source cross-spectral matrix obtained will therefore contain the effects of the jet flow in the source terms. This use of an equivalent source distribution which includes the effects of flow in the source terms was used by Holland and Nelson [62]. They measured the Green's functions between the equivalent source locations at the end of a ducted fan inlet and a microphone array with no flow present. Holland and Nelson then applied the inverse beamforming method to measurements of the fan running which will have resulted in air flowing through the duct. They noted that while the Green's functions did not include the effects of the fluid flow on the sound propagation, the effects of the flow are accounted for in the equivalent source strengths and coherence relationship between the sources. This is because the inverse method essentially removes the propagation effects defined in the Green's function matrix that is inverted from the measured pressure signals to obtain the source volume velocities. Therefore, if the flow effects are not defined in the Green's function matrix,

the estimated volume velocities will include these effects. They showed that the effective source distribution can be used to obtain the sound pressure that radiates away from a ducted fan inlet, as long as the equivalent source distribution is defined so that there are at least 2.5 sources per wavelength. Holland and Nelson discovered that if the spacing between the equivalent sources is too large, spatial aliasing will occur which will result in errors in the estimates. However, if the sources are very close together, the Green's function matrix becomes ill conditioned as there will only be very small variations in the Green's functions to each microphone in the external array.

As the inverse beamforming method uses the inverse of the Green's function matrix, the conditioning of the Green's function matrix is important (matrix conditioning is explained in Section 12.2). Figure 13.2 is a plot of the condition number of the measured Green's function matrix and a Green's function matrix which was calculated using free field Green's functions for the same 12 monopole source and microphone locations. The free field Green's functions are defined

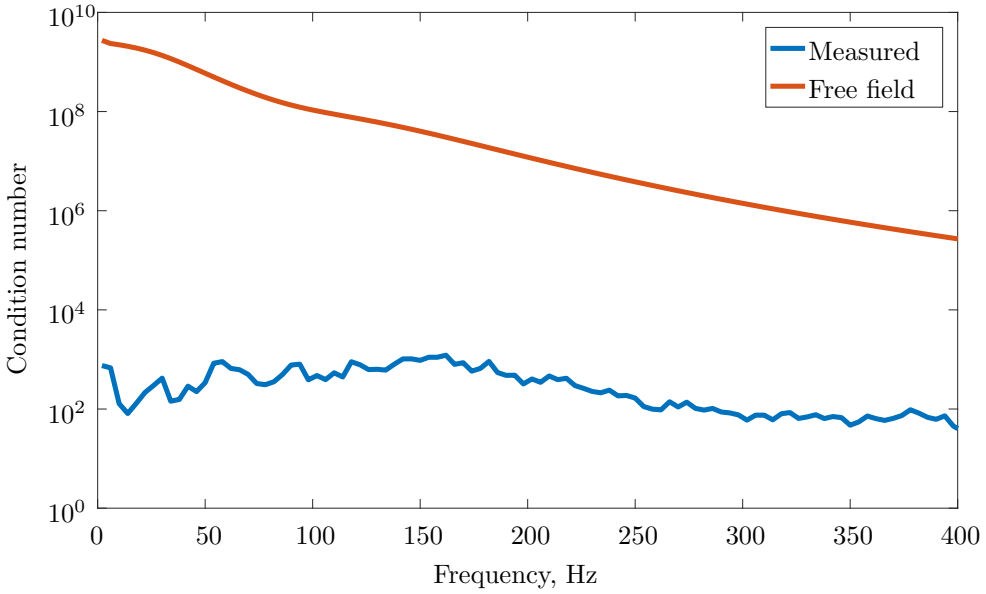

FIGURE 13.2: The condition number of the measured Green's functions and free field Green's functions matricies.

as

$$g(\mathbf{x}|\mathbf{y},\omega) = \frac{j\omega\rho_0}{4\pi r} e^{jkr} \tag{13.1}$$

where $\mathbf{x}$ defines the microphone location, $\mathbf{y}$ the source location, ρ_0 the density of air and $r = |\mathbf{x} - \mathbf{y}|$. It is clear that the measured Green's function matrix is significantly better conditioned than the free field Green's function matrix. The free field Green's function matrix is poorly conditioned because there is very little variation between the Green's functions for each of the sources for each microphone. This is because there are more than 2.5 sources within a wavelength at low frequencies and so the difference in phase and magnitude of the waves arriving from each source at the microphone is very small. This problem is compounded by the fact that the microphone array is only a small distance downstream of the hot nozzle outlet and so the variation in the Green's functions is very small. However, this limitation may be overcome using regularisation techniques which effectively reduce the number of sources. The condition number of the measured Green's functions on the other hand is significantly smaller. This is because

these Green's functions include the reflected waves in the test cell. The small phase and level variations due to the close proximity of the sources are compounded as the sound reverberates around the test cell and results in significant differences in the Green's functions for each source. The reverberation in the test cell may, therefore, be beneficial in the implementation of the inverse method when sources are in close proximity.

The magnitude of the measured and free field Green's functions for source 1 to microphone 1 (located at the centre of the array) are included as Figure 13.3. At very low frequencies the

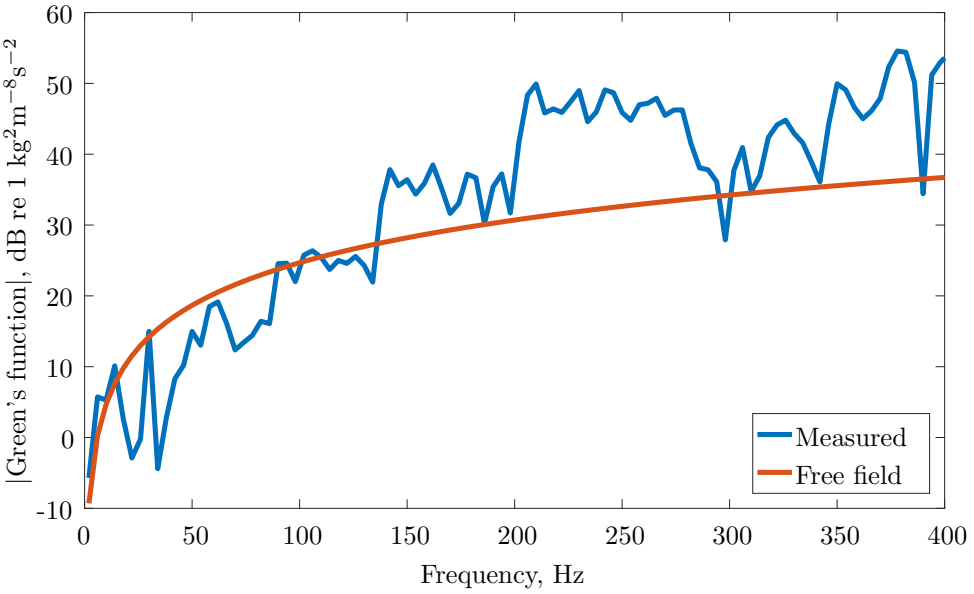

FIGURE 13.3: The magnitude of the measured and free field Green's functions between source 1 and microphone 1.

two Green's functions are similar. As frequency increases the measured Green's functions are generally larger than the free field Green's functions. This is expected given that the measured Green's functions include reflected waves arriving at the microphone constructively interfering with each other and the waves that travel directly from the source. There is significant variance in the level of the measured Green's function compared with the free field as frequency increases. This is because the relative phase of each of the waves arriving from different directions will vary with frequency and so, whether the waves are constructively or destructively interfering will depend on frequency.

13.2 Applying the inverse beamforming method to the PCCSM obtained using the 3S PCCSM method

The CSM of the volume velocities of the 12 equivalent sources can be estimated using the inverse beamforming method which is given as

$$\mathbf{G}_{qq}(\omega) = \mathbf{w}_{\text{opt}}^{\mathbf{H}}(\omega)\mathbf{G}_{pp}(\omega)\mathbf{w}_{\text{opt}}(\omega) \tag{13.2}$$

in Chapter 9 where $\mathbf{G}_{pp}(\omega)$ is the CSM of microphone pressures and $\mathbf{w}_{\text{opt}}(\omega)$ is the pseudo inverse of the matrix of Green's functions. When applying the 3S PCCSM method before applying the inverse beamforming method, the CSM of microphone pressures is replaced by the PCCSM. The autospectra of the volume velocities of the 12 sources when using the measured Green's functions are presented as Figure 13.4 and Figure 13.5 when using the microphone array CSM and PCCSM respectively for a low engine power condition. The scales for both figures are the

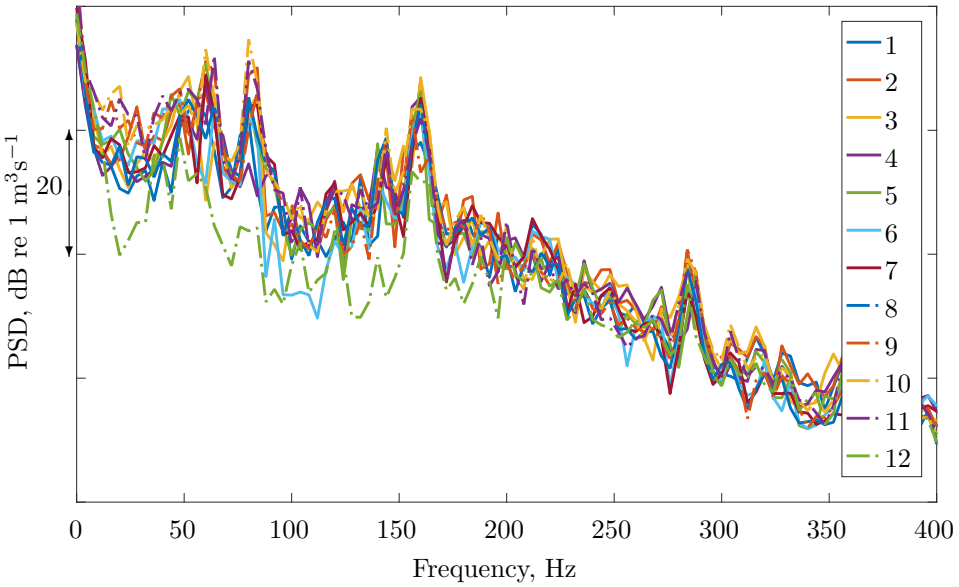

FIGURE 13.4: The autospectra of the 12 equivalent source volume velocities calculated using the measured Green's functions and microphone array pressure CSM in the inverse beamforming method for a low engine power condition.

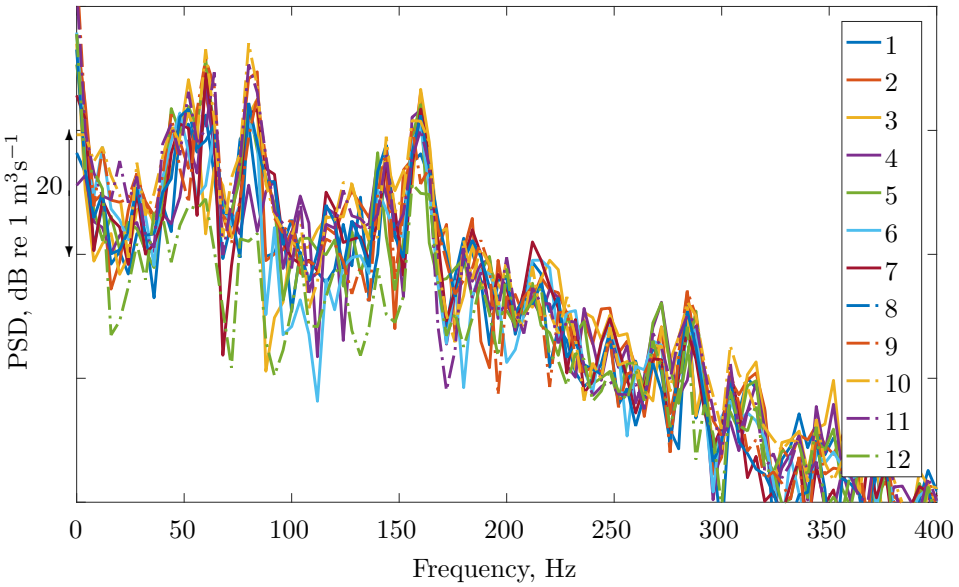

FIGURE 13.5: The autospectra of the 12 equivalent source volume velocities calculated using the measured Green's functions and microphone array pressure PCCSM in the inverse beamforming method for a low engine power condition.

same, and so, comparing Figure 13.4 to Figure 13.5, it can be seen that the volume velocities of the sources calculated using the PCCSM are smaller than those calculated using the CSM. To make this even clearer, Figure 13.6 shows the mean of the 12 volume velocities when the CSM and the PCCSM are used to calculate the volume velocities. It is as expected the the volume velocities are smaller when the PCCSM is used given that the PCCSM should contain only noise that is coherent with the in duct sensors.

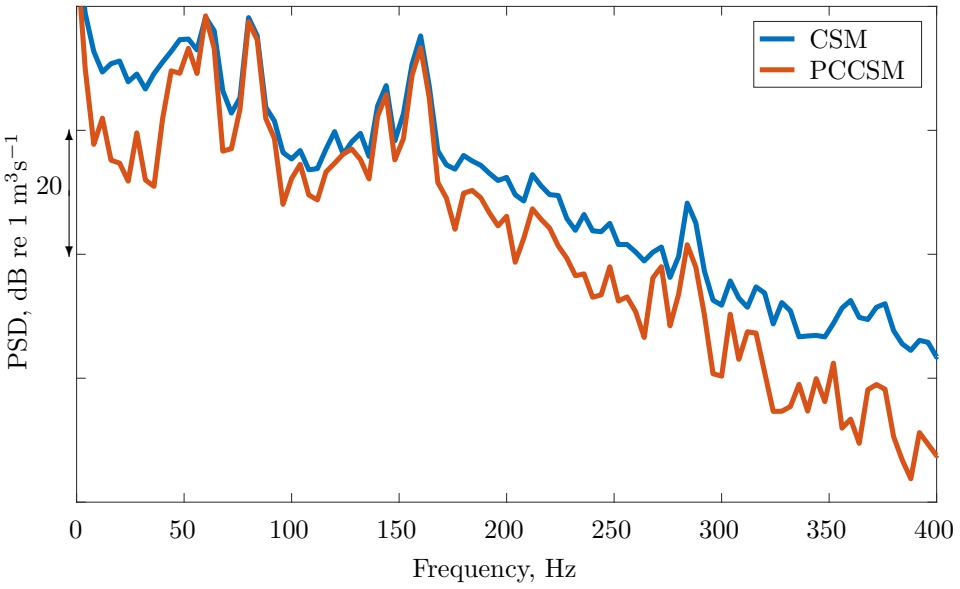

FIGURE 13.6: The autospectra of the mean of the 12 equivalent source volume velocities calculated using the measured Green's functions for a low engine power condition using the inverse beamforming method applied to the microphone array pressure CSM and the PCCSM.

The combustion noise that propagates to the far field can be calculated using the free field Green's function (Equation (13.1)) if it is assumed that the body of the engine will not have an effect on the sound which propagates in the rear arc of the engine. The effects of flow on the sound propagating to the external array microphones are incorporated into the equivalent sources and so, free field Green's functions should provide the sound radiating from the jet engine in the rear arc of the engine. There are issues with this which will be explained in the next section. If these assumptions are valid, the sound that propagates in the rear arc of the engine can be calculated. It is not possible to estimate sound that propagates from an engine operating on an aeroplane in flight using the calculated equivalent sources and free field Green's functions. This is because there will be reflections from the pylon, wing and fuselage, there will be a large relative velocity of the aeroplane to the microphone and many other factors to account for.

Before examining the combustion noise in the far field of the engine however, it is worth comparing the estimates of the combustion noise that propagates to the centre of the array using the two beamforming techniques applied to the microphone pressure CSM and the PCCSM. Figure 13.7 shows a plot of the autospectra of the centre microphone in the array, the delay-and-sum beamformer output and the inverse beamforming method using the CSM to allow for a comparison of the beamforming techniques. The estimate using the inverse method has a lower level than that of the delay-and-sum beamformer. Below 100 Hz there are a small number of frequencies where the two are within 5 dB. Above 100 Hz the two estimates deviate significantly and from

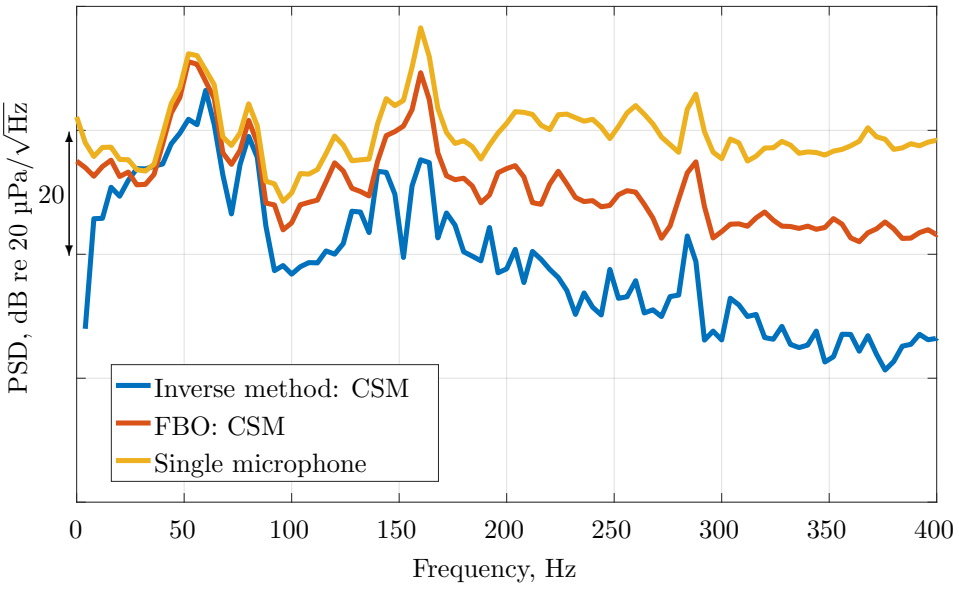

FIGURE 13.7: The autospectra of the centre microphone in the microphone array, focussed beamformer output (FBO) of the delay-and-sum beamformer, and the pressure at the centre of the array estimated using the inverse beamforming method applied to the CSM of microphone pressures.

250 Hz the difference between the two estimates is approximately constant at 20 dB. This level difference will be partly due to the inverse method rejecting noise from other directions more effectively than standard beamforming but also due to the reverberation not being present in the inverse method estimate. The estimates obtained by the standard beamforming method are significant overestimates of the sound that would travel from the hot nozzle to the array location in a free field which is as expected given the measurements take place in a highly reverberant test cell.

As explained in Chapter 9, the inverse method will provide an incorrect estimate of the noise produced from the hot nozzle if there are significant levels of unwanted noise present. The estimate produced by the inverse method applied to the microphone pressure CSM is likely an overestimate of the combustion noise radiating to the array location in a free field. This is where the combination of the 3S PCCSM method and the inverse beamforming method becomes a very useful tool in estimating the combustion noise that propagates from the hot nozzle of the engine. Figure 13.8 is a plot of the autospectra of the centre microphone in the array, the delay-and-sum beamformer output and the inverse beamforming method using the PCCSM obtained from the 3S PCCSM method. Note that the delay-and-sum beamformer applied to the PCCSM will provide the same estimate of the combustion noise as the 3S Array method as was shown in Figure 9.1. The frequency bins for which the conditions required to calculate the confidence intervals of the estimate are met are highlighted in green. Confidence intervals are not plotted for the Inverse method: PCCSM as the inverse beamforming method will introduce (or reduce) uncertainty that was not taken into account in Chapter 5. The confidence intervals are not plotted for the FBO: PCCSM for clarity but the confidence intervals for this curve are the same as those shown in Figure 6.13. The axis scale is the same as Figure 13.7 so that direct comparisons can be made. The level difference between the estimates produced by the delay-and-sum and

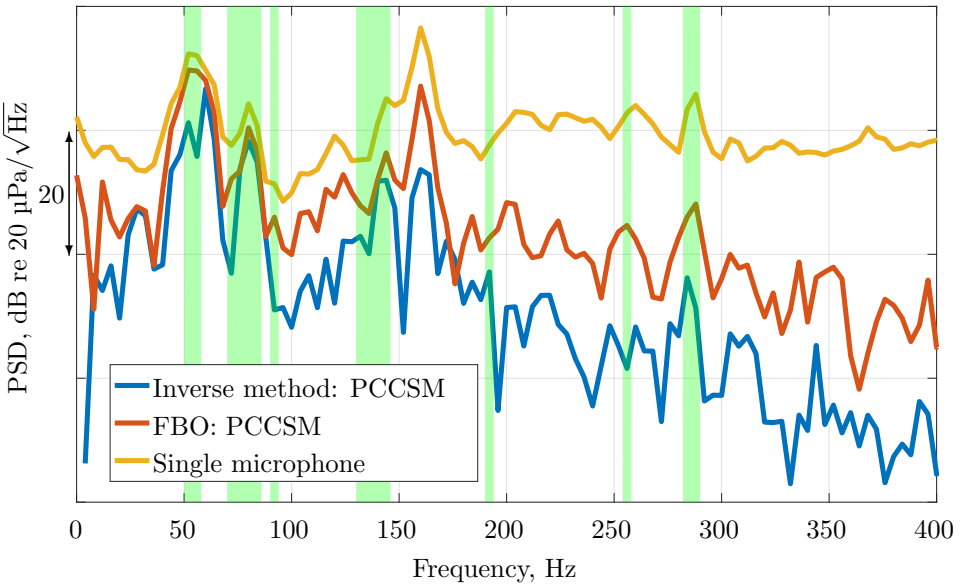

FIGURE 13.8: The autospectra of the centre microphone in the microphone array, focussed beamformer output (FBO) of the delay-and-sum beamformer, and the pressure at the centre of the array estimated using the inverse beamforming method applied to the PCCSM of microphone pressures. The frequencies at which the conditions are met for the confidence intervals to be calculated are highlighted in green.

the inverse beamforming methods using the PCCSM is similar to the methods using the CSM. This suggests that most, if not all, of the difference is due to the removal of the reflections in the inverse beamforming method as the sources which are not due to combustion noise should be significantly reduced by using the PCCSM. Since the level difference when using the CSM is approximately the same as the PCCSM, the difference will be due to reflections rather than other noise sources. The levels of the estimates using the delay-and-sum beamformer and the inverse beamformer are similar between 76 Hz and 84 Hz which is within a green highlighted region. As both estimates are providing a similar estimate in this region, it is likely that the estimate provided by the delay-and-sum beamformer (3S Array) is the level of the combustion noise measured with reverberation and the level estimated using the inverse method is the level without reverberation.

As explained in Chapter 6, the coherence between the combustior and the other sensors above 300 Hz is very small and so, the estimate obtained from the 3S PCCSM method will not be accurate. The coherence for the signals used in this chapter is the same as the coherence shown in Figures 6.8, 6.9 and 6.10. The combustion noise estimate obtained from the 3S PCCSM method combined with the inverse beamforming method is similar in shape to that of the from the 3S PCCSM method combined with the delay-and-sum beamformer below 300 Hz. At 50 Hz, 80 Hz, and 150 Hz, the combustion noise estimate using the inverse beamforming method is very similar to the combustion noise estimate using the delay-and-sum beamformer. This suggests that combustion noise is radiating very strongly from the hot nozzle directly to the microphone array at these frequencies.

Figure 13.9 shows the estimate of the noise radiating from the hot nozzle using the inverse method applied to the CSM and the combustion noise estimate using the inverse method applied to the

PCCSM. It is clear that levels of the estimates in highlighted regions below 150 Hz are similar

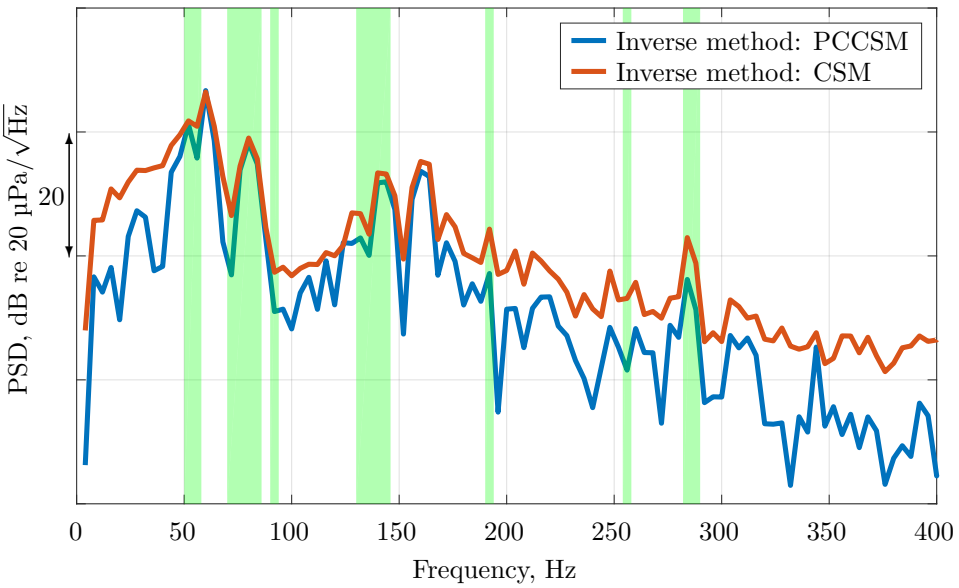

FIGURE 13.9: The autospectra of the pressure at the centre of the array estimated using the inverse beamforming method applied to the CSM and the PCCSM of microphone pressures. The frequencies at which the conditions are met for the confidence intervals to be calculated are highlighted in green.

which indicates the combustion noise is radiating strongly in these regions. In the highlighted regions above 150 Hz, the level of the combustion noise estimate using the PCCSM is lower than the core noise estimate using the CSM. This indicates that at these frequencies, the level of the combustion noise is significantly lower than the total noise that propagates from the hot nozzle.

The results presented in this section indicate that the combustion noise estimates obtained using the 3S Array method and the 3S PCCSM method combined with the inverse beamforming method provide similar results at certain low frequencies. At these frequencies, the conditions are satisfied for calculating the confidence intervals are met. This indicates that the level of the combustion noise that propagates to the centre of the array can be calculated using either method. At other frequencies however, the estimate obtained using the 3S PCCSM method combined with the inverse method is significantly lower which indicates that the 3S Array method may be overestimating the combustion noise level. This overestimation is likely due to the reverberation in the test cell combined with the delay-and-sum beamformer being close to omnidirectional at low frequencies. Low directivity of the array will result in noise sources that are not radiating from the hot nozzle but are measured at the hot nozzle sensor being coherent between the hot nozzle sensor and the beamformer output. This will result in a higher coherence between the hot nozzle and the beamformer output but reduced coherence between the other two pairs of sensors and therefore, an overestimate of the combustion noise. The 3S PCCSM method combined with a more advanced frequency domain beamforming method such as the inverse method results in a better rejection of noise arriving from directions other than that of the hot nozzle and therefore reduce the likelihood of an overestimate of the combustion noise. This represents a significant advancement in the use of coherence based measurement techniques for estimating the level of combustion noise that radiates from turbofan jet engines.

13.3 Estimating directivity of combustion noise

The purpose of using these measurement techniques is to obtain an estimate of the combustion noise that propagates to the far field. By removing the reverberation from the measured signals using the measured Green's functions it is possible to obtain these estimates. Using the free field Green's functions the combustion noise that propagates to the far field of the engine in the rear arc can be obtained. To produce accurate estimates of the combustion noise that propagates into the forward arc of the engine, Green's functions that include the geometry of the engine will be required. As stated earlier, the effects of flow are included in the equivalent sources.

Figure 13.10 is a plot of the directivity of the combustion noise in the rear arc of the engine using the combined 3S PCCSM and inverse beamforming method. The peak in the directivity is either

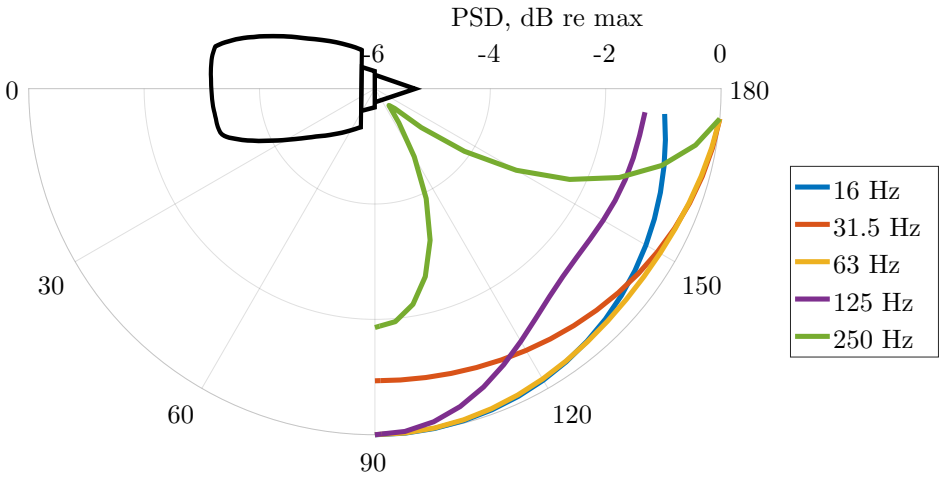

FIGURE 13.10: The estimated directivity of combution noise radiating from the hot nozzle calculated using the combined 3S PCCSM and inverse beamforming methods for 5 octave bands.

90° or 175° for all of octave bands. Pardowitz et al. [49] examine the directivity of combustion noise that propagates away from a turboshaft jet engine in a static engine test. They found that the combustion noise peaked between 120° and 150° in the frequency range of 133 Hz to 263 Hz for the TEENI turboshaft engine. The directivity plots in Figure 13.10 do not peak in this region but the 250 Hz band peaks at 175°.

As stated earlier, the equivalent sources include the effects of flow but the effect of the flow on the sound that propagates to the array microphones will vary depend on the angle to the hot nozzle. As the range of polar angles that the microphone array covers is 93° to 128° (and therefore has an aperture angle $\alpha = 35°$), the flow effects incorporated into the equivalent sources are the effects on sound that propagates in these directions. The flow effects are more prominent for sound travelling at small angles to the jet axis as sound is refracted away from the jet axis. Therefore, the directivity estimates for angles above 128° will contain more error as the angle to the intake increases. Therefore, the peak in the directivity of the 250 Hz octave band would

likely occur at a smaller angle. This could explain why the peak is at 175° and not between 120° and 150° as measured by Pardowitz et al. To improve the directivity estimates for a larger range of angles, more microphones are required to cover a larger arc of the sound field and therefore increase the aperture angle of the array. In a test cell, this can be a challenge as there is limited physical space where the microphones can be placed.

13.4 Chapter summary

The 3S PCCSM method can be used to obtain a PCCSM that can be used as an input for advanced beamforming techniques which require a CSM as an input. By using the PCCSM, a large amount of unwanted noise can be rejected which increases the usefulness of these advanced beamforming techniques like the inverse beamforming method that was used here. There is a significant benefit to using 3S PCCSM and a more advanced beamforming technique when compared to using the standard 3S Array method. The inverse beamforming method combined with the 3S PCCSM method and measured Green's functions can be used to obtain equivalent combustion noise sources at the end of the hot nozzle which include the effects of flow but do not include the reverberation in the test cell. These can then be used to estimate the level of the combustion noise that propagates to the far field, in particular, the total radiated sound power of the combustion noise, and even the directivity of the combustion noise (so long as a microphone array which covers a large range of polar angles is used).

Chapter 14

Conclusions

This thesis has focussed on the development of methods for isolating and quantifying combustion noise produced by turbofan jet engines. Improvements to an existing method currently used for combustion noise measurement have been developed as part of this work.

14.1 Main Achievements

The main achievements detailed in this thesis are:

1. Data from a short cowl turbofan engine measurements have been analysed. The limitations of a current technique for measuring combustion noise, called the 3S Array method, have been identified. The 3S Array method is limited to frequencies below the cut-on frequency of the first azimuthal mode inside the combustor due to the modes being mutually incoherent. The method is also limited by the presence of coherent unwanted noise between the pressure sensor in the hot nozzle and the microphone array external to the engine which results in an overestimate of the combustion noise at the external microphone array.

2. A method for isolating individual modes propagating inside the engine duct that can be combined with the 3S Array method has been presented. This new method extends the frequency range of the 3S Array method by maintaining the assumption of single mode propagation inside the engine duct. The modal isolation method combined with the 3S Array method can also be used to identify the contribution of individual modes that are propagating along the engine duct to the external sound level. This may be useful in developing methods for reducing the combustion noise that propagates to the far field. The method was applied to no-flow laboratory experiments and performed well.

3. A new technique called 3S PCCSM (Partially Coherent Cross-Spectral Matrix) has been presented which can be used in conjunction with advanced beamforming techniques such as the Inverse beamforming method (developed by Holland and Nelson [55]) to provide more accurate combustion noise estimates. 3S PCCSM was used in conjunction with the Inverse beamforming method on the same short cowl engine test as the 3S Array method. Combining the 3S PCCSM method with the Inverse beamforming method improves the

accuracy of the estimated source strengths obtained using the Inverse beamforming method by improving the signal to noise ratio of the cross-spectral matrix. The combined method was shown to provide similar estimates to the 3S Array method at some frequencies, indicating that this is likely the level of the combustion noise. At other frequencies however, the 3S PCCSM method combined with the inverse method provide lower estimates of the combustion noise than the 3S Array method. This is expected given that the combined method removed the effects of reverberation. The 3S Array method uses a microphone array as a delay-and-sum beamformer which is close to omnidirectional at low frequencies and results in an overestimation of the combustion noise due to noise sources located away from the hot nozzle being coherent between the hot nozzle sensor and the microphone array. The 3S PCCSM method combined with the Inverse beamforming method reduces this overestimation due to the inverse beamforming method providing better source localisation than delay-and-sum beamforming.

4. The identification of several conditions (listed in Table 5.6) that the signals used need to satisfy to ensure an accurate estimate of the combustion noise.

5. An empirical method for determining 'at-least-95%' confidence intervals of the 3S Array method has been presented. These intervals can also be applied to the original 3S method and bring a new way of determining the validity of the combustion noise estimate produced by these methods.

6. A method for separating direct and indirect combustion noise has been presented which can be used in conjunction with the 3S Array technique. This method was tested in no-flow laboratory experiments and was partially successful, achieving up to 15 dB of separation between estimates of the components of combustion noise contributing to an external microphone spectra. Further work will be needed before this method is ready to be used in an engine test and is outlined in Section 14.2.1.3.

14.2 Future work

14.2.1 Combustion noise applications

14.2.1.1 Confidence intervals for the 3S Array method

The combination of the new conditions that the measured signals have to satisfy for the estimate obtained 3S Array method to be valid along with the method for calculating confidence intervals represents a significant improvement to the existing measurement technique. Without these it was impossible to identify the accuracy of the estimate obtained using the 3S Array method. Unfortunately, the data that was used in this thesis only met the conditions over a small range of frequencies where it was clear that the estimate obtained is valid and likely to be reasonably accurate. It would be useful to develop the 3S Array method further to calculate the confidence intervals for different engine data with a much longer signal length to assess the validity of using the 3S Array method for the application to combustion noise measurements.

14.2.1.2 The 3S Array method combined with the modal isolation method

The combined 3S and modal isolation methods performed well in laboratory validation tests. To develop the method further it will need to be applied to a full-scale engine test. It would be useful to calculate confidence intervals for the combined method applied to engine data to assess whether the confidence in the estimate improves.

14.2.1.3 The 3S Array method combined with the direct and indirect combustion noise separation method

The laboratory tests of the separation method serviced as a proof of concept to show that the separation method could be combined with the 3S Array method to isolate different contributors to combustion noise that propagate to the external array. The successfulness of the separation method was found to depend on the accuracy of the estimates of the pressure-to-pressure transfer functions. A significant amount of work will be required to accurately define these transfer functions inside an annular combustor. Numerical simulations of the combustor including temperature and flow will likely be the most effective way of defining these transfer functions.

It may be necessary for the separation method to be used above the cut-on of the first higher order mode inside the combustor. The separation method could be combined with the modal isolation method to extend the frequency range beyond the first azimuthal mode cut-on frequency.

14.2.1.4 The 3S PCCSM method combined with advanced beamforming methods

The 3S PCCSM method has been used with the inverse beamforming technique on short cowl engine data measured inside a test cell. It would be useful to apply 3S PCCSM with the inverse beamforming method to both outdoor and indoor test cell measurements of the same engine. This would make it possible to establish if the method gives consistent results for the indoor measurements as the outdoor measurements when measured Green's functions are used to dereverberate the measurements. If this is the case, it would demonstrate that accurate combustion noise measurements can be obtained from indoor measurements which can be substantially cheaper to run and less reliant on weather conditions.

It would also be useful to apply other beamforming/source location techniques, for example DAMAS, which is a deconvolution method developed by Brooks et al. [63], or CLEAN-SC which was developed by Sijtsma [64]. CLEAN-SC is a modification of the CLEAN algorithm [65] that removes the part of the measured source map that is coherent with the measured peak in the map. It would be particularly useful to see whether CLEAN-SC can be successfully used with the 3S PCCSM method as most of the sound in the PCCSM should be due to sources that are coherent with the in duct probes.

14.2.1.5 Microphone array design

As was stated in Chapter 13, to obtain plots of the directivity of the combustion noise using the 3S PCCSM method with inverse beamforming, the microphone array needs to have sensors

placed over a large range of angles. Further work could be performed to design a 2D microphone array which has a well conditioned Green's functions matrix for the estimated source distribution while occupying a large range of angles to provide accurate directivity information. The design of this array will be limited by the number of microphones and data acquisition channels available.

14.2.1.6 Investigating the effects of spectral broadening on the combustion noise estimate obtained using the 3S Array method

One of the assumptions of the 3S Array technique is that there are no non-linear effects on the combustion noise that propagates from the combustor to the far field. Spectral broadening due to the propagation of the combustion noise through a turbulent shear layer is a non-linear phenomenon and could be investigated to identify whether the estimate obtained from the 3S Array method is affected. It is unclear how much spectral broadening will affect (if at all) the combustion noise as the wavelength of the combustion noise at low frequencies will be larger than the turbulent eddies. It would be useful to identify whether spectral broadening is affecting the coherence between the external array and the in-duct sensors as this could account for the low coherence in the measured data. The effects of spectral broadening could be investigated in a laboratory experiment with a sound source and microphone in a jet flow and a microphone (or array of microphones as the sound may be scattered) outside the jet. The spectral content of the microphone signals and the coherence between the signals could be measured to identify the effects of spectral broadening on the coherence between broadband signals in the frequency range of interest.

14.2.2 Other applications

All of the methods developed during this project can also be used for applications other than the measurement of turbofan jet engine combustion noise.

14.2.2.1 Measurement of turbofan jet engine bypass noise

Noise propagating from the bypass duct of a short cowl turbofan jet engine is a significant contribution to the total noise level. The 3S PCCSM with inverse beamforming could be used with source locations in the bypass nozzle as well as the hot nozzle. Sensors could be placed in the bypass to isolate the bypass noise. Due to the large diameter of the bypass duct, the modal isolation method will need to be used in the duct.

For long cowl engines there is a mixing region where the bypass and the core jets mix inside the engine before exiting the engine in a single nozzle. It is, therefore, not possible to use the inverse method to isolate the core noise and the bypass noise. It is also possible that the combustion noise could propagate into the bypass duct from the core. The bypass could still be isolated from the core noise by using the separation method to separate the sound travelling in opposite directions and remove the core noise from the bypass sensor signals. Separation of the bypass and core noise would obviously require good approximations of the pressure-to-pressure transfer functions in the bypass duct.

14.2.2.2 More general applications

For any situation where it is possible to measure the desired noise source with two sensors without other coherent noise contaminating the measurement but where the level is desired at some other location where other noise is present, it is possible to apply the 3S Array (and therefore 3S PCCSM) method provided the required assumptions are met. One such scenario could be identifying a single piece of faulty machinery in a room full of other machines producing high levels of noise. Sensors could be installed in each machine and an array of microphones could be used to apply 3S PCCSM with an advanced beamforming method for each machine in turn. The 3S PCCSM effectively increases the signal-to-noise ratio of the CSM which will improve estimates of the source strength of each noise source.

The methods presented in this thesis could also be applied to other situations where the level of noise radiating from a duct needs to be measured. Depending on the source distribution(s) inside the duct, a combination of the modal isolation and separation methods may be useful as well as the 3S PCCSM method.

Appendix A

Spiral microphone array microphone locations

Table A.1 contains the microphone locations of for the spiral array used in the short cowl engine measurements presented in Chapter 6. The microphone locations are given as displacement relative to the array centre.

x position, m	y position, m	z position, m
0.000	0.000	0.000
-0.198	0.000	-0.068
-0.140	0.000	-0.234
0.147	0.000	-0.258
0.249	0.000	-0.066
0.258	0.000	0.189
0.007	0.000	0.366
-0.319	0.000	0.254
-0.513	0.000	-0.058
-0.320	0.000	-0.422
0.099	0.000	-0.562
0.500	0.000	-0.322
0.589	0.000	0.159
0.296	0.000	0.590
-0.418	0.000	0.652
-0.743	0.000	0.257
-0.748	0.000	-0.386
-0.225	0.000	-0.854
0.496	0.000	-0.803
0.938	0.000	-0.224
0.783	0.000	0.556
0.116	0.000	0.998
-0.701	0.000	0.788

-1.157	0.000	0.019
-0.827	0.000	-0.856
0.046	0.000	-1.228
0.979	0.000	-0.841
1.285	0.000	0.115
0.779	0.000	1.081
-0.269	0.000	1.343
-1.223	0.000	0.752
-1.418	0.000	-0.426

TABLE A.1: Microphone locations relative to array centre of the spiral microphone array used in short cowl engine measurements.

References

[1] Rolls-Royce PLC, "Advanced noise technology," 2017. http://www.rolls-royce.com/sustainability/performance/case-studies/noise-technology.aspx last accessed 20/01/2017.

[2] ACARE, "About ACARE," 2017. https://www.acare4europe.org/about-acare last accessed 05/12/2018.

[3] LHR Airports Limited, "Night flights," 2017. http://www.heathrow.com/noise/heathrow-operations/night-flights last accessed 20/01/2017.

[4] Rolls-Royce PLC, "Rolls-royce lean-burn combustion test engine runs for first time," 2017. https://www.rolls-royce.com/media/press-releases/2018/06-02-2018-rr-lean-burn-combustion-test-engine-runs-for-first-time.aspx last accessed 20/01/2017.

[5] Rolls-Royce PLC, *The Jet Engine*. Wiley, 5$^{\text{th}}$ ed., 2015.

[6] A. P. Dowling and Y. Mahmoudi, "Combustion noise," *Proceedings of the Combustion Institute*, vol. 35, no. 1, pp. 65–100, 2015.

[7] F. E. Marble and S. M. Candel, "Acoustic disturbance from gas non-uniformities convected through a nozzle," *Journal of Sound and Vibration*, vol. 55, no. 2, pp. 225–243, 1977.

[8] C. K. Tam and S. Parrish, "On the generation of indirect combustion noise," in *20th AIAA/CEAS Aeroacoustics Conference*, AIAA AVIATION Forum, American Institute of Aeronautics and Astronautics, June 2014.

[9] C. K. Tam, S. A. Parrish, J. Xu, and B. Schuster, "Indirect combustion noise of auxiliary power units," *Journal of Sound and Vibration*, vol. 332, no. 17, pp. 4004–4020, 2013.

[10] D. Blackstock, *Fundamentals of physical acoustics*. John Wiley & Sons, 2000.

[11] S. Rienstra, "Sound propagation in slowly varying lined flow ducts of arbitrary cross-section," *Journal of Fluid Mechanics*, vol. 495, pp. 157–173, 2003.

[12] J. H. Miles, "Separating Turbofan Engine Noise Sources Using Auto- and Cross Spectra from Four Microphones," *AIAA Journal*, vol. 46, no. 1, pp. 61–74, 2008.

[13] B. J. Tester, T. Recoup, and G. Gabard, "Extracting engine noise source levels from phased arrays with improved internal source models and evaluation against simulated and measured

data," in *18th AIAA/CEAS Aeroacoustics Conference (33rd AIAA Aeroacoustics Conference)*, Aeroacoustics Conferences, American Institute of Aeronautics and Astronautics, June 2012.

[14] B. J. Tester, "Engine noise source breakdowns from an improved inverse method (AFINDS) of processing phased array measurements," in *20th AIAA/CEAS Aeroacoustics Conference*, AIAA AVIATION Forum, American Institute of Aeronautics and Astronautics, 2014.

[15] C. M. Ekoule, B. J. Tester, S. Funke, and C. Richter, "Development of an Improved Core Noise Prediction Method for Long-cowl Engines," in *2018 AIAA/CEAS Aeroacoustics Conference*, AIAA AVIATION Forum, American Institute of Aeronautics and Astronautics, June 2018.

[16] S. Funke, H. A. Siller, W. Hage, and O. Lemke, "Microphone-array measurements of a Rolls-Royce BR700 series aeroengine in an indoor test-bed and comparison with free-field data," in *20th AIAA/CEAS Aeroacoustics Conference*, AIAA AVIATION Forum, American Institute of Aeronautics and Astronautics, June 2014.

[17] P. Böhning, H. Siller, K. Holland, F. Arnold, A. Kempton, and U. Michel, "Novel methods for acoustic indoor measurements and applications in aero-engine test cells," in *Berlin Beamforming Conference*, 2006.

[18] H. Siller, S. Schröder, G. Saueressig, and S. Fröhlich, "Beamforming on a turbofan engine in an indoor test -facility," in *2nd International Beamforming Conference (BeBeC)*, 2008.

[19] H. Siller, U. Michel, and F. Arnold, "Investigation of aero-engine core-noise using a phased microphone array," in *7th AIAA/CEAS Aeroacoustics Conference and Exhibit*, Aeroacoustics Conferences, American Institute of Aeronautics and Astronautics, May 2001.

[20] J. H. Miles, "Separating direct and indirect turbofan engine combustion noise while estimating post-combustion (post-flame) residence time using the correlation," *NASA TM-216248*, 2011.

[21] P. Rodríguez-García and K. Holland, "Exploring and Developing Processing Techniques for the Extraction of Aircraft Combustion Noise," *20th International Conference of Sound and Vibration*, July 2013.

[22] W. G. Halvorsen and J. S. Bendat, "Noise Source Identification Using Coherent Output Power Spectra," *Sound and Vibration*, vol. 9, no. 8, pp. 15–24, 1975.

[23] A. M. Karchmer and M. Reshotko, "Core noise source diagnostics on a turbofan engine using correlation and coherence techniques," *The Journal of the Acoustical Society of America*, vol. 60, no. S1, p. 112, 1976.

[24] A. M. Karchmer, M. Reshotko, and F. J. Montegani, "Measurement of far field combustion noise from a turbofan engine using coherence functions," *4th AIAA Aeroacoustics Conference*, October 1977.

[25] M. Reshotko and A. Karchmer, "Core noise measurements on a small, general aviation class turbofan engine," *The Journal of the Acoustical Society of America*, vol. 68, no. S1, pp. S106–S106, 1980.

[26] M. Harper-Bourne, A. Moore, and H. Siller, "A Study of Large Aero-Engine Combustor Noise," in *14th AIAA/CEAS Aeroacoustics Conference (29th AIAA Aeroacoustics Conference)*, Aeroacoustics Conferences, American Institute of Aeronautics and Astronautics, May 2008.

[27] J. H. Miles, "Spectral Separation of the Turbofan Engine Coherent Combustion Noise Component," in *46th AIAA Aerospace Sciences Meeting and Exhibit*, Aerospace Sciences Meetings, American Institute of Aeronautics and Astronautics, January 2008.

[28] D. K. Boyle, B. S. Henderson, and L. S. Hultgren, "Core/combustor-noise baseline measurements for the dgen aeropropulsion research turbofan," in *2018 AIAA/CEAS Aeroacoustics Conference*.

[29] J. Chung, "Rejection of flow noise using a coherence function method," *The Journal of the Acoustical Society of America*, vol. 62, no. 2, p. 388, 1977.

[30] E. Krejsa, "New technique for the direct measurement of core noise from aircraft engines," *NASA TM-82634*, 1981.

[31] E. A. Krejsa, "Combustion noise from gas turbine aircraft engines measurement of far-field levels," in *NOISE-CON 87; Proceedings of the National Conference on Noise Control Engineering*, vol. 1, pp. 8–10, 1987.

[32] L. S. Hultgren and J. H. Miles, "Noise-Source Separation Using Internal and Far-Field Sensors for a Full-Scale Turbofan Engine," *15th AIAA/CEAS Aeroacoustics Conference (30th AIAA Aeroacoustics Conference)*, pp. 11–13, May 2009.

[33] T. Livebardon, S. Moreau, L. Gicquel, T. Poinsot, and E. Bouty, "Combining LES of combustion chamber and an actuator disk theory to predict combustion noise in a helicopter engine," *Combustion and Flame*, vol. 165, pp. 272–287, 2016.

[34] J. H. Miles, "Aligned and Unaligned Coherence: A New Diagnostic Tool," in *44th AIAA Aerospace Sciences Meeting and Exhibit*, Aerospace Sciences Meetings, American Institute of Aeronautics and Astronautics, January 2006.

[35] J. H. Miles, "Core Noise Diagnostics of Turbofan Engine Noise Using Correlation and Coherence Functions," *Journal of Propulsion and Power*, vol. 26, no. 2, pp. 303–316, 2010.

[36] J. H. Miles, "Estimation of signal coherence threshold and concealed spectral lines applied to detection of turbofan engine combustion noise.," *The Journal of the Acoustical Society of America*, vol. 129, no. 5, pp. 3068–3081, 2011.

[37] J. H. Miles and L. S. Hultgren, "Application of an aligned and unaligned signal processing technique to investigate tones and broadband noise in fan and contra-rotating open rotor acoustic spectra," *NASA TM-218865*, 2015.

[38] J. H. Miles, "Identification of Indirect Combustion Noise at the Exit of a Gas Turbine," in *49th AIAA Aerospace Sciences Meeting and Exhibit*, Aerospace Sciences Meetings, American Institute of Aeronautics and Astronautics, January 2011.

[39] J. H. Miles, "Spatial correlation in the ambient core noise field of a turbofan engine," *The Journal of the Acoustical Society of America*, vol. 131, no. 6, pp. 4625–4639, 2012.

[40] P. Rodríguez-García, K. Holland, and B. Tester, "Extraction of Turbofan Combustion Noise Spectra Using a combined Coherence-Beamforming Technique," in *20th AIAA/CEAS Aeroacoustics Conference*, AIAA Aviation, American Institute of Aeronautics and Astronautics, June 2014.

[41] P. Rodríguez-García, *Aircraft turbine combustion noise processing.* PhD thesis, University of Southampton, October 2016.

[42] J. S. Hsu and K. K. Ahuja, "A coherence-based technique to separate ejector internal mixing noise from farfield measurements," *AIAA/CEAS 4th Aeroacoustics Conference*, June 1998.

[43] J. Bendat and A. Piersol, *Random data: analysis and measurement procedures.* Wiley-Interscience, 1971.

[44] J. Mendoza, D. Nance, and K. Ahuja, "Source Separation from Multiple Microphone Measurements in the Far Field of a Full Scale Aero Engine," in *14th AIAA/CEAS Aeroacoustics Conference (29th AIAA Aeroacoustics Conference)*, Aeroacoustics Conferences, American Institute of Aeronautics and Astronautics, May 2008.

[45] Q. Leclére, J. Antoni, E. Julliard, and A. Pintado-Peño, "Consideration of estimation error in multiple coherence approaches: application to the inside/ outside coherence analysis of aircraft flight tests," in *Proceedings: ISMA 2018*, 2018.

[46] S. M. Price and R. J. Bernhard, "Virtual coherence: A digital signal processing technique for incoherent source identification," in *Proceedings: IMAC 4*, 1987.

[47] T. Minami and K. K. Ahuja, "Five-Microphone Method for Separating Two Different Correlated Noise Sources from Far-field Measurements Contaminated by Extraneous Noise," in *9th AIAA/CEAS Aeroacoustics Conference, Hilton Head, South Carolina*, pp. 12–13, May 2003.

[48] G. Bennett and J. Fitzpatrick, "A comparison of coherence based acoustic source identification techniques," *12th International Congress on Sound and Vibration*, 2005.

[49] B. Pardowitz, U. Tapken, K. Knobloch, F. Bake, E. Bouty, I. Davis, and G. Bennett, "Core noise - Identification of broadband noise sources of a turbo-shaft engine," *20th AIAA/CEAS Aeroacoustics Conference*, pp. 1–16, June 2014.

[50] G. Bennett and J. Fitzpatrick, "Noise Source Identification for Ducted Fan Systems," in *13th AIAA/CEAS Aeroacoustics Conference (28th AIAA Aeroacoustics Conference)*, Aeroacoustics Conferences, American Institute of Aeronautics and Astronautics, May 2007.

[51] G. Bennett, I. Davis, U. Tapken, and J. Mahon, "Non-linear Identification Applied to Broadband Turbomachinery Noise," in *16th AIAA/CEAS Aeroacoustics Conference*, Aeroacoustics Conferences, American Institute of Aeronautics and Astronautics, 2010.

[52] I. Davis and G. Bennett, "Spectral, modal and coherence analysis of sum and difference scattering of narrowband noise in turbomachinery," *International Journal of Aeroacoustics*, vol. 15, no. 1-2, pp. 180–206, 2016.

[53] I. Davis and G. Bennett, "Novel Noise-Source-Identification Technique Combining Acoustic Modal Analysis and a Coherence-Based Noise-Source-Identification Method," *AIAA Journal*, vol. 53, no. 10, pp. 3088–3101, 2015.

[54] G. J. Bennett, *Noise source identification for ducted fans.* Trinity College, 2006. Ph.D. Thesis.

[55] K. R. Holland and P. A. Nelson, "An experimental comparison of the focused beamformer and the inverse method for the characterisation of acoustic sources in ideal and non-ideal acoustic environments," *Journal of Sound and Vibration*, vol. 331, no. 20, pp. 4425–4437, 2012.

[56] J. Underbrink, "Aeroacoustic phased array testing in low speed wind tunnels," in *Aeroacoustic Measurements* (T. Mueller, ed.), pp. 103–141, Springer, 2002.

[57] A. Mood, F. Graybill, and D. Boes, *Introduction to the Theory of Statistics.* McGraw-Hill Series in Probability and Statistics, McGraw-Hill, third ed., 1974.

[58] "Fundamentals of gas turbine engines," tech. rep., Commercial Aviation Safety Team. CAST Safety Plan technical notes `https://www.cast-safety.org/pdf/3_engine_fundamentals.pdf` last accessed 24/10/2018.

[59] A. Hart, K. R. Holland, and P. Joseph, "A 3 microphone method to separate direct and indirect combustion noise inside a turbofan jet engine annular combustor," *24th International Conference of Sound and Vibration*, July 2017.

[60] H. Levine and J. Schwinger, "On the radiation of sound from an unflanged circular pipe," *Phys. Rev.*, vol. 73, pp. 383–406, Feb 1948.

[61] P. A. Nelson, *Advanced Applications in Acoustics, Noise and Vibration.*, ch. Source identification and location. CRC Press, 2004.

[62] K. R. Holland and P. A. Nelson, "The application of inverse methods to spatially-distributed acoustic sources," *Journal of Sound and Vibration*, vol. 332, no. 22, pp. 5727–5747, 2013.

[63] T. F. Brooks and W. M. Humphreys, "A deconvolution approach for the mapping of acoustic sources (DAMAS) determined from phased microphone arrays," *Journal of Sound and Vibration*, vol. 294, pp. 856–879, July 2006.

[64] P. Sijtsma, "CLEAN based on spatial source coherence," *International Journal of Aeroacoustics*, vol. 6, no. 4, pp. 357–374, 2009.

[65] J. Högbom, "Aperture Synthesis with a Non-Regular Distribution of Interferometer Baselines," *Astronomy and Astrophysics Supplement*, vol. 15, pp. 417–426, June 1974.